

Università degli Studi dell'Insubria
Dipartimento di Scienza e Alta Tecnologia
Dottorato di Ricerca in Fisica e Astrofisica - Ciclo XXXIII
Anno Accademico 2019/2020



BLACK HOLES IN YOUNG STAR CLUSTERS

Ugo Niccolò Di Carlo

Supervisor:
Prof. Francesco Haardt

Co-supervisor:
Prof.ssa Michela Mapelli

Controrelatori:
Dr. Fabio Antonini
Prof.ssa Michiko Fujii

*“Imparare a leggere le cose intorno a te
Finché non se ne scoprirà la realtà
Districar le regole che non ci funzionan più
Per spezzar poi tutto con radicalità”*

L'Elefante Bianco - Area

ABSTRACT

Understanding the formation channels of binary black holes (BBHs) is one of the most urgent astrophysical questions raised by the results of the LIGO-Virgo collaboration (LVC). Two of the most likely proposed scenarios are isolated binary evolution and dynamical formation in star clusters (SCs). Lots of work has been done on the effects of dynamics on gravitational wave (GW) sources. Most previous studies focus on globular clusters and nuclear SCs, neglecting young SCs. Young SCs host fewer stars than globular and nuclear SCs, but they make up the vast majority of the SCs in the Universe (Kroupa and Boily, 2002), and their cumulative contribution to black hole (BH) demography may thus be significant. The aim of this Thesis is to understand what is the global effect of dynamics of young SCs on BHs, focusing on GW sources. To investigate this topic, I make use of numerical simulations of SCs. During my PhD, I have interfaced the direct Nbody code Nbody6++GPU (Wang et al., 2015) with the population synthesis code MOBSE (Giacobbo et al., 2018), to perform accurate N-body simulations with up-to-date stellar evolution. I have run a suite of 10^4 simulations of young SCs with different initial mass ($10^3 M_\odot \leq M_{\text{SC}} \leq 3 \times 10^4 M_\odot$), metallicity and radius. I have integrated my SCs with a 40% initial binary fraction and fractal initial conditions, to mimic the clumpiness of star forming regions.

I find that dynamics significantly affects the properties of merging BBHs in young SCs: dynamical exchanges favour the formation and the merger of massive BBHs with total mass up to $m_{\text{tot}} \sim 140 M_\odot$ and with mass ratio ranging from $q \sim 1$ to $q \sim 0.1$ (although large mass ratios are more likely). For comparison, merging BBHs evolved in isolation have maximum total mass $m_{\text{tot}} \lesssim 80 M_\odot$ and a significantly stronger preference for large mass ratios. Metallicity strongly affects the mass spectrum of BHs, BBHs and merging BBHs, which tend to be more massive in metal-poor SCs. We find $\sim 6\%$, $\sim 2\%$, and $< 1\%$ of BHs with mass $m_{\text{BH}} > 60 M_\odot$ at $Z = 0.0002$, 0.002 and 0.02 , respectively. Based on our simulations, the most massive LIGO-Virgo events (GW170729 and GW190521) and the first unequal-mass merger (GW190412) can only be explained by exchanged BBHs in metal-poor SCs. Another important difference between the isolated and the dynamical channel is the merger efficiency, i.e. the ratio between the number of mergers and the total simulated mass. In our simulations, we find that while at low metallicity isolated and dynamical binaries have comparable merger efficiencies, at solar metallicity the merger efficiency of SCs is about two orders of magnitude larger. The main

reason is that dynamical encounters trigger the merger of BBHs even at high metallicity, where binary evolution is unlikely to produce mergers.

Our simulations (Di Carlo et al., 2019) predicted that BHs in the pair instability (PI) gap can form via (multiple) stellar mergers: $\sim 5.6\%$, $\sim 1.5\%$ and $\sim 0.1\%$ of all the simulated BHs have mass in the PI gap for metallicity $Z = 0.0002$, 0.002 and 0.02 , respectively. Several BHs with masses in the gap form a BBH through dynamical exchanges: $\sim 2.2\%$, $\sim 2.1\%$ and $\sim 0\%$ of all BBHs merging within a Hubble time have at least one component in the mass gap for metallicity $Z = 0.0002$, 0.002 and 0.02 , respectively. Mass-gap BBHs form preferentially in the most massive SCs ($M_{\text{SC}} \geq 6000 M_{\odot}$). We predicted that $\sim 5\%$ of all BBH mergers detected by LIGO and Virgo at design sensitivity have at least one component in the PI mass gap, under the assumption that all stars form in young SCs. These results strongly favour a dynamical formation of GW190521 via stellar mergers in SCs.

Intermediate black holes (IMBHs) with masses up to $\sim 440 M_{\odot}$ form in our simulations via the runaway collision mechanism. The fraction of IMBHs with respect to the total number of BHs is $\sim 0.4\%$, $\sim 0.2\%$ and $\sim 0.02\%$ for metallicity $Z = 0.0002$, 0.002 and 0.02 , respectively. IMBHs are extremely efficient in finding a companion BH: $\sim 70\%$ of all IMBHs reside in a BBH at the end of the simulations. SCs with IMBHs tend to expand more than SCs without IMBHs. The expansion happens in the first ~ 20 Myr. Higher Lagrangian radii expand more, meaning that the expansion is stronger in the outer region of the SCs.

Our results show that young SCs play a key role in the dynamical formation of massive BBHs and IMBHs. Our simulations have a legacy value: our unique catalogues of BBH mergers in young SCs can give an essential contribution to understanding the formation channels of BBHs, in light of future observations by LIGO and Virgo and by the next-generation ground-based GW detectors.

TABLE OF CONTENTS

Abstract	ii
1 Introduction	1
1.1 The Gravitational Waves Era	1
1.2 Gravitational waves	2
1.3 Formation Channels of Binary Black Holes	5
1.4 Star Clusters	11
1.5 Direct N-body simulations	23
2 Merging black holes in young star clusters	30
2.1 Introduction	31
2.2 Methods	34
2.3 Results	38
2.4 Comparison with previous work	55
2.5 Discussion	57
2.6 Summary	59
3 Binary black holes in the pair-instability mass gap	61
3.1 Introduction	62
3.2 Methods	63
3.3 Results	65
3.4 Conclusions	73
4 Binary black holes in young star clusters: the impact of metallicity	75
4.1 Introduction	76
4.2 Methods	78
4.3 Results	83
4.4 Discussion	95
4.5 Conclusions	98
5 Intermediate mass black holes in young star clusters	102
5.1 Introduction	103
5.2 Methods	105
5.3 Results	108
5.4 Discussion	125

5.5	Conclusions	126
5.6	Appendix A: Comparing the high-mass tails of the IMBH mass distributions at different metallicities	128
6	Conclusions	130
	List of Tables	134
	List of Figures	135
	Bibliography	137

INTRODUCTION

1.1 The Gravitational Waves Era

September 14, 2015 marks an important date in physics history. The very first gravitational wave (GW) signal, GW150914, emitted by the merger between two black holes (BHs) with masses $m_1 = 35.6M_\odot$ and $m_2 = 30.6M_\odot$, was detected by the ground-based LIGO interferometers (Abbott et al., 2016f), confirming the prediction by Albert Einstein (Einstein, 1916; Einstein, 1918). We now know that the Universe is speaking to us also through GWs, and we can use the detections to sort out many unresolved astrophysical questions. Thus, the detection of GW150914 was heralded as inaugurating a revolutionary era in multi-messenger astronomy. So far, the Ligo-Virgo collaboration (LVC) has completed three observing runs and detected the merger of several tens of compact object binaries (Abbott et al., 2016a; Abbott et al., 2016c; Abbott et al., 2016e; Abbott et al., 2017a; Abbott et al., 2017d; Abbott et al., 2017; Abbott et al., 2020a; Abbott et al., 2020b; Abbott et al., 2020). The detection of these GW signals challenged many well supported theories and taught us several new concepts about the Universe. First, GW detections provide one of the most concrete evidences for the existence of black holes to date. For instance, GW150914 suggests that the separation of the two objects prior to the merger was just 350 km (roughly four times the Schwarzschild radius corresponding to the inferred masses). The objects must therefore have been extremely compact, leaving black holes as the most plausible interpretation. The first detection also confirmed that binary black holes (BBHs) exist and can merge in less than an Hubble time. Moreover, before GW detections, the scientific community was skeptical about the existence of BHs with masses larger than $30M_\odot$, which was predicted by only few stellar evolution models (Mapelli et al., 2009; Mapelli et al., 2010; Belczynski et al.,

2010; Fryer et al., 2012; Mapelli et al., 2013; Ziosi et al., 2014; Spera et al., 2015). Last but not least, all the detections serve as a test of general relativity.

It is thus a great time to study BBHs, as they represent one of the main sources of detectable GWs so far. In my Thesis, I have investigated the formation channels of BBHs in young star clusters (YSCs) by means of state of the art direct N-body simulations coupled with up to date stellar evolution.

1.2 Gravitational waves

Gravitational waves (GW) are perturbations in the curvature of spacetime, generated by accelerated masses, that propagate as waves outward from their source at the speed of light. When a GW passes through space it deforms it proportionally to its amplitude. Figure 1.1 shows a schematic deformation for both the + (plus) and \times (cross) wave polarization modes.

The existence of GWs was predicted in 1916 by Albert Einstein in his general theory of relativity. The derivation starts from the Einstein equation:

$$R_{\alpha\beta} - \frac{1}{2}g_{\alpha\beta}R = \frac{8\pi G}{c^4}T_{\alpha\beta}, \quad (1.1)$$

where $R_{\alpha\beta}$ is the Ricci curvature tensor, $g_{\alpha\beta}$ is the metric tensor, R is the scalar curvature, G is the gravitational constant, c is the speed of light and $T_{\alpha\beta}$ is the stress-energy tensor. Now, we consider that the waves emitted by the source are so weak that the metric can be expressed as a small perturbation $h_{\alpha\beta}$ (with $|h_{\alpha\beta}| \ll 1 \forall \alpha, \beta$) of the metric of flat spacetime $\eta_{\alpha\beta}$:

$$g_{\alpha\beta} = \eta_{\alpha\beta} + h_{\alpha\beta}. \quad (1.2)$$

We now define the "trace-reversed" amplitude

$$\bar{h}_{\alpha\beta} = h - \frac{1}{2}\eta_{\alpha\beta}h, \quad (1.3)$$

where $h = h^\gamma_\gamma$. Using the Lorentz gauge conditions, we can now write the linearized Einstein equation:

$$\square \bar{h}_{\alpha\beta} = \left(-\frac{\partial^2}{\partial t^2} + \nabla^2 \right) \bar{h}_{\alpha\beta} = -\frac{16\pi G}{c^4}T_{\alpha\beta}. \quad (1.4)$$

If we assume vacuum, equation 1.4 becomes:

$$\square \bar{h}_{\alpha\beta} = 0, \quad (1.5)$$

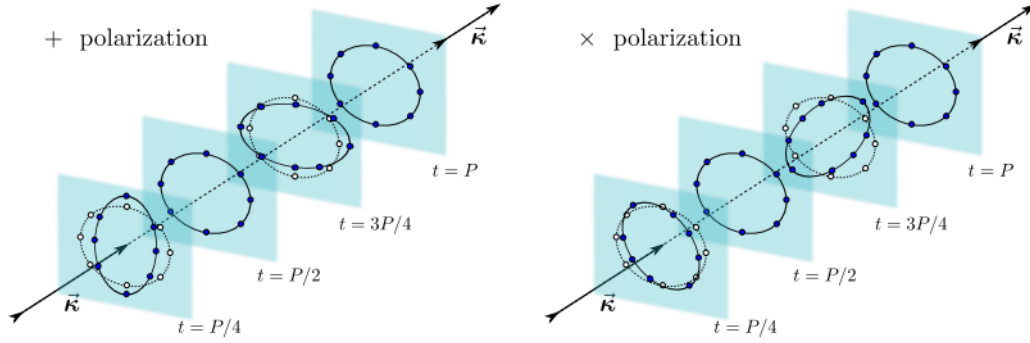


Figure 1.1: From Bishop and Rezzolla, 2016. Schematic deformations produced on a ring of freely-falling particles by GWs that are linear polarized in the “+” (“plus”) and “x” (“cross”) modes. The continuous lines and the dark filled dots show the positions of the particles at different times, while the dashed lines and the open dots show the unperturbed positions.

which has the form of a three-dimensional wave equation.

By integrating equation 1.4, Einstein derived the so called quadrupole formula for gravitational radiation:

$$\bar{h}^{ij} = \frac{2G}{c^4 r} \ddot{I}^{ij}(t - r/c), \quad (1.6)$$

where r is the source-observer distance and I^{ij} is the quadrupole moment of the mass distribution. The monopole and dipole terms disappear in the calculation. This means that the wave amplitude is proportional to the second time derivative of the quadrupole moment of the source; not all accelerating masses emit GWs, the only capable of such a job are the mass distributions with no spherical and rotational symmetry. It is important to point out that in the course of the derivation of equation 1.6, Einstein assumed that r must be much larger than the wavelength λ and that $T_{\alpha\beta}$ must not change very quickly. The result is quite accurate for all the sources, as long as the reduced wavelength $\tilde{\lambda} = \lambda/2\pi$ is much longer than the source size R .

Due to the nature of gravitational interaction, the strain of GWs in the vicinity of Earth is very small and has an order of magnitude $\lesssim 10^{-21}$. Such small perturbations are incredibly difficult to detect; this why so far, with the current detectors and data analysis techniques, we have only been able to detect one of the most powerful astrophysical GW sources: merging compact object binaries.

1.2.1 Gravitational Waves from Binary Black Holes

Among all the proposed sources of GWs, only compact binary mergers have been observed to date. This thesis focuses on binary black holes (BBHs). The life-cycle of such objects consists of three different phases: the inspiral, the merger and the ringdown. The first stage of the life of a BBH is the inspiral, during which the orbital separation gradually shrinks due to GW emission.

The formulae for the time evolution of the semi-major axis a and the eccentricity e were derived by Peters, 1964:

$$\frac{da}{dt} = -\frac{64}{5} \frac{G^3 m_1 m_2 (m_1 + m_2)}{c^5 a^3 (1 - e^2)^{\frac{7}{2}}} \left(1 + \frac{73}{24} e^2 + \frac{37}{96} e^4 \right); \quad (1.7)$$

$$\frac{de}{dt} = -\frac{304}{15} e \frac{G^3 m_1 m_2 (m_1 + m_2)}{c^5 a^4 (1 - e^2)^{\frac{5}{2}}} \left(1 + \frac{121}{304} e^2 \right); \quad (1.8)$$

where t is time, m_1 and m_2 are the masses of the primary and of the secondary BHs (with $m_1 > m_2$).

By integrating equations 1.7 and 1.8 we can estimate the merger timescale t_{GW} , i.e. the time in which the two objects reach coalescence:

$$t_{GW} = \frac{5}{264} \frac{c^5 a^4 (1 - e^2)^{\frac{7}{2}}}{G^3 m_1 m_2 (m_1 + m_2)}. \quad (1.9)$$

t_{GW} strongly depends on the orbital separation, on the eccentricity and on the masses of the BHs. It can be shown that for a Keplerian binary, the strain of emitted GWs is $h \propto \frac{1}{a}$ and the frequency of emitted GWs ω_{GW} is twice the orbital frequency of the binary ω_{orb} . As the BBH orbit shrinks, the strain and the frequency of emitted GWs increase. As the BHs get closer, GWs cause the orbit to shrink faster. When the orbital separation reaches the last stable orbit (defined as $r_{LSO} = 3 R_S$ in the case of a non-spinning BH) of the primary BH, the merger phase starts. During this phase, GW emission peaks as the two BHs merge into one. The now single black hole will oscillate to find its final equilibrium. This oscillation is damped in the ringdown stage by the emission of gravitational waves.

The only GW signals detected so far come from the merger of compact object binaries: BBHs, binary neutron stars (BNS) and BH-neutron star (BHNS) binaries. So far, the LIGO-Virgo collaboration has detected a total of 50 low false alarm rate events; some of the most interesting ones are listed in table 1.1. Among all, some of them present intriguing features: GW170817 is the first BNS merger, and its electromagnetic counterpart was observed; GW190412 is the first unequal mass merger; GW190521 has the largest progenitor masses to date, and the primary mass lies

Table 1.1: List of some of the most impactful events observed by the LIGO-Virgo collaboration

Event	Binary type	m_1 [M_\odot]	m_2 [M_\odot]	M [M_\odot]
GW150914	BBH	$35.6^{+4.8}_{-3.0}$	$30.6^{+3.0}_{-4.4}$	$63.1^{+3.3}_{-3.0}$
GW170817	BNS	$1.46^{+0.12}_{-0.1}$	$1.27^{+0.09}_{-0.09}$	$2.74^{+0.04}_{-0.01}$
GW190412	BBH	$30.0^{+4.7}_{-5.1}$	$8.3^{+1.6}_{-0.9}$	$37.3^{+3.9}_{-3.9}$
GW190521	BBH	$91.4^{+29.3}_{-17.5}$	$66.8^{+20.7}_{-20.7}$	$150.3^{+35.8}_{-20.0}$
GW190814	?	$23.2^{+1.1}_{-1.0}$	$2.59^{+0.08}_{-0.09}$	$25.6^{+1.0}_{-0.9}$

Column 1: event name; column 2: binary type; column 3: Mass of the primary BH (m_1); column 4: mass of the secondary BH (m_2); column 5: final remnant mass (M);

in the PISN mass gap; GW190814’s secondary mass lies in the mass gap between neutron stars and black holes ($2.5 - 5 M_\odot$). A detailed plot which shows all the characteristics of the detections of the observing run O3a is represented in Figure 1.3. A nice picture which shows the masses of all the mergers detected so far is shown in figure 1.4.

Sources different from compact object binaries are either too weak or emit GWs outside the LIGO-Virgo frequency range. The scientific community is working on next generation detectors which will help us to detect many more types of GW sources.

1.3 Formation Channels of Binary Black Holes

Understanding the formation channels of merging BBHs is one of the most urgent astrophysical questions raised by the results of the LIGO-Virgo collaboration (LVC). In order to better understand how BBHs can form, I will briefly summarize the main stellar evolution processes which lead to the formation of BHs.

1.3.1 Formation of Black Holes

BHs are the remnants of massive stars ($m \gtrsim 20 M_\odot$). The final mass of a BH strongly depends upon the evolutionary history of the progenitor star; mass loss through stellar winds and supernova explosion are thought to be the two main stellar evolution processes which affect the formation of the remnant.

A stellar wind is a flow of gas ejected from the upper atmosphere of a star. The different mechanisms through which the gas is ejected primarily depend on the mass, the stellar type and the metallicity of the star. Stellar winds of cold and low mass stars are powered by radiation pressure on dust particles, while winds of hot and

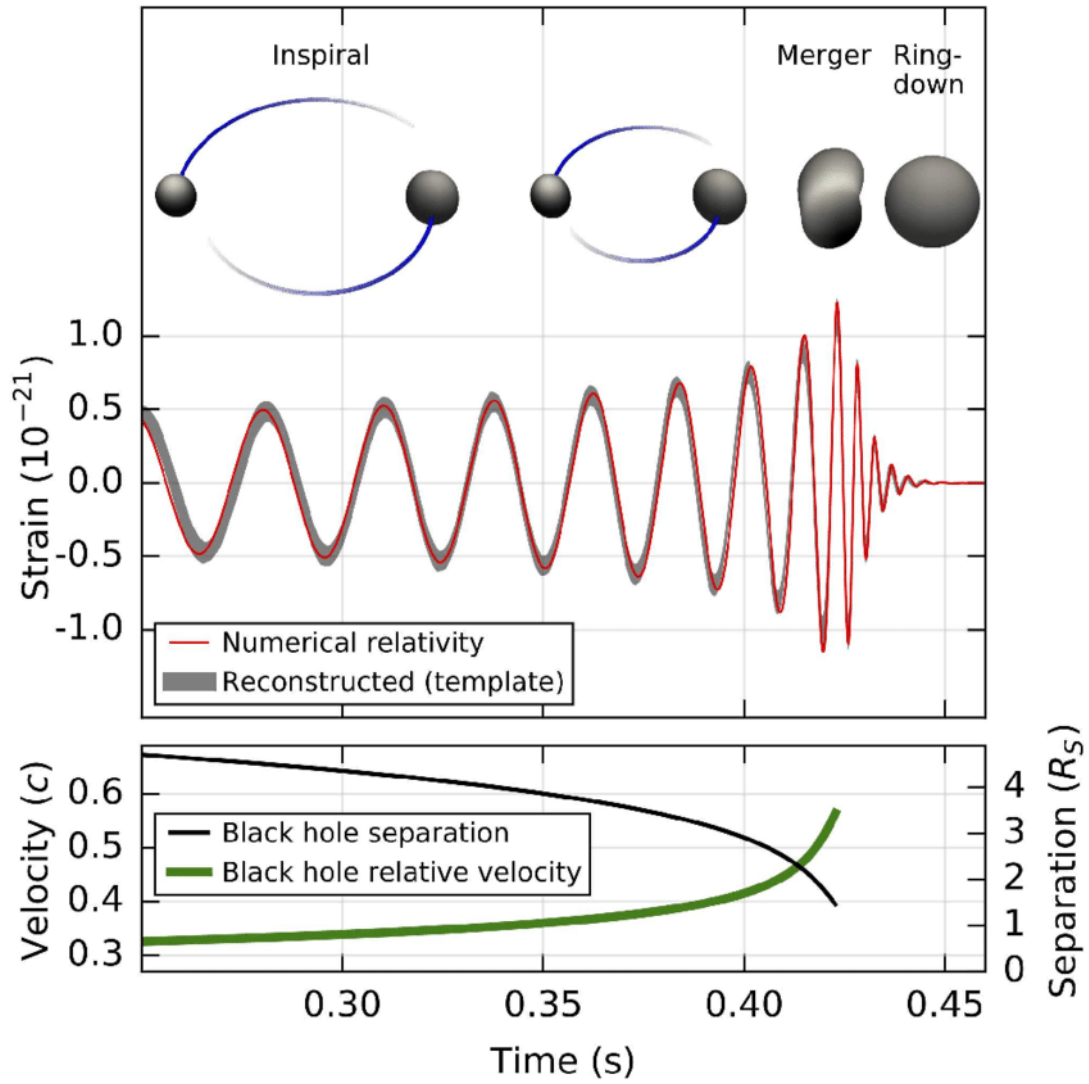


Figure 1.2: From Abbott et al., 2016a. Top: Estimated gravitational-wave strain amplitude from GW150914. Bottom: The Keplerian effective BH separation in units of Schwarzschild radii ($R_s = 2GM/c^2$) and the effective relative velocity.

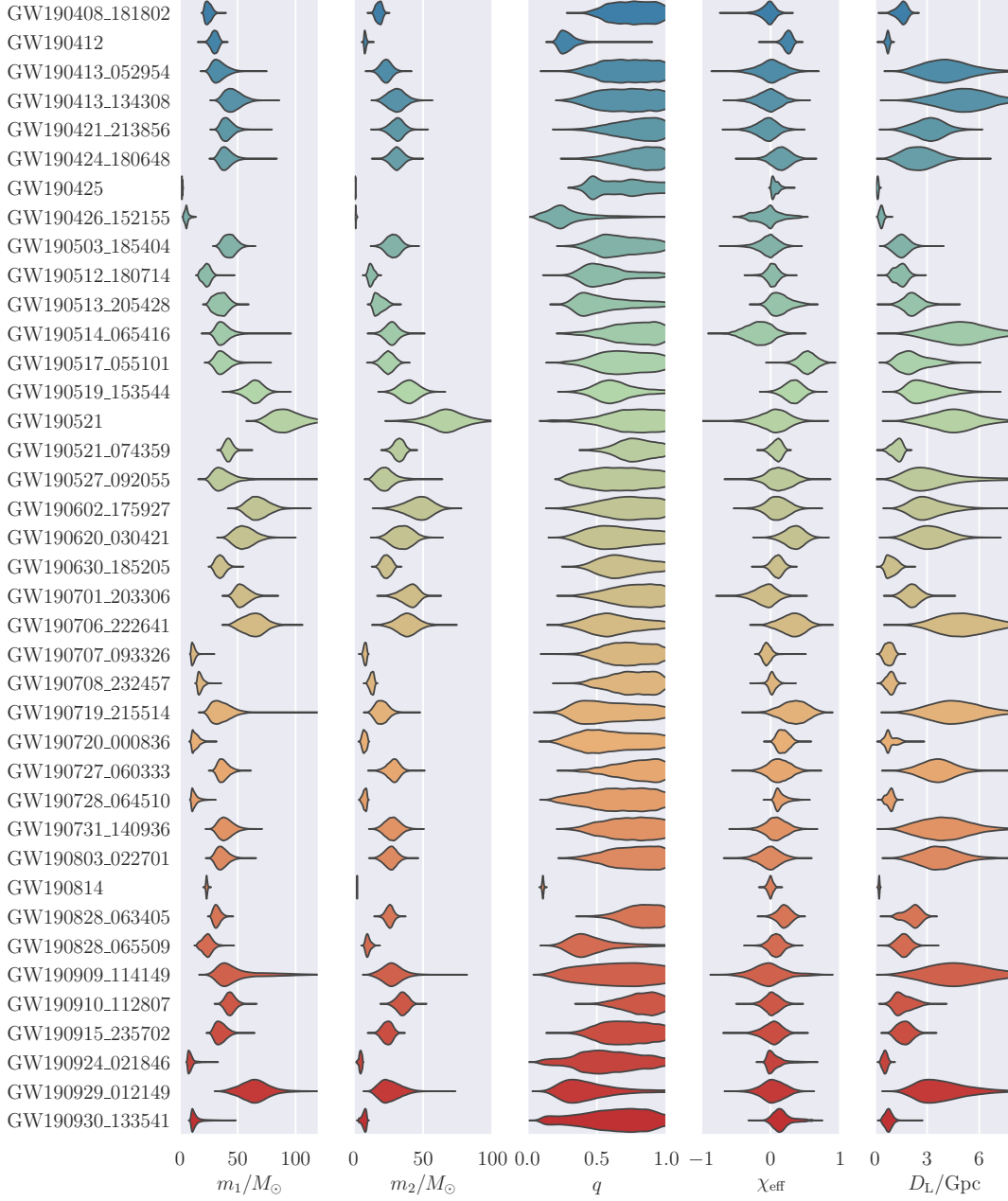


Figure 1.3: From Abbott et al., 2020a. Marginal posterior distributions on primary mass m_1 , secondary mass m_2 , mass ratio q , effective spin χ_{eff} , and the luminosity distance D_L for all candidate events in the observing run O3a. The vertical extent of each colored region is proportional to one-dimensional marginal posterior distribution at a given parameter value for the corresponding event.

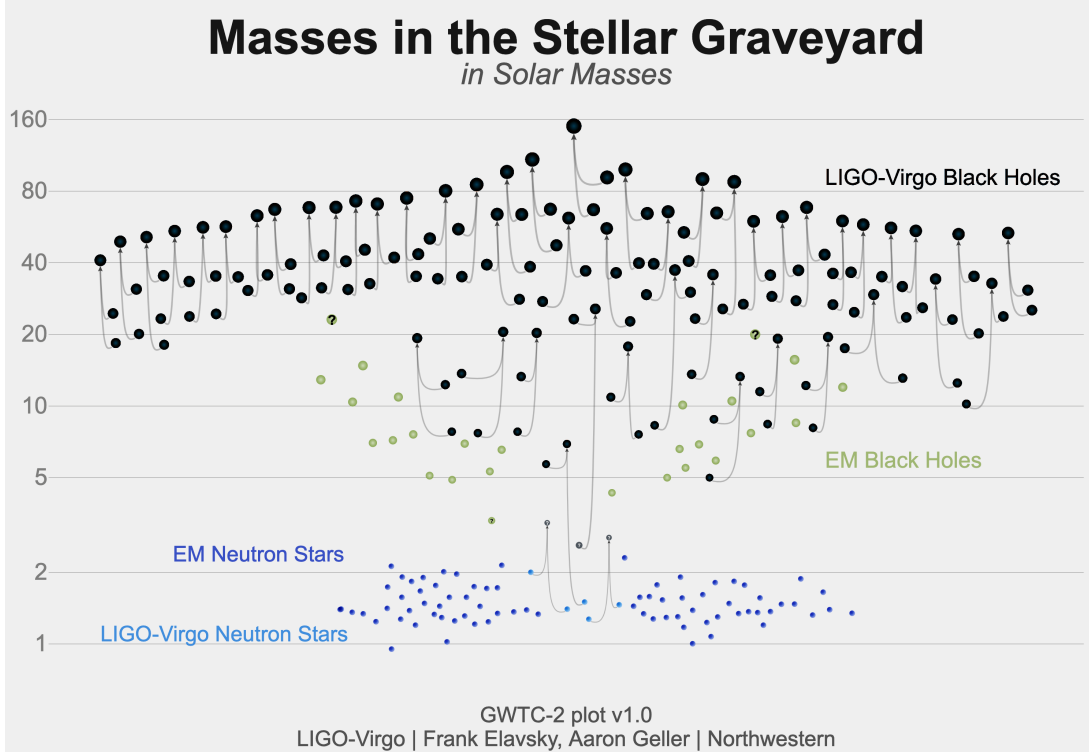


Figure 1.4: Masses of all the detected and observed NSs and BHs so far. Credits: LIGO-Virgo, F. Elavski, A. Geller

massive stars (O and B-type stars, Wolf-Rayet stars, luminous blue variable stars) are driven by radiation pressure on the resonance absorption lines of heavy elements. Mass loss through stellar winds of hot massive stars depends on the metallicity Z according to the relationship $\dot{M} \propto Z^\beta$, where β depends on the model. In this thesis we adopt the wind models used in PARSEC (Bressan et al., 2012; Chen et al., 2015):

$$\beta = \begin{cases} 0.85 & \text{if } \Gamma_e < 2/3 \\ 2.45 - 2.4\Gamma_e & \text{if } 2/3 \leq \Gamma_e < 1 \\ 0.05 & \text{if } \Gamma_e \geq 1, \end{cases} \quad (1.10)$$

where Γ_e is the Eddington factor (see e.g. Gräfener and Hamann, 2008, Chen et al., 2015). Stellar winds are the most important mass loss mechanism in single stellar evolution and they strongly affect the pre-supernova mass, which is an important parameter in the determination of the mass of the compact remnant. Another important parameter to take into account is the pre-supernova Helium core mass m_{He} . If $m_{\text{He}} \lesssim 32 M_\odot$, an iron core collapse supernova or a direct collapse take place. If $32 \lesssim m_{\text{He}} \lesssim 64$ a pulsational pair instability (PPI) takes place (Barkat et al., 1967; Woosley et al., 2007); pair production (the production of free electrons and

positrons in the collision between atomic nuclei and energetic gamma rays) temporarily reduces the internal radiation pressure of the star and the core undergoes a series of pulsations which make the star lose mass until it finds a new equilibrium. After this, the star ends its life by core-collapse supernova or by direct collapse. If $64 \lesssim m_{\text{He}} \lesssim 135 M_{\odot}$ we have a pair instability supernova (PISN); pair production becomes very efficient and the huge pressure drop leads to a partial collapse, which causes greatly accelerated burning in a runaway thermonuclear explosion, resulting in the star being blown completely apart without leaving a stellar remnant behind. If $m_{\text{He}} \gtrsim 135 M_{\odot}$, the collapse cannot be stopped, and the result is the formation of a BH via direct collapse, with no mass loss.

It is important to mention that the PISN and PPI mechanisms prevent the formation of BHs with mass between ~ 60 and $\sim 120 M_{\odot}$ from single stellar evolution. Hence, the recent detection of a BBH merger with the mass of the primary BH in the pair instability gap (GW190521, Abbott et al., 2020) challenges current models of BH formation.

1.3.2 Formation of Binary Black Holes

A BBH is a system consisting of two black holes in close orbit around each other. Such systems may form through many pathways. Two of the most studied channels are the isolated and the dynamical scenarios.

1.3.2.1 Isolated

Isolated binaries are binary systems of stars which are bound since their birth (Tutukov et al., 1973; Portegies Zwart and McMillan, 2000a; Belczynski et al., 2002; Belczynski et al., 2016b; Giacobbo and Mapelli, 2018). Binaries evolve unperturbed, going through many binary stellar evolution processes which crucially affect the evolution of the stars. If the binary survives and both the stars turn into a BH, we end up with a BBH. The most important processes for the formation of BBHs are common envelope (CE) and natal kicks.

A CE is formed in a binary star system when the orbital separation decreases rapidly or one of the stars expands rapidly. When a star overfills its Roche lobe, it starts to transfer its mass to the other member of the binary. As a consequence, the orbit will shrink further causing a runaway process of dynamically unstable mass transfer, which leads to the formation of a common envelope engulfing the companion star and thus shrinking the orbital separation of the binary (Paczynski, 1976). Orbital energy is converted into kinetic energy, which tends to unbound the envelope. If such energy is sufficient to completely eject the envelope, the binary system survives and continues its evolution, eventually turning into a BBH. The orbital shrinking operated by the CE enhances GW emission speeding up the merger of the binary. If the converted energy is not sufficient, the stars merge neglecting the formation of a BBH. A schematic representation of the CE evolution with both the possible outcomes is shown in Figure 1.5.

A natal kick is a phenomenon that causes a compact object to obtain a spatial velocity at its birth as a result of asymmetric SN explosions (Janka and Mueller, 1996) or anisotropic neutrinos emission (Woosley, 1987; Bisnovatyi-Kogan, 1993). If the SN happens in a binary, even if mass loss is completely symmetric, the orbital properties of the binary system are also affected by the so called Blaauw-kick (Blaauw, 1961). The scarcity of observations and the complexity of the phenomenon make natal kicks far from being understood. Most observational estimates of the entity of natal kicks are based on observations of Galactic neutron stars. Hobbs et al., 2005 suggest that the distribution of the kicks is fitted by a Maxwellian distribution with $\sigma = 265 \text{ km s}^{-1}$. Other studies (Fryer et al., 1998; Arzoumanian et al., 2002; Verbunt et al., 2017) suggest that the observed distribution is better fitted by bi-modal distributions. The situation for BHs is even more uncertain due to the scarcity of data and to the difficulty of interpreting them Repetto et al., 2012; Repetto et al., 2017.

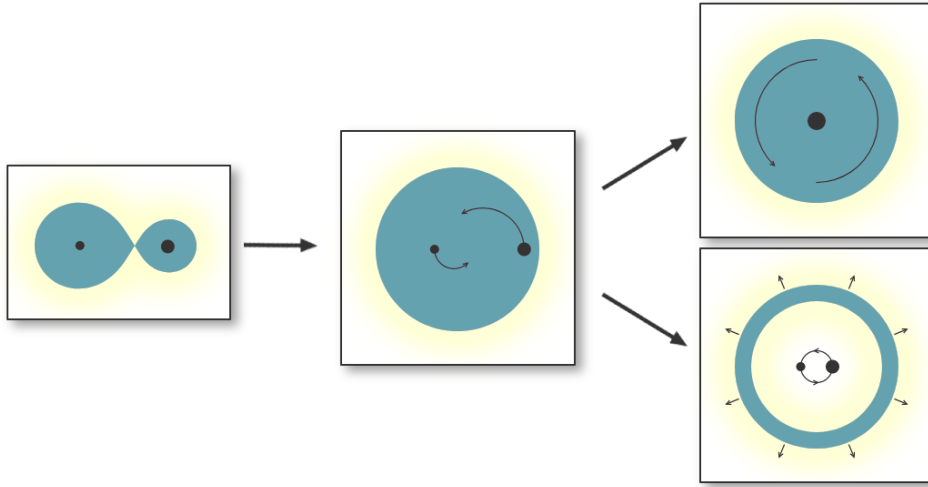


Figure 1.5: Key stages in the common envelope phase. Left: A star fills its Roche lobe. Middle: The companion is engulfed; the core of the primary and the companion spiral towards one another inside a common envelope. Top right: the two stars merge; bottom right: the envelope is ejected.

1.3.2.2 Dynamical

The isolated channel assumes that the binary systems evolve completely unperturbed, but we know that the vast majority of massive stars (i.e. the progenitors of compact objects) are born in clustered environments called star clusters (SCs, Lada and Lada, 2003). Such environments can reach very high densities (up to $10^6 M_{\odot}/\text{pc}^3$ in the core of globular clusters), where a plethora of dynamical interactions and collisions take place. A binary system which evolves in a SC will likely be affected by such processes. More details on the characteristics of SCs and on dynamical processes are given in the next section. Searching for distinctive fingerprints of dynamical evolution in the properties of BBHs may help us to understand the formation channels of the mergers detected by LIGO-Virgo.

1.4 Star Clusters

Star clusters (SCs) are self-gravitating collisional systems made up of stars. It is generally assumed that all the stars of a SC form from the same molecular cloud in a single star-formation event, so that they have approximately the same age and chemical composition. They are excellent laboratories to study stellar dynamics, stellar evolution, GW sources and the formation of massive BHs. In order to better

describe the properties of such systems, some typical size-scales and time-scales need to be defined.

1.4.1 Size-scales

Star clusters tend to be approximately spherical in space or circular on the sky, so it is useful to define some different quantities to measure their size. Lagrangian radii are the distances from the center containing specific fractions of the total mass of the cluster. The most frequently used Lagrangian radius is called half-mass radius r_{hm} and it is the one containing 50% of the mass of the cluster. A similar definition for observers can be made using fractions of projected luminosity. The analog of the half-mass radius is the half-light radius r_{hl} , sometimes also called effective radius. The virial radius is defined as:

$$r_{\text{vir}} = \frac{GM^2}{2|W|} \quad (1.11)$$

where M is the total mass of the cluster and W is the total potential energy. It is a theoretical definition used to determine sizes of systems without a sharp boundary. The tidal radius r_t is the radius where the gravitational acceleration of the cluster equals the tidal acceleration of the parent galaxy; it roughly correspond to the distance where the density of stars drops to a value comparable to the background. Finally, the core radius r_c has several definitions. Observers define it as the radius at which the surface brightness equals half of its central value. Theorists define it in two different ways. The first is:

$$r_c = \sqrt{\frac{3\langle v^2 \rangle_0}{4\pi G \rho_0}} \quad (1.12)$$

where ρ_0 and $\langle v^2 \rangle_0$ are the central density and velocity dispersion. This is roughly the distance at which the projected density drops by a factor of two. The second is generally used in N-body simulations and it's a density-weighted radius:

$$r_d = \sqrt{\frac{\sum_i \rho_i^2 r_i^2}{\sum_i \rho_i^2}} \quad (1.13)$$

1.4.2 Time-scales

There are two fundamental time scales concerning star clusters: the dynamical time scale t_{dyn} and the relaxation time scale t_{rel} .

The dynamical time-scale is the time required for a typical particle to cross the system, over which the system establishes the dynamical equilibrium. It may be defined as:

$$t_{\text{dyn}} = \frac{GM^{5/2}}{(-4E)^{3/2}}, \quad (1.14)$$

where E is the total energy of the cluster. Another definition for systems in virial equilibrium is:

$$t_{\text{dyn, vir}} = \left(\frac{GM}{r_{\text{vir}}^3} \right)^{-1/2} \sim 2 \times 10^4 \text{ yr} \left(\frac{M}{10^6 M_{\odot}} \right)^{-1/2} \left(\frac{r_{\text{vir}}}{1 \text{ pc}} \right)^{3/2}. \quad (1.15)$$

The relaxation time is the time over which stars reach equilibrium through mutual interactions and lose memory of their initial velocities. An expression for the local relaxation time is:

$$t_{\text{rl}} = \frac{\langle v^2 \rangle^{3/2}}{15.4 G^2 m \rho \ln \Lambda}, \quad (1.16)$$

where m is the local mean mass, ρ is the local density and $\ln \Lambda$ is the Coulomb logarithm. This process will be described in Section 1.4.4.

1.4.3 Properties of cluster systems

We observe at least four different kinds of SCs.

Globular clusters (GCs) are nearly spherical systems made up of $10^4 - 10^6$ population II low mass stars ($m \lesssim 1 M_{\odot}$). They do not contain gas and dust and their age is comparable to the age of the Universe. GCs are extremely dense: their core can reach densities up to $\sim 10^6 M_{\odot} \text{ pc}^{-3}$. They mainly reside in the halos of galaxies, orbiting the galactic core. GCs also show the feature of multi-population: they contain several distinct and discrete populations of stars distinguished by their chemical composition. Many aspects about GCs are still unconstrained: their formation, the onset of multiple populations and their role in galactic evolution are unclear and matter of debate (see e.g. Gratton et al., 2019).

Open Clusters (OCs) are loosely bound systems made up of $10 - 10^4$ stars. They may still contain gas and are younger and less dense than GCs ($\rho \lesssim 10^3 M_{\odot} \text{ pc}^{-3}$). OCs reside in the disk of galaxies. In the Milky Way, some of them are visible to the naked eye (e.g. Hyades in figure 1.6 or the Pleyades).

Young Massive Clusters (YMCs) are very young ($t \lesssim 100 \text{ Myr}$) systems composed of $10^3 - 10^5$ young stars which may still contain gas. They have smaller size than GCs but their densities are comparable. This makes them have a faster dynamical evolution due to two-body relaxation, a process which will be better explained in

Table 1.2: Comparison of fundamental parameters for star cluster families: open clusters (OCs), globular clusters (GCs), young massive clusters (YMCs) and nuclear star clusters (NSCs). The numbers in the columns are intended to be indicative.

Cluster	Age [Gyr]	m_{to} [M_{\odot}]	M [M_{\odot}]	r_{vir} [pc]	ρ_c [M_{\odot}/pc^3]	Location	t_{dyn} [Myr]	t_{rh} [Myr]
OC	$\lesssim 0.3$	$\lesssim 4$	$\lesssim 10^3$	~ 1	$\lesssim 10^3$	disk	~ 1	$\lesssim 100$
GC	$\gtrsim 10$	~ 0.8	$\gtrsim 10^5$	~ 10	$\gtrsim 10^3$	halo	$\gtrsim 1$	$\gtrsim 1000$
YMC	$\lesssim 0.1$	$\gtrsim 5$	$\gtrsim 10^4$	~ 1	$\gtrsim 10^3$	disk	$\gtrsim 1$	$\lesssim 100$
NSC	$\gtrsim 10$	-	$10^6 - 10^8$	$2 - 5$ pc	$10^6 - 10^7$	center	$\gtrsim 1$	$\gtrsim 1000$

Column 1: SC type; column 2: SC age; column 3: turn-off mass; column 4: total SC mass; column 5: virial radius; column 6: core density; column 7: location where these clusters are found; column 8: dynamical timescale; column 9: relaxation time scale.

section 1.4.4. They reside in the disk of galaxies and since they are so young they have a much larger fraction of massive stars than other kinds of SCs; we know that some YMCs like R136 (figure 1.6) host some stars with masses larger than $150M_{\odot}$. Nuclear Star Clusters (NSCs) are star clusters with high density and high luminosity which reside near the center of mass of most galaxies. NSCs are amongst the most dense stellar structures ever observed and they are made of both young and old stars. We observe a NSC in the center of the Milky Way, surrounding the super massive black hole (Schödel et al., 2014). The formation of NSCs is a controverted topic; two of the main proposed theories are in situ formation of stars and the formation by accretion of other smaller clusters which inspiral and merge (Antonini et al., 2012).

Finally, it is important to mention OB stellar associations. A stellar association is defined as a gravitationally unbound SC, which is usually a very loose system which contains $\sim 10 - 100$ stars. OB associations contain mostly massive stars of spectral class O and B. OB associations are thought to be the result of the expansion of initially gravitationally-bound SCs. However, recent results (see e.g. Ward et al. 2020) show that they may form in the low density regions of molecular clouds, never being part of a larger bound SC.

Some fundamental parameters of these kinds of SCs and their location in the Milky Way are reported in table 1.2 and in figure 1.7 for comparison.



Figure 1.6: Left: HST image of the open cluster NGC265 in the Small Magellanic Cloud. The image is ~ 25 pc per edge. Center: M4, a globular cluster in the Milky Way. It is one of the closest GCs to the Solar System, with an estimated age of 12.2 Gyr. Image from the MPG/ESO 2.2-metre telescope at ESO's La Silla Observatory. The image is ~ 20 pc per edge. Right: an HST image of R136, a YMC near the center of the 30 Doradus region in the LMC. The image is ~ 50 pc per edge.

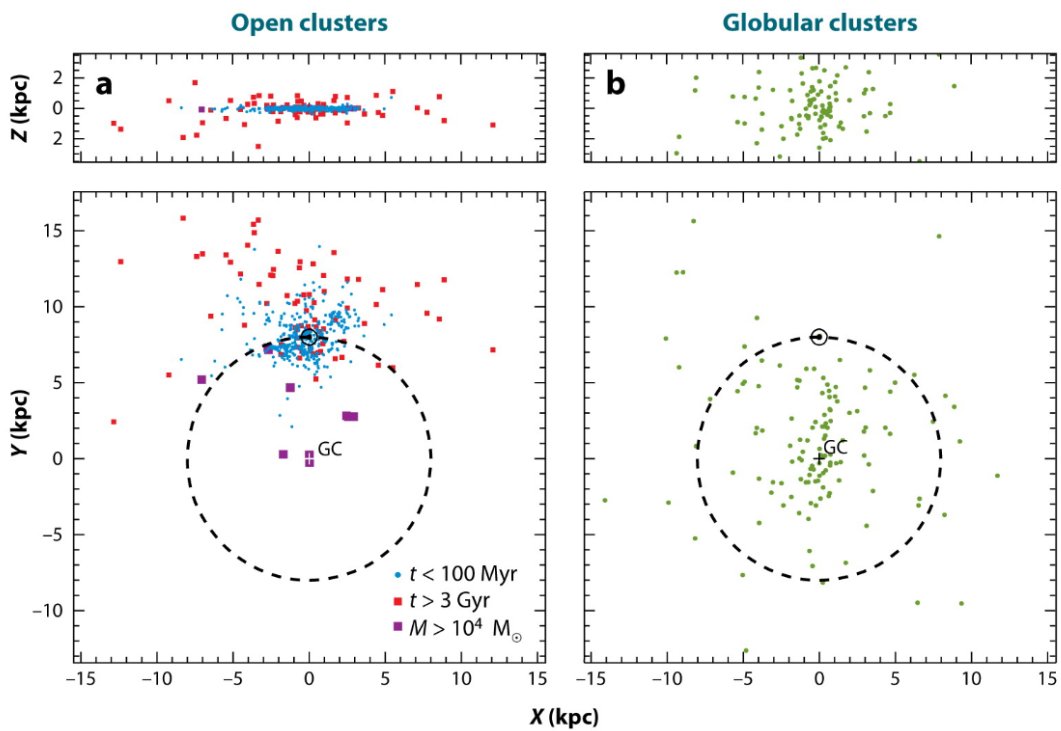


Figure 1.7: Distribution of star clusters in the Milky Way. The Galaxy is seen edge-on (face-on) in the top (bottom) panels. The black dashed circle is the Sun's orbit around the Milky Way, the small black circle represents the Sun. Left: distribution of open clusters and young massive clusters (from the Dias 2012 catalogue). Right: distribution of GCs (from the Harris 1996 Catalogue). It's clear that GCs are spherically distributed around the center of the Galaxy while the other clusters are in the disk. The majority of known OCs is near the Sun because of the extinction of dust which does not allow us to observe them over certain distances (from Lada and Lada, 2003).

1.4.4 Dynamics of SCs

The dynamical evolution of SCs is driven by many different processes acting together. We can distinguish two main stages in the evolution of a SC:

- The first Myr in which star formation is still in action and the cluster still contains gas from its parent molecular cloud.
- The phase subsequent to gas evaporation in which purely stellar dynamical processes dominate.

The first phase is shorter, but is the most complex and less understood since it is a complex mix of gas dynamics, stellar dynamics, stellar evolution, and radiative transfer. After few Myr, the most massive stars explode as supernovae and inject energy into the embedded gas which eventually becomes gravitationally unbound from the cluster and dissolves. Gas loss removes potential energy from the cluster, which loses some stars or may completely dissolve (infant mortality). After the gas is radiated away, the SC can be seen as a system of point masses (stars) which interact between each other by means of gravitational force.

It is important to state that simulating gas evolution along with accurate dynamical evolution of stars is extremely computationally expensive, and thus the vast majority of dynamical simulations of SCs so far (and the ones performed in this thesis) do not include gas evolution. However, the most dense regions of molecular clouds where YSCs form have a very large star formation efficiency, meaning that the amount of gas in such regions after the SC has formed is much lower than that of stars (see e.g. Krause et al. 2016; Ballone et al. 2020).

SCs are collisional systems, which means that interactions between particles are efficient with respect to the lifetime of the system. On the contrary, collisionless systems are systems where interactions are negligible, so that particles move under the influence of the gravitational field generated by a smooth mass distribution rather than a collection of point masses. To distinguish between these two kinds of systems we use the relaxation timescale t_{rl} , defined in equation 1.16. In particular, we say that a system is collisional/collisionless if its lifetime is shorter/longer than t_{rl} . The process which relaxes the system is called two-body relaxation, which is the main process that drives the dynamical evolution of SCs.

1.4.4.1 Two-Body Relaxation

Two-body relaxation is the result of many long range two-body gravitational interactions. On timescales longer than t_{rl} these interactions slowly redistribute energy between particles and make them lose memory of their initial velocity. The two-body relaxation timescale can be derived following the motion of an individual particle across the SC, and seeking an estimate of the difference between the initial velocity of this particle and the velocity that it has after one system crossing. We consider an idealized system of N particles with mass m , size R and uniform density. The test star passes close to a field star with relative velocity v and impact parameter b as schematized in figure 1.8. Each time this happens, its velocity changes by a small amount, so we assume that $\delta v/v \ll 1$ and that the field star is stationary. After many of these interactions, the velocity changes completely, or in other words the variation of velocity becomes of the same order of magnitude as the initial velocity:

$$\frac{\Delta v}{v} \sim 1. \quad (1.17)$$

The perpendicular gravitational force between the two particles is:

$$F_{\perp} = \frac{G m^2}{r^2} \cos\theta = \frac{G m^2 b}{(b^2 + x^2)^{3/2}} = \frac{G m^2}{b^2} \left[1 + \left(\frac{vt}{b} \right)^2 \right]^{-3/2}. \quad (1.18)$$

The quantities are defined in figure 1.8. We can infer the change in velocity by integrating the second Newton's law:

$$\delta v = \frac{1}{m} \int_{-\text{inf}}^{+\text{inf}} F_{\perp} dt = \frac{2Gm}{bv} \quad (1.19)$$

The surface density of stars in our system is $N/\pi r^2$ so, after crossing the whole system once, the subject star has suffered $\delta n = \frac{N}{\pi r^2} 2\pi b db$ encounters with impact parameter between b and $b + db$. The resulting average velocity change is zero because each encounter produces a randomly oriented perturbation. The quadratic mean velocity change is not zero:

$$\sum \delta v^2 = \delta v^2 \delta n = 8N \left(\frac{Gm}{vR} \right)^2 \frac{db}{b}. \quad (1.20)$$

Integrating this quantity over all the possible impact parameters¹ we obtain:

$$\Delta v^2 = 8N \left(\frac{Gm}{vR} \right)^2 \ln \Lambda \quad (1.21)$$

¹i.e. between b_{\min} and b_{\max} , where the former is the minimum distance at which our approximation of small velocity changes holds ($b_{\min} = 2Gm/v^2$), and the latter is the size R of the system.

where $\ln \Lambda = \ln \frac{2Gm}{v^2 R}$ is called Coulomb logarithm, and its value for typical SCs is ~ 10 . If we assume that the system is in virial equilibrium, the typical velocity of a particle can be expressed as:

$$v^2 = \frac{GNm}{R}. \quad (1.22)$$

We can now infer the change in velocity after one system crossing:

$$\frac{\Delta v^2}{v^2} = \frac{8 \ln N}{N}. \quad (1.23)$$

Requiring the condition of equation 1.17 we get the needed number of crossings to relax the system:

$$n_{\text{cross}} = \frac{N}{8 \ln N}. \quad (1.24)$$

The needed number of crossings can also be expressed as $n_{\text{cross}} = t_{\text{rl}} / t_{\text{cross}}$, so we can finally derive the two-body relaxation timescale:

$$t_{\text{rl}} = \frac{N}{8 \ln N} \frac{R}{v}. \quad (1.25)$$

After one relaxation timescale, the orbit of the particles is considerably different from the one they would have if the mass was smoothly distributed. A better formulation with less approximations and based on local parameters rather than global ones was derived by Spitzer, 1987:

$$t_{\text{rl}} = \frac{\langle v^2 \rangle^{3/2}}{15.4 G^2 m_m \rho \ln \Lambda}, \quad (1.26)$$

where $\langle v^2 \rangle$ is the local velocity dispersion, m_m is the local mean mass and ρ is the local density. When applied to SCs, the local relaxation timescale is usually evaluated at the core (core relaxation timescale t_{rc}) and at the half-mass radius (half-mass relaxation timescale t_{rh}). An expression of t_{rh} with handy units is:

$$t_{\text{rh}} = 190 \text{ Myr} \left(\frac{r_{\text{vir}}}{1 \text{ pc}} \right)^{3/2} \left(\frac{M}{10^6 M_{\odot}} \right)^{1/2} \left(\frac{\langle m \rangle}{1 M_{\odot}} \right)^{-1} \left(\frac{\ln \Lambda}{10} \right)^{-1}. \quad (1.27)$$

Values of t_{rh} for some observed SCs of the Milky Way are shown in figure 1.9.

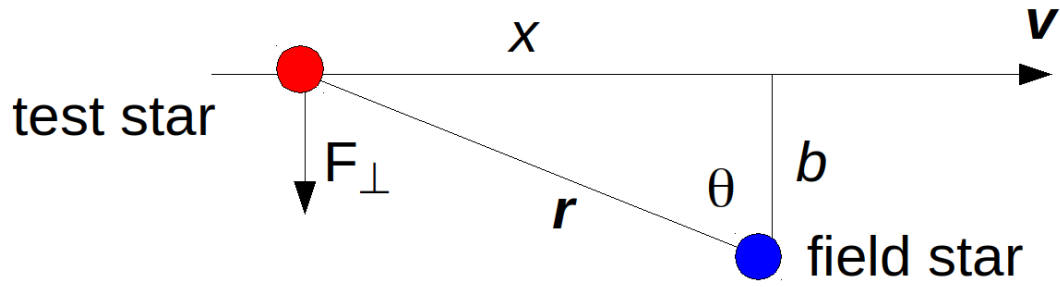


Figure 1.8: Schematic representation of one of the many two-body encounters by which the test particle is affected. The particles experience a change in velocity due to gravitational forces.

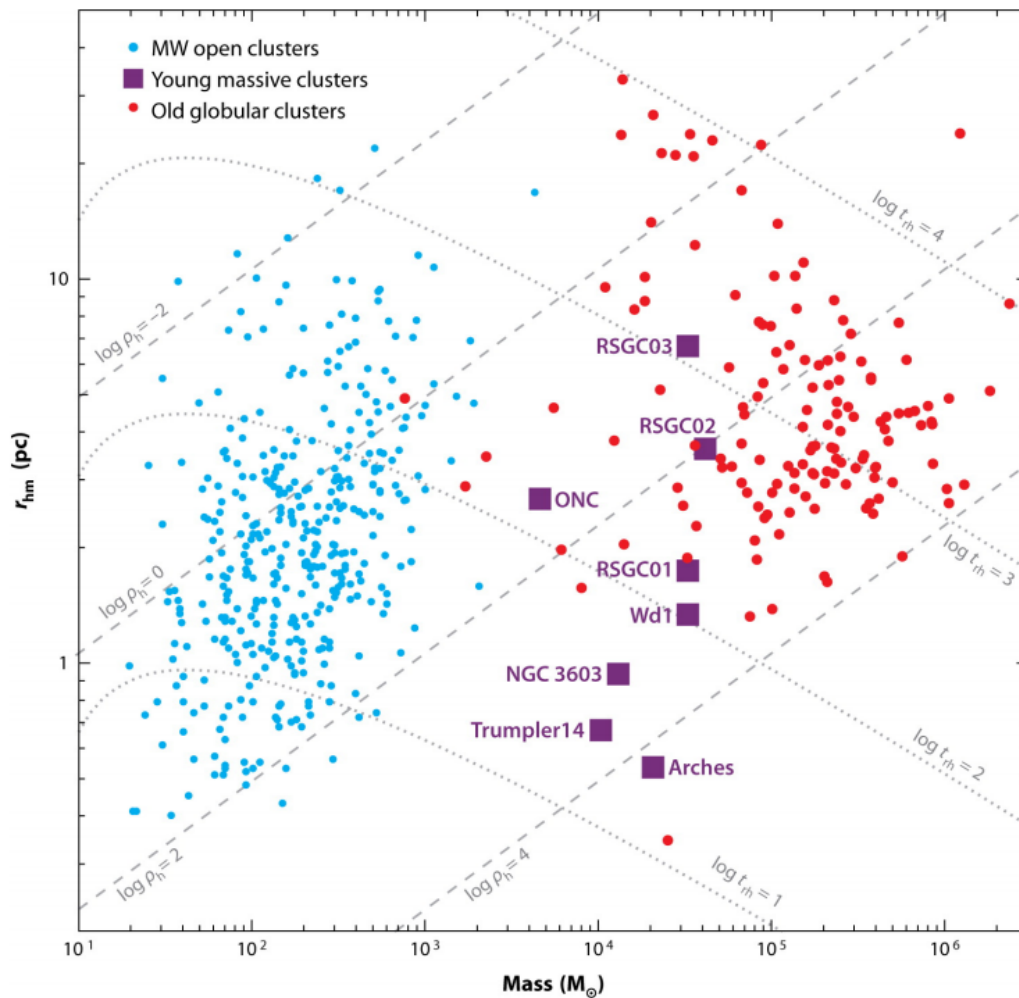


Figure 1.9: From Portegies Zwart et al., 2010. Radius-mass diagram of Milky Way SCs. The dotted lines represent constant relaxation timescale. Open clusters and young massive clusters have shorter relaxation timescales with respect to globular clusters.

1.4.4.2 Core Collapse

There are phenomena which happen even faster than two-body relaxation in SCs. One of these is the core collapse or gravothermal catastrophe, which for a realistic young SC happens on a time scale of Portegies Zwart et al., 2010:

$$t_{\text{cc}} \sim 0.2 t_{\text{rl}}. \quad (1.28)$$

If a SC survives infant mortality, two-body relaxation makes the core contract. The contraction of the core is a runaway process which leads to a collapse. The physical process behind this is called gravothermal instability, which I describe below. We assume that the SC is in virial equilibrium, hence:

$$2K + W = 0, \quad (1.29)$$

where K and W are the total kinetic energy of the SC and the total gravitational potential, respectively. Two-body relaxation redistributes energy between the stars in the core and some of them gain enough kinetic energy to escape from the core to the halo. By escaping, they take away from the core both their potential and kinetic energy. Since the escaping stars are the fastest, they take away more kinetic energy than potential energy. The most energetic stars escape the SC, thus the lost kinetic energy cannot be restored by stars flowing from the halo to the core. The core of the cluster becomes sub-virial ($2K + W < 0$) and contracts, increasing the velocity dispersion of its stars and thus the number of escapers, becoming more and more sub-virial. This leads to a catastrophic collapse. This process occurs even if all the stars have equal mass.

If we consider a multi-mass system the collapse is even faster due to dynamical friction, a process which makes massive stars lose energy and fall towards the center of the cluster. Dynamical friction is the loss of orbital energy of a body through gravitational interactions with surrounding bodies (Chandrasekhar, 1943). An intuition for this effect can be obtained by thinking that as a large object moves through a sea of smaller objects, the gravitational effect of the larger object pulls the smaller objects towards it. This produces a concentration of smaller objects behind the larger body, as it has already moved past its previous position. This concentration of small objects behind the larger body exerts a collective gravitational force on the large object, slowing it down.

The collapse should proceed indefinitely, but since we do observe SCs older than the collapse timescale, there should be something that reverts the collapse. In particular, there has to be something that injects energy inside the core and helps it

to expand. The energy we are seeking for is stored in binary stars and mass loss by stellar winds and SNe explosion. The majority of the energy needed to reverse the core collapse is usually provided by the hardening of binaries in the core. Since the core contracts during core collapse, the core density increases and three-body encounters become more frequent, helping the reversal. After the core collapse is reverted the core starts to expand and the half-mass radius of the cluster evolves through the relation (Elson et al., 1987):

$$r_{\text{hm}} \propto t^{2/3}. \quad (1.30)$$

1.4.4.3 Dynamics and GW Sources

Binaries which evolve in SCs are subject to many dynamical interactions with other stars due to their large cross sections (Heggie, 1975). Especially the most massive ones (which are more likely to become BBHs) tend to undergo more encounters due to their stronger gravitational potential. During a three-body encounter between a binary and a single star, there is an exchange between the internal energy of the binary and the kinetic energy of the stars. If the binary becomes less bound, the single star transfers part of its kinetic energy to soften the binary. If the binary becomes more bound, the kinetic energy of the system increases and the binary hardens. In some cases, there can also be an exchange between the single star and a member of the binary, or the binary may break ending up with three single stars. A scheme showing how a hardening and an exchange may take place is shown in figure 1.10. Binaries can form even with the interaction between three single objects, where one component is ejected and the other two are paired together. This is the main mechanism for the initial assembly of BH binaries in massive star clusters such as globular and nuclear clusters.

Moreover, stars which create as a product of the collision/merger of other stars may be retained by the host SC and continue interacting with other stars. Such interactions are crucial mechanisms for the formation of GW sources. Exchanges may produce systems which would never form accounting for binary stellar evolution only. Hardening may lead to the merger of binaries which would not have merged in isolation. Systems which would have merged may break or loosen. In addition, we know that stellar mergers may lead to the formation of BHs with mass in the PISN mass gap (Spera et al., 2019a; Di Carlo et al., 2019) or intermediate mass black holes (IMBHs) via the runaway collision mechanism (e.g. Portegies Zwart and McMillan 2002). If such BHs form from the merger of an isolated binary, they will remain single BHs. In contrast, if they form in a SC, they might acquire another companion by dynamical exchange and merge by gravitational wave emission.

Lots of work has been done on the effect of dynamics on GW sources (Sigurdsson and Hernquist, 1993; Sigurdsson and Phinney, 1995; O’Leary et al., 2006; Sadowski et al., 2008; Miller and Lauburg, 2009; O’Leary et al., 2009; Downing et al., 2010; Downing et al., 2011; Mapelli et al., 2013; Mapelli and Zampieri, 2014; Ziosi et al., 2014; Rodriguez et al., 2015; Kimpson et al., 2016; Mapelli, 2016; Antonini and Rasio, 2016; Hurley et al., 2016; VanLandingham et al., 2016; O’Leary et al., 2016; Rodriguez et al., 2016; Askar et al., 2017a; Chatterjee et al., 2017; Zevin et al., 2017; Antonini et al., 2019a; Askar et al., 2018; Arca-Sedda and Gualandris, 2018; Hoang

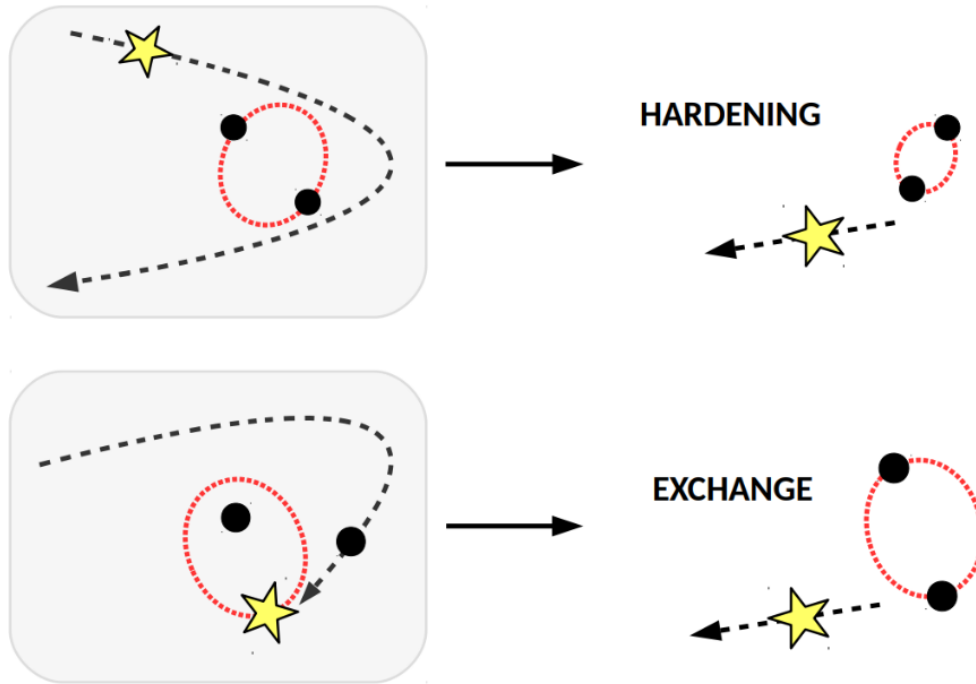


Figure 1.10: Schematic representation of 3 body encounters between a binary and a single object. Top panels: a BBH hardens after an encounter with a star; bottom panels: a BH replaces a star in a binary, forming a BBH.

et al., 2018; Rodriguez et al., 2018; Samsing, 2018; Kumamoto et al., 2019b; Rastello et al., 2019; Kumamoto et al., 2020; Kremer et al., 2020). Despite this, most of these studies focus on GCs and NSCs, neglecting YSCs. The reason behind this is partially that YSCs are clumpy, asymmetric and host a large fraction of binaries, thus requiring computationally expensive direct N-body simulations. YSCs host fewer stars than globular clusters and other massive clusters, but they make up the vast majority of the SCs in the Universe (Kroupa and Boily, 2002), and their cumulative contribution to BH statistics may thus be significant.

The main aim of my thesis is understanding what is the global effect of dynamics of YSCs on BHs, focusing on GW sources. This is of utmost importance for the interpretation of current and future GW detections. To investigate this topic, I made use of numerical simulations of SCs.

1.5 Direct N-body simulations

The two main ingredients which govern the evolution of SCs are gravity and single/binary stellar evolution. This is why to properly simulate a SC we need to use

both an N-Body integrator (for gravity) and a population synthesis code (for stellar evolution). The first step of my thesis consisted in interfacing the population synthesis code MOBSE with the direct N-Body code NBODY6++GPU. This allowed me to produce state-of-the-art dynamical simulations of SCs with up to date stellar evolution.

1.5.1 MOBSE

The population synthesis code MOBSE (massive objects binary stellar evolution) (Mapelli et al., 2017; Giacobbo et al., 2018; Giacobbo and Mapelli, 2018; Giacobbo and Mapelli, 2019; Mapelli and Giacobbo, 2018) is an upgraded and customized version of BSE (Hurley et al., 2000; Hurley et al., 2002). MOBSE utilizes polynomial fitting formulas to describe the evolution of the fundamental stellar parameters as a function of time. MOBSE implements some of the most recent stellar wind models for massive hot stars (Vink et al., 2001; Gräfener and Hamann, 2008; Vink et al., 2011; Vink, 2016), including the impact of the Eddington factor Γ_e on mass loss (Gräfener and Hamann, 2008; Chen et al., 2015). Γ_e is defined as:

$$\log\Gamma_e = -4.813 + \log(1 + X_H) + \log(L/L_\odot) - \log(M/M_\odot), \quad (1.31)$$

where X_H is the Hydrogen fraction, L is the stellar luminosity and M is the stellar mass.

In MOBSE the mass loss of massive hot stars (O- and B-type main sequence stars, luminous blue variable stars and Wolf-Rayet stars) scales as $\dot{M} \propto Z^\beta$, where β is defined as (Giacobbo and Mapelli, 2018)

$$\beta = \begin{cases} 0.85 & \text{if } \Gamma_e < 2/3 \\ 2.45 - 2.4\Gamma_e & \text{if } 2/3 \leq \Gamma_e < 1 \\ 0.05 & \text{if } \Gamma_e \geq 1 \end{cases} \quad (1.32)$$

MOBSE includes two different prescriptions for core-collapse supernovae (SNe) from Fryer et al., 2012: the *rapid* and the *delayed* SN models. The former model assumes that the SN explosion only occurs if it is launched $\lesssim 250$ ms after the bounce, while the latter has a longer timescale ($\gtrsim 500$ ms). In both models, a star is assumed to directly collapse into a BH if its final carbon-oxygen mass is $\gtrsim 11 M_\odot$. Recipes for electron-capture SNe are also included in MOBSE (Hurley et al., 2000; Fryer et al., 2012; Giacobbo and Mapelli, 2019).

Prescriptions for pair instability SNe (PISNe) and pulsational pair instability (PPI) are implemented using the fitting formulas by Spera and Mapelli, 2017. In particular, stars which grow a helium core mass $64 \leq m_{\text{He}}/M_{\odot} \leq 135$ are completely disrupted by a PISN and leave no compact object, while stars with $32 \leq m_{\text{He}}/M_{\odot} < 64$ undergo PPI: they pulsate, losing some of their mass, till they find a new equilibrium. Finally, they undergo a direct collapse, giving birth to a smaller BH than they would have produced without PPI.

MOBSE includes two main prescriptions for natal kicks. In the first prescription (Fryer et al., 2012), kick velocities are drawn by a Maxwellian distribution with one-dimensional root-mean square $\sigma = 265 \text{ km s}^{-1}$ (Hobbs et al., 2005) and then modulated by the fallback as $V_{\text{KICK}} = (1 - f_{\text{fb}}) V$, where f_{fb} is the fallback parameter described in Fryer et al., 2012 and V is the velocity drawn from the Maxwellian distribution.

In the second and most recent prescription (Giacobbo and Mapelli, 2020), kick velocities are calculated as $V_{\text{KICK}} \propto m_{\text{ej}} m_{\text{rem}}^{-1} V$, where m_{ej} is the mass of the ejecta, m_{rem} is the mass of the compact remnant (neutron star or BH) and V is drawn by a Maxwellian distribution with one-dimensional root-mean square $\sigma = 265 \text{ km s}^{-1}$ (Hobbs et al., 2005). The latter prescription is based on the conservation of linear momentum and assumes that the asymmetry leading to the natal kick scales with the mass of the ejecta.

Binary evolution processes such as tidal evolution, Roche lobe overflow, common envelope and GW energy loss are taken into account as described in Hurley et al., 2002. In particular, the treatment of common envelope depends on two parameters: α (describing the efficiency of energy transfer) and λ (describing the geometry of the envelope and the importance of thermal energy and recombinations).

Orbital decay and circularization by GW emission are calculated according to Peters, 1964 without explicitly including post-Newtonian terms. The standard version of BSE calculates GW energy loss only if the two binary members are closer than $10 R_{\odot}$, which has been shown to lead to a serious underestimate of the merger rate of eccentric binaries in dynamical simulations (Samsing, 2018). In MOBSE, GW decay is calculated for all binaries of two compact objects (white dwarfs, NSs and BHs) without a distance threshold.

1.5.2 NBody6++GPU

NBODY6++GPU (Wang et al., 2015) is a code designed for an accurate integration of many bodies based on the direct integration of the Newtonian equations of mo-

tion. It is optimal for collisional systems like SCs. NBODY6++GPU is an upgraded version of the widely used code NBODY6 (Aarseth, 2003), which exploits GPU and MPI parallelization to improve the performance and speed up the integration. The code makes use of a fourth-order Hermite prediction scheme with block time steps, a neighbour scheme and regularization of close encounters.

1.5.2.1 Block Time Steps

When integrating an N-body system, choosing the same timestep for all particles may be too computationally expensive. Particles which undergo close encounters need short timesteps, because they are experiencing rapid force variations. On the other hand, other particles subject to weaker interactions can be integrated with longer timesteps without losing much accuracy. Thus, it is convenient to choose different timesteps for particles depending on how fast the forces acting on them are changing. NBODY6++GPU evaluates the timesteps using the generalised Aarseth criterion (Aarseth, 2003; Nitadori and Makino, 2008). For a particle i with acceleration a_i the timestep is:

$$\Delta t_i = \eta \left(\frac{A_i^{(1)}}{A_i^{(4)}} \right)^{1/3}, \quad (1.33)$$

where:

$$A_i^{(k)} = \sqrt{|\mathbf{a}_i^{(k-1)}| |\mathbf{a}_i^{(k+1)}| + |\mathbf{a}_i^{(k)}|^2}. \quad (1.34)$$

η is a user defined quantity called accuracy parameter (usually set to $\eta = 0.02$) and \mathbf{a}_i^k is the k -th derivative of the acceleration of particle i (if $k = 0$, \mathbf{a}_i^k is the acceleration of particle i). Having a different timestep for each particle, however, may create problems with the synchronization of the particles. To solve this problem, NBODY6++GPU uses the technique of block timesteps: particles are grouped replacing their individual timesteps Δt_i with a block timestep:

$$\Delta t_{i,b} = \left(\frac{1}{2} \right)^n, \quad (1.35)$$

where n is chosen according to:

$$\left(\frac{1}{2} \right)^n \leq \Delta t_i < \left(\frac{1}{2} \right)^{n-1}. \quad (1.36)$$

This choice imposes that $t/\Delta t_{i,b} \in \mathbb{N}$ and ensures that all the particles can be easily synchronized. To avoid bottlenecks, a minimum threshold for $\Delta t_{i,b}$ is usually set to $\Delta t_{\min} = 2^{-23}$.

1.5.2.2 The Hermite Scheme

We consider a system of N stars and we assume that the i -th particle has, at time t a mass $m_{i,0}$, a position $\mathbf{r}_{i,0}$, a velocity $\mathbf{v}_{i,0}$ and an individual timestep $\Delta t_{i,0} = h$. The acceleration and jerk of the particles are given by:

$$\mathbf{a}_{i,0} = - \sum_{j \neq i} G m_j \frac{\mathbf{R}}{R^3}, \quad (1.37)$$

$$\dot{\mathbf{a}}_{i,0} = - \sum_{j \neq i} G m_j \left[\frac{\mathbf{V}}{R^3} + \frac{3\mathbf{R}(\mathbf{V} \cdot \mathbf{R})}{R^5} \right], \quad (1.38)$$

where G is the gravitational constant and $\mathbf{R} \equiv \mathbf{r}_i - \mathbf{r}_j$ and $\mathbf{V} \equiv \mathbf{v}_i - \mathbf{v}_j$ are the relative positions and velocities between particle i and j , respectively. The generic Hermite's step is composed by three sub-steps: a prediction, an evaluation and a correction.

1. Prediction step: positions and velocities of all stars at time $t + h$ are predicted using their known values using a Taylor expansion:

$$\mathbf{r}_{i,p} = \mathbf{r}_{i,0} + \mathbf{v}_{i,0}h + \mathbf{a}_{i,0} \frac{h^2}{2} + \dot{\mathbf{a}}_{i,0} \frac{h^3}{6}, \quad (1.39)$$

$$\mathbf{v}_{i,p} = \mathbf{v}_{i,0} + \mathbf{a}_{i,0}h + \dot{\mathbf{a}}_{i,0} \frac{h^2}{2}, \quad (1.40)$$

2. Evaluation step: $\mathbf{a}_{i,p}$ and $\dot{\mathbf{a}}_{i,p}$ are determined by putting 1.39 and 1.40 in 1.37 and 1.38.

The values of acceleration and jerk at time $t + h$ are determined by the Taylor expansion:

$$\mathbf{a}_{i,1} = \mathbf{a}_{i,0} + \dot{\mathbf{a}}_{i,0}h + \ddot{\mathbf{a}}_{i,0} \frac{h^2}{2} + \dddot{\mathbf{a}}_{i,0} \frac{h^3}{6}, \quad (1.41)$$

$$\dot{\mathbf{a}}_{i,1} = \dot{\mathbf{a}}_{i,0} + \ddot{\mathbf{a}}_{i,0}h + \dddot{\mathbf{a}}_{i,0} \frac{h^2}{2}. \quad (1.42)$$

Here, the values of $\mathbf{a}_{i,0}$ and $\dot{\mathbf{a}}_{i,0}$ are already known, but we need to infer $\ddot{\mathbf{a}}_{i,0}$ and $\dddot{\mathbf{a}}_{i,0}$. We put $\mathbf{a}_{i,p}$ and $\dot{\mathbf{a}}_{i,p}$ in the left-hand sides of 1.41 and 1.42. We then solve equation 1.42 for $\ddot{\mathbf{a}}_{i,0}$ and put it into 1.41, which yields the third derivative of acceleration:

$$\ddot{\mathbf{a}}_{i,0} = 12 \frac{\mathbf{a}_{i,0} - \mathbf{a}_{i,p}}{h^3} + 6 \frac{\dot{\mathbf{a}}_{i,0} + \dot{\mathbf{a}}_{i,p}}{h^2}. \quad (1.43)$$

Similarly, substituting 1.43 into 1.41, we get the jerk:

$$\ddot{\mathbf{a}}_{i,0} = -6 \frac{\mathbf{a}_{i,0} - \mathbf{a}_{i,p}}{h^2} - 2 \frac{2\dot{\mathbf{a}}_{i,0} + \dot{\mathbf{a}}_{i,p}}{h}. \quad (1.44)$$

3. Correction step: finally, we can infer the corrected values of $\mathbf{r}_{i,p}(t)$ and $\mathbf{v}_{i,p}(t)$, extending the Taylor expansion by two more orders:

$$\mathbf{r}_{i,1} = \mathbf{r}_{i,p} + \ddot{\mathbf{a}}_{i,0} \frac{h^4}{24} + \dddot{\mathbf{a}}_{i,0} \frac{h^5}{120}, \quad (1.45)$$

$$\mathbf{v}_{i,1} = \mathbf{v}_{i,p} + \ddot{\mathbf{a}}_{i,0} \frac{h^3}{6} + \dddot{\mathbf{a}}_{i,0} \frac{h^4}{24}. \quad (1.46)$$

The integration cycle for the successive steps may now be repeated from the beginning.

1.5.2.3 The Ahmad Cohen Scheme

Force calculation can be extremely time consuming for systems with very large N . To speed up the integration, NBODY6++GPU uses the Ahmad-Cohen neighbour scheme (Ahmad and Cohen, 1973; Makino and Aarseth, 1992). The basic idea is to split the force on a given particle i into two parts, an irregular and a regular component:

$$\mathbf{a}_i = \mathbf{a}_{i,irr} + \mathbf{a}_{i,reg}. \quad (1.47)$$

The irregular acceleration results from particles within a certain sphere centered in i (neighbours), while the regular acceleration results from all the other particles. The size of the sphere is controlled iteratively in order to keep an optimal customizable number of neighbours. The force exerted by the particles inside the sphere changes more rapidly, so it is determined more frequently than the regular one, because the more distant particles that do not change their relative distance to i so quickly. The regular timestep Δt_{reg} is divided in smaller substeps Δt_{irr} . The Hermite predictor-corrector algorithm is applied to the neighbours every Δt_{irr} and to the other particles every Δt_{reg} . After every irregular timestep, the regular term $\mathbf{a}_{i,reg}$ is extrapolated without applying the correction to save computational time while preserving accuracy. The neighbour list is updated every Δt_{reg} .

With a number of neighbours $N_{nb} \ll N$, this scheme can dramatically increase the efficiency of the code. To further speed up the calculation, regular forces are computed on GPUs using the CUDA libraries, while the irregular forces are calculated on the CPUs, exploiting OpenMP parallelization.

1.5.2.4 Regularization

During the dynamical evolution of SCs, it is very likely that two or more stars come very close together. As the stars approach, the so-called UV divergence occurs: their relative distance tends to zero and thus gravitational potential tends to infinity. Because of this, truncation errors grow due to the singularity in the gravitational potential and the timesteps reduce, resulting in a dramatic slowdown of the computation.

To avoid this, NBODY6++GPU makes use of the regularization technique. Regularization is an elegant mathematical trick developed in order to deal with such close encounters and avoid divergences. The main algorithms used in NBODY6++GPU are the KS regularization (Kustaanheimo and Stiefel, 1965) and the chain regularization (Mikkola and Aarseth, 1993a). KS regularization consists in a change of the time coordinate to a coordinate system where the singularity in $|\mathbf{R}| = 0$ does not exist.

In the Mikkola chain regularization, the adopted coordinate transformation is $ds = \frac{dt}{U_{i,j}}$, where $U_{i,j}$ is the N-body gravitational potential. The price to pay for using this regularization is a small time error, which is generally very small. Using this trick, the close encounter between the two particles can be integrated fast and without losing precision. If more than two particles participate to the same close encounter simultaneously, NBODY6++GPU makes use of the chain regularization. The basic idea is to connect the dominant two-body interactions by a chain of KS-type variables. The chain is the shortest inter-particle vector between the particles elected for regularization. The full mathematical explanation of the chain regularization algorithm turns out to be quite cumbersome; all the details can be found in Mikkola and Aarseth, 1993a.

Regularization is a fundamental technique for studying compact objects in SCs: their small radii and large masses makes them perfect candidates for close encounters during the dynamical evolution of SCs.

MERGING BLACK HOLES IN YOUNG STAR CLUSTERS

Searching for distinctive signatures, which characterize different formation channels of binary black holes (BBHs), is a crucial step towards the interpretation of current and future gravitational wave detections. Here, we investigate the demography of merging BBHs in young star clusters (SCs), which are the nursery of massive stars. We performed 4×10^3 N-body simulations of SCs with metallicity $Z = 0.002$, initial binary fraction 0.4 and fractal initial conditions, to mimic the clumpiness of star-forming regions. Our simulations include a novel population-synthesis approach based on the code MOBSE. We find that SC dynamics does not affect the merger rate significantly, but leaves a strong fingerprint on the properties of merging BBHs. More than 50 % of merging BBHs in young SCs form by dynamical exchanges in the first few Myr. Dynamically formed merging BBHs are significantly heavier than merging BBHs in isolated binaries: merging BBHs with total mass up to $\sim 120 M_{\odot}$ form in young SCs, while the maximum total mass of merging BBHs in isolated binaries with the same metallicity is only $\sim 70 M_{\odot}$. Merging BBHs born via dynamical exchanges tend to have smaller mass ratios than BBHs in isolated binaries. Furthermore, SC dynamics speeds up the merger: the delay time between star formation and coalescence is significantly shorter in young SCs. In our simulations, massive systems such as GW170729 form only via dynamical exchanges. Finally ~ 2 % of merging BBHs in young SCs have mass in the pair-instability mass gap ($\sim 60 - 120 M_{\odot}$). This represents a unique fingerprint of merging BBHs in SCs.

Based on:

Di Carlo U. N., Giacobbo N., Mapelli M., Pasquato M., Spera M., Wang L., Haardt F., MNRAS, 2019, Volume 487, Issue 2, p.2947-2960

2.1 Introduction

The recent detection of gravitational waves (GWs, Abbott et al. 2016a) by LIGO (Aasi et al. et al., 2015) and Virgo (Acernese et al., 2015) has opened up a new way to investigate the Universe. Out of the 11 GW events reported so far, 10 have been interpreted as the merger of two black holes (BHs, Abbott et al. 2016a; Abbott et al. 2016e; Abbott et al. 2016d; Abbott et al. 2017a; Abbott et al. 2017b; Abbott et al. 2017c; Abbott et al. 2019b; Abbott et al. 2019a) and one as the merger of two neutron stars (NSs, Abbott et al. 2017d). The double NS merger was accompanied by electromagnetic emission almost in all the electromagnetic spectrum, from radio to gamma rays (Abbott et al., 2017e; Abbott et al., 2017; Goldstein et al., 2017; Savchenko et al., 2017; Margutti et al., 2017; Coulter et al., 2017; Soares-Santos et al., 2017; Chornock et al., 2017; Cowperthwaite et al., 2017; Nicholl et al., 2017; Pian et al., 2017; Alexander et al., 2017).

Seven out of 10 binary BH (BBH) mergers observed by the LIGO-Virgo collaboration harbour BHs with mass $\gtrsim 30 M_{\odot}$, significantly higher than the range inferred from dynamical measurements of BH masses in nearby X-ray binaries (Orosz, 2003; Özel et al., 2010; Farr et al., 2011). Such massive stellar BHs are expected to form from the direct collapse of massive metal-poor stars (e.g. Heger et al. 2003; Mapelli et al. 2009; Mapelli et al. 2010; Belczynski et al. 2010; Fryer et al. 2012; Mapelli et al. 2013; Spera et al. 2015; Spera and Mapelli 2017). Dynamical interactions in dense environments are also expected to significantly affect the mass spectrum of BHs (e.g. Portegies Zwart and McMillan 2000b; Portegies Zwart and McMillan 2002; Portegies Zwart et al. 2004; Gürkan et al. 2006; Giersz et al. 2015; Mapelli 2016). Alternatively, primordial BHs, which were predicted to form from gravitational instabilities in the very early Universe (Carr et al., 2016; Raccaanelli et al., 2016; Sasaki et al., 2016; Scelfo et al., 2018) might also have a mass of $\sim 30 - 40 M_{\odot}$.

Not only the mass spectrum of compact objects but also the formation channels of compact-object binaries are matter of debate. Double compact objects might result from the evolution of isolated stellar binaries, i.e. systems of two stars which are gravitationally bound since their birth. An isolated binary is expected to undergo a number of processes during its life (including mass transfer, common envelope episodes, tidal forces and supernova explosions). Binary population-synthesis codes are generally used to study the formation of double compact objects from the evolution of isolated stellar binaries (e.g. Tutukov et al. 1973; Flannery and van den Heuvel 1975; Bethe and Brown 1998; Portegies Zwart and Yungelson 1998; Belczynski et al. 2002; Voss and Tauris 2003; Podsiadlowski et al. 2004; Podsiadlowski et

al. 2005; Belczynski et al. 2007; Belczynski et al. 2008; Moody and Sigurdsson 2009; Mennekens and Vanbeveren 2014; Tauris et al. 2015; Tauris et al. 2017; Marchant et al. 2016; Shao and Li 2018; Giacobbo et al. 2018; Giacobbo and Mapelli 2019) and to estimate their merger rate density (e.g. Dominik et al. 2013; Dominik et al. 2015; Belczynski et al. 2016b; de Mink and Mandel 2016; Mapelli et al. 2017; Chruslinska et al. 2018; Mapelli and Giacobbo 2018; Mapelli et al. 2018; Giacobbo and Mapelli 2018; Kruckow et al. 2018; Spera et al. 2019a; Eldridge et al. 2019; Mapelli et al. 2019a).

Alternatively, dynamics in dense environments, such as young star clusters (SCs), open clusters (Mapelli et al., 2013; Mapelli and Zampieri, 2014; Ziosi et al., 2014; Mapelli, 2016; Kimpson et al., 2016; Chatterjee et al., 2017; Kumamoto et al., 2019a; Rastello et al., 2019), globular clusters (Sigurdsson and Hernquist, 1993; Sigurdsson and Phinney, 1995; O’Leary et al., 2006; Sadowski et al., 2008; Downing et al., 2010; Downing et al., 2011; Rodriguez et al., 2015; Rodriguez et al., 2016; Rodriguez et al., 2018; Antonini and Rasio, 2016; Antonini et al., 2019a; Hurley et al., 2016; O’Leary et al., 2016; Askar et al., 2017a; Askar et al., 2018; Zevin et al., 2017; Samsing, 2018) and nuclear SCs (O’Leary et al., 2009; Miller and Lauburg, 2009; VanLandingham et al., 2016; Hoang et al., 2018; Arca-Sedda and Gualandris, 2018; Antonini et al., 2019a), can drive the formation and the evolution of compact-object binaries.

For example, dynamical exchanges can bring BHs into existing stellar binaries. BHs are particularly efficient in acquiring companions via exchanges, because they are among the most massive objects in a star cluster and exchanges tend to produce more and more massive binaries (Hills and Fullerton, 1980). For this reason, Ziosi et al., 2014 find that $\gtrsim 90$ per cent of BBHs in open clusters form via dynamical exchanges. Binaries formed through exchanges have a characteristic signature: they tend to be more massive than average, have high initial orbital eccentricity and mostly misaligned spins.

Furthermore, dynamical hardening via three- or multi-body encounters can also affect the evolution of “hard” binaries (i.e. binaries whose binding energy is higher than the average kinetic energy of other SC members Heggie 1975), by shrinking their orbital separation until they enter the regime where GW emission proceeds efficiently (see e.g. Mapelli 2018 for a recent review). Finally, “soft” binaries (i.e. binaries whose binding energy is lower than the average kinetic energy of other SC members) might even be broken by three-body and multi-body encounters. Other dynamical processes which might affect the evolution of compact-object binaries include runaway collisions (e.g. Mapelli 2016), Spitzer’s instability (Spitzer, 1969), Kozai-Lidov resonances (Kozai, 1962; Lidov, 1962), and dynamical ejections (e.g.

Downing et al. 2011). Three-body and multi-body scattering experiments have shown that these effects are crucial for the demography of BBHs in SCs (Goodman and Hut, 1993; Kulkarni et al., 1993; Miller and Hamilton, 2002; Colpi et al., 2003; Antonini et al., 2016; Zevin et al., 2019a; Arca-Sedda et al., 2018; Samsing and D’Orazio, 2018).

Dynamics is a crucial ingredient to understand the formation of compact-object binaries because massive stars (which are thought to be the progenitors of BHs and NSs) form preferentially in young SCs and associations (Lada and Lada, 2003; Portegies Zwart et al., 2010). Thus, it is reasonable to expect that compact objects and their stellar progenitors participate in the dynamics of their parent SC, before being ejected or scattered into the field.

Despite this, most studies of BH dynamics neglect young SCs and star-forming regions, with few exceptions (Portegies Zwart and McMillan, 2002; Banerjee et al., 2010; Kouwenhoven et al., 2010; Ziosi et al., 2014; Goswami et al., 2014; Mapelli, 2016; Banerjee, 2018b; Banerjee, 2018a; Fujii et al., 2017; Kumamoto et al., 2019a; Rastello et al., 2019). The relative scarcity of studies about BHs in young SCs is partially due to the fact that these are small, generally clumpy and asymmetric stellar systems, mostly composed of few hundred to several thousand stars: they cannot be modelled with fast Monte Carlo techniques, but require expensive direct N-body simulations. Moreover, stellar evolution is a key ingredient in the life of young SCs, because their age is comparable with the lifetime of massive stars: mass loss by stellar winds and supernova (SN) explosions contribute significantly to the dynamical evolution of young stellar systems (e.g. Mapelli and Bressan 2013; Trani et al. 2014). This implies that dynamical models of young SCs should also include stellar evolution through accurate population synthesis.

Furthermore, observations suggest that young embedded SCs are characterised by clumpiness (e.g. Cartwright and Whitworth 2004; Gutermuth et al. 2005) and high fractions of binaries (e.g. Sana et al. 2012), whereas most simulations of young SCs adopt idealized initial conditions, consisting of monolithic King models (King, 1966) and assuming a very small fraction of binaries ($f \sim 0 - 0.1$).

Our aim is to study the demography of double compact objects in young SCs, following a novel approach: we have run a large set of N-body simulations of young SCs with fractal initial conditions (which mimic the clumpy and asymmetric structure of star-forming regions, e.g. Goodwin and Whitworth 2004) and with a high initial binary fraction ($f_{\text{bin}} = 0.4$). The initial masses of our SCs have been randomly drawn according to a power-law distribution $dN/dM_{\text{SC}} \propto M_{\text{SC}}^{-2}$ (from $M_{\text{SC}} = 10^3 M_{\odot}$ to $3 \times 10^4 M_{\odot}$), consistent with the mass distribution of young SCs in the Milky

Way (Elmegreen and Efremov, 1997; Lada and Lada, 2003). While these SCs host fewer stars than globular clusters and other massive clusters, they make up the vast majority of the SCs in the Universe (Kroupa and Boily, 2002), and their cumulative contribution to BH statistics may thus be significant. We evolve each SC with an accurate treatment of dynamics (Wang et al., 2015) and with up to date binary population-synthesis models (Giacobbo et al., 2018).

2.2 Methods

The simulations were done using the direct summation N-Body code NBODY6++GPU (Wang et al., 2015) coupled with the new population synthesis code MOBSE (Giacobbo et al., 2018).

2.2.1 Direct N-Body

NBODY6++GPU is the GPU parallel version of NBODY6 (Aarseth, 2003). It implements a 4th-order Hermite integrator, individual block time-steps (Makino and Aarseth, 1992) and Kustaanheimo-Stiefel (KS) regularization of close encounters and few-body subsystems (Stiefel, 1965).

A neighbour scheme (Nitadori and Aarseth, 2012) is used to compute the force contributions at short time intervals (*irregular* force/timesteps), while at longer time intervals (*regular* force/timesteps) all the members in the system contribute to the force evaluation. The irregular forces are evaluated using CPUs, while the regular forces are computed on GPUs using the CUDA architecture. This version of NBODY6++GPU does not include post-Newtonian terms¹.

2.2.2 Population synthesis

In its original version, NBODY6++GPU is coupled with the population synthesis code BSE (Hurley et al., 2000; Hurley et al., 2002). For this work, we modified NBODY6++GPU, coupling it with the new population synthesis code MOBSE (Mapelli et al., 2017; Giacobbo et al., 2018; Giacobbo and Mapelli, 2018; Giacobbo and Mapelli, 2019; Mapelli and Giacobbo, 2018), an updated version of BSE.

¹In other versions of NBODY, general relativity is taken into account in the algorithmic regularization routine via post-Newtonian terms. As recently discussed in several works (Samsing et al., 2017; Rodriguez et al., 2018; Samsing et al., 2018; Arca-Sedda et al., 2018; Zevin et al., 2019a), including post-Newtonian terms in N-body simulations might increase the chance for BBHs to merge inside the cluster before ejection, thus increasing the total number of merging events.

NBODY6++GPU and MOBSE are perfectly integrated: they update stellar parameters and trajectories simultaneously during the computation.

MOBSE implements some of the most recent stellar wind models for massive hot stars (Vink et al., 2001; Gräfener and Hamann, 2008; Vink et al., 2011; Vink, 2016), including the impact of the Eddington factor Γ_e on mass loss (Gräfener and Hamann, 2008; Chen et al., 2015). Here, we adopt the following definition of Γ_e :

$$\log \Gamma_e = -4.813 + \log(1 + X_H) + \log(L/L_\odot) - \log(M/M_\odot), \quad (2.1)$$

where X_H is the Hydrogen fraction, L is the stellar luminosity and M is the stellar mass.

In MOBSE the mass loss of massive hot stars (O- and B-type main sequence stars, luminous blue variable stars and Wolf-Rayet stars) scales as $\dot{M} \propto Z^\beta$, where β is defined as (Giacobbo and Mapelli, 2018)

$$\beta = \begin{cases} 0.85 & \text{if } \Gamma_e < 2/3 \\ 2.45 - 2.4\Gamma_e & \text{if } 2/3 \leq \Gamma_e < 1 \\ 0.05 & \text{if } \Gamma_e \geq 1 \end{cases} \quad (2.2)$$

MOBSE includes two different prescriptions for core-collapse supernovae (SNe) from Fryer et al., 2012: the *rapid* and the *delayed* SN models. The former model assumes that the SN explosion only occurs if it is launched $\lesssim 250$ ms after the bounce, while the latter has a longer timescale ($\gtrsim 500$ ms). In both models, a star is assumed to directly collapse into a BH if its final Carbon-Oxygen mass is $\gtrsim 11 M_\odot$. For the simulations described in this paper we adopt the *delayed* model. Recipes for electron-capture SNe are also included in MOBSE (Hurley et al., 2000; Fryer et al., 2012; Giacobbo and Mapelli, 2019).

Prescriptions for pair instability SNe (PISNe) and pulsational pair instability SNe (PPISNe) are implemented using the fitting formulas by Spera and Mapelli, 2017. In particular, stars which grow a Helium core mass $64 \leq m_{\text{He}}/M_\odot \leq 135$ are completely disrupted by a PISN and leave no compact object, while stars with $32 \leq m_{\text{He}}/M_\odot < 64$ undergo a PPISN: they evolve through a set of pulsations, which enhance mass loss and cause the final remnant mass to be significantly smaller than they would be if we had accounted only for core-collapse SNe. According to our current knowledge of PISNe and PPISNe and to the stellar evolution prescriptions implemented in MOBSE, we expect no compact objects in the mass range $\sim 60 - 120 M_\odot$ from single stellar evolution. Binary evolution might affect this range. For example, mass accretion onto an evolved star (or the merger between a post-main sequence star

and a main sequence star) might increase the mass of the Hydrogen envelope without significantly affecting the Helium core: at the time of collapse, such star will have a Helium core mass below the PPISN/PISN range, but a significantly larger Hydrogen envelope. By direct collapse, this star might produce a BH with mass $\geq 60 M_{\odot}$. Clearly, the possibility of forming BHs with mass in the PPISN/PISN gap depends on the assumptions about efficiency of mass accretion, about mass loss after stellar mergers and about core-collapse SNe.

Thanks to these assumptions for massive star evolution and SNe, the BH mass spectrum predicted by MOBSE depends on progenitor's metallicity (the maximum BH mass being higher at lower metallicity) and is consistent with LIGO-Virgo detections ² (Abbott et al., 2016d; Abbott et al., 2016a; Abbott et al., 2016e; Abbott et al., 2017a; Abbott et al., 2017b; Abbott et al., 2017c; Abbott et al., 2019b).

Natal kicks are randomly drawn from a Maxwellian velocity distribution. A one-dimensional root mean square velocity $\sigma_{\text{CCSN}} = 265 \text{ km s}^{-1}$ and $\sigma_{\text{ECSN}} = 15 \text{ km s}^{-1}$ are adopted for core-collapse SNe (Hobbs et al., 2005) and for electron-capture SNe (Dessart et al., 2006; Jones et al., 2013; Schwab et al., 2015; Giacobbo and Mapelli, 2019), respectively. Kick velocities of BHs are reduced by the amount of fallback as $V_{\text{KICK}} = (1 - f_{\text{fb}}) V$, where f_{fb} is the fallback parameter described in Fryer et al., 2012 and V is the velocity drawn from the Maxwellian distribution.

Binary evolution processes such as tidal evolution, Roche lobe overflow, common envelope and GW energy loss are taken into account as described in Hurley et al., 2002. In particular, our treatment of common envelope depends on two parameters: α (describing the efficiency of energy transfer) and λ (describing the geometry of the envelope and the importance of recombinations). In this work, we assume $\alpha = 3$, while λ is derived by MOBSE as described in Claeys et al., 2014.

Orbital decay and circularisation by GW emission are calculated according to Peters, 1964 without explicitly including post-Newtonian terms. The standard version of BSE calculates GW energy loss only if the two binary members are closer than $10 R_{\odot}$, which has been shown to lead to a serious underestimate of the merger rate of eccentric binaries in dynamical simulations (Samsing, 2018). In MOBSE, we remove the $10 R_{\odot}$ limit: GW decay is calculated for all binaries of two compact objects (white dwarfs, NSs and BHs).

Finally, if two stars merge during the N-body simulations, the amount of mass loss is decided by MOBSE, which adopts the same prescriptions as BSE, but for one exception: if a star merges with a BH or a NS, MOBSE assumes that the entire mass

²The BHs detected thus far by LIGO and Virgo are consistent with a power law mass distribution with index $1.6_{-1.7}^{+1.5}$ (at 90% credibility) and with maximum mass $\sim 45 M_{\odot}$ (e.g. Abbott et al. 2019a).

of the star is immediately lost by the system and the BH (or NS) does not accrete it (while the version of BSE implemented in NBODY6++GPU assumes that the entire mass is absorbed by the compact object). This assumption by MOBSE is very conservative, because it is highly unlikely that the compact object can accrete a substantial fraction of the stellar mass, but it is hard to quantify the actual mass accretion.

2.2.3 Initial conditions

We generate the initial conditions with MCLUSTER (Küpper et al., 2011), which allows to produce models with different degrees of fractal substructures (Goodwin and Whitworth, 2004). The level of fractality is decided by the parameter D (where $D = 3$ means homogeneous distribution of stars). In this work, we adopt $D = 1.6$ (high-fractality runs³) and $D = 2.3$ (low-fractality runs). The qualitative difference between these two fractal dimensions is represented in Figure 2.1.

In this work, we have simulated 4×10^3 fractal young SCs: half of them with $D = 1.6$ (HF sample) and the remaining half with $D = 2.3$ (LF sample). The total mass M_{SC} of each SC (ranging from $1000 M_{\odot}$ to $30000 M_{\odot}$) is drawn from a distribution $dN/dM_{\text{SC}} \propto M_{\text{SC}}^{-2}$, as the embedded SC mass function described in Lada and Lada, 2003. Thus, the mass distribution of our simulated SCs mimics the mass distribution of SCs in Milky Way-like galaxies. We choose the initial SC half mass radius r_h according to the Marks & Kroupa relation (Marks et al., 2012), which relates the total mass M_{SC} of a SC at birth with its initial half mass radius r_h :

$$r_h = 0.10^{+0.07}_{-0.04} \text{ pc} \left(\frac{M_{\text{SC}}}{M_{\odot}} \right)^{0.13 \pm 0.04}. \quad (2.3)$$

The SCs are initialised in virial equilibrium.

All simulated SCs have stellar metallicity $Z = 0.002$, i.e. 1/10 of the solar metallicity (if we assume solar metallicity $Z_{\odot} = 0.02$). The stars in the simulated SCs follow a Kroupa, 2001 initial mass function, with minimum mass $0.1 M_{\odot}$ and maximum mass $150 M_{\odot}$.

We assume an initial binary fraction $f_{\text{bin}} = 0.4$. The orbital periods, eccentricities and mass ratios of binaries are drawn from Sana et al., 2012. In particular, we obtain the mass of the secondary m_2 as follows:

$$\mathfrak{F}(q) \propto q^{-0.1} \quad \text{with } q = \frac{m_2}{m_1} \in [0.1 - 1], \quad (2.4)$$

³Portegies Zwart, 2016 suggest that the fractal dimension of young SCs should be ~ 1.6 by comparing observations of the Orion Trapezium Cluster with N-body simulations.

the orbital period P from

$$\mathfrak{F}(r) \propto (r)^{-0.55} \quad \text{with } r = \log_{10}(P/\text{day}) \in [0.15 - 5.5] \quad (2.5)$$

and the eccentricity e from

$$\mathfrak{F}(e) \propto e^{-0.42} \quad \text{with } 0 \leq e < 1. \quad (2.6)$$

The force integration includes a solar neighbourhood-like static external tidal field. In particular, the potential is point-like and the simulated SCs are assumed to be on a circular orbit around the centre of the Milky Way with a semi-major axis of 8 kpc (Wang et al., 2016). Each SC is evolved until its dissolution or for a maximum time $t = 100$ Myr. The choice of terminating the simulations at $t = 100$ Myr is motivated by the fact that our tidal field model tends to overestimate the lifetime of SCs because we do not account for massive perturbers (e.g. molecular clouds), which accelerate the SC disruption (Gieles et al., 2006).

We compare the results of the SC simulations with isolated binary simulations performed with the standalone version of MOBSE. In particular, we simulate 10^7 isolated binaries (IBs) with the same initial conditions as SC binaries, i.e. metallicity $Z = 0.002$, primary mass drawn from a Kroupa (Kroupa, 2001) mass function between 0.1 and $150 M_{\odot}$, secondary mass, eccentricity and orbital periods derived from Sana et al., 2012.

A summary of the initial conditions of the performed simulations is reported in Table 2.1. In the following, we consider four simulation sets: i) HF: simulated SCs with high level of fractality ($D = 1.6$); ii) LF: simulated SCs with low level of fractality ($D = 2.3$); iii) SC: all simulated SCs (considering HF and LF simulations together); iv) IB: isolated binary simulations run with the standalone version of MOBSE.

2.3 Results

2.3.1 Statistics of dynamically formed binary BHs (BBHs)

First, we estimate how many BBHs form via dynamical channels in our simulations. We define *exchanged binaries* as binaries formed via dynamical exchanges, whereas those binaries which were generated in the initial conditions are dubbed as *original binaries*⁴. At the end of the simulations ($t = 100$ Myr), $\sim 85 - 89$ % of

⁴Usually, dynamicists use the adjective *primordial* to refer to binaries which are already present in the initial conditions, but we use a different adjective to avoid confusion with primordial BHs (i.e. BHs which originate from gravitational instabilities in the early Universe Carr et al. 2016).

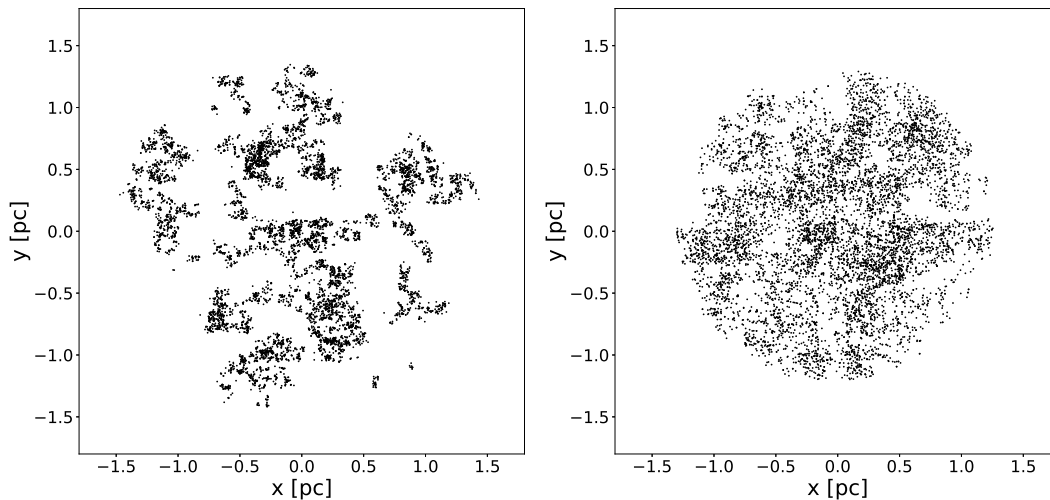


Figure 2.1: SC models generated with the MCLUSTER code. Each point represents a star. Both SCs have a total mass of $5000 M_{\odot}$. Top: model with fractal dimension $D = 1.6$. Bottom: model with fractal dimension $D = 2.3$.

Table 2.1: Initial conditions.

Set	Run number	$M_{\text{SC}} [M_{\odot}]$	$r_{\text{h}} [\text{pc}]$	Z	f_{bin}	D	IMF	$m_{\text{min}} [M_{\odot}]$	$m_{\text{max}} [M_{\odot}]$
HF	2×10^3	$10^3 - 3 \times 10^4$	$0.1 \times (M_{\text{SC}}/M_{\odot})^{0.13}$	0.002	0.4	1.6	Kroupa (2001)	0.1	150
LF	2×10^3	$10^3 - 3 \times 10^4$	$0.1 \times (M_{\text{SC}}/M_{\odot})^{0.13}$	0.002	0.4	2.3	Kroupa (2001)	0.1	150
SC	4×10^3	$10^3 - 3 \times 10^4$	$0.1 \times (M_{\text{SC}}/M_{\odot})^{0.13}$	0.002	0.4	1.6, 2.3	Kroupa (2001)	0.1	150
IB	10^7	–	–	0.002	1.0	–	Kroupa (2001)	5	150

Column 1: Name of the simulation set. HF: high fractality ($D = 1.6$) N-body simulations; LF: low fractality ($D = 2.3$) N-body simulations; SC: all N-body simulations considered together (i.e. set HF + set LF); IB: isolated binaries (population synthesis simulations run with MOBSE, without dynamics). Column 2: Number of runs; column 3: total mass of SCs (M_{SC}); column 4: half-mass radius (r_{h}); column 5: metallicity (Z); column 6: initial binary fraction (f_{bin}); column 7: fractal dimension (D); column 8: initial mass function (IMF); column 9: minimum mass of stars (m_{min}); column 10: maximum mass of stars (m_{max}).

all surviving BBHs are exchanged binaries. Thus, dynamical exchanges give an important contribution to the population of BBHs. We find no significant differences between runs with high fractal number (HF) and with low fractal number (LF). Table 2.2 shows the statistics for the different simulation sets.

We check how many of these BBHs are expected to merge by GW decay within a Hubble time ($t_{\text{H}} = 14 \text{ Gyr}$). No binaries merge during the dynamical simulations. Thus, to calculate the merging time, we use the following equation (Peters, 1964)

$$t_{\text{GW}} = \frac{5}{256} \frac{c^5 a^4 (1 - e^2)^{7/2}}{G^3 m_1 m_2 (m_1 + m_2)}, \quad (2.7)$$

where c is the speed of light, G is the gravitational constant, e is the eccentricity of the binary, a is the semi-major axis of the binary, m_1 and m_2 are the masses of the

primary and of the secondary BH, respectively. For each binary, we take the values of a and e at the end of the simulation (during the simulation, MOBSE integrates the change of eccentricity and semi-major axis driven by GW decay using a similar formalism, derived from Peters 1964).

The number of BBHs merging within a Hubble time (hereafter, merging BBHs) is also shown in Table 2.2. More than half of merging BBHs ($\sim 50\%$ and $\sim 56\%$ in HF and LF simulations, respectively) are exchanged binaries, confirming the importance of dynamical exchanges for merging BBHs. Moreover, only 4 merging BBHs ($\lesssim 2\%$ per cent of all merging BBHs) are still members of their parent SC at the end of the simulation, while the others have all been dynamically ejected.

These results confirm the importance of dynamics, and in particular of dynamical exchanges, for the demography of BBHs in small young SCs. Interestingly, the vast majority (if not all) of dynamically formed merging BBHs are no longer members of their parent SC when they merge, because of dynamical ejections.

Overall, the populations of merging BBHs in HF and LF simulations show a similar trend. For this reason, in the rest of the paper, we will consider HF and LF simulations as a single simulation set (SC simulations), unless otherwise specified. We will discuss the differences between HF and LF simulations in Section 2.3.6.

2.3.2 BH mass distribution

The next step is to understand whether BBHs formed in young SCs have distinctive features with respect to isolated binaries. In this section, we consider the mass of BHs.

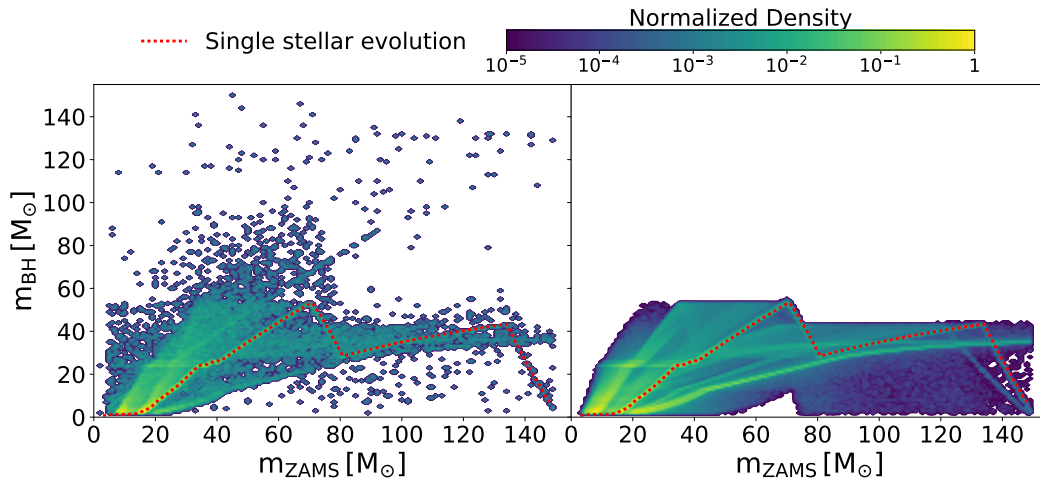


Figure 2.2: BH mass (m_{BH}) as a function of the zero-age main sequence (ZAMS) mass of the progenitor stars (m_{ZAMS}) in the SC simulations (left), and in IBs evolved with MOBSE (right). The logarithmic colour bar represents the number of BHs per cell, normalized to the maximum cell-value of each plot. Each cell is a square with a side of $1.5 M_{\odot}$. The red dashed line represents the mass spectrum of compact objects obtained from single stellar evolution. Dynamical interactions trigger the formation of more massive BHs. Intermediate-mass BHs (IMBHs, i.e. BHs with mass $m_{\text{BH}} > 150 M_{\odot}$) and second-generation BHs (Gerosa and Berti 2017, i.e. the products of the merger of two BHs) are not shown in this Figure.

2.3.2.1 BH mass versus ZAMS mass

Figure 2.2 shows the mass of all simulated BHs with mass $m_{\text{BH}} < 150 M_{\odot}$ (both single and binary BHs) as a function of the zero-age main sequence (ZAMS) mass of the progenitor star. The left-hand panel shows the results of the SC simulations (considering BBHs from models HF and LF together, because the level of fractality does not significantly affect the masses, see Table 2.3), while the right-hand panel shows the comparison sample of isolated binaries (IB). The BH mass we obtain from the evolution of single stars is shown as a red dotted line in both plots.

Dynamics does not affect significantly the mass of the majority of BHs: the most densely populated regions of the plot are the same in both panels. Binary evolution processes (especially mass transfer and common envelope) have a much stronger impact than dynamics on the mass of most BHs. For example, the large number of BHs with mass higher than expected from single star evolution (red dotted line) for progenitors with ZAMS mass $M_{\text{ZAMS}} < 60 M_{\odot}$ is an effect of mass accretion, while most of the BHs with mass lower than expected from single star evolution originate from donor stars whose envelope was peeled off (see Giacobbo and Mapelli 2018 and Spera et al. 2019a for more details on the effects of binary evolution on BH masses).

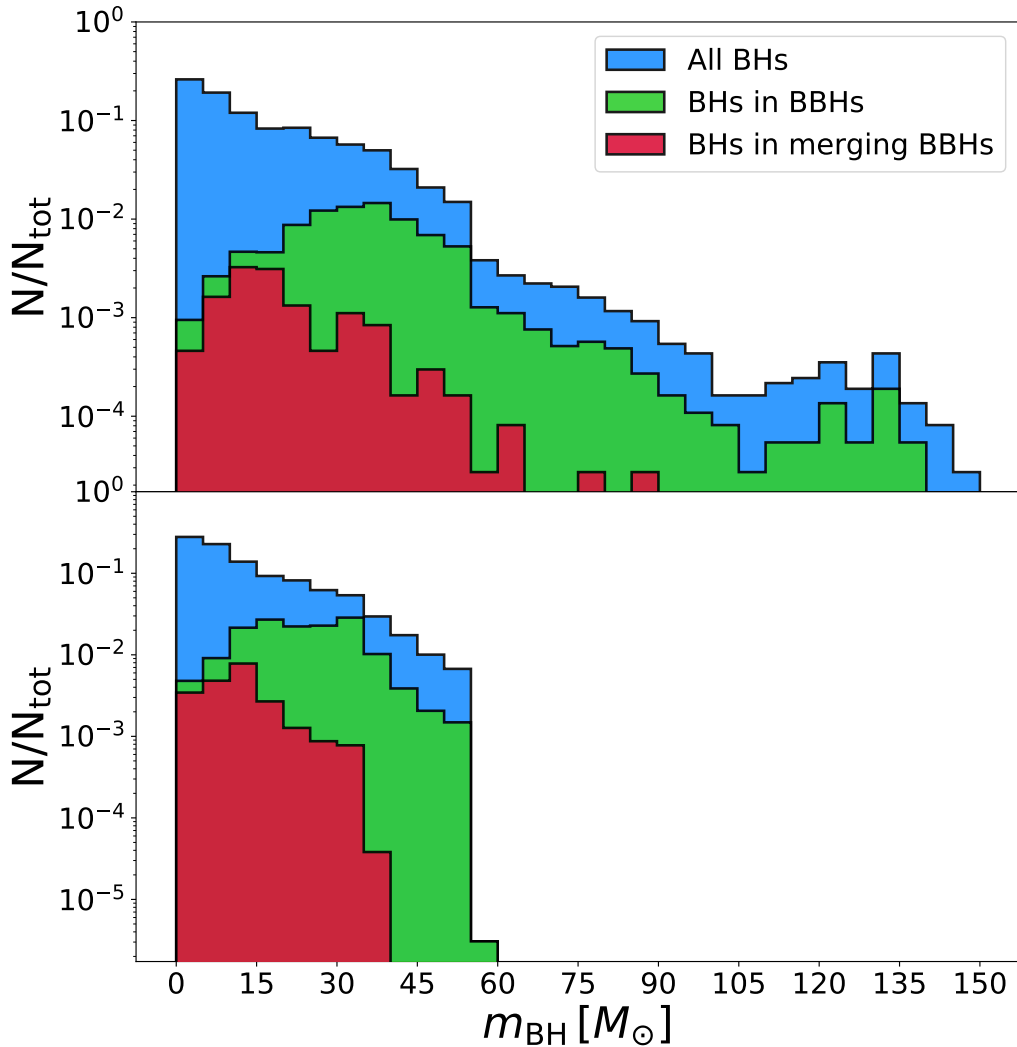


Figure 2.3: Top (Bottom) panel: distribution of BH masses in the SC (IB) simulations. Blue: all BHs excluding IMBHs and second-generation BHs; green: BHs which reside in BBH systems at the end of the simulations; red: BHs in merging BBH systems.

However, dynamics crucially affects the maximum mass of BHs (see also Fig. 2.3). In the N-body simulations, BHs with mass up to $\sim 440 M_{\odot}$ are allowed to form, while the maximum mass of BHs formed from isolated binary evolution is $\sim 60 M_{\odot}$. In Figures 2.2 and 2.3, we show only BHs with mass $< 150 M_{\odot}$ for clarity. BHs with mass $> 150 M_{\odot}$ are very rare and including them would make these figures more difficult to read. Figure 2.4 shows the BHs with mass $m_{\text{BH}} \geq 150 M_{\odot}$. These are intermediate-mass BHs (IMBHs) formed by runaway collisions of stars in the early evolution of the SC (see e.g. Portegies Zwart and McMillan 2002; Portegies Zwart et al. 2004; Giersz et al. 2015; Mapelli 2016). In our simulations, we find 24 IMBHs, which represent only the 0.065 % of all simulated BHs.

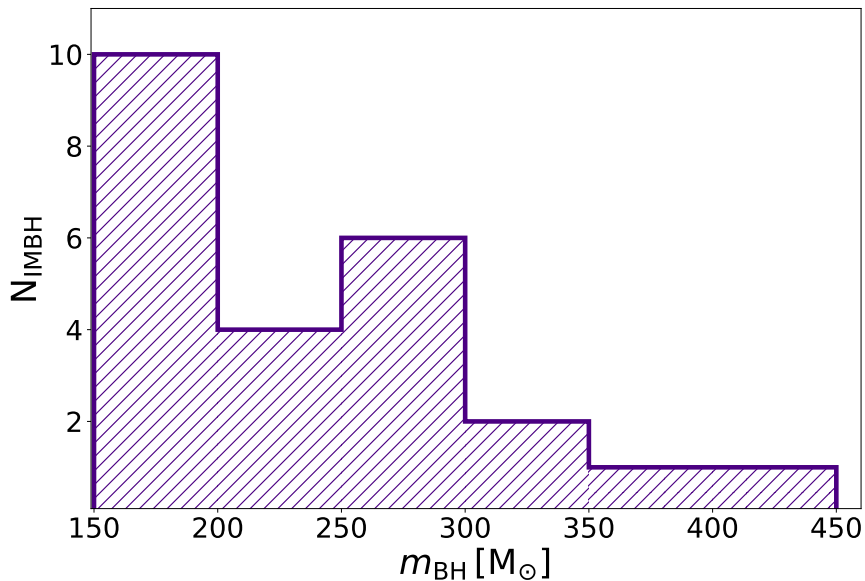


Figure 2.4: Mass distribution of the 24 IMBHs formed by runaway collisions in our SC simulations.

The percentage of BHs with mass $> 70 M_{\odot}$ in the N-body simulations is only $\sim 1\%$ of all BHs ($\sim 0.92\%$ and $\sim 0.96\%$ in LF and HF simulations, respectively). Thus, they are very rare, but their large mass is a clear signature of dynamical origin. These massive BHs form because of multiple stellar mergers, which can happen only in SCs. In fact, if the two members of an isolated binary merge together, the probability that their merger product acquires a new companion is negligible; whereas the merger product of a binary in a SC has a good chance to acquire a new companion dynamically (especially if it is particularly massive) and might merge also with new companion (Mapelli, 2016). Of course, these multiple mergers are mostly mergers of stars, because mergers of BBHs are much rarer events (see next section). In particular, the most massive BHs in our simulations form from the merger of at least four stars.

Because the most massive BHs originate from multiple stellar mergers (or even runaway collisions), the maximum BH mass in the N-body simulations essentially does not depend on the ZAMS mass of the progenitor (in the case of mergers, Figure 2.2 shows the ZAMS mass of the most massive among the stellar progenitors).

We expect PISNe and PPISNe to prevent the formation of BHs with mass $\sim 60 - 120 M_{\odot}$ from single stellar evolution (Belczynski et al., 2016a; Spera and Mapelli, 2017; Woosley, 2017). On the other hand, Spera et al., 2019a have already shown that binary evolution might produce few BHs in the mass gap. For example, the merger between an evolved star (with an already well developed Helium or Carbon-

Table 2.2: Number of SC BBHs.

Set	Exchanged BBHs	Original BBHs	Merging Exchanged BBHs	Merging Original BBHs
HF	710	124	60	59
LF	786	98	62	48

Number of BBHs in HF and LF simulations. Column 1: Name of the simulation set; column 2: number of BBHs that formed from dynamical exchanges and that are still bound at the end of the simulations ($t = 100$ Myr); column 3: number of BBHs that formed from original binaries and that are still bound at the end of the simulations ($t = 100$ Myr); column 4: number of BBHs that formed from dynamical exchanges and that merge within a Hubble time (hereafter merging exchanged BBHs); column 5: number of BBHs that formed from original binaries and that merge within a Hubble time (hereafter merging original BBHs).

Oxygen core) and a main sequence star might produce a very massive star with a large Hydrogen envelope but with a Helium core smaller than required to enter the pair-instability range. Such star might end its life directly collapsing to a BH with mass in the pair instability gap. In a SC, such massive BHs have additional chances to form (see e.g. Mapelli 2016), because multiple mergers between stars are likely. Moreover, if a BH with mass $\sim 60 - 120 M_{\odot}$ forms from the merger of an isolated binary, it will remain a single BH. In contrast, if a BH with mass $60 - 120 M_{\odot}$ forms from a binary in a SC, it might acquire another companion by dynamical exchange and merge via GW emission (see Section 3.2.3 for more details on these systems).

2.3.2.2 Mass of single versus binary BHs

The top panel of Figure 2.3 compares the mass distribution of all BHs with $m_{\text{BH}} < 150 M_{\odot}$ formed in the N-body simulations (including merger products) with the mass of BHs which are members of BBHs by the end of the N-body simulations. Light BHs are less likely to be members of a binary than massive BHs: just $\sim 4\%$ of BHs with mass lower than $30 M_{\odot}$ reside in BBHs by the end of the SC simulations, while $\sim 29\%$ of BHs with mass larger than $30 M_{\odot}$ have a BH companion by the end of the SC simulations.

The bottom panel of Figure 2.3 shows the same quantities for the IB simulations. The difference between top and bottom panel is apparent: no BHs with mass larger than $60 M_{\odot}$ form in the IB simulations at metallicity $Z = 0.002$, while SC dynamics induces the formation of BHs with mass up to $\sim 440 M_{\odot}$ (Fig. 2.4).

We stress that BHs with mass $\gtrsim 60 M_{\odot}$ are inside the mass gap expected from PISNe and PPISNe (Belczynski et al., 2016b; Woosley, 2017; Spera and Mapelli, 2017): they can form dynamically because of multiple mergers between stars.

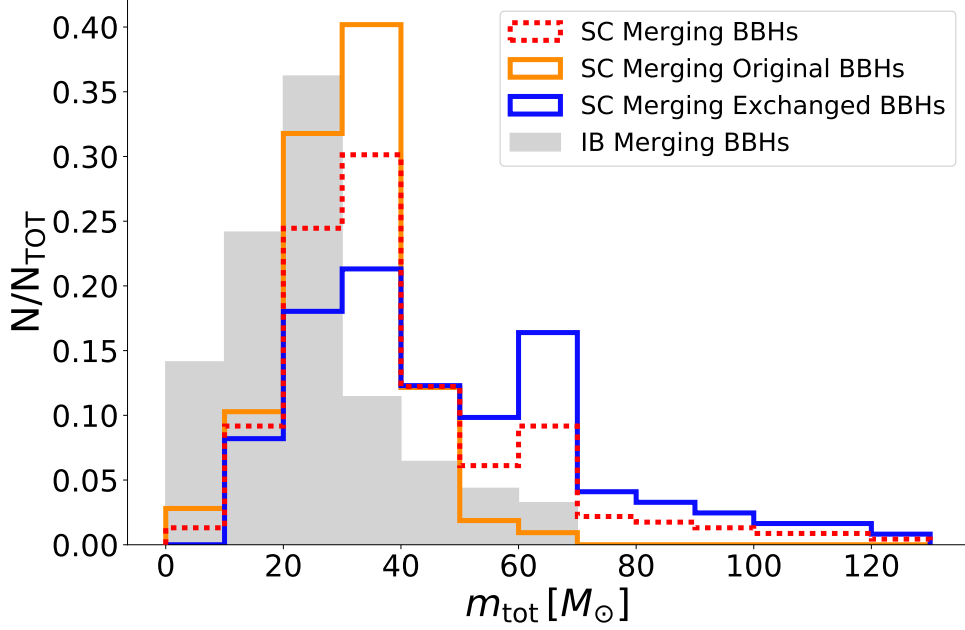


Figure 2.5: Distribution of total masses ($m_{\text{tot}} = m_1 + m_2$) of merging BBHs. Orange solid line: original BBHs formed in SCs; blue solid line: exchanged BBHs formed in SCs; red dashed line: all merging BBHs formed in SCs (original+exchanged); grey filled histogram: BBHs formed in isolated binaries (IBs). Each distribution is normalized to its total number of elements.

2.3.2.3 Mass of merging BHs: exchanged, original and isolated binaries

From Fig. 2.3 it is apparent that the most massive BHs do not merge within a Hubble time, in both IBs and SCs. This effect was already discussed in previous work (Giacobbo et al., 2018; Giacobbo and Mapelli, 2018; Spera et al., 2019a) and is a consequence of the stellar radius evolution of the progenitors of such massive BHs.⁵

If we compare the two red histograms in the top and bottom panel, we see that the maximum mass of merging BHs is larger in SCs than in IBs. Thus, dynamics triggers the merger of some massive ($> 40 M_{\odot}$) BHs, which cannot merge if they evolve in IBs.

Figure 2.5 shows the total masses ($m_{\text{tot}} = m_1 + m_2$) of merging exchanged and original BBHs in SCs. The former are merging BBHs which form from exchanged bina-

⁵Unless chemical homogeneous evolution is assumed, the radii of massive stars ($m_{\text{ZAMS}} \gtrsim 40 M_{\odot}$) reach values of several hundred to several thousand R_{\odot} . Stellar binaries with initial orbital separation larger than these radii survive early coalescence and can evolve into massive BBHs, but the latter cannot merge via GW decay because their semi-major axis is too large. In contrast, stellar binaries with smaller orbital separations either merge before becoming BHs or undergo a non-conservative mass transfer (or common envelope) process. At the end of this process, the binary might survive and evolve into a BBH, but the mass of the two BHs will be significantly smaller than expected from single stellar evolution, because of mass loss during mass transfer (Giacobbo and Mapelli, 2018; Spera et al., 2019a).

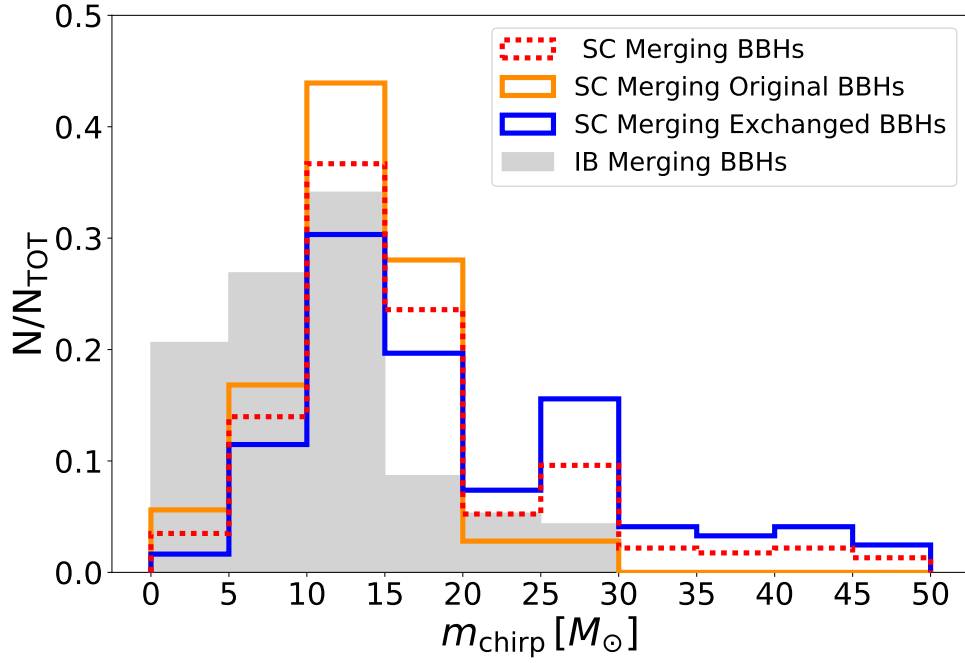


Figure 2.6: Same as Figure 2.5, but for the distribution of chirp masses $m_{\text{chirp}} = (m_1 m_2)^{3/5} (m_1 + m_2)^{-1/5}$ of merging BBHs.

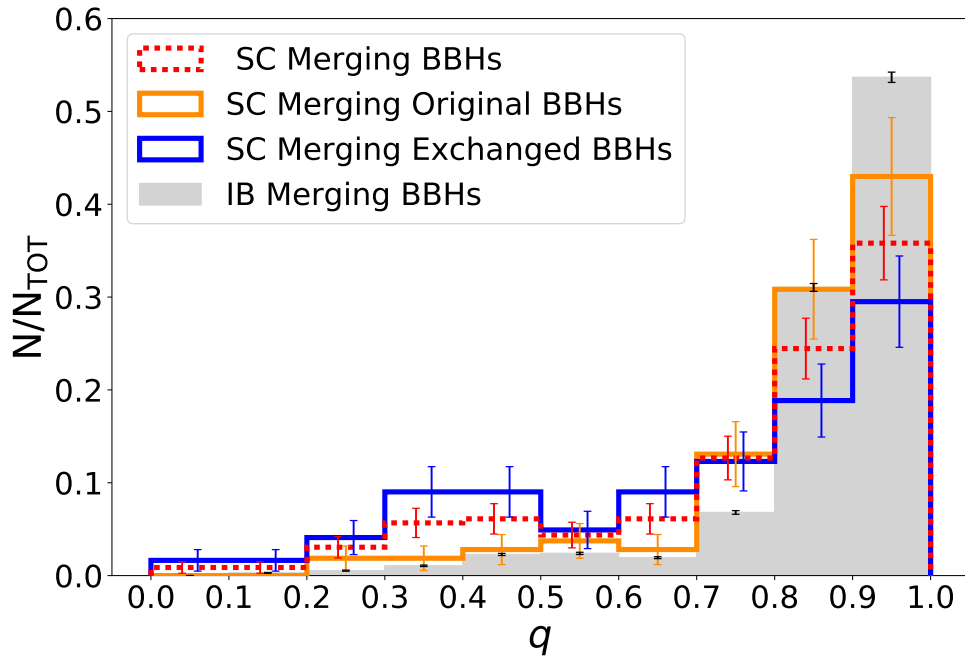


Figure 2.7: Same as Figure 2.5, but for the distribution of mass ratios $q = m_2/m_1$ of merging BBHs. The error bars represent Poisson uncertainties.

ries in SC simulations, while the latter are merging BBHs which form from original binaries in SC simulations. For comparison, we also show the total masses of merging BBHs from IB simulations. The distribution of exchanged BBHs is markedly different from the other two. In particular, merging exchanged BBHs tend to be more massive than original BBHs: $m_{\text{tot}} \leq 70 M_{\odot}$ for both isolated BBHs and original BBHs, while merging exchanged BBHs can reach $m_{\text{tot}} \sim 120 M_{\odot}$. Table 2.3 shows the results of the Wilcoxon U-test (Bauer, 1972; Hollander and Wolfe, 1999) and of the Kolmogorov-Smirnov (KS) test (Birnbaum, Tingey, et al., 1951; Wang et al., 2003), which confirm that the mass distribution of merging exchanged BBHs is not consistent with the other two classes of merging BBHs.

This large difference can be easily explained with the properties of dynamical exchanges: exchanges tend to favour the formation of more and more massive binaries because these are more energetically stable (see e.g. Hills and Fullerton 1980). Interestingly, the mass distribution of merging original BBHs is also significantly different from the distribution of merging BBHs formed from IB simulations (see Table 2.3). Since both IBs and original binaries in SCs were evolved with the same population synthesis code (MOBSE), dynamical effects are the only way to explain this difference. Even if they do not form through dynamical exchanges, also original BBHs participate in the dynamical life of a SC: they can be hardened or softened or even ionized by three-body encounters. More massive BBHs are more likely to be hardened by three-body encounters, while light BBHs are more likely to be softened or ionized. This explains why merging original BBHs tend to be more massive than merging BBHs in IBs. Thus, dynamics affects almost the entire population of merging BBHs in SCs: not only exchanged BBHs, but also original BBHs.

Similar considerations apply also to the distribution of chirp masses $m_{\text{chirp}} = (m_1 m_2)^{3/5} (m_1 + m_2)^{-1/5}$ (Figure 2.6): we find no merging original BBHs with $m_{\text{chirp}} > 30 M_{\odot}$, while merging exchanged BBHs reach $m_{\text{chirp}} \sim 50 M_{\odot}$.

Figure 2.7 shows the mass ratios of merging BBHs (defined as $q = m_2/m_1$). All distributions peak at $q \sim 1$. However, small mass ratios are significantly more likely in merging exchanged BBHs than in both merging original and isolated BBHs. Moreover, merging exchanged BBHs show a (marginally statistically significant) bump around $q \sim 0.4$.

Table 2.3 confirms that the distribution of q of the merging exchanged BBHs is significantly different from both merging original BBHs and isolated binaries. This can be easily explained with the different formation channels. If two BHs form from the same close stellar binary, mass transfer and common envelope episodes tend to “redistribute” the mass inside the system, leading to the formation of two BHs with

Table 2.3: Results of the U-Test and KS-Test to compare two BBH samples.

BBH sample 1	BBH sample 2	Distribution	U-Test	KS-Test	Median 1	Median 2
HF – Merging BBHs	LF – Merging BBHs	m_{tot}	0.57	0.20	32.8 M_{\odot}	35.4 M_{\odot}
HF – Merging BBHs	LF – Merging BBHs	m_{chirp}	0.51	0.50	14.0 M_{\odot}	14.6 M_{\odot}
HF – Merging BBHs	LF – Merging BBHs	q	0.03	0.05	0.88	0.81
HF – Merging BBHs	LF – Merging BBHs	t_{exch}	0.04	0.11	1.9 Myr	2.8 Myr
SC – Merging BBHs	IB – Merging BBHs	m_{tot}	0	0	34.7 M_{\odot}	24.0 M_{\odot}
SC – Merging BBHs	IB – Merging BBHs	m_{chirp}	0	0	14.2 M_{\odot}	10.4 M_{\odot}
SC – Merging BBHs	IB – Merging BBHs	q	10^{-7}	10^{-7}	0.84	0.89
SC – Merging Exchanged BBHs	SC – Merging Original BBHs	m_{tot}	10^{-8}	10^{-8}	41.5 M_{\odot}	30.2 M_{\odot}
SC – Merging Exchanged BBHs	IB – Merging BBHs	m_{tot}	0	0	41.5 M_{\odot}	24.0 M_{\odot}
SC – Merging Original BBHs	IB – Merging BBHs	m_{tot}	10^{-9}	10^{-9}	30.2 M_{\odot}	24.0 M_{\odot}
SC – Merging Exchanged BBHs	SC – Merging Original BBHs	m_{chirp}	10^{-5}	10^{-7}	16.9 M_{\odot}	13.2 M_{\odot}
SC – Merging Exchanged BBHs	IB – Merging BBHs	m_{chirp}	0	0	16.9 M_{\odot}	10.4 M_{\odot}
SC – Merging Original BBHs	IB – Merging BBHs	m_{chirp}	10^{-9}	10^{-9}	13.2 M_{\odot}	10.4 M_{\odot}
SC – Merging Exchanged BBHs	SC – Merging Original BBHs	q	10^{-4}	10^{-4}	0.78	0.89
SC – Merging Exchanged BBHs	IB – Merging BBHs	q	10^{-9}	10^{-9}	0.78	0.89
SC – Merging Original BBHs	IB – Merging BBHs	q	0.27	0.14	0.89	0.89

In this Table we apply the U- and KS- tests to compare different samples of merging BBHs (i.e. BBHs merging within a Hubble time). Columns 1 and 2: the two BBH samples to which we apply the U- and KS- test. Each sample comes from one of the simulation sets (HF, LF, SC and IB, see Table 2.1). For the SC sample we also distinguish between “Exchanged BBHs” and “Original BBHs” (see Section 3.1 for the definition). Column 3: distribution to which we apply the U- and KS- tests. We consider total BBH masses (m_{tot}), chirp masses (m_{chirp}), mass ratios (q) and time of the exchange (t_{exch} , for exchanged binaries only). Columns 4 and 5: probability that the two samples are drawn from the same distribution according to the U-Test and to the Kolmogorov-Smirnov (KS) Test, respectively. Values smaller than 10^{-20} are indicated with 0. Columns 6 and 7: median values of the distributions of BBH sample 1 and 2, respectively.

similar mass. In contrast, if two BHs enter the same binary by exchange, after they formed, their mass cannot change anymore and even extreme mass ratios $q \sim 0.1$ are possible.

Finally, Figure 2.8 shows the mass of the primary BH versus the mass of the secondary BH of merging systems. The first 10 GW events associated with BBHs are also shown. It must be kept in mind that we are not weighing the simulated distributions for the probability of observing them with LIGO-Virgo (e.g. more massive BHs can be observed to a farther distance than light BHs, Abbott et al. 2016b). From this Figure, it is apparent that the LIGO-Virgo BBHs lie in a region of the $m_1 - m_2$ plane which is well populated by both IB and SC merging BBHs at metallicity $Z = 0.002$. Merging exchanged BHs are clearly different from the other two populations, both in terms of masses and in terms of mass ratios. Interestingly, the most massive event GW170729 (Abbott et al., 2019b) lies in a region that is populated only by merging exchanged BBHs.

Table 2.4 summarizes the masses of the most massive merging BBHs in our simu-

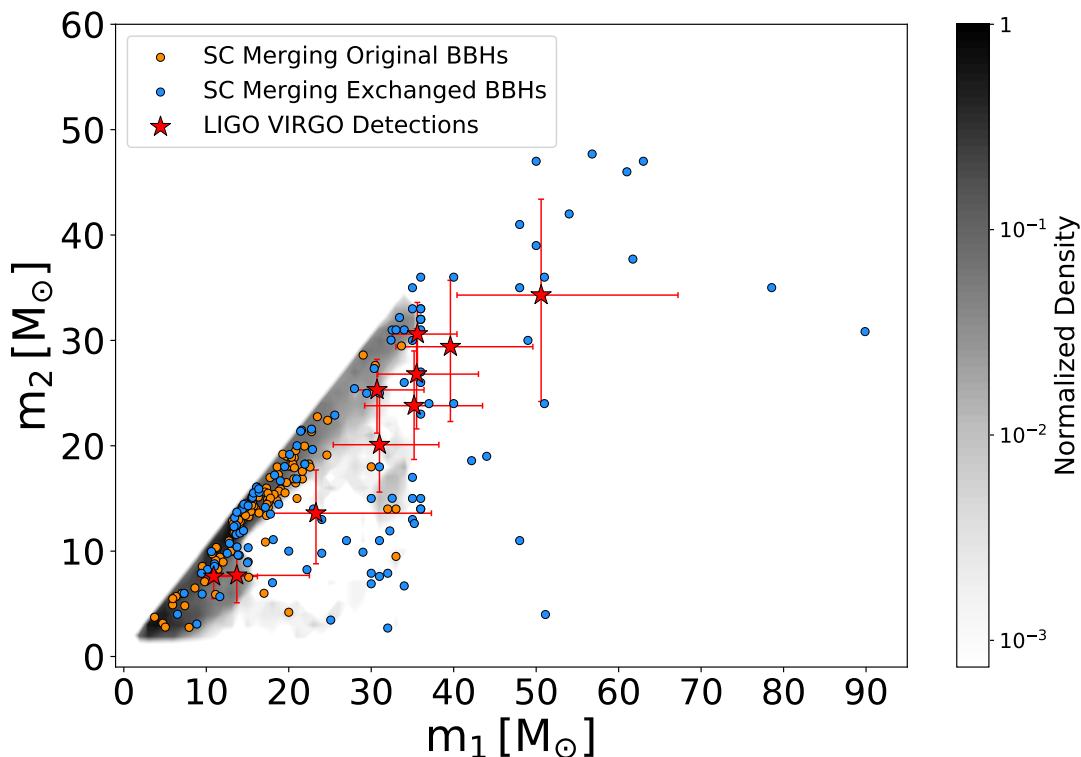


Figure 2.8: Mass of the primary BH (m_1) versus mass of the secondary BH (m_2) of merging BBHs. Filled contours (with grey colour map): IBs; orange circles: SC merging original BBHs; blue circles: SC merging exchanged BBHs; red stars with error bars: LIGO-Virgo detections of BH mergers – GW150914 (Abbott et al., 2016a), GW151012 (Abbott et al., 2016d), GW151226 (Abbott et al., 2016e), GW170104 (Abbott et al., 2017a), GW170608 (Abbott et al., 2017b), GW170729 (Abbott et al., 2019b), GW170809 (Abbott et al., 2019b), GW170814 (Abbott et al., 2017c), GW170818 (Abbott et al., 2019b) and GW170823 (Abbott et al., 2019b). Error bars indicate 90% credible levels.

lations (with $m_{\text{tot}} \geq 70 M_\odot$). All of them are SC exchanged BBHs. The mass of the primary spans from 35 to 90 M_\odot , with five BHs more massive than 60 M_\odot (these lie in the mass gap produced by PPISNe and PISNe). The mass of the secondary ranges from 24 to 48 M_\odot . These massive merging BBHs have median mass ratio $q = 0.75$, significantly lower than 1. The most massive binary ($m_1 = 90 M_\odot$, $m_2 = 31 M_\odot$) has also the lowest mass ratio $q = 0.34$.

2.3.3 Orbital eccentricity of merging BBHs

Orbital eccentricity is another feature which can be probed with current and future GW detectors (Nishizawa et al., 2016; Nishizawa et al., 2017; Rodriguez et al., 2018). Dynamical exchanges tend to produce more eccentric binaries, although GW emission circularizes them very efficiently. Thus, even binaries with extreme eccentric-

Table 2.4: Heavy merging BBHs.

m_1 (M_\odot)	m_2 (M_\odot)	q
90	31	0.34
79	35	0.44
63	47	0.75
62	38	0.53
61	46	0.75
57	48	0.84
54	42	0.78
51	36	0.71
51	24	0.47
50	47	0.94
50	39	0.78
48	41	0.85
48	35	0.73
49	30	0.61
40	36	0.78
36	36	1.00
35	35	1.00

Properties of merging BBHs with total mass $m_{\text{tot}} \geq 70 M_\odot$. Column 1: primary mass (m_1); column 2: secondary mass (m_2); column 3: mass ratio (q). All these binaries are exchanged BBHs.

ity might achieve almost null eccentricity when they reach the LIGO-Virgo band (> 10 Hz). However, a significant fraction of exchanged BBHs formed in SCs (e.g. Rodriguez et al. 2018; Samsing 2018; Arca-Sedda et al. 2018) or nuclear SCs (e.g. Antonini and Rasio 2016) is predicted to have eccentricity $e \gtrsim 10^{-2}$ when entering the LISA band ($\sim 10^{-4} - 1$ Hz).

Figure 2.9 shows the initial eccentricity e_{in} of our merging BBHs (i.e. the orbital eccentricity of the binary when it becomes a BBH binary) and the eccentricity e_{LISA} when the orbital frequency is $f_{\text{orb}} = 10^{-2}$ Hz (approximately associated to the maximum sensitivity of LISA, see Amaro-Seoane et al. 2017a). To estimate e_{LISA} , we evolve the BBHs up to $f_{\text{orb}} = 10^{-2}$ Hz following Peters, 1964 equations.

The initial eccentricity distribution of SC merging exchanged BBHs shows an upturn for $e_{\text{in}} > 0.6$ and is clearly different from both SC merging original BBHs and IBs. In contrast, when entering the LISA band, all systems (including exchanged BBHs) have significantly circularized. The minimum detectable eccentricity by LISA is $e_{\text{LISA}} \sim 10^{-2}$, according to Nishizawa et al., 2016. Only ~ 2.5 % (~ 1.6 %) merging exchanged BBHs (merging BBHs in IBs) have $e_{\text{LISA}} \gtrsim 10^{-2}$.

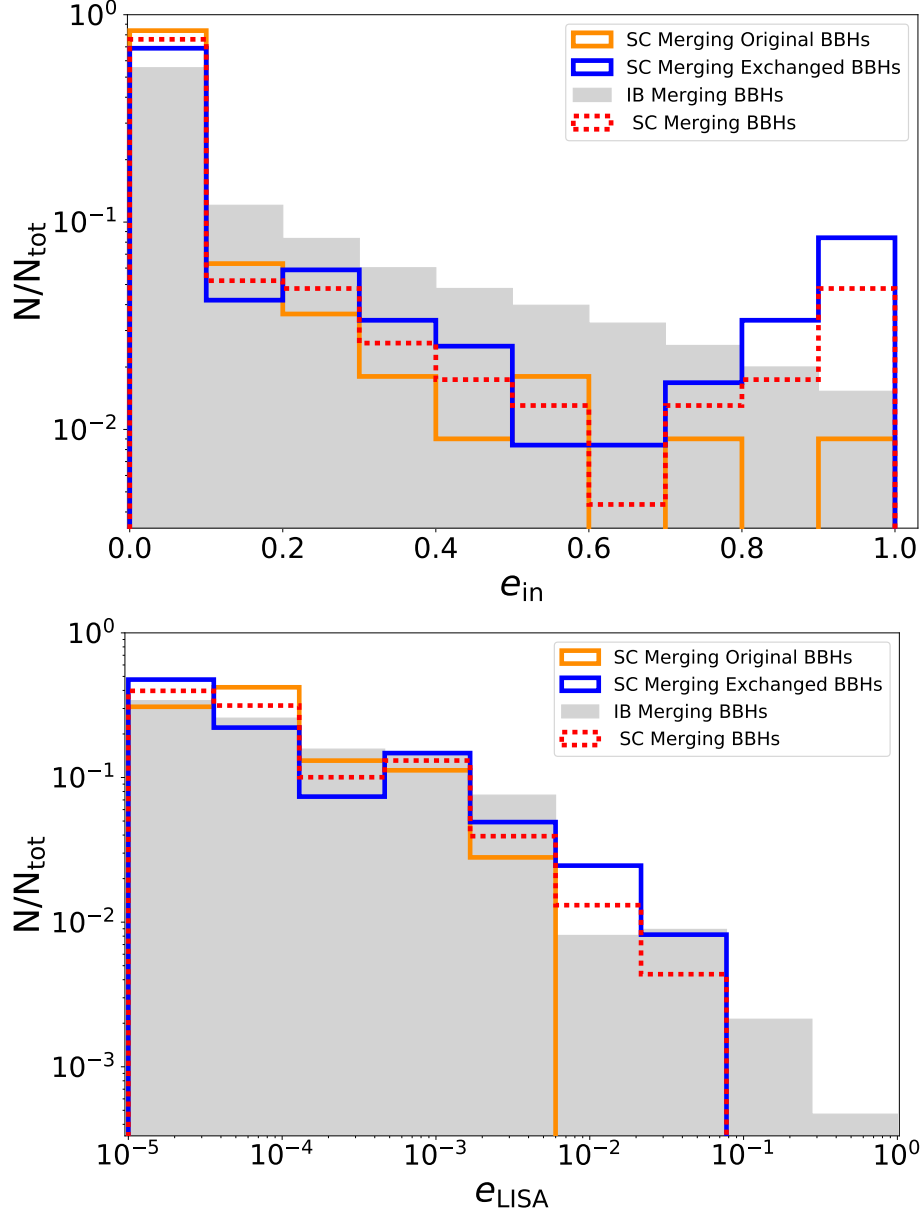


Figure 2.9: Distribution of eccentricities of merging BBHs in SCs and in IBs. All merging BBHs in SCs are shown by the dashed red line. BBHs in IBs are shown by the filled grey histogram. SC merging original BBHs and SC merging exchanged BBHs are shown with an orange and blue line, respectively. The eccentricity e_{in} (left) is calculated when the binary becomes a BBH, while e_{LISA} (right) is calculated when the orbital frequency is $f_{\text{orb}} = 10^{-2}$ Hz (where the sensitivity of LISA is approximately maximum). In the right-hand panel, eccentricities e_{LISA} equal to zero have been set equal to 10^{-5} .

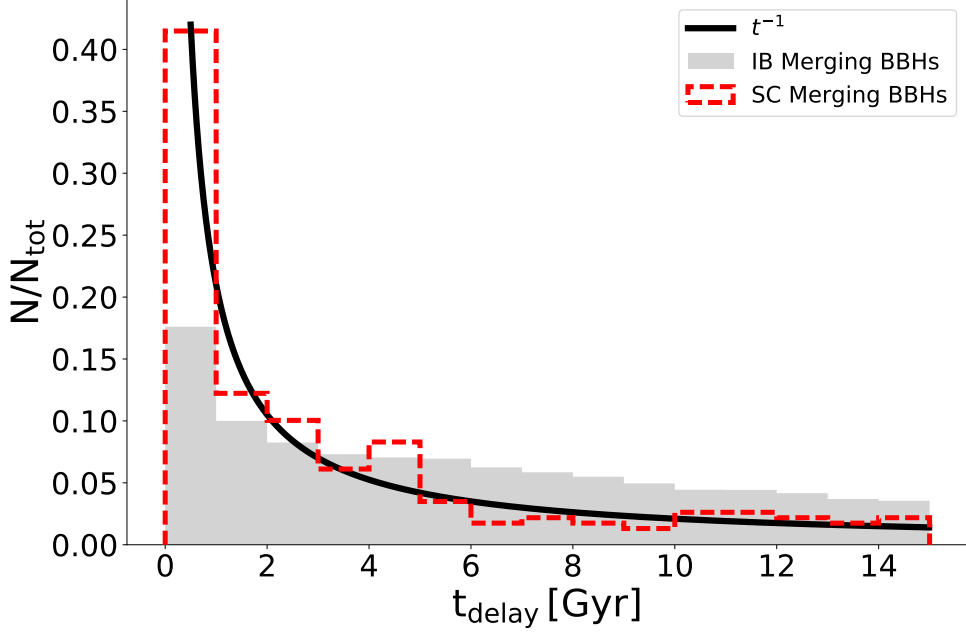


Figure 2.10: Distribution of the delay timescales t_{delay} of merging BBHs. Grey shaded histogram: merging BBHs in IBs; red dashed line: all merging BBHs from SC simulations (exchanged BBHs plus original BBHs).

Our results confirm that BBHs formed by exchange have significantly larger eccentricity at formation than other BBHs (see e.g. Ziosi et al. 2014). However, the maximum eccentricity of young SC BBHs in the LISA band is significantly smaller than the distribution of BBHs in both globular clusters and nuclear SCs (Nishizawa et al., 2016; Nishizawa et al., 2017; Rodriguez et al., 2018).

2.3.4 Delay time distribution

A key quantity to predict the merger rate and the properties of merging BBHs is the delay time, i.e. the time elapsed between the formation of the stellar progenitors and the merger of the two BHs.

Figure 2.10 shows that SC BBHs undergo a faster merger than BBHs in IBs. In particular, the distribution of delay times for SC merging BBHs scales as $dN/dt_{\text{delay}} \propto t_{\text{delay}}^{-1}$ while IB merging BBHs follow a shallower slope, with significantly less mergers in the first Gyr and a more populated tail with $t_{\text{delay}} \gtrsim 5$ Gyr. This suggests that dynamical interactions in young SCs can speed up the merger of BBHs.

Furthermore, the delay time distribution of BBHs in our IB sample is significantly shallower than $\propto t_{\text{delay}}^{-1}$, which is the slope found by Dominik et al., 2012 in their population-synthesis simulations. In IBs, the distribution of delay times depends

on progenitor’s metallicity, common envelope efficiency (described by α) and natal kicks (see [Giacobbo and Mapelli 2018](#) for more details). In particular, if we assume $\alpha \geq 3$ the fraction of BBHs with $t_{\text{delay}} \leq 1$ Gyr is significantly reduced with respect to lower values of α (see Figure 6 of [Giacobbo and Mapelli 2018](#)). This explains why our merging BBHs in IBs (simulated with $\alpha = 3$) have a delay time distribution significantly flatter than that of [Dominik et al., 2012](#), which assume $\alpha = 1$.

2.3.5 Number of mergers per unit stellar mass

Does SC dynamics boost the merger rate, too?

The simulations presented in this paper are not sufficient to estimate the merger rate, because we considered only one stellar metallicity and we know from previous papers ([Giacobbo and Mapelli, 2018](#)) that the merger rate of BBHs is very sensitive to stellar metallicity. However, we can estimate the merger efficiency, i.e. the number of mergers per unit stellar mass for a given metallicity $N_m(Z)$, integrated over the Hubble time.

As detailed in [Giacobbo et al., 2018](#), $N_m(Z)$ is the number of BBH mergers we find in the simulated sample (N_{merger}), divided by the total initial mass of the stellar population (M_*):

$$N_m(Z) = \frac{N_{\text{merger}}}{M_*}. \quad (2.8)$$

For the N-body simulations, M_* is just the total initial stellar mass of the simulated SCs, because the simulated SCs already include star masses ranging between 0.1 and 150 M_\odot and because we use a quite realistic initial binary fraction ($f_{\text{bin}} = 0.4$). In contrast, in the IB simulations, $M_* = M_{*,\text{sim}} / (f_{\text{bin}} f_{\text{corr}})$, where $M_{*,\text{sim}}$ is the total initial stellar mass of the simulated IBs, $f_{\text{bin}} = 0.4$ accounts for the fact that we are simulating only binaries and not single stars, and f_{corr} accounts for the missing low-mass stars between 0.1 and 5 M_\odot (see [Table 2.1](#)).

The values of $N_m(Z = 0.002)$ for the four simulation sets presented in this paper are shown in [Table 2.5](#). The merger efficiency of the four simulation sets are remarkably similar. This implies that dynamics in young SCs does not affect the merger rate significantly.

Indeed, dynamics changes the properties of merging binaries (leading to the formation of more massive BBHs), but does not change their number significantly. The number of merging BBHs which form by exchange or harden by dynamical interactions appears to be compensated by the suppression of light merging BBHs (see [Figure 2.5](#)). In a forthcoming study ([Di Carlo et al., in prep.](#)) we will check whether

Table 2.5: Number of mergers per unit stellar mass.

Set	$N_m(Z = 0.002)$ [M_\odot^{-1}]
HF	1.75×10^{-5}
LF	1.61×10^{-5}
SC	1.68×10^{-5}
IB	1.70×10^{-5}

Column 1: Name of the simulation set; column 2: $N_m(Z = 0.002)$ as defined in equation 2.8.

this result depends on stellar metallicity or on other properties of the simulated SCs.

2.3.6 Impact of fractality

So far, we have considered HF and LF simulations as a single simulation sample (SC simulations), because fractality does not significantly affect most of BBH properties (e.g. the number of merging BBHs, the merger efficiency and the mass of merging BHs, see Table 2.3). Thus, we can conclude that the level of substructures does not significantly affect the merger of BBHs and can be neglected in future studies. This result is important because it removes one of the possible parameters which were thought to affect the statistics of BBHs.

However, there are a couple of intriguing differences between HF and LF simulations (see Table 2.3), although these differences are only marginally significant.

First, the HF clusters tend to produce merging BBHs with larger mass ratios than the LF clusters (median values of $q = 0.9$ and $q = 0.8$ in HF and LF simulations, respectively, see Table 2.3). Secondly, the median time of dynamical exchange for merging exchanged BBHs (t_{exch} , i.e. the time when a dynamical exchange leads to the formation of the binary which then becomes a merging BBH) is $t_{\text{exch}} = 1.9$ Myr and 2.8 Myr for HF and LF clusters, respectively (see also Figure 2.11).

Although only marginally significant, these differences are consistent with our expectations. In fact, the more fractal (i.e. sub-structured) a SC is, the shorter is its two-body relaxation timescale t_{rlx} (see e.g. Fujii and Portegies Zwart 2014). A shorter two-body relaxation timescale implies also a shorter core-collapse timescale. Core collapse is the moment of the life of a SC when three-body encounters and exchanges are more likely to occur, because of the boost in the central density. Thus, we expect dynamical exchanges (leading to the formation of merging BBHs) to occur earlier in HF simulations than in LF simulations.

Moreover, if $t_{\text{exch}} < 3$ Myr, the exchange occurs before the binary has turned into a BBH, because the lifetime of the most massive stars is $\gtrsim 3$ Myr. If the binary which forms after an exchange is still composed of two non-degenerate stars (or a star and a BH), it may still undergo mass transfer and common envelope after the exchange. This mass transfer or common envelope is expected to “redistribute” the mass between the two members of the binary, leading to the formation of an almost equal mass BBH. In contrast, if $t_{\text{exch}} \gg 3$ Myr, the outcome of the exchange is already a BBH, which cannot undergo mass transfer and whose mass ratio can be small. For this reason, the fact that t_{exch} is significantly shorter in HF clusters than in LF clusters implies that the median q of the former is larger than the median q of the latter, because exchanged binaries in HF clusters have more chances to undergo common envelope than exchanged binaries in LF clusters.

2.4 Comparison with previous work

Our BH mass spectrum (Figure 2.3) is significantly different from the one reported by previous papers on BBHs in young SCs. In comparison with the BH mass spectrum reported by Banerjee, 2018a and Banerjee et al., 2019, our mass spectrum is broader, we form more massive BHs and our distribution peaks at a lower mass value (see Figure 1 of Banerjee 2018a and the top panel of our Figure 2.3). As a result, we form merging BBHs with both lower and higher total masses. This may be a consequence of our different wind mass loss and supernova prescriptions (Banerjee 2018a use the standard version of BSE). Another possibility could be that the smaller initial mass and relaxation time of our SCs may lead to an increased number of runaway stellar mergers.

Furthermore, we find significantly smaller eccentricities in the LISA band (e_{LISA}); this could depend on post-Newtonian terms, which are not included in our study and are taken into account in Banerjee, 2018a. Similarly, Rastello et al., 2019 find only very eccentric merging BBHs ($e \geq 0.99$), while most our merging BBHs have a nearly circular orbit.

In contrast, the eccentricity (Figure 2.9) and delay time distribution (Figure 2.10) of merging BBHs in our simulations are in good agreement with Kumamoto et al., 2019a. Similar to Kumamoto et al., 2019a, we find that most exchanged merging BBHs undergo the first exchange before the second BH has formed: these systems undergo a common envelope after the first exchange.

Another parameter that may affect the statistics of BBHs is the initial binary fraction f_{bin} . We assume $f_{\text{bin}} = 0.4$, while observations seem to indicate $f_{\text{bin}} \sim 0.6 - 0.7$

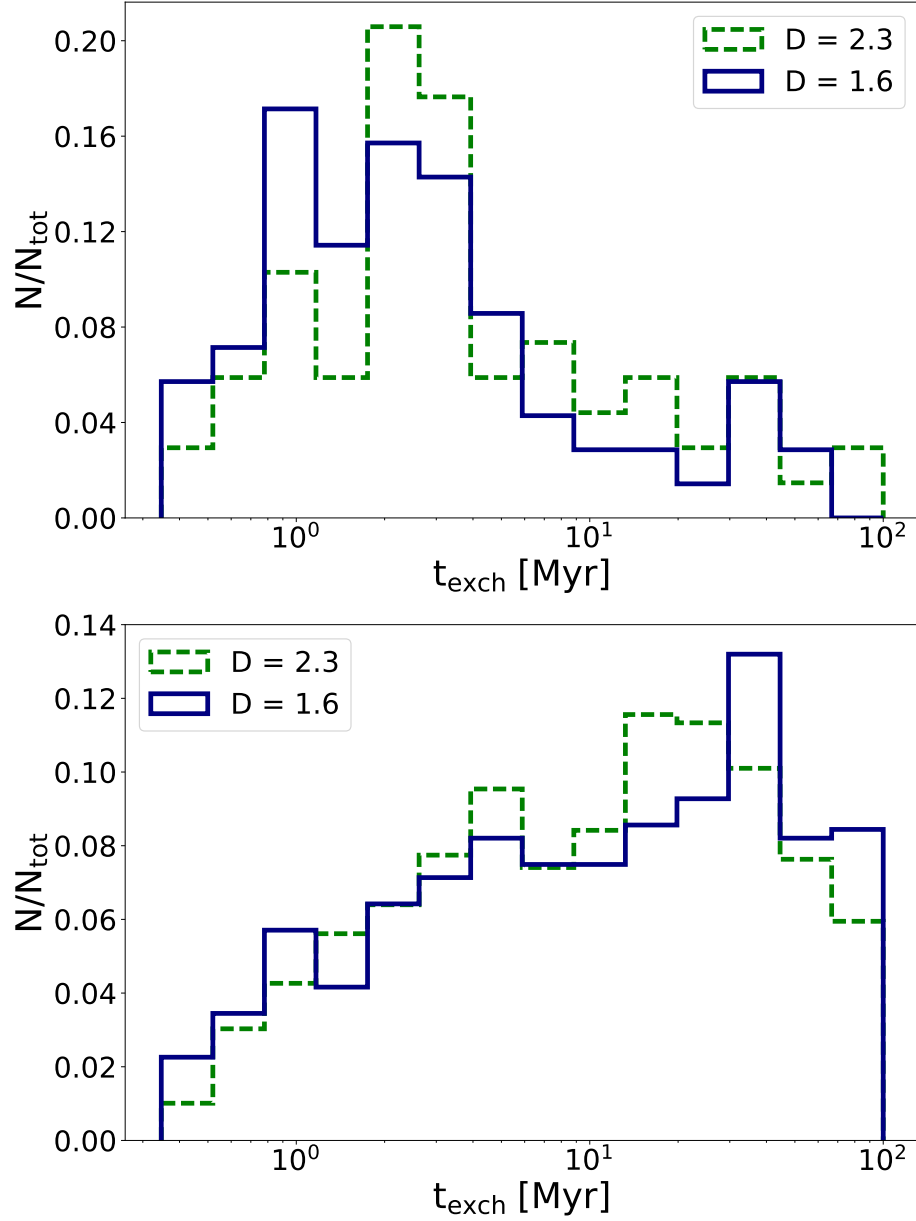


Figure 2.11: Formation times of merging exchanged BBHs (top panel) and of all exchanged BBHs (bottom). The formation time is defined as the time interval between the beginning of the simulation and the moment in which the binary forms. We show the distributions for fractal dimensions $D = 2.3$ (green dashed) and for $D = 1.6$ (blue solid). Each distribution is normalized to its total number of elements.

(Sana et al., 2012). We stress that $f_{\text{bin}} = 0.4$ is the highest initial binary fraction ever assumed in a large set of direct N-body simulations studying BBHs, because the number of initial binaries is the bottleneck of direct N-body simulations. Indeed, most previous studies of BBHs in young SCs assume no initial binaries (e.g. Banerjee et al. 2010; Banerjee 2018b; Mapelli 2016; Kumamoto et al. 2019a) or lower values of f_{bin} (e.g. $f_{\text{bin}} = 0.2$ in Ziosi et al. 2014). Assuming a higher value of f_{bin} would likely affect the number of original BBHs only: Mapelli and Zampieri, 2014 find that the number of original BH binaries grows almost linearly with f_{bin} , while the number of exchanged BH binaries remains almost unchanged.

2.5 Discussion

We have shown that young SC dynamics crucially affects the main properties (mass, eccentricity and delay time) of merging BBHs, but how common is the dynamical formation of BBHs in young SCs?

Star formation (and especially massive star formation) is expected to occur mostly in young SCs and associations (Lada and Lada, 2003; Portegies Zwart et al., 2010). This implies that most BBH progenitors were born in SCs or OB associations, and a significant fraction of them underwent dynamical interactions before being ejected from their parent SC, or before the SC dissolved in the galactic tidal field. Is the time spent by a BBH (or BBH progenitor) in the parent SC sufficient to significantly affect the properties of merging BBHs?

The crucial point is to understand when merging exchanged BBHs form in our simulations. In fact, our simulations include a static tidal field, assuming that the simulated SCs are on circular orbits approximately at the location of the Sun. This approach tends to overestimate the lifetime of SCs, because we do not account for orbits closer to the galactic centre and, most importantly, we do not account for massive perturbers (e.g. molecular clouds), which might accelerate the disruption of the parent SC (Gieles et al., 2006).

Figure 2.11 shows the time of the dynamical exchange for merging exchanged BBHs (top) and for all exchanged BBHs (bottom). While most exchanged BBHs form at late stages in the evolution of their parent SC, the majority of merging exchanged BBHs form in the first ~ 10 Myr. This guarantees that the majority of merging exchanged BBHs would have formed even if the tidal field was locally stronger.

The difference between top and bottom panel of Figure 2.11 can be explained straightforwardly with the nature of the exchanged binaries: only ~ 13 % of merging

exchanged BBHs originate from a dynamical exchange which leads to the immediate formation of a BBH, while the dynamical exchange produces a new star–star binary (i.e. a binary system composed of two stars) and a BH–star binary in the $\sim 77\%$ and 10% of systems, respectively. In contrast, $\sim 59\%$ of all exchanged BBHs form from dynamical exchanges which lead to the formation of a BBH directly, while 37% (4%) exchanges produce star–star (BH–star) binaries. This implies that binaries which undergo an exchange before both stars have turned into BHs are more likely to merge within a Hubble time. The reason is that exchanged star–star binaries and BH–star binaries can still undergo common envelope episodes, which shrink their orbital separation significantly and favour their merger within a Hubble time. Thus, in young SCs, stellar binary evolution and dynamics strictly cooperate to the formation of merging exchanged BBHs.

In contrast, double degenerate binaries can shrink only by three-body encounters and by GW decay, which are not as efficient as common envelope. Thus, most exchanged BBHs which form at late times cannot merge within a Hubble time. In this regard, young SCs are quite different from globular clusters (Rodriguez et al., 2015; Rodriguez et al., 2016; Askar et al., 2017a): a large fraction of exchanged BBHs in globular clusters remain inside the parent SCs for many Gyr, undergoing several exchanges and shrinking efficiently by dynamical hardening, while most exchanged binaries in young SCs undergo a single exchange and harden for a short time span. In this work, we have chosen to stop the integration of our SCs 100 Myr after their formation. A possible issue connected with this choice is whether dynamical exchanges and hardening might have played a role even after 100 Myr. According to Gieles et al., 2006, the estimated lifetime of a SC with mass $10^4 M_\odot$ in the solar neighbourhood is ~ 1 Gyr. Only $\lesssim 6\%$ of our simulated SCs have mass $M_{\text{SC}} \geq 10^4 M_\odot$, while most of them have a mass of $\sim 10^3 M_\odot$. Thus, their lifetime is $\ll 1$ Gyr. Moreover, we expect that dynamics does not affect much the statistics of merging BBHs after 100 Myr, because we find that on average only ~ 0.23 BBHs and ~ 0.41 single BHs per SC are still inside their parent SC at the end of the simulations. A further crucial question is whether there are unique signatures of merging exchanged BBHs, which can be chased by GW detectors. The masses of merging BBHs formed via SC and IB simulations are remarkably different in our simulations. However, lower progenitor metallicity can induce the formation of more massive merging BBHs in IBs (e.g. Giacobbo and Mapelli 2018). Thus, the effects of metallicity and dynamics are somewhat degenerate.

On the other hand, the most straightforward smoking gun of dynamical evolution is the formation of merging BHs in the mass range forbidden by (pulsational) pair

instability ($\approx 60 - 120 M_{\odot}$, Spera and Mapelli 2017). In our dynamical simulations, only 5 out of 229 merging BBHs ($\sim 2\%$ of all merging BBHs) fall in this forbidden mass range. A detailed analysis on BHs in the pair instability mass gap has been done in Chapter 3. In Chapter 4, we generalize our results to different stellar metallicities.

2.6 Summary

We have investigated the formation of BBHs in young star clusters (SCs) and open clusters. These SCs represent the bulk of star formation in galaxies. For our study, we have integrated the new population synthesis code MOBSE, which implements up-to-date stellar winds, binary evolution and supernova models (Mapelli et al., 2017; Giacobbo et al., 2018; Giacobbo and Mapelli, 2018), with the direct summation N-Body code NBODY6++GPU, which allows us to account for close encounters and dynamical exchanges (Wang et al., 2015).

We find that dynamics significantly affects the properties of merging BBHs: dynamical exchanges favour the formation and the merger of massive BBHs with total mass up to $m_{\text{tot}} \sim 120 M_{\odot}$ and with mass ratio ranging from $q \sim 1$ to $q \sim 0.1$ (although large mass ratios are more likely).

For comparison, merging BBHs evolved in IBs (run with the same population synthesis code) have maximum total mass $m_{\text{tot}} \lesssim 70 M_{\odot}$ and a significantly stronger preference for large mass ratios.

The masses of merging BBHs in our simulations are consistent with the first 10 BBHs observed by the LIGO-Virgo collaboration (Abbott et al., 2019b; Abbott et al., 2019a). At the simulated metallicity ($Z = 0.002$), the BH mass of GW170729 ($m_1 = 50.6_{-10.2}^{+16.6}$, $m_2 = 34.4_{-10.1}^{+9.1} M_{\odot}$, Abbott et al. 2019b) can be matched only by dynamically formed BBHs, within the 90% credible interval.

On the other hand, young SC dynamics does not affect the merger rate. We find almost the same merger efficiency ($N_m \sim 1.7 \times 10^{-5} M_{\odot}^{-1}$) in SC and in IB simulations. The formation of massive merging BBHs by dynamical exchanges is compensated by the loss of light merging BBHs, which are softened or ionized by interactions.

Almost all BBHs in our simulations merge after they were ejected from the SC or after the SC dissolved and became field.

Dynamics tends to speed up the merger of BBHs: the delay time between the formation of the stellar progenitors and the merger of the BBH scales approximately as $dN/dt_{\text{delay}} \propto t_{\text{delay}}^{-1}$ for SC merging BBHs, while the trend is shallower for IB merging BBHs.

Finally, about 2 % of merging BHs formed in young SCs have mass $\gtrsim 60 M_{\odot}$, lying in the “forbidden” region by (pulsational) pair instability ($m_{\text{BH}} \sim 60 - 120 M_{\odot}$, e.g. Spera and Mapelli 2017). These BHs form by the merger of two or more stars. According to our prescriptions, merged metal poor stars with a Helium core smaller than $\sim 60 M_{\odot}$ might retain a large hydrogen envelope: they avoid the pair instability SN window and might collapse to massive BHs. In the field, such massive BHs remain single, while in young SCs they can acquire companions dynamically and merge by GW emission. Thus, observing a rare merging BBH with mass $\gtrsim 60 M_{\odot}$ would be a strong signature of dynamical formation.

BINARY BLACK HOLES IN THE PAIR-INSTABILITY MASS GAP

Pair instability (PI) and pulsational PI prevent the formation of black holes (BHs) with mass $\gtrsim 60 M_{\odot}$ from single star evolution. Here, we investigate the possibility that BHs with mass in the PI gap form via stellar mergers and multiple stellar mergers, facilitated by dynamical encounters in young star clusters. We analyze 10^4 simulations, run with the direct N-body code `NBODY6++GPU` coupled with the population synthesis code `MOBSE`. We find that up to $\sim 6\%$ of all simulated BHs have mass in the PI gap, depending on progenitor's metallicity. This formation channel is strongly suppressed in metal-rich ($Z = 0.02$) star clusters, because of stellar winds. BHs with mass in the PI gap are initially single BHs but can efficiently acquire companions through dynamical exchanges. We find that $\sim 21\%$, 10% and 0.5% of all binary BHs have at least one component in the PI mass gap at metallicity $Z = 0.0002$, 0.002 and 0.02 , respectively. Based on the evolution of the cosmic star formation rate and metallicity, and under the assumption that all stars form in young star clusters, we predict that $\sim 5\%$ of all binary BH mergers detectable by advanced LIGO and Virgo at their design sensitivity have at least one component in the PI mass gap.

Based on:

Di Carlo U. N., Mapelli M., Bouffanais Y., Giacobbo N., Santoliquido F., Bressan A., Haardt F., MNRAS, 2020, Volume 497, pp.1043–1049

3.1 Introduction

The mass function of stellar black holes (BHs) is highly uncertain, as it crucially depends on complex physical processes affecting the evolution and the final fate of massive stars. For a long time, we had to rely on a scanty set of observational data, mostly dynamical mass measurements of compact objects in X-ray binaries (Özel et al., 2010; Farr et al., 2011). In the last four years, gravitational wave (GW) data have completely revolutionised our perspective: ten binary black holes (BBHs) have been observed during the first and the second observing run of the LIGO-Virgo collaboration (LVC, Abbott et al. 2016a; Abbott et al. 2016d; Abbott et al. 2019b; Abbott et al. 2019a) and we expect that several tens of new BBH mergers will be available as a result of the third observing run. GW data will soon provide a Rosetta Stone to decipher the mass function of BBHs. Thus, it is particularly important to advance our theoretical understanding of BH formation and BH mass function, in order to provide an interpretative key for future GW data. We currently believe that the mass of a BH depends mainly on the final mass of its progenitor star and on the details of the supernova (SN) explosion (e.g. Heger et al. 2003; Mapelli et al. 2009; Mapelli et al. 2010; Mapelli et al. 2013; Belczynski et al. 2010; Fryer et al. 2012; Spera et al. 2015; Limongi and Chieffi 2018). Among all types of SN explosion, pair instability SNe (PISNe) and pulsational pair instability SNe (PPISNe) are expected to leave a strong fingerprint on the mass function of BHs. If the He core mass is larger than $\sim 30 M_{\odot}$, soon after carbon burning when the stellar core temperature reaches $\sim 7 \times 10^8$ K, effective pair production softens the equation of state, leading to a loss of pressure. The stellar core contracts, triggering neon, oxygen and even silicon burning in a catastrophic way, known as pair instability (PI). Stars developing a helium core mass $64 \leq m_{\text{He}}/M_{\odot} \leq 135$ are thought to be completely disrupted by a PISN, leaving no compact object (Heger et al., 2003). Stars with a smaller helium core ($32 \lesssim m_{\text{He}}/M_{\odot} \lesssim 64$) undergo pulsational PI: they go through a series of pulsations, losing mass with an enhanced rate, till their cores leave the mass range for PI (Woosley et al., 2007). The combination of PISNe and PPISNe leads to a mass gap in the BH mass function between $\sim 60 M_{\odot}$ and $\sim 120 M_{\odot}$. Both the lower and the upper edge of the mass gap depend on the details of massive star evolution. In particular, the lower edge of the mass gap might span from $\sim 40 M_{\odot}$ up to $\sim 65 M_{\odot}$, depending on the details of PI, stellar evolution and core-collapse SNe (Belczynski et al., 2016a; Woosley, 2017; Woosley, 2019; Spera and Mapelli, 2017; Giacobbo et al., 2018; Giacobbo and Mapelli, 2018; Marchant et al., 2019; Mapelli et al., 2019b; Stevenson et al., 2019; Farmer et al., 2019; Renzo et al., 2020). The upper edge of the

gap is even more uncertain. LIGO-Virgo data from the first and second observing run are consistent with a maximum BH mass of $\approx 45 M_{\odot}$, in agreement with the existence of a PI mass gap (Abbott et al., 2019a). However, some exotic BH formation channels might populate the PI gap. Hence, the detection of a BH in the mass gap by the LVC would possibly provide a smoking gun for these exotic channels. Primordial BHs (i.e. BHs formed from the collapse of gravitational instabilities in the early Universe, e.g. Carr and Hawking 1974; Carr et al. 2016) might have a mass in the gap. Alternatively, BHs with mass in the gap can form as “second-generation” BHs (Gerosa and Berti, 2017), i.e. BHs born from the merger of two smaller BHs. Finally, Spera et al., 2019b and Di Carlo et al., 2019 proposed a third possible channel to produce BHs in the mass gap. If a massive star with a well-developed helium core merges with a non-evolved companion (a main sequence or an Hertzsprung-gap star), it might give birth to an evolved star with an over-sized hydrogen envelope. If the helium core remains below $\sim 32 M_{\odot}$ and the star collapses to a BH before growing a much larger core and before losing a significant fraction of its envelope, the final BH might be in the PI mass gap. If a second-generation BH or a BH born from stellar merger form in the field, they remain single objects and we do not expect to observe them in a BBH merger. In contrast, if they form in a dense stellar cluster they might capture a new companion through a dynamical exchange, possibly becoming a BBH (Miller and Hamilton, 2002; Di Carlo et al., 2019; Rodriguez et al., 2019; Gerosa and Berti, 2019). Here, we focus on BHs in the PI gap formed from stellar mergers and we estimate their mass range, merger efficiency and detection probability.

3.2 Methods

The simulations discussed in this paper were done using the same code and methodology as described in Di Carlo et al., 2019. In particular, we use the direct summation N-Body code NBODY6++GPU (Wang et al., 2015) coupled with the new population synthesis code MOBSE (Mapelli et al., 2017; Giacobbo et al., 2018; Giacobbo and Mapelli, 2018). MOBSE includes up-to-date prescriptions for massive star winds, for core-collapse SN explosions and for PISNe and PPISNe.

In this work, we have analyzed the simulations of 10^4 fractal young star clusters (SCs); 4000 of them are the simulations presented in Di Carlo et al., 2019, while the remaining 6000 are discussed in Di Carlo et al., 2020a. The initial conditions of the simulations presented in this paper are summarized in Table 3.1. Unlike globular clusters, young SCs are asymmetric, clumpy systems. Thus, we model them with

fractal initial conditions (Küpper et al., 2011), to mimic initial clumpiness (Goodwin and Whitworth, 2004). The level of fractality is decided by the parameter D (where $D = 3$ means homogeneous distribution of stars). In this work, we assume $D = 1.6, 2.3$.

The total mass M_{SC} of each SC (ranging from $10^3 M_{\odot}$ to $3 \times 10^4 M_{\odot}$) is drawn from a distribution $dN/dM_{\text{SC}} \propto M_{\text{SC}}^{-2}$, as the embedded SC mass function described in Lada and Lada, 2003. We choose to simulate SCs with mass $M_{\text{SC}} < 30000 M_{\odot}$ for computational reasons. Thus, the mass distribution of our simulated SCs mimics the mass distribution of SCs in Milky Way-like galaxies. We choose the initial SC half mass radius r_{h} according to the Marks & Kroupa relation (Marks et al., 2012) in 7000 simulations, and we adopt a fix value $r_{\text{h}} = 1.5$ pc for the remaining 3000 simulations.

The stars in the simulated SCs follow a Kroupa, 2001 initial mass function, with minimum mass $0.1 M_{\odot}$ and maximum mass $150 M_{\odot}$. We assume an initial binary fraction $f_{\text{bin}} = 0.4$. The orbital periods, eccentricities and mass ratios of binaries are drawn from Sana et al., 2012. We simulate each star cluster for 100 Myr in a rigid tidal field corresponding to the Milky Way tidal field at the orbit of the Sun. We refer to Di Carlo et al., 2019 for further details on the code and on the initial conditions. We consider three different metallicities: $Z = 0.0002, 0.002$ and 0.02 (approximately $1/100, 1/10$ and $1 Z_{\odot}$). We divide our simulations in three sets, corresponding to metallicity $Z = 0.0002$ (2000 runs), 0.002 (6000 runs) and 0.02 (2000 runs). The simulations with $Z = 0.002$ are the union of the 4000 runs presented in Di Carlo et al., 2019 and 2000 runs discussed in Di Carlo et al., 2020a. The simulations with $Z = 0.02$ and $Z = 0.0002$ are both from Di Carlo et al., 2020a. The main differences between the simulations already presented in Di Carlo et al., 2019 and the new runs from Di Carlo et al., 2020a are i) the efficiency of common envelope ejection ($\alpha = 3$ in Di Carlo et al. 2019 and $\alpha = 5$ in Di Carlo et al. 2020a), and ii) the model of core-collapse supernova (the rapid and the delayed models from Fryer et al. 2012 are adopted in Di Carlo et al. 2019 and in Di Carlo et al. 2020a, respectively). Putting together these different samples is not a completely consistent approach, but is justified by the fact that the population of BHs with mass in the $60 - 150 M_{\odot}$ range is not strongly affected by these different assumptions. For example, in Di Carlo et al., 2020a, we showed that our different assumptions change the percentage of BHs in the gap by a factor of $\sim 1.1 - 1.5$ (this is much less than the impact of stellar metallicity we want to probe here). Finally, putting together different SC models is important to filter out stochastic fluctuations, since the formation of BHs in the gap is a rare event and our simulations are computationally expensive.

Table 3.1: Initial conditions.

Set	Z	N_{sim}	r_{h}	D	ref.
Z0002	0.0002	1000	M2012	1.6	D2020
	0.0002	1000	1.5 pc	1.6	D2020
Z002	0.002	2000	M2012	2.3	D2019
	0.002	3000	M2012	1.6	D2019, D2020
	0.002	1000	1.5 pc	1.6	D2020
Z02	0.02	1000	M2012	1.6	D2020
	0.02	1000	1.5 pc	1.6	D2020

Column 1: Name of the simulation set. Column 2: metallicity Z . Column 3: Number of runs performed per each set. Column 4: half-mass radius r_{h} . M2012 indicates that half-mass radii have been drawn according to Marks et al., 2012. Column 5: fractal dimension (D). Column 6: reference for each simulation set. D2019 and D2020 correspond to Di Carlo et al., 2019 and Di Carlo et al., 2020a, respectively.

3.3 Results

From our simulations, we extract information on BHs with mass in the PI gap, between 60 and 150 M_{\odot} (given the uncertainties on the edges of the mass gap, we make a conservative assumption for both the lower and the upper edge of the mass gap). In Di Carlo et al., 2019, we have already discussed the properties of BHs that form from stars with $Z = 0.002$, have mass in the PI gap and merge with other BHs in less than a Hubble time. Here, we extend our study to other progenitor’s metallicities ($Z = 0.02$ and 0.0002), because stellar metallicity is a crucial ingredient to understand how many BHs can form with mass in the PI gap. Moreover, we discuss the formation pathways of BHs born from stellar mergers, by looking at the core and envelope evolution of their progenitors (Figure 3.1). We consider all BHs that form in the PI mass gap (both single and binary BHs) and we investigate their properties. Finally, we estimate the detectability of BHs in the mass gap by LIGO and Virgo at design sensitivity.

3.3.1 Formation channels of BHs in the gap

The vast majority of BHs with mass in the PI gap that form in our simulation originates from the merger of an evolved star (with a developed helium core of mass $\approx 15 - 30 M_{\odot}$) and a main sequence companion. The merger is generally triggered by dynamical perturbations. In several cases, the evolved star is the result of multiple mergers between other stars, facilitated by the dense dynamical environment. This process of multiple mergers occurring in a very short time span is known as

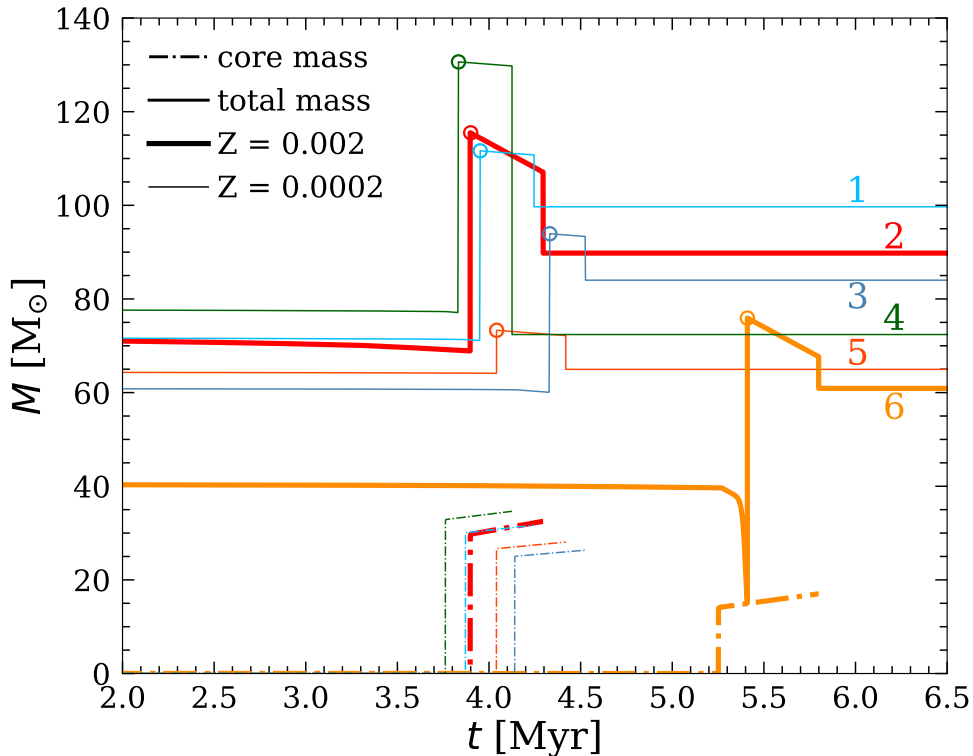


Figure 3.1: Evolution of the total mass (solid lines) and the core mass (dot-dashed lines) of the progenitors of a sample of BHs with mass in the gap. The open circle marks the time of the merger with a companion star. Thick lines: $Z = 0.002$; thin lines: $Z = 0.0002$. Models 1, 3 and 4 (light blue, blue and green) are stars that become single BHs; models 2, 5 and 6 (red, orange and yellow) are stars which end up in merging BBHs.

runaway collision and was already discussed in several papers (see e.g. Portegies Zwart and McMillan 2002; Portegies Zwart et al. 2004; Giersz et al. 2015; Mapelli 2016; Gieles et al. 2018).

Figure 3.1 shows the evolution of six stellar progenitors of BHs in the PI mass gap. Three of these BHs become members of BBHs and merge within a Hubble time, while the other three objects leave single BHs. We find no significant difference between the formation channel of merging BHs in the PI mass gap and that of single BHs or non-merging BBHs with mass in the PI gap.

The stars shown in Figure 3.1 undergo a merger with a main-sequence companion in their late evolutionary stages ($\sim 4 - 6$ Myr), when they are Hertzsprung gap or core helium burning stars. We assume that there is no mass loss during the merger. The merger products are not significantly rejuvenated, because they already developed a He core. They are evolved based on their mass and are subject to stellar winds, depending on their metallicity. Their final He core is $\sim 17 - 32 M_{\odot}$ (below the PPISN/PISN gap), while their hydrogen envelope is over-sized with respect to

single star evolution, because of the merger. While most stars in Figure 3.1 simply merge with another star without previous mass transfer episodes, star number 6 shows signature of mass transfer. This star fills its Roche lobe after leaving the main sequence and its hydrogen envelope is removed. At the end of mass transfer, it merges with its companion.

In all the simulations, the post-merger star evolves for $t_{\text{post-merg}} = t_{\text{He}} + t_{\text{C}} + t_{\text{Ne}} + t_{\text{O}} + t_{\text{Si}} \sim t_{\text{He}}$, where $t_{\text{post-merg}}$ is the time remaining to collapse, while t_{He} , t_{C} , t_{Ne} , t_{O} and t_{Si} are the timescale of helium, carbon, neon, oxygen and silicon burning, respectively. During $t_{\text{post-merg}}$, the star converts a mass $\Delta M_{\text{He}} \sim \dot{M}_{\text{He}} t_{\text{post-merg}}$ into heavier elements, where

$$\begin{aligned} \dot{M}_{\text{He}} \lesssim & 2 \times 10^{-5} M_{\odot} \text{yr}^{-1} \left(\frac{L_*}{10^6 L_{\odot}} \right) \\ & \times \left(\frac{6.3 \times 10^{18} \text{erg g}^{-1}}{\eta_{\text{CNO}}} \right) \left(\frac{0.5}{X} \right). \end{aligned} \quad (3.1)$$

In equation 3.1, L_* is the stellar luminosity, X is the hydrogen fraction and η_{CNO} is the efficiency of mass-to-energy conversion during the CNO cycle (e.g. Prialnik 2000).

If the final mass of the helium core $M_{\text{He},f} = M_{\text{He}} + \Delta M_{\text{He}} < 32 M_{\odot}$, where M_{He} is the mass of the helium core before the last stellar merger, then the star with an oversized hydrogen envelope can avoid PI and directly collapses to a BH, possibly with mass $> 60 M_{\odot}$. This is just an order of magnitude estimation, more refined calculations would require a hydrodynamical simulation to follow the merger (see e.g. Gaburov et al. 2010) and a stellar-evolution code to integrate nuclear burning and stellar evolution.

Once they form, BHs with mass in the gap are efficient in acquiring companions: $\sim 21\%$ and $\sim 10\%$ of all BBHs have at least one member with mass in the PISN gap at $Z = 0.0002$ and $Z = 0.002$, respectively. This is expected, because these BHs are significantly more massive than the other BHs and stars in the SCs, and dynamical exchanges favour the formation of more massive binaries, which are more energetically stable (see e.g. Hills and Fullerton 1980).

If we consider only BBHs merging within a Hubble time (14 Gyr) due to GW emission, only $\sim 2.2\%$ and $\sim 2.1\%$ of them have at least one BH in the PI gap at $Z = 0.0002$ and $Z = 0.002$, respectively. We find only 11 merging BBHs with a BH in the PI gap, hence these percentages are affected by stochastic fluctuations (see Table 3.2 for an estimate of the uncertainties). These BBHs merge after being ejected from their parent young SC. Finally, we find no merging BBHs with members in the PI gap at solar metallicity.

None of the BBHs in our simulations hosts a second-generation BH (i.e. a BH that forms from the merger of two BHs). The low escape velocity from our SCs (up to few km s^{-1} in the most massive SCs) prevents second-generation BHs from remaining inside the cluster: all of them are ejected and cannot acquire a new companion. In contrast, in massive SCs (like globular clusters and nuclear star clusters) second-generation BHs have a significantly higher chance of remaining inside their parent cluster and acquiring a companion (see e.g. Miller and Hamilton 2002; Colpi et al. 2003; Antonini and Rasio 2016; Rodriguez et al. 2019; Arca Sedda and Benacquista 2019; Arca Sedda et al. 2020).

It is important to highlight several caveats inherent with our analysis. First, MOBSE assumes that no mass is lost during the merger while hydrodynamical simulations have shown that mass ejecta can represent up to $\sim 25\%$ of the total mass (Gaburov et al. 2010, see also Dale and Davies 2006; Justham et al. 2014; Vigna-Gómez et al. 2019; Wu et al. 2020). We have re-simulated the six objects in Figure 3.1 assuming that all of them lose 25% of their mass after each merger. The masses of the resulting BHs are lower by $\sim 22 - 28\%$; three of the six BHs in Figure 3.1 are still in the mass gap (tracks 1, 2 and 3), while the remaining three have mass $< 60 M_{\odot}$.

Furthermore, the polynomial fitting formulas implemented in MOBSE might be inaccurate to describe the final evolution of such post-merger massive stars. In a follow-up work, we will evolve our post-collision models with a stellar evolution code¹, to check any deviations from MOBSE. In addition, we assume that the final hydrogen envelope entirely collapses to a BH. This final outcome depends on the final binding energy of the envelope (see e.g. Sukhbold et al. 2016 for a discussion). Finally, we model PPISNe with a fitting formula (Spera and Mapelli, 2017) to the models by Woosley, 2017. However, the models by Woosley, 2017 are suited for stars following regular single stellar evolution, that could be significantly different from merger products.

3.3.2 Mass distribution

Figure 3.2 shows the mass ratio $q = M_2/M_1$ (where $M_1 > M_2$) and the total mass $M_{\text{tot}} = M_1 + M_2$ of all BBHs that have at least one member in the PI gap. We form

¹Glebbeeck et al., 2009 re-simulated a runaway collision product with a stellar evolution code. They find that mass loss strongly suppresses the formation of massive mergers at solar metallicity, while a final stellar mass $\sim 260 M_{\odot}$ is possible at $Z = 0.001$. This is similar to our findings. However, their results are not directly comparable with ours, because the original N -body simulation they start from is composed of 131072 particles; thus, the runaway collision product is significantly more massive than ours.

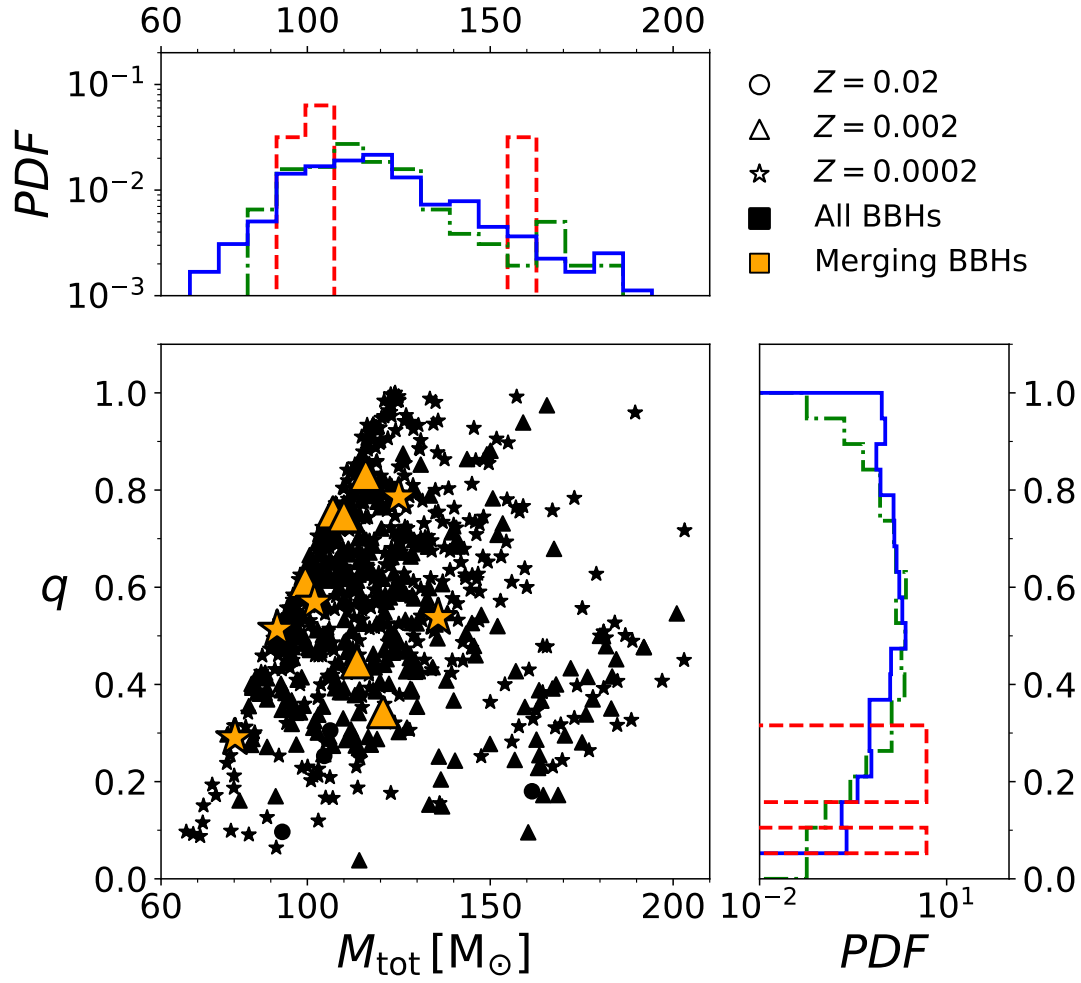


Figure 3.2: Mass ratio $q = M_2/M_1$ versus total mass $M_{\text{tot}} = M_1 + M_2$ of BHs with mass in the gap that are members of BBHs by the end of the simulations. Circles, triangles and stars refer to $Z = 0.02$, 0.002 and 0.0002 , respectively. Orange and black symbols refer to BBHs merging within a Hubble time and to all BBHs, respectively. Marginal histograms show the distribution of q (on the y -axis) and M_{tot} (on the x -axis). Solid blue, dot-dashed green and dashed red histograms refer to $Z = 0.0002$, 0.002 and 0.02 , respectively.

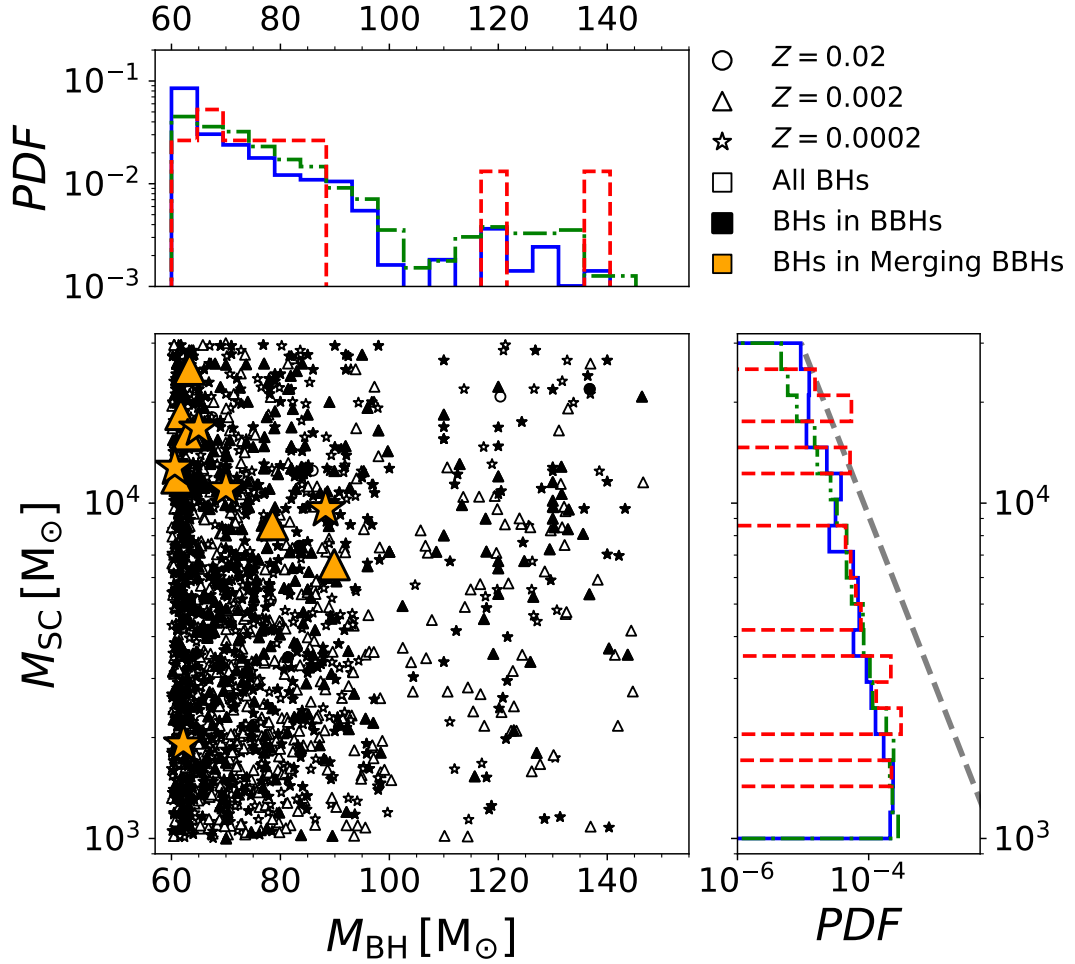


Figure 3.3: Mass of the host star cluster (M_{SC}) versus the mass M_{BH} of a BH in the PI gap. Marginal histograms show the distribution of M_{SC} (on the y -axis) and M_{BH} (on the x -axis). Orange and black filled symbols refer to BBHs merging within a Hubble time and to all BBHs, respectively. Open symbols show single BHs. Solid blue, dot-dashed green and dashed red histograms refer to $Z = 0.0002$, 0.002 and 0.02 , respectively. The grey dashed line shows the mass function of M_{SC} in our simulation set ($dN/dM_{\text{SC}} \propto M_{\text{SC}}^{-2}$).

Table 3.2: Fraction of BHs, BBHs and merging BBHs with mass in the PI gap.

Z	$f_{\text{PI,BHs}}$	$f_{\text{PI,BBHs}}$	$f_{\text{PI,GW}}$	$p_{\text{det}}^{\text{PI}}$
0.0002	$5.6 \pm 0.3 \%$	$20.8 \pm 1.7 \%$	$2.2 \pm 1.9 \%$	11.2 %
0.002	$1.5 \pm 0.1 \%$	$9.6 \pm 1.0 \%$	$2.1 \pm 1.6 \%$	10.0 %
0.02	$0.1 \pm 0.04 \%$	$0.5 \pm 0.5 \%$	0.0 %	0.0 %
S2020	–	–	0.5 %	5.3 %

Column 1 (Z): progenitor’s metallicity; S2020 indicates that we accounted for progenitor’s metallicity evolution as a function of redshift, as described in Santoliquido et al., 2020; column 2 ($f_{\text{PI,BHs}}$): percentage of BHs with mass in the PI gap with respect to all simulated BHs at a given Z ; column 3 ($f_{\text{PI,BBHs}}$): percentage of BBHs that have at least one member with mass in the PI gap with respect to all BBHs at a given Z formed by the end of the simulations. column 4 ($f_{\text{PI,GW}}$): percentage of merging BBHs that have at least one member with mass in the PI gap with respect to all merging BBHs at a given Z (a merging BBH is defined as a BBH which merges in less than a Hubble time by GW emission). Errors on $f_{\text{PI,BHs}}$, $f_{\text{PI,BBHs}}$ and $f_{\text{PI,GW}}$ correspond to 95% credible intervals on binomial distributions, using a Wald method for approximation. Column 5 ($p_{\text{det}}^{\text{PI}}$): percentage of detectable BBH mergers that have at least one member with mass in the PI gap with respect to all detectable BBH mergers at a given Z (see equation 3.3).

BHs with masses in the entire range of the PI gap between $\sim 60 - 150 M_{\odot}$, with a preference for masses around $60 - 70 M_{\odot}$.

Values of mass ratio $q \gtrsim 0.4$ are the most likely, but we find binaries with q as low as ~ 0.04 . The binary with the smallest value of q has secondary mass $M_2 \sim 4.2 M_{\odot}$. The largest secondary mass is $M_2 \sim 110 M_{\odot}$. Overall, binaries hosting a BH with mass in the gap have lower mass ratios than other BBHs (see Figure 7 of Di Carlo et al. 2019, where we show that the vast majority of BBHs in young SCs have $q \sim 0.9 - 1$).

Figure 3.3 shows the mass of the host SC as a function of the mass of BHs in the PI gap (here we include also BHs that remain single). BHs in the mass gap form more efficiently in massive young SCs, where dynamics is more important. Ten out of eleven merging BBHs are hosted in star clusters with $M_{\text{SC}} > 6000 M_{\odot}$, among the most massive young SCs in our sample.

3.3.3 Merger and detection efficiency

We find that only $\sim 0 - 2.2 \%$ of all merging BBHs have at least one member with mass in the PI gap, depending on metallicity. However, these systems are more massive than other merging BBHs, thus they have a higher detection chance. To properly take into account these selection effects, we followed a similar approach as in Finn and Chernoff, 1993, Dominik et al., 2015 and Bouffanais et al., 2019.

We associate to each mock source (in our catalogue of 534 merging BBHs) the optimal signal-to-noise ratio (SNR) ρ_{opt} that corresponds to the case where the source is optimally oriented and located in the sky. Since real-life sources have different orientations and locations, we then reweigh the SNR as $\rho = \omega \times \rho_{opt}$, where ω takes randomly generated values between 0 and 1, and the probability of detecting a source is given by

$$p_{\text{det}} = 1 - F_{\omega}(\rho_{\text{thr}}/\rho_{\text{opt}}). \quad (3.2)$$

In this equation, F_{ω} is the cumulative function of ω and ρ_{thr} is a detection threshold. We use $\rho_{\text{thr}} = 8$, that was shown to be a good approximation for a network of detectors (Abadie et al., 2010; Abbott et al., 2016). We used the software PyCBC (Dal Canton et al., 2014; Usman et al., 2016) to generate both the waveforms (IMRPhenomB with zero spins) and the noise power spectral densities of advanced LIGO at design sensitivity (Abbott et al., 2018), and the package gwdet (Gerosa, 2019) to evaluate the function F_{ω} .

From there, we ran two different analysis: one where each set of metallicity is treated independently, and the other where we combine them together using a model describing redshift and metallicity evolution. In the first scenario, for each metallicity set we construct a catalogue of 10^6 sources where the masses are drawn uniformly from the catalogue and redshifts are drawn uniformly in comoving volume between 0 and 1. In the second scenario, we first compute the merger rate at the detector as a function of redshift, by making use of the `cosmoRate` code (Santoliquido et al., 2020). In particular, following Santoliquido et al., 2020, we assume that all stars form in young SCs, we account for the cosmic star formation rate (Madau and Fragos, 2017) and for the stellar metallicity evolution (De Cia et al., 2018), and we take cosmological parameters from Planck Collaboration et al., 2016. From there, we build a catalogue of 10^6 sources, by making use once again of the `cosmoRate` code (Santoliquido et al., 2020), to have the distribution of masses as a function of redshift.

Finally, to obtain the probability of detecting a source with at least one component in the PI mass gap, we computed the following quantity for both analyses:

$$p_{\text{det}}^{\text{PI}} = \sum_{i \in \text{PI}} p_{\text{det}}^i / \sum_j p_{\text{det}}^j, \quad (3.3)$$

where the sum in the numerator is done only over sources where at least one component lies in the mass gap while the sum in the denominator is done over all sources in our catalogue of merging BBHs.

We find $p_{\text{det}}^{\text{PI}} = 0 - 11\%$, depending on metallicity (see the last column of Table 3.2). This means that, under our assumption that all stars form in young SCs, up to 11%

of all BBHs detected by LIGO-Virgo at design sensitivity have at least one component in the PI mass gap. If we assume a model-dependent BBH merger rate evolution with redshift (based on the cosmic star formation rate density and on the average metallicity evolution, Santoliquido et al. 2020), we find $p_{\text{det}}^{\text{PI}} \sim 5\%$, under the assumption that all cosmic star formation takes place in young SCs like the ones we simulated.

3.4 Conclusions

Pair instability (PI) and pulsational PI prevent the formation of BHs with mass between ~ 60 and $\sim 150 M_{\odot}$ from single stellar evolution. However, binary evolution processes (such as stellar mergers) and dynamical processes might allow the formation of BHs with masses in the gap.

Here, we investigate the possibility that BHs with mass in the gap form through stellar mergers and multiple stellar mergers in young SCs. The merger between an evolved star (a giant with a well developed helium core) and a main sequence star can give birth to a BH with mass in the gap, provided that the star collapses before its helium core grows above $\sim 32 M_{\odot}$. In our simulations, these stellar mergers are facilitated by the SC environment: dynamical encounters perturb a binary star, affecting its orbital properties and increasing the probability of a merger between its components. Some massive stars even undergo runaway collisions: they go through multiple mergers over few Myrs. When a BH with mass in the PI gap forms in this way, it is initially a single object. If it remains in the SC, it can acquire a new companion through dynamical exchanges. In contrast, BHs that form via stellar mergers in the field remain single BHs. Moreover, BHs with masses $> 60 M_{\odot}$ are much harder to form in isolated binaries, because non-conservative mass transfer peels-off the primary before the merger. Dynamical encounters perturb the binary and induce a fast merger without episodes of mass transfer.

We have investigated the formation and the dynamical evolution of BHs with masses in the gap through 10^4 direct N-body simulations of young SCs with metallicity $Z = 0.0002, 0.002$ and 0.02 and with total mass between 10^3 and $3 \times 10^4 M_{\odot}$. Hence, we focused on relatively small young SCs. At the end of our simulations, $\sim 5.6\%$, $\sim 1.5\%$ and $\sim 0.1\%$ of all BHs have mass in the PI gap for metallicity $Z = 0.0002, 0.002$ and 0.02 , respectively. Metal-poor stars are more efficient in producing these BHs, because they lose less mass by stellar winds. In our simulations, we do not include prescriptions for BH spins, because the connection between the spin of the progenitor star and the spin of the BH is highly uncertain (see e.g. Heger

et al. 2005; Lovegrove and Woosley 2013; Belczynski et al. 2017; Qin et al. 2018; Qin et al. 2019; Fuller et al. 2019; Fuller and Ma 2019). We can speculate that stellar mergers spin up the progenitor stars, but we cannot tell whether this spin-up translates into a higher BH spin.

The treatment of the merger of two stars in our simulations is simplified: we assume no mass loss and no chemical mixing during the merger and we require that the merger product reaches hydro-static equilibrium instantaneously. The merger product is rejuvenated according to Hurley et al., 2002 simple prescriptions. Hydrodynamical simulations of a stellar merger are required in order to have a better understanding of the final outcome. Thus, our results should be regarded as an upper limit to the formation of BHs in the PI mass gap via stellar mergers.

In our simulations, several BHs with masses in the gap end up forming a BBH through dynamical exchanges. BBHs having at least one component in the mass gap are $\sim 20.6\%$, $\sim 9.8\%$ and $\sim 0.5\%$ of all BBHs in our simulations, for metallicity $Z = 0.0002$, 0.002 and 0.02 , respectively. Thus, BHs with masses in the gap are quite efficient in forming BBHs. The total masses of these BBHs are typically around $M_{\text{TOT}} \sim 90 - 130 M_{\odot}$ and the most likely mass ratios are $q \gtrsim 0.4$.

In our simulations, $\sim 2.1\%$ ($\sim 2.2\%$) of all BBHs merging within a Hubble time have at least one component in the mass gap for metallicity $Z = 0.002$ ($Z = 0.0002$). We find no merging BBHs in the mass gap at solar metallicity. Merging BBHs in the mass gap form preferentially in the most massive SCs we simulate ($M_{\text{SC}} \geq 6000 M_{\odot}$). Hence, BBH mergers in the mass gap might be even more common in higher mass SCs (e.g. globular clusters) than the ones we simulate. Since merging BBHs in the mass gap form through dynamical exchanges, their spins will be isotropically oriented with respect to the orbital angular momentum of the binary system.

Finally, we calculate the probability that advanced LIGO and Virgo at design sensitivity detect the merger of BBHs in the mass gap. Modelling the dependence of the merger rate on the cosmic star formation rate density and metallicity evolution (Santoliquido et al., 2020), we predict that $\sim 5\%$ of all BBH mergers detected by LIGO and Virgo at design sensitivity have at least one component in the PI mass gap, under the assumption that all stars form in young SCs. If the proposed mechanism to form BHs in the mass gap is actually at work, the LIGO-Virgo collaboration might be able to witness these events in the next few years.

BINARY BLACK HOLES IN YOUNG STAR CLUSTERS: THE IMPACT OF METALLICITY

Young star clusters are the most common birth-place of massive stars and are dynamically active environments. Here, we study the formation of black holes (BHs) and binary black holes (BBHs) in young star clusters, by means of 6000 N-body simulations coupled with binary population synthesis. We probe three different stellar metallicities ($Z = 0.02, 0.002$ and 0.0002) and two initial density regimes (density at the half-mass radius $\rho_h \geq 3.4 \times 10^4$ and $\geq 1.5 \times 10^2 M_\odot pc^{-3}$ in dense and loose star clusters, respectively). Metal-poor clusters tend to form more massive BHs than metal-rich ones. We find ~ 6 , ~ 2 , and < 1 % of BHs with mass $m_{BH} > 60 M_\odot$ at $Z = 0.0002, 0.002$ and 0.02 , respectively. In metal-poor clusters, we form intermediate-mass BHs with mass up to $\sim 320 M_\odot$. BBH mergers born via dynamical exchanges (exchanged BBHs) can be more massive than BBH mergers formed from binary evolution: the former (latter) reach total mass up to $\sim 140 M_\odot$ ($\sim 80 M_\odot$). The most massive BBH merger in our simulations has primary mass $\sim 88 M_\odot$, inside the pair-instability mass gap, and a mass ratio of ~ 0.5 . Only BBHs born in young star clusters from metal-poor progenitors can match the masses of GW170729, the most massive event in O1 and O2, and those of GW190412, the first unequal-mass merger. We estimate a local BBH merger rate density ~ 110 and $\sim 55 Gpc^{-3} yr^{-1}$, if we assume that all stars form in loose and dense star clusters, respectively.

Based on:

Di Carlo, U. N., Mapelli M., Giacobbo N., Spera M., Bouffanais Y., Rastello S., Santoliquido F., Pasquato M, Ballone A., Trani A. A., Torniamenti S., Haardt F, MNRAS, 498, Issue 1, pp.495-506

4.1 Introduction

About four years ago, the LIGO-Virgo collaboration (LVC, Aasi et al. et al. 2015; Acernese et al. 2015) reported the very first direct detection of gravitational waves, GW150914, interpreted as the merger of two massive stellar black holes (BHs, Abbott et al. 2016a; Abbott et al. 2016b). After GW150914, nine additional binary black holes (BBHs) and one binary neutron star (BNS) were observed by the LVC during the first and second observing run (hereafter O1 and O2, Abbott et al. 2016d; Abbott et al. 2019b; Abbott et al. 2019a). The third observing run of LIGO and Virgo has recently been completed and has already led to one additional BNS (GW190425, Abbott et al. 2020b), the first unequal-mass BBH merger (GW190412, Abbott et al. 2020a) and tens of public alerts¹.

Understanding the formation channels of BBHs is one of the most urgent astrophysical questions raised by LVC observations. Several authors suggest that about a hundred of detections are sufficient to say something on the formation channels of BBHs, thanks to their distinctive signatures (e.g. Fishbach and Holz 2017; Gerosa and Berti 2017; Stevenson et al. 2017; Gerosa et al. 2018; Bouffanais et al. 2019).

Isolated binary evolution, either via common envelope (e.g. Tutukov et al. 1973; Bethe and Brown 1998; Portegies Zwart and Yungelson 1998; Belczynski et al. 2002; Voss and Tauris 2003; Podsiadlowski et al. 2004; Belczynski et al. 2008; Dominik et al. 2012; Dominik et al. 2013; Mennekens and Vanbeveren 2014; Belczynski et al. 2016b; Mapelli et al. 2017; Mapelli and Giacobbo 2018; Giacobbo et al. 2018; Giacobbo and Mapelli 2018; Kruckow et al. 2018; Spera et al. 2019a; Mapelli et al. 2019a; Neijssel et al. 2019; Tang et al. 2020) or via chemically homogeneous scenarios (de Mink and Mandel, 2016; Mandel and de Mink, 2016; Marchant et al., 2016), predicts the formation of BBHs with primary mass up to $\sim 40 - 65 M_{\odot}$ (see, e.g., Mapelli et al. 2020a and references therein), with a strong preference for equal-mass systems, mostly aligned spins and zero eccentricity in the LVC band.

In contrast, dynamical formation in star clusters might lead to even larger primary masses (e.g. McKernan et al. 2012; Mapelli 2016; Antonini and Rasio 2016; Gerosa and Berti 2017; Stone et al. 2017; McKernan et al. 2018; Di Carlo et al. 2019; Di Carlo et al. 2020a; Rodriguez et al. 2019; Yang et al. 2019; Arca Sedda and Benacquista 2019; Arca Sedda et al. 2020), mass ratios ranging from $q \sim 0.1$ to $q \sim 1$ (e.g. Di Carlo et al. 2019), isotropic spin distribution, and, in some rare but not negligible cases, non-zero eccentricity in the LVC band (e.g. Samsing 2018; Samsing and D’Orazio 2018; Samsing et al. 2018; Rodriguez et al. 2018; Zevin et al. 2019b).

¹<https://gracedb.ligo.org/>

The zoology of star clusters found in the Universe is rich and includes systems that are extremely different from each other (both in terms of mass and lifetime), but share a similar dynamical evolution: almost all star clusters are collisional systems, i.e. stellar systems in which the two-body relaxation timescale is shorter than their lifetime (e.g. Spitzer 1987). Hence, close encounters between single and binary (or multiple) stars drive the evolution of star clusters and have a crucial impact on the formation of binary compact objects.

The dynamical evolution of BBHs in nuclear star clusters (e.g. O’Leary et al. 2009; Miller and Lauburg 2009; McKernan et al. 2012; McKernan et al. 2018; VanLandingham et al. 2016; Stone et al. 2017; Hoang et al. 2018; Arca-Sedda and Gualandris 2018; Antonini et al. 2019a) and globular clusters (e.g. Sigurdsson and Hernquist 1993; Sigurdsson and Phinney 1995; Portegies Zwart and McMillan 2000b; O’Leary et al. 2006; Sadowski et al. 2008; Downing et al. 2010; Downing et al. 2011; Tanikawa 2013; Rodriguez et al. 2015; Rodriguez et al. 2016; Rodriguez et al. 2018; Antonini and Rasio 2016; Antonini et al. 2019a; Hurley et al. 2016; O’Leary et al. 2016; Askar et al. 2017a; Askar et al. 2018; Zevin et al. 2017; Choksi et al. 2019) has been extensively investigated. These are the most massive, long-lived and predominantly old stellar systems; hence their relatively high escape velocity allows a fraction of the merger remnants to stay in the cluster, leading to a population of hierarchical mergers (Miller and Hamilton, 2002; Arca Sedda and Benacquista, 2019; Gerosa and Berti, 2019; Rodriguez et al., 2019).

Young star clusters (YSCs) and open clusters are generally smaller and shorter-lived than globular clusters (Portegies Zwart et al., 2010). Nonetheless, they are site of strong dynamical interactions and they are the nursery of massive stars in the Universe: the vast majority of massive stars, which are the progenitors of compact objects, form in YSCs (e.g. Lada and Lada 2003; Portegies Zwart et al. 2010). Hence, the majority of BHs have likely spent the first part of their life in star clusters, undergoing dynamical encounters. Several studies demonstrate that dynamics has a major role in the formation of BH binaries in YSCs (Portegies Zwart and McMillan, 2002; Banerjee et al., 2010; Mapelli et al., 2013; Mapelli and Zampieri, 2014; Ziosi et al., 2014; Goswami et al., 2014; Mapelli, 2016; Banerjee, 2018b; Banerjee, 2018a; Fujii et al., 2017; Rastello et al., 2019; Di Carlo et al., 2019; Kumamoto et al., 2019b; Kumamoto et al., 2020).

In particular, Di Carlo et al., 2019 showed that about half of BBHs born in YSCs form via dynamical exchanges at metallicity $Z = 0.002$. BBHs formed in YSCs are significantly more massive than BBHs formed from isolated binary evolution and tend to have smaller mass ratios. About $\sim 2\%$ of all BBH mergers originating from

YSCs have primary mass $\gtrsim 60 M_{\odot}$, falling inside the pair-instability mass gap (e.g. Woosley 2017; Spera and Mapelli 2017; Stevenson et al. 2019; Marchant et al. 2019; Farmer et al. 2019; Mapelli et al. 2020a; Di Carlo et al. 2020a; Renzo et al. 2020). The sample presented in Di Carlo et al., 2019 is the largest simulation set of YSCs used to study BBHs, but is limited to one metallicity $Z = 0.002$. Since metallicity has a crucial impact on the mass of BHs (Mapelli et al., 2009; Mapelli et al., 2010; Zampieri and Roberts, 2009; Belczynski et al., 2010; Spera et al., 2015), it is essential to study the evolution of BBHs in star clusters with different metallicity. In this paper, we present the result of a new set of simulations where we consider three different metallicities ($Z = 0.02, 0.002$ and 0.0002) and two initial density regimes (density at the half-mass radius $\rho_h \geq 3.4 \times 10^4$ and $\geq 1.5 \times 10^2 M_{\odot} \text{pc}^{-3}$ in dense and loose star clusters, respectively).

4.2 Methods

The simulations discussed in this paper were done using the same code and methodology as described in Di Carlo et al., 2019. In particular, we use the direct summation N-Body code NBODY6++GPU (Wang et al., 2015) coupled with the population synthesis code MOBSE (Mapelli et al., 2017; Giacobbo et al., 2018; Giacobbo and Mapelli, 2018).

4.2.1 Direct N-Body

NBODY6++GPU is the GPU parallel version of NBODY6 (Aarseth, 2003). It implements a 4th-order Hermite integrator, individual block time-steps (Makino and Aarseth, 1992) and Kustaanheimo-Stiefel (KS) regularization of close encounters and few-body subsystems (Stiefel, 1965; Mikkola and Aarseth, 1993b).

A neighbour scheme (Nitadori and Aarseth, 2012) is used to compute the force contributions at short time intervals (*irregular* force/timesteps), while at longer time intervals (*regular* force/timesteps) all the members in the system contribute to the force evaluation. The irregular forces are evaluated using CPUs, while the regular forces are computed on GPUs using the CUDA architecture. This version of NBODY6++GPU does not include post-Newtonian terms.

4.2.2 Population synthesis

MOBSE (Mapelli et al., 2017; Giacobbo et al., 2018; Giacobbo and Mapelli, 2018; Giacobbo and Mapelli, 2019; Mapelli and Giacobbo, 2018) is a customized and up-

graded version of BSE (Hurley et al., 2000; Hurley et al., 2002) which includes up-to-date prescriptions for massive star winds, for core-collapse supernova (SN) explosions and for pair instability and pulsational-pair instability SNe. It has been integrated with NBODY6++GPU by taking advantage of the pre-existing interface between the N-body code and BSE.

Stellar winds are implemented assuming that the mass loss of massive hot stars (O and B-type stars, Wolf-Rayet stars, luminous blue variable stars) depends on metallicity as $\dot{M} \propto Z^\beta$, where β is defined as in Giacobbo et al., 2018

$$\beta = \begin{cases} 0.85 & \text{if } \Gamma_e < 2/3 \\ 2.45 - 2.4\Gamma_e & \text{if } 2/3 \leq \Gamma_e < 1 \\ 0.05 & \text{if } \Gamma_e \geq 1. \end{cases} \quad (4.1)$$

Here Γ_e is the Eddington factor (see e.g. Gräfener and Hamann 2008; Chen et al. 2015).

The outcome of core-collapse SNe is highly uncertain and none of the prescriptions available in the literature is completely satisfactory (e.g. Burrows et al. 2018; Mapelli et al. 2020a). Hence, our prescriptions should be regarded as reasonable “toy models”. In this paper, we adopt the rapid core-collapse supernova model described in Fryer et al., 2012. In this formalism, the mass of the compact object is $m_{\text{rem}} = m_{\text{proto}} + m_{\text{fb}}$, where $m_{\text{proto}} = 1 M_\odot$ is the mass of the proto-compact object and m_{fb} is the mass accreted by fallback. Note that this is different from Di Carlo et al., 2019, where we adopted the delayed model from Fryer et al., 2012.

When the helium core of a star becomes $64 \leq m_{\text{He}}/M_\odot \leq 135$, the star is completely destroyed by pair instability. If the helium core reaches a size $32 \leq m_{\text{He}}/M_\odot < 64$, pulsational pair instability is expected to take place (Woosley, 2017) and the final mass of the compact object is estimated as $m_{\text{rem}} = \alpha_P m_{\text{noPPI}}$, where m_{noPPI} is the mass of the compact object we would have obtained if we had not included pulsational pair instability in our analysis and α_P is a fitting parameter (Spera and Mapelli, 2017; Mapelli et al., 2020a). Finally, electron-capture supernovae are implemented as described in Giacobbo and Mapelli, 2019.

Natal kicks are randomly drawn from a Maxwellian velocity distribution. A one-dimensional root mean square velocity $\sigma = 15 \text{ km s}^{-1}$ is adopted for core-collapse SNe and for electron-capture SNe (Giacobbo and Mapelli, 2019). Kick velocities of BHs are reduced by the amount of fallback as $V_{\text{KICK}} = (1 - f_{\text{fb}}) V$, where f_{fb} is the fallback parameter described in Fryer et al., 2012 and V is the velocity drawn from the Maxwellian distribution².

²This kick model was chosen because it leads to a BNS merger rate in agreement with the range

Table 4.1: Initial conditions.

Set	Z	N_{SC}	$M_{\text{SC}} [M_{\odot}]$	$r_{\text{h}} [\text{pc}]$
YSC	0.02, 0.002, 0.0002	6000	$10^3 - 3 \times 10^4$	$1.5, 0.1 (M_{\text{SC}}/M_{\odot})^{0.13}$
A	0.02, 0.002, 0.0002	3000	$10^3 - 3 \times 10^4$	$0.1 (M_{\text{SC}}/M_{\odot})^{0.13}$
B	0.02, 0.002, 0.0002	3000	$10^3 - 3 \times 10^4$	1.5
IB	0.02, 0.002, 0.0002	3×10^7	–	–
A02	0.02	1000	$10^3 - 3 \times 10^4$	$0.1 (M_{\text{SC}}/M_{\odot})^{0.13}$
A002	0.002	1000	$10^3 - 3 \times 10^4$	$0.1 (M_{\text{SC}}/M_{\odot})^{0.13}$
A0002	0.0002	1000	$10^3 - 3 \times 10^4$	$0.1 (M_{\text{SC}}/M_{\odot})^{0.13}$
B02	0.02	1000	$10^3 - 3 \times 10^4$	1.5
B002	0.002	1000	$10^3 - 3 \times 10^4$	1.5
B0002	0.0002	1000	$10^3 - 3 \times 10^4$	1.5
IB02	0.02	10^7	–	–
IB002	0.002	10^7	–	–
IB0002	0.0002	10^7	–	–

Column 1: Name of the simulation set; YSC stands for all dynamical simulations (set A and set B) considered together, while IB stands for isolated binaries. Column 2 (Z): stellar metallicity; column 3 (N_{SC}): Number of runs; column 4: YSC mass (M_{SC}); column 5: initial half-mass radius (r_{h}).

Binary evolution processes (tides, mass transfer, common envelope and gravitational-wave orbital decay) are implemented as in Hurley et al., 2002. In this work, we assume $\alpha = 5$ (it was $\alpha = 3$ in Di Carlo et al. 2019), while λ is derived by MOBSE as described in Claeys et al., 2014.

Consistently with Di Carlo et al., 2019, when two stars merge, the amount of mass loss is decided by MOBSE, which adopts the same prescriptions as BSE, but if a star merges with a BH or a neutron star, MOBSE assumes that the entire mass of the star is immediately lost by the system and the compact object does not accrete it. This assumption by MOBSE is very conservative, because it is unlikely that the compact object can accrete a substantial fraction of the stellar mass, but it is hard to quantify the actual mass accretion.

4.2.3 Initial conditions

We have simulated 6000 YSCs considering three different metallicities ($Z = 0.02, 0.002, \text{ and } 0.0002$) and two definitions for the initial half-mass radius r_{h} (Ta-
inferred from the LVC (Baibhav et al., 2019), but is in tension with the proper motions of young Galactic pulsars (Hobbs et al., 2005). In a recent work (Giacobbo and Mapelli, 2020), we have revised our kick prescriptions and we have shown that the value of σ adopted in this work has negligible effect on the properties and on the merger rate of BBHs (because V_{KICK} is dominated by fallback).

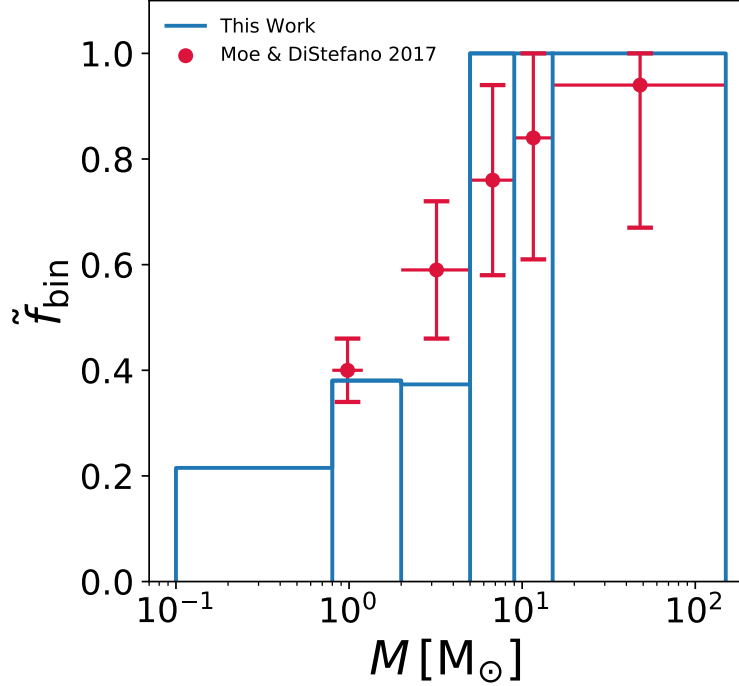


Figure 4.1: Initial binary fraction \tilde{f}_{bin} as a function of stellar mass. \tilde{f}_{bin} is defined as $N_{\text{bin}}/(N_{\text{bin}} + N_{\text{sin}})$, where N_{bin} is the total number of binaries and N_{sin} is the total number of single stars in the YSC at the beginning of the simulation. The blue line represents the binary fraction for one of our simulated star clusters, while the red circles come from the observational results (Moe and Di Stefano, 2017) and represent the fraction of stars with at least one companion.

ble 4.1). Simulations of set A (3000 simulations, 1000 per each considered metallicity) were performed choosing r_h according to the Marks & Kroupa relation (Marks et al., 2012), which relates the total mass M_{SC} of a star cluster at birth with its initial half mass radius r_h :

$$r_h = 0.10^{+0.07}_{-0.04} \text{pc} \left(\frac{M_{\text{SC}}}{M_{\odot}} \right)^{0.13 \pm 0.04}. \quad (4.2)$$

Simulations of set B (3000 simulations, 1000 per each considered metallicity) assume $r_h = 1.5 \text{pc}$. The initial densities of the YSCs at the half-mass radius are $\rho_h = 500 (M_{\text{SC}}/M_{\odot})^{0.61} M_{\odot} \text{pc}^{-3}$ and $4/27 (M_{\text{SC}}/M_{\odot}) M_{\odot} \text{pc}^{-3}$ for set A and B, respectively. We also refer to set A/set B SCs as dense/loose ones.

As already discussed in Di Carlo et al., 2019, we model YSCs with fractal initial conditions, because this mimics the initial clumpiness and asymmetry of embedded star clusters (Cartwright and Whitworth, 2004; Gutermuth et al., 2005; Goodwin and Whitworth, 2004; Ballone et al., 2020). We adopt a fractal dimension $D = 1.6$ and generate the initial conditions with MCLUSTER (Küpper et al., 2011). In Di Carlo et al., 2019, we have shown that larger values of the fractal dimension ($D \leq 2.3$) do

not significantly affect the statistics of BBHs. The velocities of the stars are isotropic and drawn from a Gaussian distribution.

The total mass M_{SC} of each star cluster (ranging from 1000 M_{\odot} to 30000 M_{\odot}) is drawn from a distribution $dN/dM_{\text{SC}} \propto M_{\text{SC}}^{-2}$, as the embedded star cluster mass function described in Lada and Lada, 2003. Thus, the mass distribution of our simulated star clusters mimics the mass distribution of star clusters in Milky Way-like galaxies. The star clusters are initialised so that the virial ratio $\alpha_{\text{vir}} = T/|V| = 0.5$, where T and V are the total kinetic and potential energy of the YSC, respectively.

The stars in the simulated star clusters follow a Kroupa, 2001 initial mass function, with minimum mass 0.1 M_{\odot} and maximum mass 150 M_{\odot} . We assume an initial binary fraction $f_{\text{bin}} = 0.4$, meaning that 40% of the stars are members of binary systems. The orbital periods, eccentricities and mass ratios of binaries with primary more massive than 5 M_{\odot} are drawn from Sana et al., 2012 distributions, as already described in Di Carlo et al., 2019. Stars with a mass larger than 5 M_{\odot} , starting from the most massive, are paired with the star which better matches the mass ratio drawn from the distribution. Stars under 5 M_{\odot} are randomly paired until the required binary fraction is reached. This procedure results in a mass-dependent initial binary fraction which is larger for more massive binaries, consistent with the multiplicity properties of O/B-type stars (e.g. Sana et al. 2012; Moe and Di Stefano 2017), as shown in Figure 4.1.

The force integration includes a solar neighbourhood-like static external tidal field (Wang et al., 2016). Each star cluster is evolved until its dissolution or for a maximum time $t = 100$ Myr. The most massive star clusters in our sample are not completely disrupted at $t = 100$ Myr, but our static tidal field model tends to overestimate the lifetime of star clusters, because it does not account for massive perturbers (e.g. molecular clouds), which can accelerate star cluster disruption (Gieles et al., 2006). Hence, our choice is quite conservative. When the N -body simulation stops, we extract all the BBHs and we evolve their semi-major axis and eccentricity using the timescale formula presented in Peters, 1964, which describes the evolution of the orbit due to GW emission. We classify as merging BBHs all BBHs that merge within a Hubble time ($t_{\text{H}} = 14$ Gyr) by gravitational wave decay.

For comparison, we have also run a set of isolated binary simulations with the stand-alone version of MOBSE. In particular, we simulated 10^7 isolated binaries (IBs) per each considered metallicity ($Z = 0.02, 0.002$ and 0.0002). Primary masses of the IBs are drawn from a Kroupa (Kroupa, 2001) mass function between 5 and 150 M_{\odot} . Orbital periods and eccentricities are randomly drawn from the same distribution as the dynamical simulations, but for one difference: the maximum orbital pe-

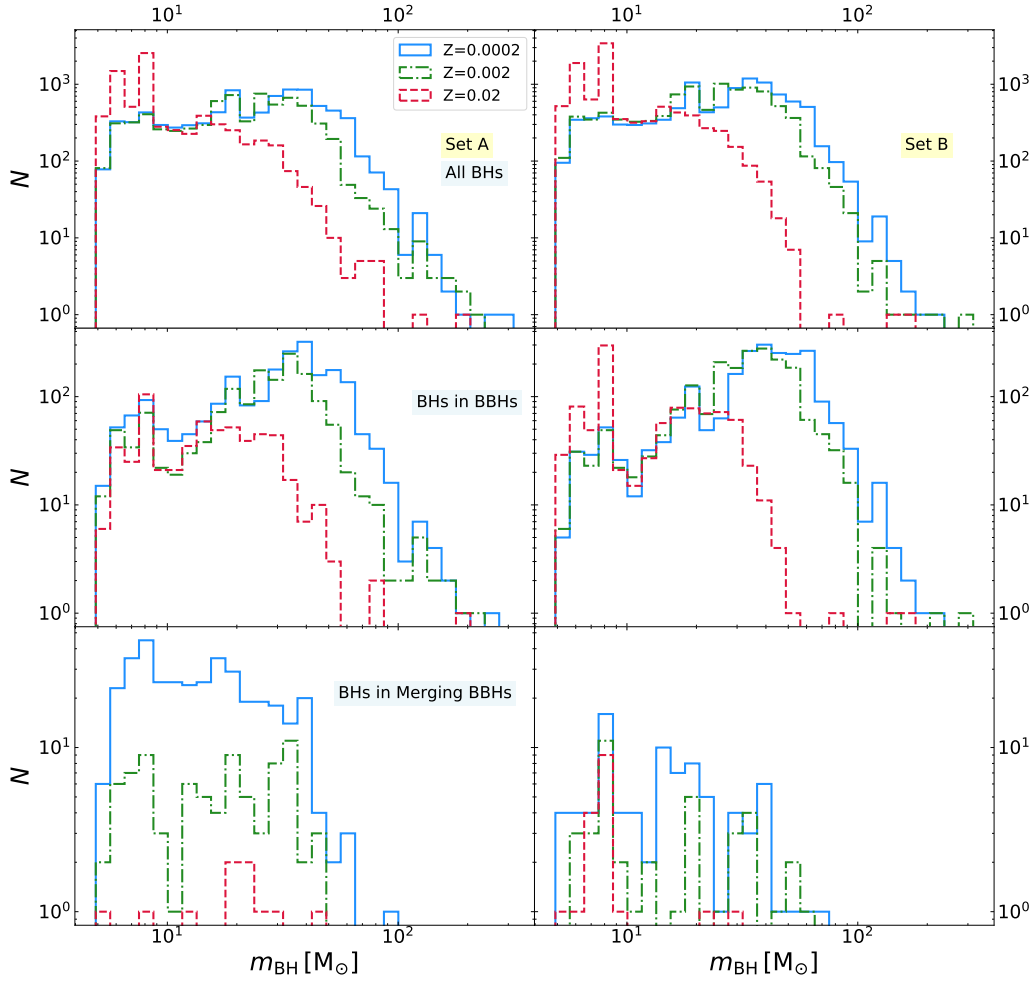


Figure 4.2: Distribution of BH masses in the simulations. Left-hand panels: set A; right-hand panels: set B; top: all BHs; middle: BHs which are members of BBHs at the end of the simulations; bottom: BHs in merging BBHs. Blue solid line: $Z = 0.0002$; green dot-dashed line: $Z = 0.002$; red dashed line: $Z = 0.02$.

riod is $\log(P_{\max}/\text{days}) = 5.5$ and $\log(P_{\max}/\text{days}) = 6.7$ in the isolated binaries and in the dynamical simulations, respectively. We checked that this difference has a negligible impact on our results. A summary of the initial conditions of the performed simulations is reported in Table 4.1.

4.3 Results

4.3.1 BH mass distribution

Figure 4.2 shows the mass distribution of all simulated BHs. The overall mass range of BHs, considering both single and binary BHs, spans from $5 M_{\odot}$ (the minimum

BH mass according to the rapid model by Fryer et al. 2012) to $320 M_{\odot}$.

The maximum BH mass and the slope of the BH mass function depend on metallicity: BHs born from metal-rich stars ($Z = 0.02$) tend to be less massive than BHs born from metal-poor stars ($Z = 0.0002 - 0.002$).

In the case of single stars and isolated binaries, MOBSE predicts a maximum BH mass of $\sim 65 M_{\odot}$ (see Figure 4 of Giacobbo et al. 2018), while in our dynamical simulations we find BHs with mass up to $\sim 320 M_{\odot}$. This difference is a result of multiple stellar mergers in YSCs, which build up a significantly more massive BH population in star clusters than in the field. This produces a non negligible population of BHs with mass in the pair-instability gap, between ~ 60 and $\sim 120 M_{\odot}$: $\sim 5.0\%$, 1.5% and 0.2% ($\sim 5.7\%$, $\sim 2.2\%$ and $\sim 0.01\%$) of the simulated BHs have mass in the pair-instability gap in our set A (set B) at $Z = 0.0002, 0.002$ and 0.02 , respectively.

Intermediate-mass BHs (IMBHs), defined as BHs with $m_{\text{BH}} \geq 100 M_{\odot}$, are $\sim 0.5\%$, $\sim 0.3\%$ and $\sim 0.03\%$ ($\sim 0.4\%$, $\sim 0.1\%$ and $\sim 0.02\%$) of all our BHs in set A (set B) at $Z = 0.0002, 0.002$ and 0.02 , respectively. They form through (multiple) stellar mergers, whose probability is enhanced by the short dynamical friction timescale in our clusters ($t_{\text{df}} \lesssim 1$ Myr for a star with zero-age main-sequence mass $m_{\text{ZAMS}} \gtrsim 20 M_{\odot}$): the most massive stars and binary stars sink to the core of the cluster before they become BHs; once in the core, they interact with each other triggering the mechanism known as runaway collision (e.g. Portegies Zwart and McMillan 2002; Portegies Zwart et al. 2004; Giersz et al. 2015; Mapelli 2016).

The mass distribution of BHs in dense clusters (set A) and loose clusters (set B) are similar. The main difference is the percentage of BBHs that merge within a Hubble time (hereafter, merging BBHs), especially at low metallicity: these are $\sim 17.1\%$, $\sim 5.7\%$ and $\sim 1.7\%$ ($\sim 3.9\%$, $\sim 2.0\%$ and $\sim 1.8\%$) in set A (set B) for a progenitor metallicity $Z = 0.0002, 0.002$ and 0.02 , respectively. Hence, star cluster density plays an important role in shrinking the orbit of BBHs. From these numbers, it is also apparent that BBH mergers are more common at low metallicity.

4.3.2 Properties of merging BBHs

Here, we focus on merging BBHs, i.e. BBHs that reach coalescence within a Hubble time. We call dynamical BBHs and isolated BBHs those merging BBHs that form in YSCs and in isolated binaries, respectively. We further divide dynamical BBHs into exchanged BBHs (i.e. dynamical BBHs that form from dynamical exchanges) and

Table 4.2: Percentage of original and exchanged BBHs.

Set	$f_{\text{orig,all}}$	$f_{\text{exch,all}}$	$f_{\text{orig,merger}}$	$f_{\text{exch,merger}}$
YSC	22 %	78 %	58 %	42 %
A	18 %	82 %	58 %	42 %
B	25 %	75 %	65 %	35 %
A02	7 %	93 %	0 %	100 %
A002	15 %	85 %	36 %	64 %
A0002	24 %	76 %	65 %	35 %
B02	28 %	72 %	67 %	33 %
B002	22 %	78 %	75 %	25 %
B0002	25 %	75 %	60 %	40 %

Column 1: Name of the simulation set; column 2: $f_{\text{orig,all}}$, percentage of original BBHs with respect to all BBHs at the end of the simulations; column 3 $f_{\text{exch,all}}$, percentage of exchanged BBHs with respect to all BBHs at the end of the simulations; column 4: $f_{\text{orig,merger}}$, percentage of merging original BBHs with respect to all merging BBHs; column 5: $f_{\text{exch,merger}}$, percentage of merging exchanged BBHs with respect to all merging BBHs.

original BBHs (i.e. dynamical BBHs that form from binary stars which were already present in the initial conditions³).

Table 4.2 shows the percentage of original and exchanged BBHs for each set. About 78% of all BBHs are exchanged, but only $\sim 43\%$ of the merging BBHs are exchanged. This indicates that a large fraction of exchanged BBHs are loose binaries and cannot harden fast enough to merge within a Hubble time. The percentage of exchanged BBHs in set A is higher than that of set B: binaries in dense star clusters undergo more exchanges than in loose star clusters.

The fraction of exchanged BBHs increases with metallicity in set A, while it is almost constant with metallicity in set B. For example, the percentages of exchanged BBHs and merging exchanged BBHs are $\sim 76\%$ and $\sim 35\%$ in set A0002, and rise to $\sim 93\%$ and 100% in set A02. In contrast, the percentages of exchanged BBHs and merging exchanged BBHs are $\sim 75\%$ and $\sim 40\%$ in set B0002, and remain very similar ($\sim 72\%$ and 33%) in set B02.

Table 4.3 shows the results of the Kolmogorov-Smirnov (hereafter, KS) test (Birnbauer, Tingey, et al., 1951; Wang et al., 2003) and of the U-test (Bauer, 1972; Hollander and Wolfe, 1999). We find that the masses of merging BBHs in set A and in

³In papers about star cluster dynamics, original BBHs are usually referred to as ‘primordial BBHs’ or ‘BBHs born from primordial binaries’, because the binary stars which were already present in the initial conditions are usually called ‘primordial binaries’. Here, we name them original BBHs to avoid confusion with primordial BHs that might form from gravitational instabilities in the early Universe (e.g. Carr and Hawking 1974; Carr et al. 2016).

Table 4.3: Results of the KS-Test and U-Test to compare sets of merging BBHs.

Set 1	Set 2	Distribution	KS-Test	U-Test
A – Original	B – Original	m_{tot}	0.82	0.56
A – Exchanged	B – Exchanged	m_{tot}	0.36	0.55
A – All	B – All	m_{tot}	0.65	0.50
A – Original	B – Original	m_{chirp}	0.57	0.35
A – Exchanged	B – Exchanged	m_{chirp}	0.56	0.59
A – All	B – All	m_{chirp}	0.33	0.38
A – Original	B – Original	q	0.05	0.14
A – Exchanged	B – Exchanged	q	0.84	0.59
A – All	B – All	q	0.50	0.54
A – Original	B – Original	t_{delay}	0.43	0.35
A – Exchanged	B – Exchanged	t_{delay}	0.99	0.94
A – All	B – All	t_{delay}	0.88	0.50

In this Table, we apply the KS- and U- tests to compare different samples of BBHs. Columns 1 and 2: the two BBH samples to which we apply the KS- and U- test. Each sample comes from one of the simulation sets (see Table 4.1). Column 3: distribution to which we apply the KS- and U- tests. We consider total BBH masses (m_{tot}), chirp masses (m_{chirp}), mass ratios (q) and delay times (t_{delay}). Columns 4 and 5: probability that the two samples are drawn from the same distribution according to the Kolmogorov-Smirnov (KS) Test and to the U-Test, respectively.

set B are not consistent with being drawn from two different underlying distributions. Based on this result and to filter out stochastic fluctuations, we consider BBH mergers of set A and set B together in the following analysis.

Figures 4.3, 4.4 and 4.5 show the total mass ($m_{\text{TOT}} = m_1 + m_2$), the chirp mass [$m_{\text{chirp}} = (m_1 m_2)^{3/5} (m_1 + m_2)^{-1/5}$] and the mass ratio ($q = m_2/m_1$, where $m_1 \geq m_2$) of merging BBHs, respectively. In these figures, the three metallicity samples and the two simulation sets are stacked together.

The total masses of dynamical BBH mergers range from ~ 10 to $\sim 140 M_{\odot}$, while the chirp masses span from ~ 4.8 to $\sim 55.8 M_{\odot}$. Mass ratios of order of one are most common, but the distributions reach a minimum value of $q \sim 0.18$.

Exchanged BBHs reach significantly larger total masses and chirp masses and smaller values of q than both original BBHs and isolated BBHs. The typical masses of original BBHs are similar to those of isolated BBHs. This confirms the results of Di Carlo et al., 2019, who considered only one metallicity ($Z = 0.002$).

Figure 4.6 shows the mass of the secondary BH (m_2) versus the mass of the primary BH (m_1), distinguishing between different metallicities. The most massive objects

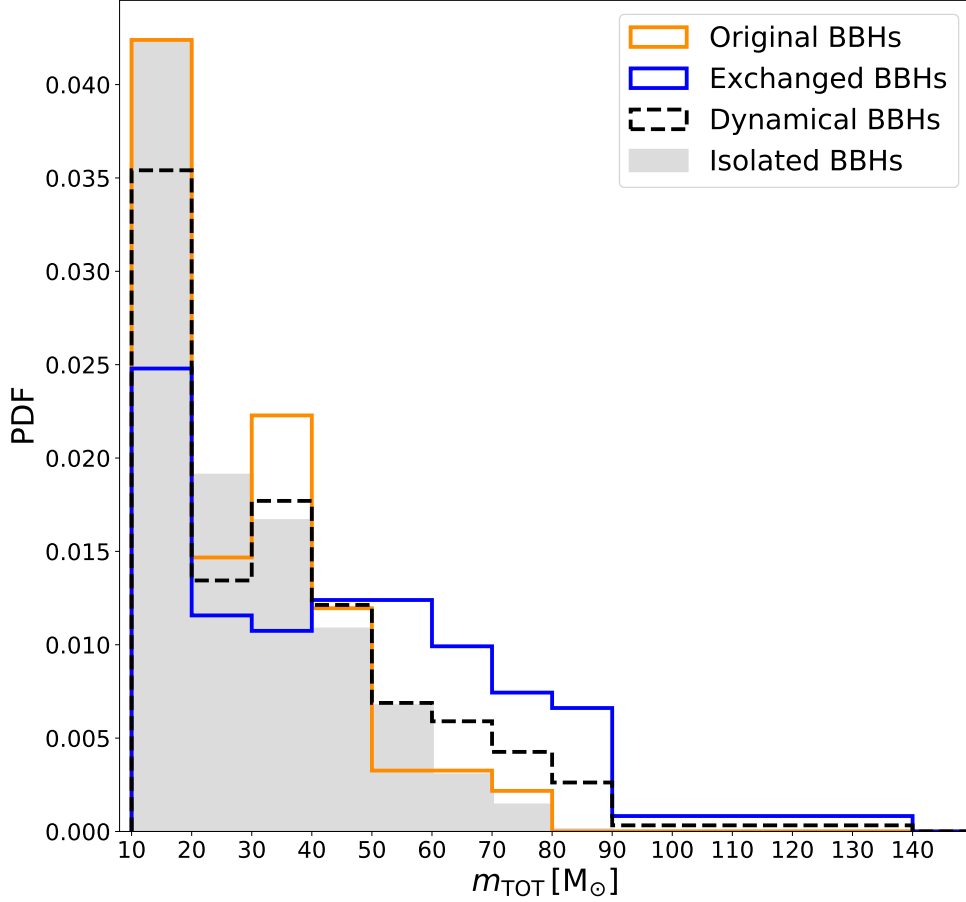


Figure 4.3: Distribution of total masses ($m_{\text{TOT}} = m_1 + m_2$) of merging BBHs. Set A and B are stacked together. Orange solid line: original BBHs; blue solid line: exchanged BBHs; black dashed line: all dynamical BBHs (original+exchanged); gray filled histogram: isolated BBHs.

($m_1 > 45 M_{\odot}$) form only at low metallicity ($Z = 0.0002, 0.002$) and are exclusively exchanged BBHs.

Table 4.4 shows the masses, metallicities and delay times of BBH mergers with primary mass $m_1 \geq 45 M_{\odot}$. All of them are exchanged BBHs and (according to our population-synthesis model) cannot form by isolated binary evolution. We choose this threshold of $45 M_{\odot}$, because Abbott et al., 2019a indicate that the mass distribution of the primary BH in O1 and O2 LVC events is well approximated by models with no more than 1 % of BHs more massive than $45 M_{\odot}$. In our simulations, we show that these BBH mergers are impossible to form via isolated binary evolution, but can arise from dynamical exchanges in YSCs. These massive BBH mergers are 4.3% and 7.0% of all the BBH mergers we find in set A and set B, respectively. Most of them have mass ratios different from one.

Figure 4.7 shows the evolution of the most massive BBH merger in our simulations,

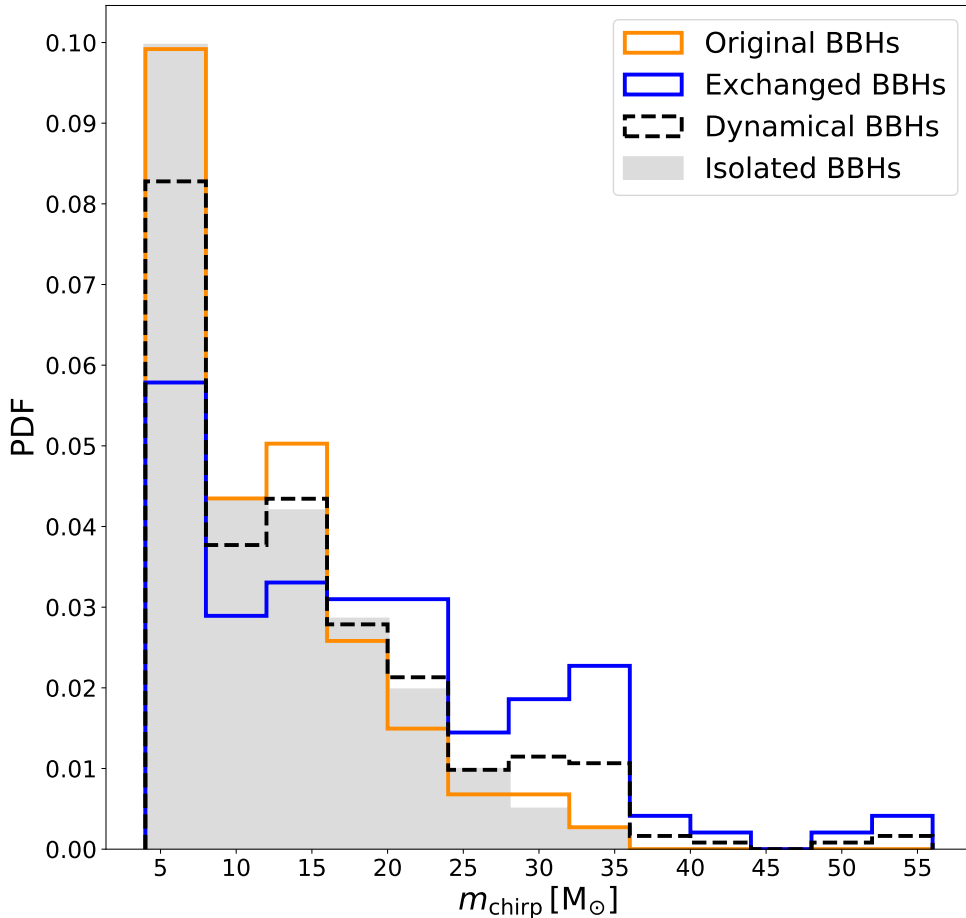


Figure 4.4: Same as Figure 4.3, but for the distribution of chirp masses $m_{\text{chirp}} = (m_1 m_2)^{3/5} (m_1 + m_2)^{-1/5}$ of merging BBHs.

with a primary mass $m_1 = 88 M_\odot$ and a secondary mass $m_2 = 48 M_\odot$. Both the primary and the secondary BH in this system form from the merger of two progenitor stars and become bound by exchange. The mass of the primary BH is within the pair instability mass gap. This happens because the merger between a core helium burning (cHeB) star and a main sequence (MS) star produces a new cHeB star with a large hydrogen envelope and with a helium core below the threshold for (pulsational) pair instability (see Di Carlo et al. 2020a for further details). The merger between the $57.4 M_\odot$ cHeB and the $41.9 M_\odot$ MS is triggered by a dynamical encounter. If we simulate a binary with the same initial conditions using the stand-alone version of MOBSE (i.e. without dynamical perturbations), the binary does not merge at 4.3 Myr and leaves a smaller remnant.

The yellow stars in Figure 4.6 show the 10 BBHs detected by the LVC during O1 and O2 (Abbott et al., 2019b) plus GW190412, the first published BBH merger of O3 and the first event showing evidence of unequal mass components (Abbott et al.,

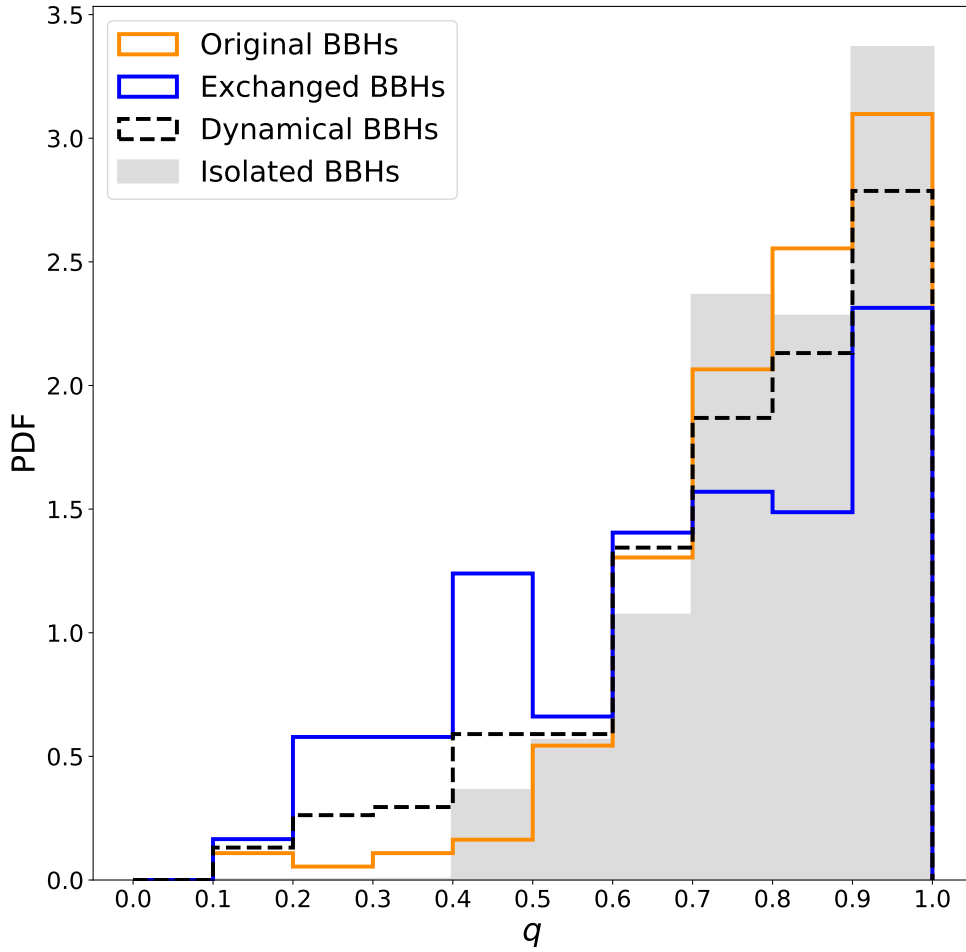


Figure 4.5: Same as Figure 4.3, but for the distribution of mass ratios $q = m_2/m_1$ of merging BBHs.

2020a). Our simulated BBH mergers match all O1–O2 BBHs including GW170729. GW170729, the most massive event detected in O1 and O2, is consistent only with BBHs formed in YSCs (mostly exchanged BBHs): our models cannot form GW170729 via isolated binary evolution, even at the lowest considered metallicity. This result strongly favours a dynamical formation for GW170729. Even GW190412 can be matched only by dynamical BBHs born from metal-poor progenitors, because isolated binaries can hardly account for its mass ratio in our models.

Figure 4.8 shows the distribution of delay times for our simulated BBHs. We find no significant differences between the delay time distribution of set A and set B (see Table 4.3). The two distributions are broadly consistent with $dN/dt \propto t^{-1}$ (Dominik et al., 2012) if $t_{\text{delay}} \gtrsim 400$ Myr, but bend with respect to this scaling at shorter times. As a result, the overall distributions are not consistent with $\propto t^{-1}$, unless we neglect delay times shorter than 400 Myr.

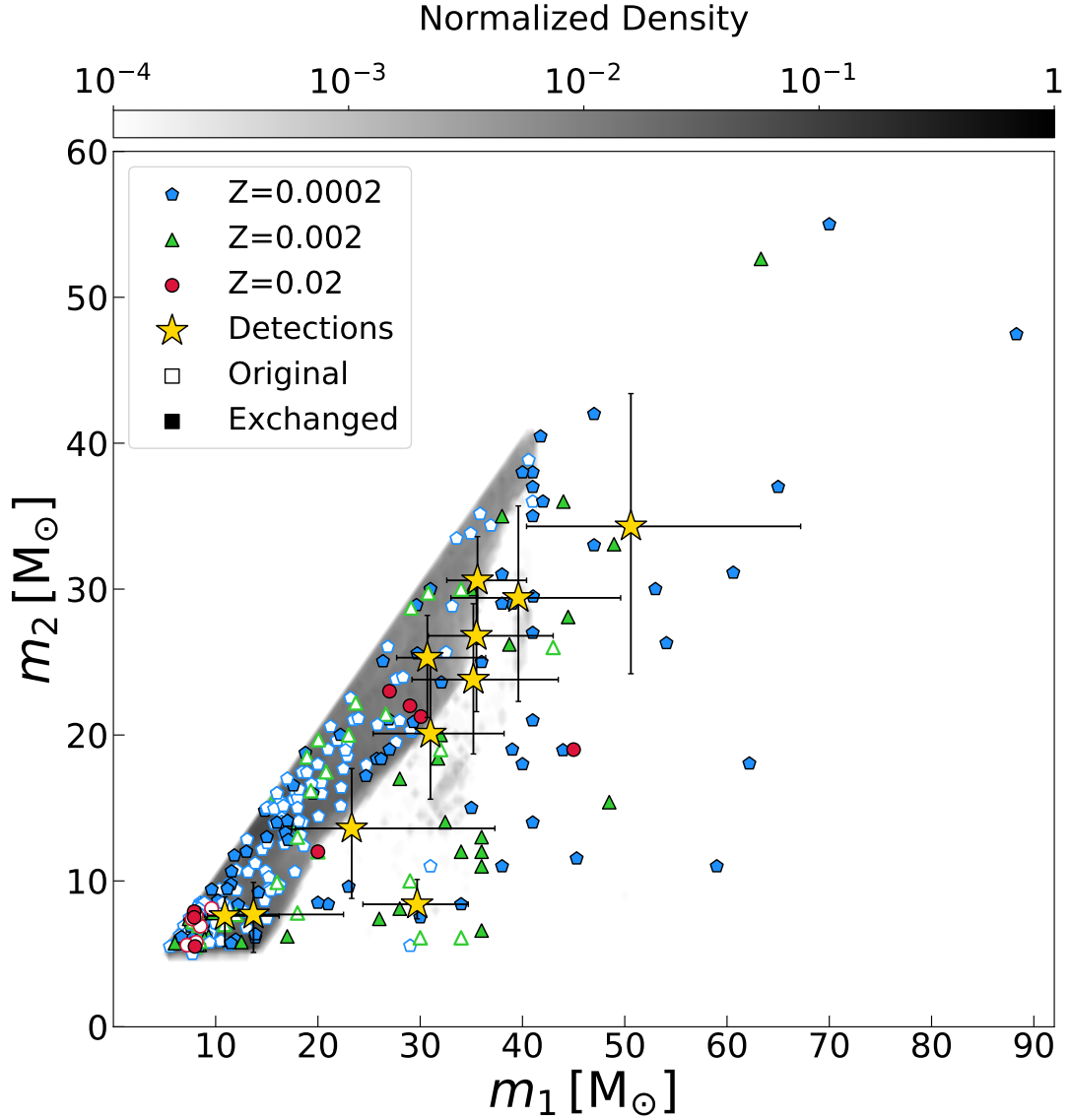


Figure 4.6: Mass of the primary BH (m_1) versus mass of the secondary BH (m_2) of merging BBHs. Set A and B are stacked together. Empty symbols: original BBHs; filled symbols: exchanged BBHs. Blue, green and red symbols represent $Z = 0.0002$, 0.002 and 0.02 , respectively. Filled contours (with gray colour map): isolated BBHs. Yellow stars with error bars: LVC BBHs [GW150914 (Abbott et al., 2016a), GW151012 (Abbott et al., 2016d), GW151226 (Abbott et al., 2016e), GW170104 (Abbott et al., 2017a), GW170608 (Abbott et al., 2017b), GW170729 (Abbott et al., 2019b), GW170809 (Abbott et al., 2019b), GW170814 (Abbott et al., 2017c), GW170818 (Abbott et al., 2019b), GW170823 (Abbott et al., 2019b), GW190412 (Abbott et al., 2020a)]. Error bars indicate 90% credible levels.

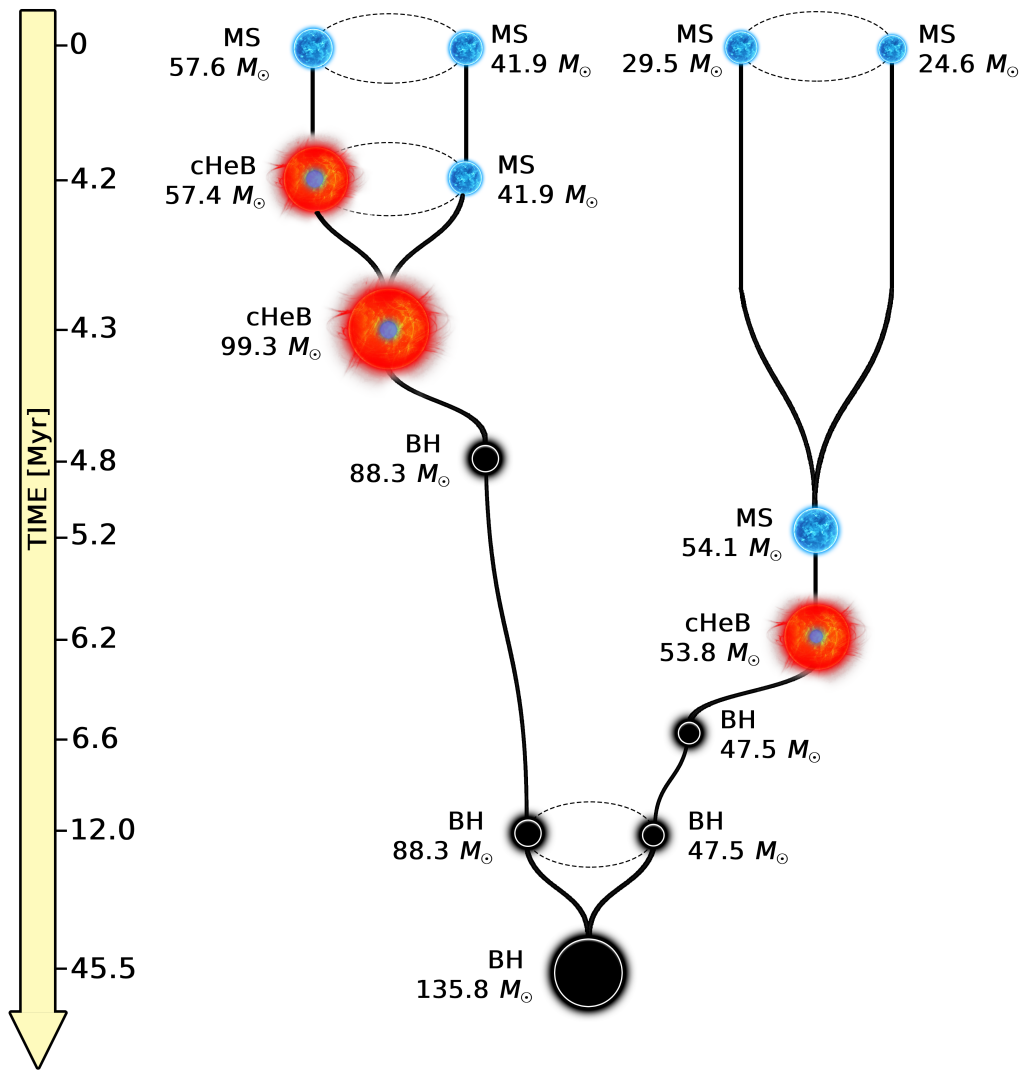


Figure 4.7: Evolution of the most massive BBH merger in our simulations. Blue stars represent main sequence stars (with label MS); red stars with a blue core represent core helium burning stars (label cHeB); black circles represent black holes (label BH). The mass of each object is shown next to them. The time axis and the size of the objects are not to scale. The primary BH with $m_1 = 88.3 M_{\odot}$ lies in the pair-instability mass gap. The merging BBH forms because of dynamical interactions.

Table 4.4: List of the BBH mergers with primary mass $m_1 \geq 45 M_\odot$ in our simulations.

$m_1 [M_\odot]$	$m_2 [M_\odot]$	q	Z	$t_{\text{delay}} [\text{Gyr}]$	Set
88.3	47.5	0.54	0.0002	0.046	A
70.0	55.0	0.79	0.0002	1.679	B
65.0	37.0	0.57	0.0002	0.0324	A
63.3	52.6	0.83	0.002	11.008	B
62.2	18.0	0.29	0.0002	0.264	B
60.6	31.1	0.51	0.0002	5.876	A
59.0	11.0	0.19	0.0002	0.499	A
54.1	26.3	0.49	0.0002	0.253	A
53.0	30.0	0.57	0.0002	7.0178	A
49.0	33.1	0.68	0.002	0.505	B
48.5	15.4	0.32	0.002	0.117	A
47.0	42.0	0.89	0.0002	0.0447	A
47.0	33.0	0.70	0.0002	0.437	B
45.3	11.5	0.25	0.0002	3.586	A
45.0	19.0	0.42	0.02	0.308	A

Column 1: Mass of the primary BH (m_1); column 2: mass of the secondary BH (m_2); column 3: mass ratio (q); column 4: progenitor's metallicity (Z); column 5: delay time (t_{delay}); column 6: simulation set.

4.3.3 Merger efficiency and local merger rate

Figure 4.9 shows the merger efficiency $\eta(Z)$ defined as in Giacobbo and Mapelli, 2018:

$$\eta(Z) = \frac{N_{\text{TOT}}(Z)}{M_*(Z)}, \quad (4.3)$$

where $N_{\text{TOT}}(Z)$ is the total number of BBHs (formed at a given metallicity) with delay time shorter than the Hubble time, while $M_*(Z)$ is the total initial stellar mass of the simulated population at a given metallicity. For isolated binaries (Giacobbo and Mapelli, 2018), $M_*(Z) = M_{*,\text{sim}}(Z)/(f_{\text{bin}} f_{\text{corr}})$, where $M_{*,\text{sim}}(Z)$ is the total initial mass of the simulated binaries, $f_{\text{bin}} = 0.4$ accounts for the fact that we simulated only binaries and not single stars, and f_{corr} accounts for the missing low-mass stars between 0.1 and 5 M_\odot . The merger efficiency is a useful quantity to understand the impact of stellar metallicity on the merger rate of binary compact objects.

The most remarkable difference between isolated BBHs and dynamical BBHs is that, at solar metallicity ($Z = 0.02$), the merger efficiency of the latter is higher by two orders of magnitude than the merger efficiency of the former. In YSCs, exchanges lead to the formation of BBHs and dynamical encounters harden existing massive binary stars, even at solar metallicity. In contrast, isolated BBH mergers

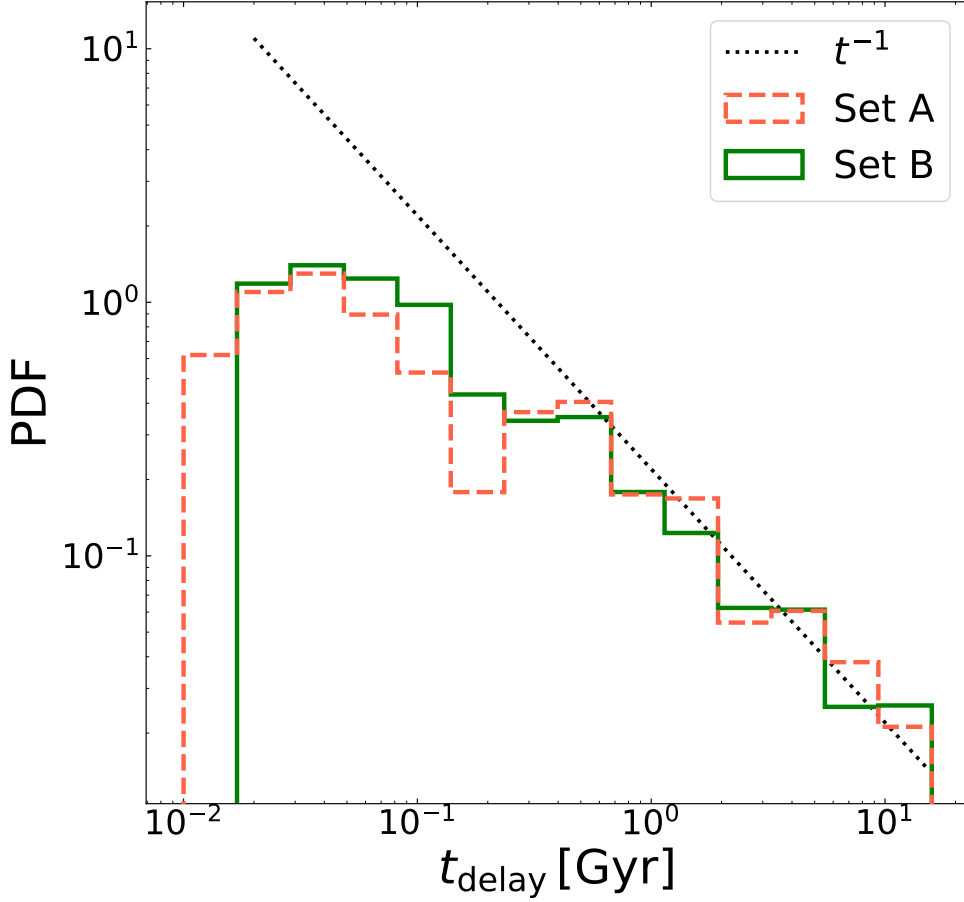


Figure 4.8: Distribution of delay times t_{delay} of merging BBHs. Orange dashed line: set A; green solid line: set B. Dotted black line: scaling as $dN/dt \propto t^{-1}$.

are much rarer at solar metallicity, because stellar winds are efficient: the vast majority of massive stars become Wolf-Rayet stars before they can start a Roche lobe episode and do not undergo a common envelope phase; hence, most of the isolated BBHs which form at solar metallicity are too wide to merge within a Hubble time (Giacobbo and Mapelli, 2018).

From the merger efficiency $\eta(Z)$, we can estimate the local merger rate density \mathcal{R}_{BBH} , as already described in Santoliquido et al., 2020:

$$\mathcal{R}_{\text{BBH}} = \frac{1}{t_{\text{lb}}(z_{\text{loc}})} \int_{z_{\text{max}}}^{z_{\text{loc}}} \psi(z') \frac{dt_{\text{lb}}}{dz'} dz' \times \int_{Z_{\text{min}}(z')}^{Z_{\text{max}}(z')} \eta(Z) \mathcal{F}(z', z_{\text{loc}}, Z) dZ, \quad (4.4)$$

where $t_{\text{lb}}(z_{\text{loc}})$ is the look-back time evaluated in the local universe ($z_{\text{loc}} \leq 0.1$), $\psi(z')$ is the cosmic SFR density at redshift z' (from Madau and Fragos 2017), $Z_{\text{min}}(z')$ and

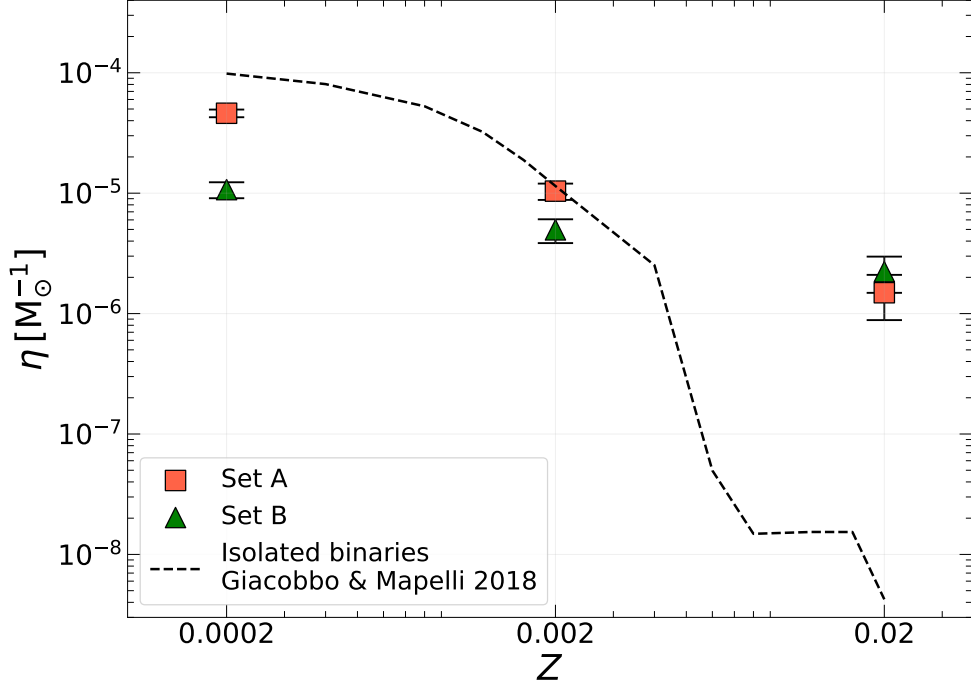


Figure 4.9: Merger efficiency $\eta(Z)$, defined as the number of mergers per solar mass, as a function of metallicity. The black dashed line shows the values from Giacobbo and Mapelli, 2018. Orange squares and green triangles refer to set A and set B, respectively. Error bars represent Poisson uncertainties.

$Z_{\max}(z')$ are the minimum and maximum metallicity of stars formed at redshift z' and $\mathcal{F}(z_{\text{loc}}, z', Z)$ is the fraction of BBHs that form at redshift z' from stars with metallicity Z and merge at redshift z_{loc} normalized to all BBHs that form from stars with metallicity Z . To calculate the lookback time t_{lb} we take the cosmological parameters (H_0 , Ω_{M} and Ω_{Λ}) from Ade et al., 2016. We integrate equation 4.4 up to redshift $z_{\max} = 15$, which we assume to be the epoch of formation of the first stars. From equation 4.4 we obtain a local merger rate density $\mathcal{R}_{\text{BBH}} \sim 55$ and ~ 110 $\text{Gpc}^{-3} \text{yr}^{-1}$ for set A and B, respectively, by assuming that all the cosmic star formation rate occurs in YSCs like the ones we simulated in this paper. If we repeat the same procedure for the isolated BBHs, we find $\mathcal{R}_{\text{BBH}} \sim 50$ $\text{Gpc}^{-3} \text{yr}^{-1}$. Set B gives the highest local merger rate density, because it has a higher number of BBH mergers at solar metallicity (which is the dominant metallicity at low redshift) with relatively short delay times. Considering the small sample of BBH mergers at $Z = 0.02$ (5 BBHs in set A and 8 BBHs in set B), the difference of a factor of 2 between the two local merger rates is likely due to stochastic fluctuations.

The inferred merger rates are upper limits, since we do not take into account infant mortality of YSCs (Brinkmann et al., 2017; Shukirgaliyev et al., 2017), we do not use

an observation-based local number density of YSCs (Portegies Zwart and McMillan, 2000b) and we assume that all stars form in YSCs like the ones we simulated in this paper. It is more likely that a fraction of all mergers comes from YSCs and another fraction from isolated binaries, globular clusters or nuclear star clusters. In a follow-up paper (Bouffanais et al., in prep), we will try to constrain these percentages based on current LVC results.

4.4 Discussion

4.4.1 Merger efficiency: dynamical versus isolated BBHs

Why the merger efficiency of dynamical BBHs is lower than that of isolated BBHs at low metallicity, but higher at high metallicity? This result springs from two opposite effects. On the one hand, dynamical encounters tend to break some BBHs, especially low-mass BBHs with a relatively large orbital separation (see e.g. Zevin et al. 2017 and Di Carlo et al. 2019). On the other hand, dynamics enhances the merger of massive BBHs by exchanges and by hardening. The former effect tends to decrease the merger efficiency, while the latter tends to increase it.

At solar metallicity ($Z = 0.02$), the merger efficiency of isolated BBHs is drastically low (2–3 orders of magnitude lower than at $Z \leq 0.002$). This implies that, at solar metallicity, even if dynamics ionizes all the low-mass original BBHs, this has no effect on the merger efficiency, because these low-mass original BBHs were not going to merge anyway. Thus, the loss of BBH mergers due to binary ionization/softening is minimum at high Z . In contrast, the few dynamical BBH mergers at high Z all come from dynamical hardening and dynamical exchanges. The net effect is that the merger efficiency of dynamical BBHs is higher than that of isolated BBHs at solar metallicity.

At low Z , the situation is inverted. Most of the mergers from isolated BBHs come from low-mass BBHs (see e.g. Giacobbo et al. 2018). Hence, when dynamics suppresses the merger of these low-mass BBHs (by softening or ionization), it removes most of potential merging systems from the game. In metal-poor clusters, dynamical hardening and exchanges are efficient in forming massive BBHs and in triggering their merger, but these massive binaries are not sufficiently numerous to compensate for the loss of low-mass mergers. Hence, the net effect is that the merger efficiency of dynamical BBHs is lower than that of isolated BBHs at low Z .

There is also a difference between Set A (dense clusters) and Set B (loose clusters). At low Z , the merger efficiency of Set A is a factor of ~ 5 higher than that of Set B,

while at higher Z the two sets have almost the same merger efficiency. The main reason for this difference is that, at low Z , where BH masses are higher, dynamical hardening and exchanges are more effective in the dense clusters of set A than in the loose clusters of set B.

4.4.2 When do the exchanges happen?

Table 4.5 shows that most of the exchanged BBHs that merge within a Hubble time undergo their first exchange when the binary system is still composed of two stars, i.e. before the collapse of the primary component to a BH. The percentage of exchanges whose result is a binary composed of two stars is $\sim 54\%$ and $\sim 72\%$ for set A and B, respectively.

The percentage of exchanges that lead to the formation of a BH – star binary is zero in set B and up to $\sim 17\%$ in set A. Finally, $\sim 30\%$ of all exchanges that lead to BBH mergers happen when the two BHs have already formed.

Figure 4.10 confirms this result: the dynamical exchanges that lead to the formation of merging systems happen in the first ~ 10 Myr of the star cluster life. Most of these exchanges happen earlier ($t \ll 1$ Myr) in the star clusters of set B than in those of set A ($t \sim 2 - 3$ Myr).

This reflects a difference in the timescale for the collapse of the core of the cluster (hereafter, core collapse), because most interactions happen during core collapse. In set B, the single sub-clumps of our fractal initial conditions undergo core collapse before they have completed the hierarchical assembly into the larger star cluster. Hence, most exchanges and dynamical interactions happen in this very early stage, $t < 1$ Myr. In contrast, the clusters of set A are so dense that the sub-clumps hierarchically assemble to form one monolithic cluster before they undergo individual core collapse. Hence, the first core collapse in set A is the collapse of the core of the global cluster at $t \sim 2 - 3$ Myr. As already discussed by Fujii and Portegies Zwart, 2013a, the build up and merger of massive binaries is suppressed if the sub-clumps collapse before the hierarchical assembly of the global cluster. Hence, we expect the binaries of set A to start their dynamical activity later but to have more dynamical interactions with respect to the binaries of set B.

4.4.3 Integration time and merger rates

We integrated all the simulated YSCs until their dissolution or for a maximum time $t = 100$ Myr. Would a longer integration time significantly affect the number of mergers? At the end of the simulations, our YSCs retain between 50% and 70%

of their initial mass and $\sim 60\%$ of the total BBHs. However, the vast majority of these in-cluster BBHs are loose binaries ($\sim 99.5\%$ of them have an orbital separation $a > 10^2 R_\odot$) and would therefore require many strong dynamical interactions to harden and enter the GW regime. In a future work, we will integrate our clusters up to 1 Gyr to check the impact of the integration time on BBHs, but we do not expect it to significantly affect the number of mergers.

4.4.4 Comparison with previous studies

Kumamoto et al., 2019b and Kumamoto et al., 2020 evaluate the BBH merger rate from open clusters, whose masses and scales are comparable to our fractal YSCs. Kumamoto et al., 2019b find that exchanges leading to BBH mergers happen mostly between stellar progenitors (before their collapse to BH), consistently with our results (see also Di Carlo et al. 2019). Moreover, Kumamoto et al., 2020 predict a local BBH merger rate density $\sim 35 \text{ Gpc}^{-3} \text{ yr}^{-1}$, similar to our result. Banerjee, 2020 produced a set of simulations of more massive YSC, with masses between 10^4 and $10^5 M_\odot$ and with lower binary fractions ($0 < f_{\text{bin}} < 0.1$). Banerjee, 2020 finds a mass spectrum of merging BBHs which is similar to our result; the main difference is that we find systems with lower mass ratios. Moreover, while 97% of our BBH mergers take place outside the YSC, most of the mergers in Banerjee, 2018b and Banerjee, 2020 happen inside the cluster, likely because of the higher star cluster mass in these studies with respect to our simulations.

These results for both YSCs (Di Carlo et al., 2019; Di Carlo et al., 2020a) and open clusters (Banerjee et al., 2010; Ziosi et al., 2014; Banerjee, 2018b; Banerjee, 2018a) remark a crucial difference with respect to globular clusters (e.g. Portegies Zwart and McMillan 2000b; Morscher et al. 2015; Rodriguez et al. 2015; Rodriguez et al. 2016; Rodriguez et al. 2018; Askar et al. 2017a) and nuclear star clusters (e.g. Antonini and Rasio 2016; Arca Sedda and Benacquista 2019). Globular and nuclear clusters are significantly more long-lived than open and young clusters. Hence, BBHs born in the former clusters have more time to harden by gravitational encounters and to undergo exchanges before they merge. This is expected to boost the merger efficiency per globular/nuclear cluster. On the other hand, most globular clusters formed ~ 12 Gyr ago; hence, their contribution to the *local* merger rate density is relatively small ($< 20 \text{ Gpc}^{-3} \text{ yr}^{-1}$, e.g. Askar et al. 2017a; Rodriguez and Loeb 2018).

In contrast, YSCs are short-lived, but form all the time across cosmic history. Thus, they might have a larger cumulative effect on the local merger rate density of BBHs.

Table 4.5: Progenitors of exchanged BBH mergers at the time of the first exchange

Set	$f_{\text{star-star}}$	$f_{\text{star-BH}}$	f_{BBH}
YSC	57%	12%	31%
A	54%	14%	32%
B	72%	0%	28%
A02	0%	0%	100%
A002	45%	9%	46%
A0002	60%	17%	23%
B02	67%	0%	33%
B002	60%	0%	40%
B0002	80%	0%	20%

Column 1: Simulation set; column 2: percentage of exchanged BBH mergers in which the result of the first exchange is a star-star binary ($f_{\text{star-star}}$); column 3: percentage of exchanged BBH mergers in which the result of the first exchange is a star-BH binary ($f_{\text{star-BH}}$); column 4: percentage of exchanged BBH mergers in which the outcome of the first exchange is already a BBH (f_{BBH}).

Moreover, YSCs are the main birth-place of massive stars, and, when they are disrupted by gas evaporation or by the tidal field, they release their stellar content into the field. Thus, a large fraction of the field binaries might have formed in a YSC and might have taken part in dynamical encounters before their ejection/evaporation (Kruijssen, 2012).

A further difference between BBHs born in globular clusters and YSCs is the location of the mergers. About half of BBHs born in globular clusters are expected to merge inside the cluster (Banerjee, 2018b; Rodriguez et al., 2018; Samsing, 2018; Zevin et al., 2019b). In contrast, $\sim 97\%$ of our merging BBHs reach coalescence after they were ejected from the YSC, because of the low escape velocity and of the short lifetime of these systems. Hence, most BBHs born in YSCs merge in the galactic field and might represent a large fraction of field mergers.

4.5 Conclusions

We have investigated the formation of BBH mergers in young star clusters (YSCs) with different metallicity, from $Z = 0.0002$ to $Z = 0.02$, by means of N-body simulations, coupled with the binary population-synthesis code MOBSE (Giacobbo et al., 2018; Di Carlo et al., 2019). We probe two different density regimes for YSCs: dense clusters (set A, i.e. clusters with half mass radius following the Marks et al. 2012 relation, corresponding to a density $\rho_h \geq 3.4 \times 10^4 \text{ M}_\odot \text{ pc}^{-3}$) and loose clusters

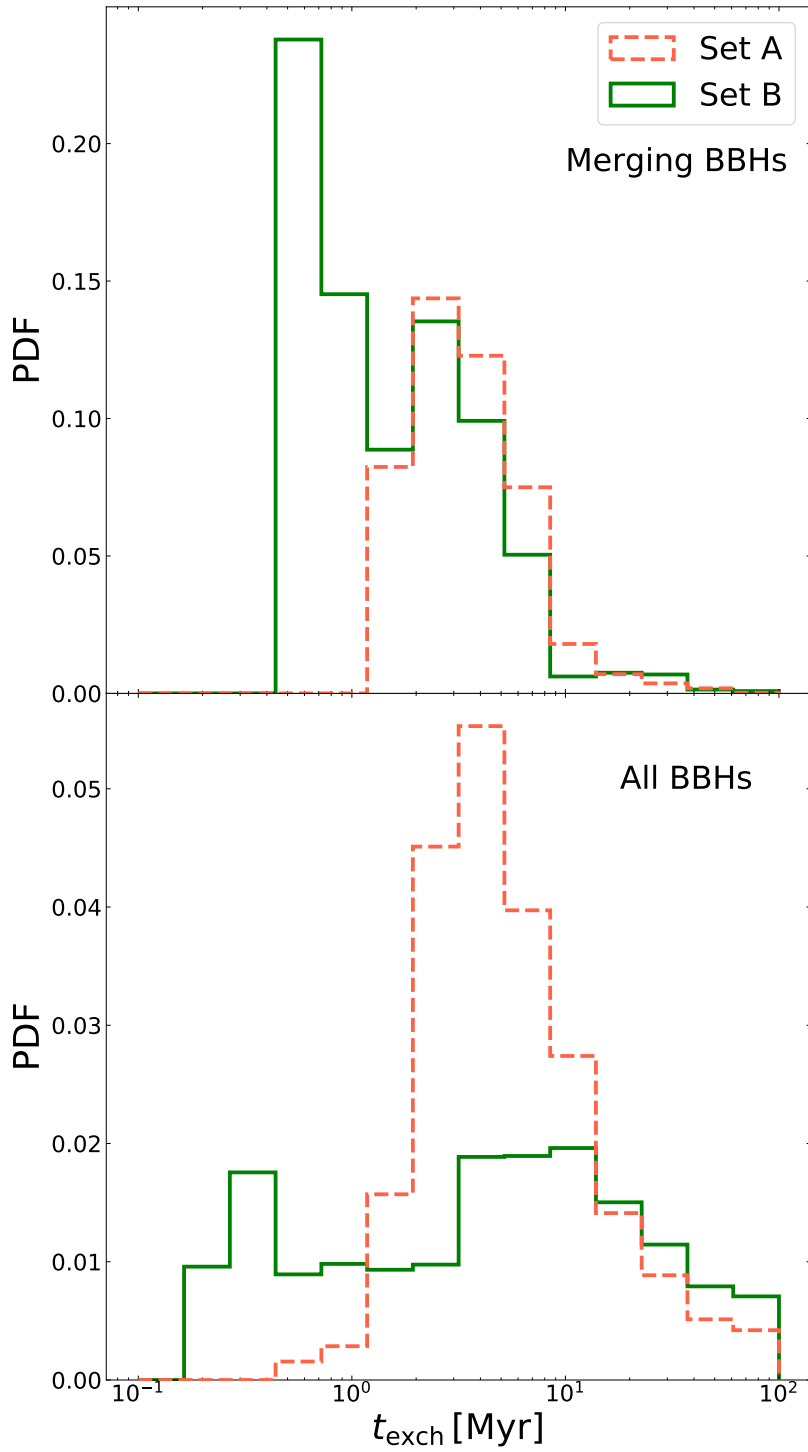


Figure 4.10: Time when the first exchange took place for exchanged BBHs in set A (orange dashed line) and set B (green solid line). Top panel: merging BBHs only. Bottom panel: all BBHs.

(set B, i.e. clusters with half-mass radius $r_h = 1.5$ pc, corresponding to a density $\rho_h \geq 1.5 \times 10^2 M_\odot \text{pc}^{-3}$, depending on star cluster mass).

We have shown that BHs and BBHs can reach higher masses at lower metallicity ($Z \leq 0.002$) with respect to solar metallicity (Fig. 4.2). In our simulations, we can form IMBHs as massive as $\sim 320 M_\odot$, through multiple stellar collisions. Stellar collisions also allow the formation of BHs with mass in the pair-instability mass gap (Di Carlo et al., 2020a) even at solar metallicity, although their incidence is much higher at low metallicity ($Z \leq 0.002$). We find that $\sim 6\%$ ($\sim 2\%$) of all BHs formed at $Z = 0.0002$ ($Z = 0.002$) have mass $m_{\text{BH}} > 60 M_\odot$, while at solar metallicity ($Z = 0.02$) the percentage is $< 1\%$ in both set A and B.

The mass function of BHs and BBHs does not show significant differences between loose clusters (set B) and dense clusters (set A). In particular, IMBHs form nearly with the same frequency in both loose and dense clusters.

We focus on the sub-sample of BBHs that merge within a Hubble time. About 60% of them come from original binaries (i.e. binary stars that are already there in the initial conditions), while the remaining $\sim 40\%$ form from dynamical exchanges. Exchanges in YSCs mostly involve stars before they collapse to BHs, because of the short core-collapse timescale of YSCs (< 3 Myr).

Exchanged BBH mergers reach higher total masses (up to $\sim 140 M_\odot$) than original and isolated BBH mergers (maximum total mass $\sim 80 M_\odot$, Fig. 4.3). The reason is that non-conservative mass transfer tends to reduce the maximum mass of BBH mergers in isolated and original binaries. Moreover, exchanged BBHs tend to have lower mass ratios ($q = m_2/m_1$) than original and isolated BBHs (Fig. 4.5).

In our models, the most massive event reported by the LVC in O1 and O2, GW170729 (Abbott et al., 2019b; Abbott et al., 2019a), can be explained only with dynamical BBHs: almost all of them are exchanged BBHs and come from metal-poor progenitors (Fig. 4.6). Even GW190412, the first unequal-mass BBH merger, can be explained only by BBHs born in YSCs: isolated binaries can hardly explain such extreme mass ratios, according to the models presented here.

The most massive BBH merger in our simulations has $m_{\text{TOT}} \sim 136 M_\odot$, primary mass $m_1 \sim 88 M_\odot$ and secondary mass $m_2 \sim 48 M_\odot$ (Table 4.4). The primary mass is inside the pair-instability mass gap and the total mass of the merger product classifies it as in IMBH. This system is more massive than all the O1 and O2 LVC BBHs, and has very similar characteristics to GW190521 (Abbott et al., 2020), the most massive BBH merger detected to date.

The merger efficiency (i.e. the number of mergers divided by the total simulated mass) is about two orders of magnitude higher for dynamical BBHs than for isolated

BBHs at solar metallicity (Fig. 4.9). The main reason is that dynamical encounters and hardening trigger the merger of BBHs even at high metallicity, where binary evolution is unlikely to produce mergers.

The main difference between loose and dense clusters is the merger efficiency. At low metallicity, the merger efficiency of loose clusters is a factor of ~ 5 lower than that of dense cluster, while at higher metallicity the merger efficiencies are comparable. Assuming that all the cosmic star formation rate takes place in YSCs, we find a local merger rate ~ 55 (~ 110) $\text{Gpc}^{-3} \text{yr}^{-1}$ in set A (set B), respectively. This shows that most BBH mergers might have originated in YSCs. Future studies will quantify the impact of YSCs on the total merger rate of BBHs, BHNSs and BNSs, based on the comparison with LVC observations.

INTERMEDIATE MASS BLACK HOLES IN YOUNG STAR CLUSTERS

Intermediate mass black holes (IMBHs) in the mass range $10^2 - 10^5 M_{\odot}$ bridge the gap between stellar black holes (BHs) and supermassive BHs. Here, we investigate the possibility that IMBHs form in young star clusters via runaway collisions and BH mergers. We analyze 10^4 simulations of dense young star clusters, featuring up-to-date stellar wind models and prescriptions for core collapse and (pulsational) pair instability. In our simulations, only 9 IMBHs out of 218 form via binary BH mergers, with a mass $\sim 100 - 140 M_{\odot}$. This channel is strongly suppressed by the low escape velocity of our star clusters. In contrast, IMBHs with masses up to $\sim 438 M_{\odot}$ efficiently form via runaway stellar collisions, especially at low metallicity. Up to $\sim 0.2\%$ of all the simulated BHs are IMBHs, depending on progenitor's metallicity. The runaway formation channel is strongly suppressed in metal-rich ($Z = 0.02$) star clusters, because of stellar winds. IMBHs are extremely efficient in pairing with other BHs: $\sim 70\%$ of them are members of a binary BH at the end of the simulations. However, we do not find any IMBH–BH merger. More massive star clusters are more efficient in forming IMBHs: $\sim 8\%$ ($\sim 1\%$) of the simulated clusters with initial mass $10^4 - 3 \times 10^4 M_{\odot}$ ($10^3 - 5 \times 10^3 M_{\odot}$) host at least one IMBH.

Based on:

Di Carlo, U. N., Mapelli M., Pasquato M., Rastello, S., Ballone A., Dall'Amico, M., Giacobbo N., Iorio, G., Spera M., Torniamenti S., Haardt F., MNRAS, 507, Issue 4, pp.5132-5143

5.1 Introduction

Intermediate-mass black holes (IMBHs), with mass in the range $10^2 - 10^5 M_{\odot}$, bridge the gap between stellar-sized black holes (BHs) and super-massive BHs. IMBHs might be the building blocks for super massive BHs in the early Universe (Madau and Rees, 2001), as suggested by the discovery of quasars at redshift as high as ~ 6 (e.g. Fan et al., 2001). Currently, we lack unambiguous evidence of IMBH existence from electromagnetic observations, but a number of potential candidates were proposed in the last decades. Several globular clusters, including 47 Tucanae (Kızıltan et al., 2017) and G1 (Gebhardt et al., 2005), have been claimed to host IMBHs, based on indirect dynamical evidences (Gerssen et al., 2002; Gebhardt et al., 2002; Anderson and van der Marel, 2010; van der Marel and Anderson, 2010; Lützgendorf et al., 2011; Lützgendorf et al., 2013; Miller-Jones et al., 2012; Nyland et al., 2012; Strader et al., 2012; Lanzoni et al., 2013; Baumgardt, 2017; Perera et al., 2017; Lin et al., 2018; Tremou et al., 2018; Baumgardt et al., 2019; Zocchi et al., 2019; Mann et al., 2019). The hyperluminous X-ray source HLX-1 in the galaxy ESO 243-49 (Farrell et al., 2009; Godet et al., 2014) is possibly the strongest IMBH candidate among ultra-luminous X-ray sources (e.g., Kaaret et al., 2001; Matsumoto et al., 2001; Strohmayer and Mushotzky, 2003; van der Marel, 2004; Miller and Colbert, 2004; Swartz et al., 2004; Mapelli et al., 2010; Feng and Soria, 2011; Sutton et al., 2012; Mezcua et al., 2015; Kaaret et al., 2017; Lin et al., 2020). Several BHs with mass $\sim 10^5 M_{\odot}$ might lurk in the nuclei of dwarf galaxies (Filippenko and Sargent, 1989; Filippenko and Ho, 2003; Barth et al., 2004; Greene and Ho, 2004; Greene and Ho, 2007; Seth et al., 2010; Dong et al., 2012; Kormendy and Ho, 2013; Baldassare et al., 2015; Reines and Volonteri, 2015; Mezcua et al., 2016; Mezcua et al., 2018; Reines et al., 2020). Finally, some candidates with mass $\sim 10^4 - 10^5 M_{\odot}$ may lie in high-velocity compact clouds (Tanaka, 2018; Takekawa et al., 2019; Takekawa et al., 2020). We point to Mezcua, 2017 and Greene et al., 2020 for two recent reviews.

The gravitational wave event GW190521 (Abbott et al., 2020; Abbott et al., 2020b), associated to the merger of a binary BH (BBH) with a total mass of $\sim 150 M_{\odot}$, recently provided strong evidence for IMBHs and paved the ground for further observations with current (Aasi et al. et al., 2015; Acernese et al., 2015) and future gravitational wave detectors (Amaro-Seoane et al., 2017b; Punturo et al., 2010; Reitze et al., 2019; Kalogera et al., 2019; Maggiore et al., 2020). Moreover, GW190521 confirms the merger formation scenario for IMBHs, where smaller BHs, likely of stellar origin, repeatedly merge in a dense environment, such as a star cluster (SC, Miller and Hamilton, 2002; McKernan et al., 2012; Giersz et al., 2015; Fishbach and

Holz, 2017; Gerosa and Berti, 2017; Gerosa and Berti, 2019; Rodriguez et al., 2019; Antonini et al., 2019b; Fragione et al., 2020; Arca Sedda et al., 2020; Mapelli et al., 2020a; Mapelli et al., 2021; Tagawa et al., 2021b; Tagawa et al., 2021a). Other possible formation scenarios are the collapse of very massive ($> 230 M_{\odot}$) metal-poor stars (Bond et al., 1984; Madau and Rees, 2001; Heger and Woosley, 2002; Schneider et al., 2002; Spera and Mapelli, 2017; Tanikawa et al., 2021), primordial IMBHs from gravitational instabilities in the early Universe (Kawaguchi et al., 2008; Carr et al., 2016; Raccanelli et al., 2016; Sasaki et al., 2016; Scelfo et al., 2018; Clesse and Garcia-Bellido, 2020; De Luca et al., 2021) and runaway collisions of stars in SCs (Colgate, 1967; Sanders, 1970; Portegies Zwart and McMillan, 2002; Portegies Zwart et al., 2004; Gürkan et al., 2004; Freitag et al., 2006a; Giersz et al., 2015; Mapelli, 2016; Kremer et al., 2020; Chon and Omukai, 2020; Rizzuto et al., 2021; Das et al., 2021).

Different formation channels may be at work in different environments (Volonteri, 2010), with SCs representing the ideal place both for repeated mergers of stellar-mass BHs (e.g., Miller and Hamilton, 2002) and for the formation of very massive stars through runaway collisions in the early stages of the cluster's evolution (e.g., Fujii and Portegies Zwart, 2013b). The internal dynamics of SCs is expected to play a key role in modulating the efficiency of the BBH merger scenario, with core collapse being closely tied to increased dynamical interactions (Spitzer, 1987; Goodman and Hut, 1989) and to the dynamical hardening of binary systems (Sugimoto and Bettwieser, 1983; Goodman and Hut, 1993; Trenti et al., 2007; Hurley and Shara, 2012; Beccari et al., 2019; Di Cintio et al., 2021). The main advantage of the repeated merger mechanism is that it works for the entire lifetime of a SC: the IMBH can assemble and grow as long as the SC survives (Giersz et al., 2015). However, a merger chain can come to an abrupt end if the BBH merger product is ejected from the SC due to gravitational-wave recoil (Merritt et al., 2004; Madau and Quataert, 2004; Holley-Bockelmann et al., 2008). The magnitude of such kick can largely exceed the escape velocity of the host SC (Favata et al., 2004; Lousto and Zlochower, 2011), thus the hierarchical build up of an IMBH via repeated BBH mergers is more likely to take place in the most massive SCs, like nuclear SCs, because of their large escape velocity (Antonini et al., 2019b; Fragione et al., 2020; Mapelli et al., 2021).

The runaway collision mechanism, on the other hand, can be effective even in less massive SCs, like young SCs. The most massive stars in a young SC are more likely to undergo collisions than lighter stars, because dynamical friction quickly brings them to the core (Gaburov et al., 2008). The high central density of young SCs, which is further enhanced in the first Myr due to gravothermal collapse, greatly

Table 5.1: Initial conditions.

Set	Z	N_{sim}	r_{h}	D	ref.
D2019HF	0.002	2000	M12	2.3	D19
D2019LF	0.002	2000	M12	1.6	D19
D2020A	0.02	1000	M12	1.6	D20
	0.002	1000	M12	1.6	D20
	0.0002	1000	M12	1.6	D20
D2020B	0.02	1000	1.5 pc	1.6	D20
	0.002	1000	1.5 pc	1.6	D20
	0.0002	1000	1.5 pc	1.6	D20

Column 1: name of the simulation set; column 2: metallicity Z ; column 3: number of runs performed per each set; column 4: half-mass radius r_{h} . M12 indicates that half-mass radii have been drawn according to Marks and Kroupa, 2012. Column 5: fractal dimension (D); column 6: reference for each simulation set. D19 and D20 correspond to and Di Carlo et al., 2020a, respectively.

favours stellar collisions (Freitag et al., 2006b; Portegies Zwart et al., 2010), which help to build up very massive stars that may collapse into IMBHs. The main issue is that very massive stars lose a conspicuous portion of their mass through stellar winds (e.g. Vink et al., 2011). The IMBH can form only if the star preserves enough mass, so this mechanism is more efficient at lower metallicity, where stellar winds are less powerful (Mapelli, 2016). Moreover, all the collisions need to take place before the massive stars in the SC turn into BHs, which happens in a few Myr.

Despite being less massive than globular clusters and nuclear SCs, young SCs make up the vast majority of SCs in the Universe (Kroupa and Boily, 2002), and their cumulative contribution to IMBH statistics may thus be significant. In this paper, we study the demography of IMBHs in young SCs through N -body simulations, including up-to-date stellar wind models and a treatment for (pulsational) pair instability in massive and very massive stars. We present a set of 10^4 state of the art direct N -body simulations with fractal initial conditions (to mimic the clumpiness of star forming regions, e.g. Goodwin and Whitworth, 2004) and with a large initial binary fraction ($f_{\text{bin}} = 1$ for stars with mass $> 5 M_{\odot}$).

5.2 Methods

The simulations discussed in this paper were performed using the same codes and methodology described in. We use the direct summation N -Body code NBODY6++GPU (Wang et al., 2015), which we coupled with the population synthe-

sis code MOBSE (Mapelli et al., 2017; Giacobbo et al., 2018). MOBSE includes up-to-date prescriptions for massive stellar winds (Giacobbo and Mapelli, 2018), electron-capture supernovae (Giacobbo and Mapelli, 2019), core-collapse supernovae (Fryer et al., 2012), natal kicks (Giacobbo and Mapelli, 2020) and (pulsational) pair instability supernovae (Mapelli et al., 2020b). Orbital decay induced by gravitational wave emission is treated as described in Peters, 1964. If a star merges with a BH or with a neutron star, MOBSE assumes that the entire mass of the star is lost by the system and not accreted by the compact object.

In this work, we have analyzed 10^4 simulations of young SCs; 4000 of them are the simulations presented in, while the remaining 6000 are the ones discussed in Di Carlo et al., 2020a. The initial conditions of the simulations are summarized in Table 5.1. Young SCs are asymmetric, clumpy systems. Thus, we model them with fractal initial conditions (Küpper et al., 2011), to mimic the clumpiness of star forming regions (Goodwin and Whitworth, 2004). The level of fractality is decided by the parameter D , where $D = 3$ means homogeneous distribution of stars. In this work, we assume $D = 1.6$ in most of our simulations (8000 runs). We also probe a lower degree of fractality ($D = 2.3$) in the remaining 2000 runs. The total initial mass M_{SC} of each SC ranges from $10^3 M_{\odot}$ to $3 \times 10^4 M_{\odot}$ and it is drawn from a distribution $dN/dM_{\text{SC}} \propto M_{\text{SC}}^{-2}$, as the SC initial mass function described in Lada and Lada, 2003. Thus, the mass distribution of our simulated SCs mimics the mass distribution of SCs in Milky Way-like galaxies. We choose the initial half-mass radius r_{h} according to Marks and Kroupa, 2012 in 7000 simulations, and we adopt a fixed value $r_{\text{h}} = 1.5$ pc for the remaining 3000 simulations. These different choices of r_{h} have a strong impact on the density of the SCs, as shown in Figure 5.1.

We generated the initial conditions with MCLUSTER (Küpper et al., 2011). The initial masses of the stars follow a Kroupa, 2001 initial mass function, with minimum mass $0.1 M_{\odot}$ and maximum mass $150 M_{\odot}$. We set an initial total binary fraction of $f_{\text{bin}} = 0.4$. Since MCLUSTER pairs up the most massive primary stars first, according to a distribution $\mathcal{P}(q) \propto q^{-0.1}$ (where $q = m_2/m_1 \in [0.1, 1]$, Sana et al. 2012), all the stars with mass $m \geq 5 M_{\odot}$ are members of binary systems, while stars with mass $m < 5 M_{\odot}$ are randomly paired until a total binary fraction $f_{\text{bin}} = 0.4$ is reached. This procedure results in a mass-dependent initial binary fraction consistent with the multiplicity properties of O/B-type stars (Sana et al. 2012; Moe and Di Stefano 2017). The orbital periods and eccentricities are also drawn from the distributions described in Sana et al., 2012¹.

¹The same binary properties could have been obtained using the binary eigen-evolution and mass-feeding method described in Belloni et al., 2018.

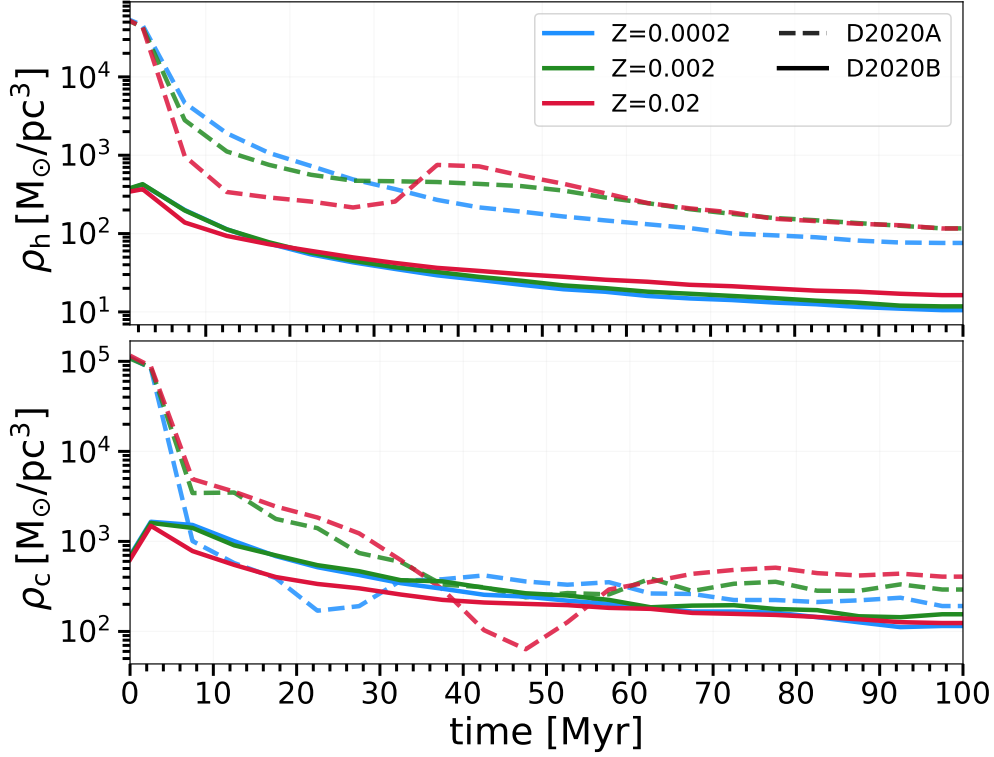


Figure 5.1: Evolution of the median of the mass density at the half mass radius (ρ_h , top panel) and at the core radius (ρ_c , bottom panel) for the SCs in sets D2020A (r_h from Marks and Kroupa 2012, dashed lines) and D2020B ($r_h = 1.5$ pc, solid lines) at different metallicities.

We simulate SCs with three different metallicities: $Z = 0.0002$, 0.002 and 0.02 (approximately $1/100$, $1/10$ and $1 Z_\odot$, assuming $Z_\odot = 0.02$ from Anders and Grevesse 1989). Each SC is simulated for 100 Myr in a solar neighbourhood-like static external tidal field (Wang et al., 2016). At 100 Myr, we extract the BBHs which are still present in our simulations and we integrate their semi-major axis and eccentricity evolution by gravitational wave emission up to a Hubble time (13.6 Gyr), according to Peters, 1964.

The main differences between the simulations in and Di Carlo et al., 2020a are the efficiency of common envelope ejection ($\alpha = 3$ in and $\alpha = 5$ in Di Carlo et al. 2020a), and the chosen model of core-collapse supernova (the rapid and the delayed models from Fryer et al. 2012 are adopted in and in Di Carlo et al. 2020a, respectively). The population of IMBHs is not strongly affected by these differences. We divide the simulations in four different sets whose names and properties are shown in Table 5.1. We refer to and Di Carlo et al., 2020a for further details on the code and on the simulations.

Table 5.2: Percentage of SCs that form 0, 1 and 2 IMBHs per different metallicity, initial SC mass and simulation set.

Set	0 IMBHs	1 IMBH	2 IMBHs
All	97.97 %	1.97 %	0.06 %
$Z = 0.02$	99.85 %	0.15 %	0 %
$Z = 0.002$	97.81 %	2.17 %	0.02 %
$Z = 0.0002$	96.5 %	3.25 %	0.25 %
$10^3 \leq M_{\text{SC}}/M_{\odot} < 5 \times 10^3$	99.01 %	0.99 %	0 %
$5 \times 10^3 \leq M_{\text{SC}}/M_{\odot} < 10^4$	95.73 %	4.12 %	0.15 %
$10^4 \leq M_{\text{SC}}/M_{\odot} \leq 3 \times 10^4$	92.13 %	7.42 %	0.45 %
D2019HF	96.90 %	3.05 %	0.05 %
D2019LF	98.2 %	1.80 %	0.0 %
D2020A	98.03 %	1.94 %	0.03 %
D2020B	98.47 %	1.40 %	0.13 %

Column 1: Simulation set; column 2: percentage of SCs that form no IMBHs; column 3: percentage of SCs that form 1 IMBH; column 4: percentage of SCs that form 2 IMBHs.

5.3 Results

5.3.1 Formation of IMBHs

We find a total of 218 IMBHs, which make up only $\sim 0.2\%$ of all the BHs formed in our simulations. The formation of IMBHs is a rare event in our simulations: as shown in Table 5.2, only 1.97% of all the simulated SCs form one IMBH, and only 0.06% of them form two IMBHs. The vast majority of the simulated IMBHs (209) form via the runaway collision mechanism, while only 9 IMBHs form via BBH merger. This is expected, because the low escape velocity ($\lesssim 10 \text{ km s}^{-1}$) of our simulated SCs makes the BBH merger scenario less efficient.

Figure 5.2 shows the masses of all the formed IMBHs for each metallicity. IMBHs form with mass up to $\sim 438 M_{\odot}$, but $\sim 78\%$ of all the formed IMBHs has a mass between $100 M_{\odot}$ and $150 M_{\odot}$. Less massive IMBHs are more likely to form. A schematic formation history of the most massive IMBH is shown in Figure 5.3; this IMBH forms via runaway collision: a total of 10 stars participate to the formation of a very massive star which promptly undergoes direct collapse to form the IMBH. All the other IMBHs which form via runaway collision follow a similar pattern, involving multiple stellar mergers in the first few Myr of our simulations. The mass evolution of three stars which end up forming an IMBH is shown in Figure 5.4. We see that mass growth via stellar mergers overcomes stellar wind mass loss. The for-

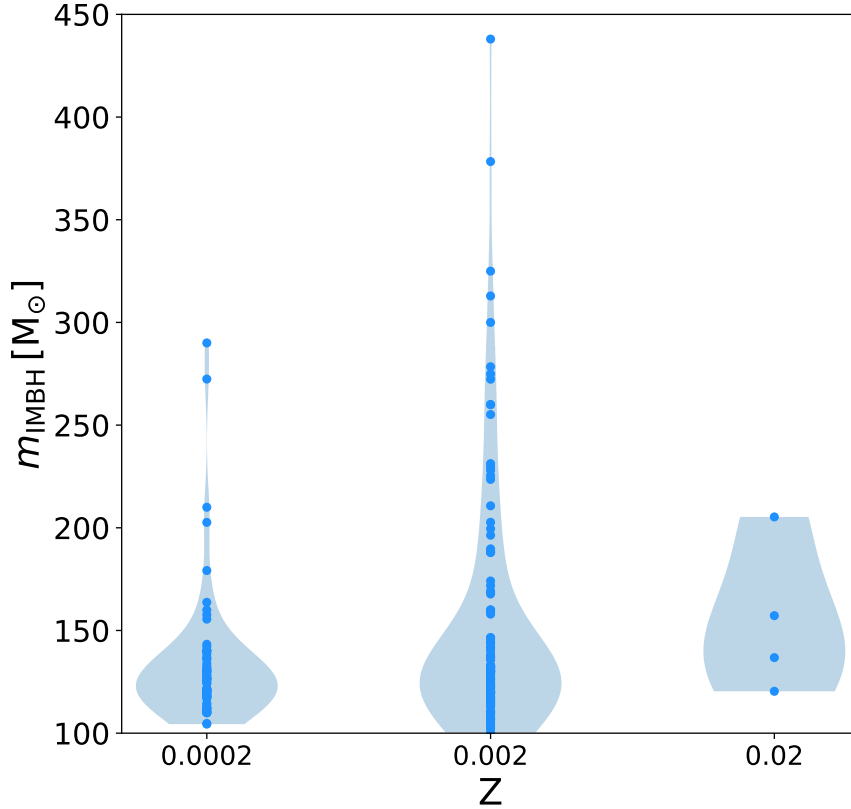


Figure 5.2: Distributions of IMBH masses for each metallicity. Blue filled circles mark the values of the masses, while the horizontal extent of each light blue region (violin plot) is proportional to the number of IMBHs at a given mass value.

mation of the IMBHs via runaway collision always occurs within the first ~ 5 Myr from the beginning of the simulation.

As expected, IMBH formation is much less efficient at higher metallicity because stellar winds are more powerful; only four IMBHs form at solar metallicity. The fraction of IMBHs with respect to the total number of BHs per each metallicity is $\sim 0.4\%$, $\sim 0.2\%$ and $\sim 0.02\%$ for $Z = 0.0002$, 0.002 and 0.02 , respectively. Table 5.2 shows that the percentage of simulated SCs which form at least one IMBH grows as the metallicity decreases, going from 0.15% at $Z = 0.02$ to 3.5% at $Z = 0.0002$. We obtained a larger absolute number of IMBHs at metallicity $Z = 0.002$ (Fig. 5.2), only because we ran three times more simulations with $Z = 0.002$ than with either $Z = 0.02$ or $Z = 0.0002$ (Table 5.1). We performed several statistical tests to check if the fact that the most massive IMBHs form at $Z = 0.002$ is statistically significant or is just another effect of the larger number of simulation at this metallicity. Our tests suggest that intermediate-metallicity SCs (with $Z = 0.002 = 0.1 Z_{\odot}$) tend to form more massive IMBHs than metal-poor SCs (with $Z = 0.0002 = 0.01 Z_{\odot}$), even if there

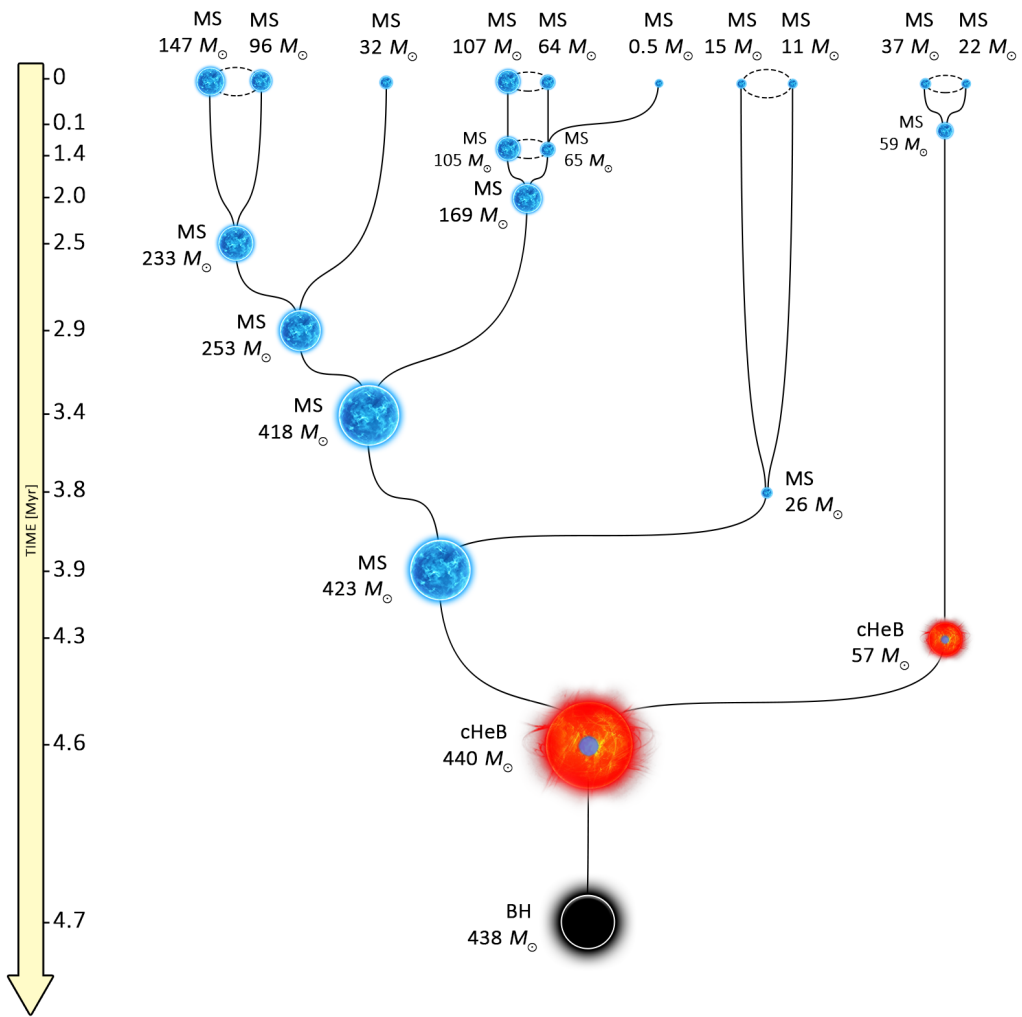


Figure 5.3: Formation history of the most massive IMBH found in our simulations. Main sequence stars (with label MS) are represented as blue stars; core helium burning stars (label cHeB) are visualized as red stars with a blue core; black holes (label BH) are shown as black circles. The mass of each object is shown next to them. The time axis and the size of the objects are not to scale. The formation of this IMBH takes place in a SC with metallicity $Z = 0.002$.

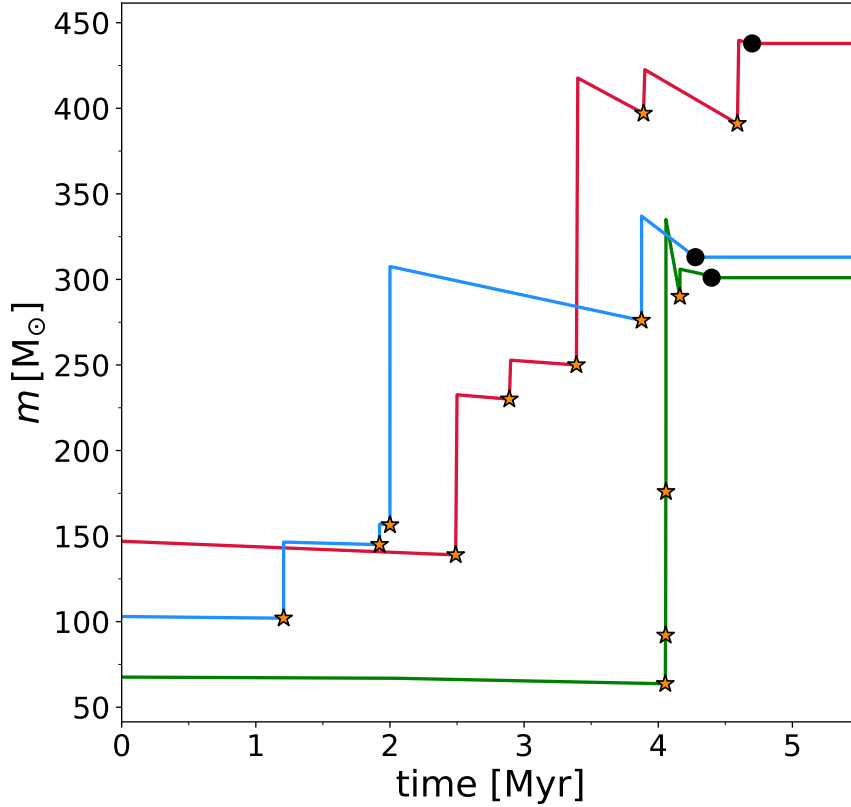


Figure 5.4: Mass evolution of three stars which end up forming an IMBH. The yellow stars mark stellar mergers. The black filled circles indicate the moment when the IMBH form.

is no conclusive evidence for this result (see Appendix 5.6 for details). This possible difference could be interpreted as the interplay between relatively inefficient mass loss and large maximum stellar radii (Chen et al., 2015): at $Z = 0.002$ stellar winds are still rather inefficient (as for lower metallicity), but massive stars can develop very large radii (in the terminal-age main sequence and the giant phase), enhancing the probability of collisions with other stars.

5.3.2 Distance from centre of mass

Figure 5.5 shows the evolution of the median distance of the IMBHs with respect to the centre of mass of the host SCs. In order to undergo a sufficient number of stellar mergers, we expect the progenitor stars of IMBHs to lie in the densest central regions of the SC. In our simulations, we find that this is not completely the case: IMBH progenitors (i.e. before $t \sim 5$ Myr) tend to lie outside the 10% Lagrangian radius. This is likely a consequence of the fractal initial conditions, because the IMBH formation may take place in a clump far away from the centre of mass of the

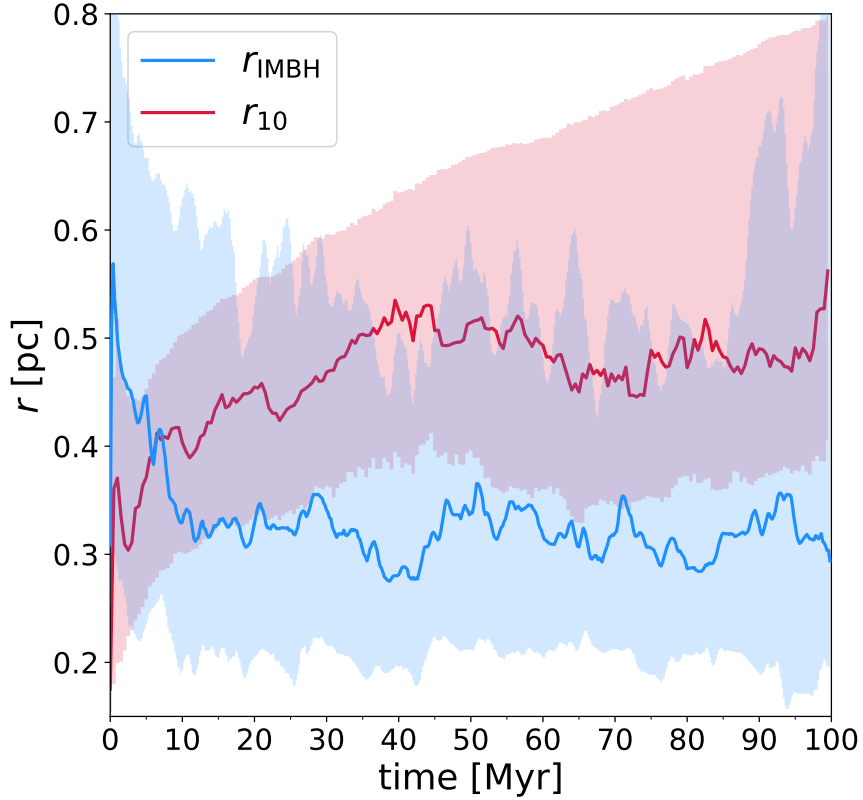


Figure 5.5: Evolution of the distance of an IMBH from the centre of mass of its host SC (r_{IMBH}). The blue line shows the median of the values of r_{IMBH} , while the red line is the median of the 10% Lagrangian radii (r_{10}) of the host SCs. The filled areas represent the 25th–75th percentile confidence intervals. Only IMBHs which do not escape from their host SC are shown in this Figure. A simple moving average over 5 time-steps has been performed to filter out statistical fluctuations.

SC, before the mergers between the clumps take place. After the IMBHs form, they tend to rapidly sink towards the centre of the SC and to remain there until the end of the simulation.

5.3.3 Escaped IMBHs

Figure 5.5 shows only IMBHs which do not escape from their host SC. In our simulations, particles escape from the SC when their distance from the center of mass becomes larger than twice the tidal radius. We find that $\sim 54\%$ of all the formed IMBHs are ejected or evaporate from the SC in the first 100 Myr. The percentage of IMBHs with mass $m_{\text{IMBH}} < 150 M_{\odot}$ that escape from their host SC is $\sim 57.0\%$, and only $\sim 31.8\%$ for IMBHs with $m_{\text{IMBH}} \geq 150 M_{\odot}$. This means that the most massive IMBHs are more likely to be retained inside their host SC.

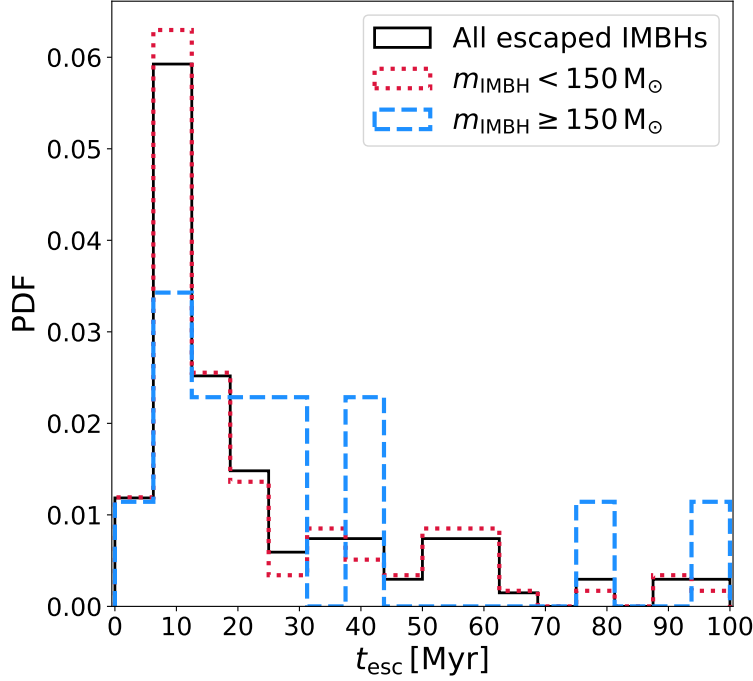


Figure 5.6: Probability distribution function of the escape time t_{esc} of IMBHs. All the ejected IMBHs are shown by the solid black line. IMBHs with mass $m_{\text{IMBH}} < 150 M_{\odot}$ are shown by the dotted red line, while IMBHs with mass $m_{\text{IMBH}} \geq 150 M_{\odot}$ are shown by the dashed blue line.

Figure 5.6 shows the distribution of the escape times t_{esc} of ejected IMBHs. All IMBHs and especially the less massive ones tend to be ejected within the first 25 Myr, with a strong peak between 5 and 15 Myr. More massive IMBHs tend to escape at later times with respect to the less massive ones. Figure 5.7 distinguishes between IMBHs that formed in SCs with initial mass smaller and larger than $5 \times 10^3 M_{\odot}$. Both distributions peak around 10 Myr, but all the ejected IMBHs which form in the less massive SCs escape within the first 40 Myr, while IMBHs born in more massive SCs may escape at later times.

We find that the percentages of escaped IMBHs which form in SCs with initial mass $M_{\text{SC}} < 5000 M_{\odot}$ and $M_{\text{SC}} \geq 5000 M_{\odot}$ are 37.7% and 59.8%, respectively. This means that IMBHs are more likely to be ejected from more massive SCs. This may seem surprising, because we expect more massive SCs to retain more IMBHs due to their larger escape velocities. Massive SCs, however, have denser cores where dynamical interactions that may eject IMBHs are more frequent.

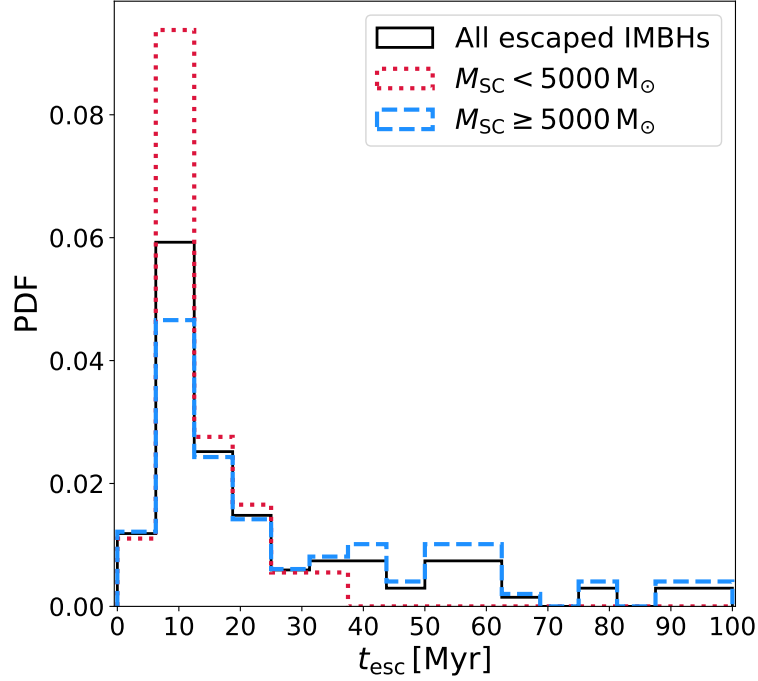


Figure 5.7: Probability distribution function of the escape time t_{esc} of the IMBHs. All the ejected IMBHs are shown by the solid black line. IMBHs formed in SCs with mass $M_{\text{SC}} < 5000 M_{\odot}$ are shown by the dotted red line, while IMBHs formed in SCs with mass $M_{\text{SC}} \geq 5000 M_{\odot}$ are shown by the dashed blue line.

5.3.4 IMBHs in binary systems

IMBHs are the most massive objects which form in our simulations, and therefore they are likely to interact with other stars and form binary systems (Blecha et al., 2006; MacLeod et al., 2016). In our simulations, IMBHs spend $\sim 85\%$ of the time, on average, being part of a binary or triple system. Figure 5.8 shows the evolution of the companion mass m_{comp} , orbital eccentricity e and semi-major axis a for the five most massive IMBHs that form in our simulations. All these five massive IMBHs spend almost all their time in binary systems, except for one of them, which is ejected from the SC after ~ 10 Myr.

These binaries are subject to continuous dynamical interactions which perturb their orbital properties. Eccentricity wildly oscillates and tends to assume values between 0.6 and 0.9 (Figure 5.8). Each variation of eccentricity corresponds to a smaller variation of the semi-major axis, which tends to shrink over time. At the end of the simulation, two of the IMBHs shown in Figure 5.8 are still members of a binary system with a companion BH. We have re-simulated the host SCs of these IMBHs for up to 1 Gyr to check for possible mergers, but none of these binary sys-

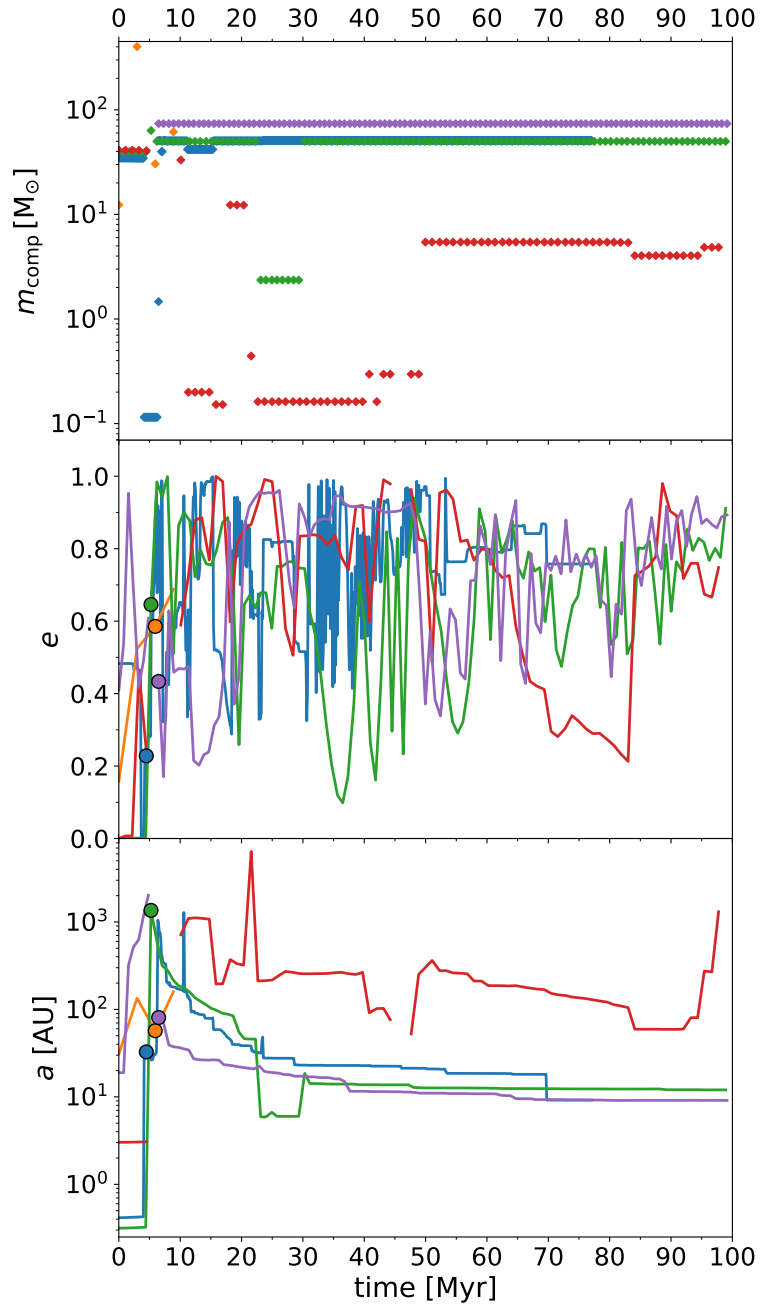


Figure 5.8: Evolution of the mass of the IMBH companion m_{comp} (upper panel), eccentricity e (middle panel) and semi-major axis a (lower panel) of the binaries which contain the five most massive IMBHs formed in our simulations. Coloured filled circles represent the formation time of the IMBH, i.e. the time when the progenitor star becomes an IMBH. The red circle is missing because the progenitor of this IMBH is single when it collapses to a BH.

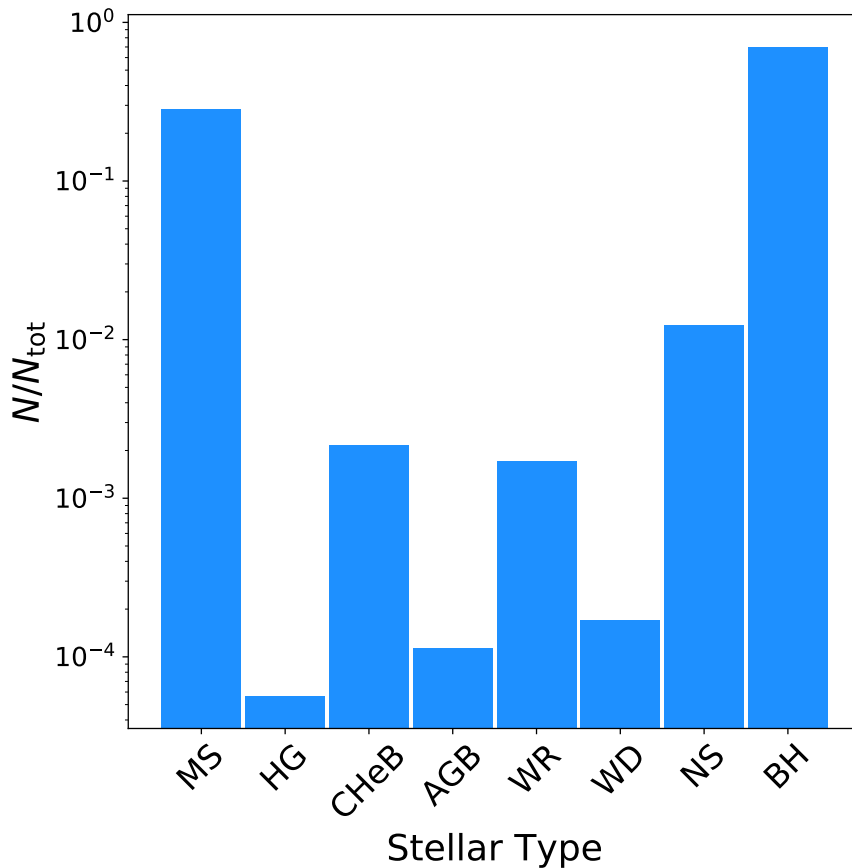


Figure 5.9: Distribution of the stellar types of the companions of all the simulated IMBHs throughout the entire simulation (0 – 100 Myr). The values on the y -axis are normalized to the total number of companions N_{tot} . The represented stellar types are: main sequence (MS); Hertzsprung gap (HG); core helium burning (CHeB); asymptotic giant branch (AGB); Wolf-Rayet (WR); white dwarf (WD); neutron star (NS) and black hole (BH).

tems does merge².

The simulated IMBHs tend to couple with other massive members of the SC, because dynamical exchanges generally lead to the build up of more and more massive binaries (Hills and Fullerton, 1980). Figure 5.9 shows the distribution of the stellar types of the IMBH’s companions. Besides main sequence stars, which are the most common stellar type in the simulated SCs, the most common binary companions of IMBHs are BHs and neutron stars.

²NBODY6++GPU does not include a treatment for post-Newtonian terms. We cannot exclude the possibility that dynamical interactions combined with a treatment of post-Newtonian terms might allow the merger of some of our IMBH–BH binaries.

5.3.4.1 IMBH–BH binaries

We analyze the properties of all BBHs which host at least one IMBH in our simulations (hereafter, IMBH–BH binaries). From Figure 5.9, it is apparent that IMBHs are extremely efficient in finding a companion BH: $\sim 70\%$ of all IMBHs reside in a BBH at the end of the simulations. Figure 5.10 shows the total mass of the binaries $M_{\text{tot}} = m_1 + m_2$ as a function of the mass ratio $q = m_2/m_1$ (with $m_2 \leq m_1$) of all the IMBH–BH systems. The binary with the smallest mass ratio has $q \sim 0.04$ and secondary mass $m_2 \sim 4.2 M_\odot$. The most massive IMBH–BH binary has masses $m_1 \sim 438 M_\odot$ and $m_2 \sim 50 M_\odot$. Values of the mass ratio $q \lesssim 0.6$ are the most likely ones, but we find some binaries with q up to ~ 0.99 . Overall, the IMBH–BH binaries have lower mass ratios than other BBHs (see Figure 5 of Di Carlo et al. 2020b, where we show that the vast majority of BBHs in young SCs have $q \sim 0.9 - 1$). This is expected, because SCs with more than one IMBH are very rare, and IMBHs can thus couple only with lower mass BHs.

We find no mergers of IMBH–BH binaries in our simulations. Adding post-Newtonian terms to our simulations might enhance the chances of IMBH–BH merger during resonant encounters (e.g., Samsing, 2018; Zevin et al., 2019b; Kremer et al., 2019). However, our SCs are relatively small and disrupt quickly, so that these binaries do not have enough time to harden via dynamical interactions. Mergers of BBHs with at least one IMBH component seem to be extremely rare events even in much more massive SCs (e.g., Kremer et al., 2020).

We find only one binary composed of two IMBHs (hereafter, binary IMBH), with masses $m_1 \sim 113 M_\odot$ and $m_2 \sim 114 M_\odot$. Its formation history is shown in Figure 5.11. First, two massive BHs of $m_1 \sim 113 M_\odot$ and $m_a \sim 57 M_\odot$, which formed via runaway collision, dynamically couple and form a BBH. Then, a third BH of mass $m_b \sim 57 M_\odot$ perturbs the BBH and in the process merges with the secondary BH of the binary, forming the binary IMBH. The formation of this binary involves both the runaway collision and the BBH merger mechanisms.

In our simulations, we do not include relativistic kicks. Were they included, they might have split this binary IMBH at birth. Thus, we calculated a posteriori the relativistic kick induced by the merger of two BHs with $m_a = m_b = 57.4 M_\odot$, according to the formulas presented in Maggiore, 2018. To calculate the kick, we randomly drew the spin magnitudes of the two BHs from a Maxwellian distribution with $\sigma = 0.1$ and the spin directions as isotropically distributed over the sphere (see, e.g., Bouffanais et al. 2021 for a discussion of these assumptions). We repeated the calculation of the kick 10^5 times for different random draws of the spin magnitudes and

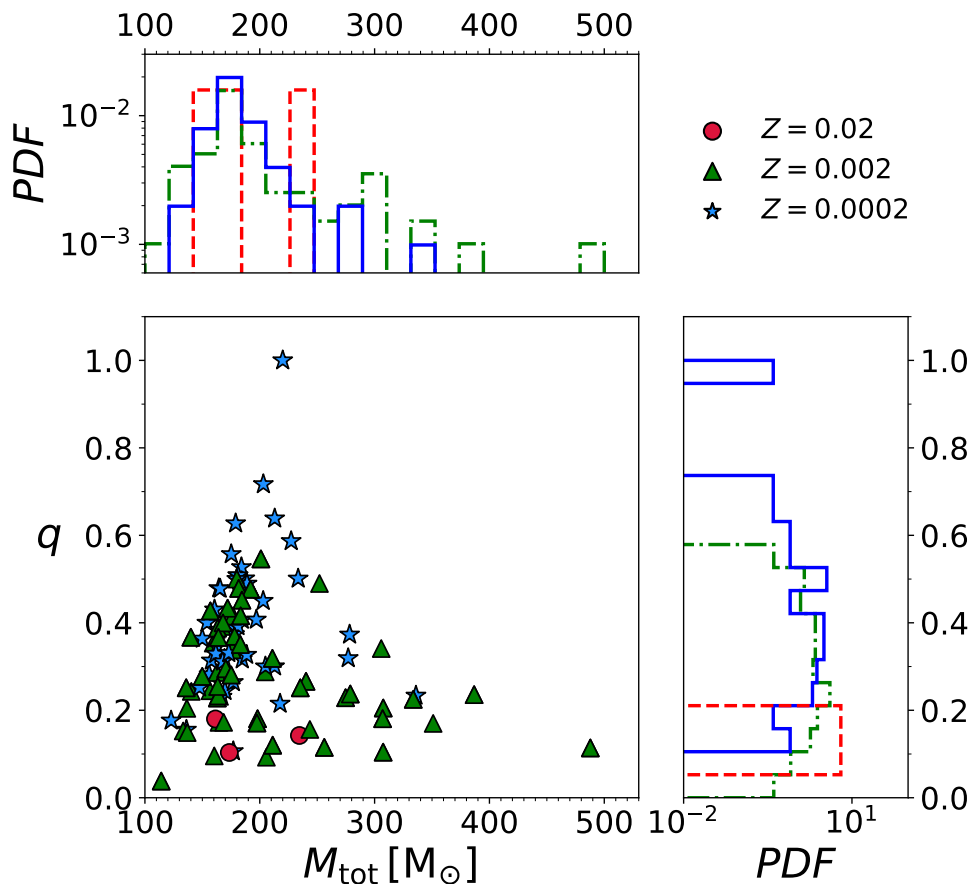


Figure 5.10: Mass ratio $q = m_2/m_1$ versus total mass $M_{\text{tot}} = m_1 + m_2$ of IMBH–BH binaries. Circles, triangles and stars refer to $Z = 0.02$, 0.002 and 0.0002 , respectively. The marginal histograms show the distribution of q (on the y -axis) and M_{tot} (on the x -axis). Solid blue, dot-dashed green and dashed red histograms refer to $Z = 0.0002$, 0.002 and 0.02 , respectively.

tilts. We then calculated the probability that the binary system composed of the merger remnant and of the third BH with mass $m_1 = 113 M_\odot$ remains bound after the relativistic kick. We calculate the mass of the merger remnant from Jiménez-Forteza et al., 2017, yielding $m_{\text{rem}} \sim 109 M_\odot$. To estimate the orbital properties of the binary IMBH with masses m_1 and m_{rem} we start from an eccentricity $e = 0.5$ and a semi-major axis $a = 75.5 \text{ AU}$, which are the values given by NBODY6++GPU at the time of the merger between m_a and m_b , and we calculate the final semi-major axis and eccentricity (after the relativistic kick) following the equations detailed in the Appendix A of Hurley et al., 2002. We find that the binary IMBH remains bound in $\sim 38\%$ of our random realizations. If the kicks are drawn from a Maxwellian distribution with $\sigma = 0.01$ (very small kicks, as predicted by Fuller et al. 2019), the binary IMBH remains bound in $\sim 98\%$ of the random realizations. The relativistic kick even favours the merger of the final binary IMBH in a few realizations ($\sim 0.05\%$).

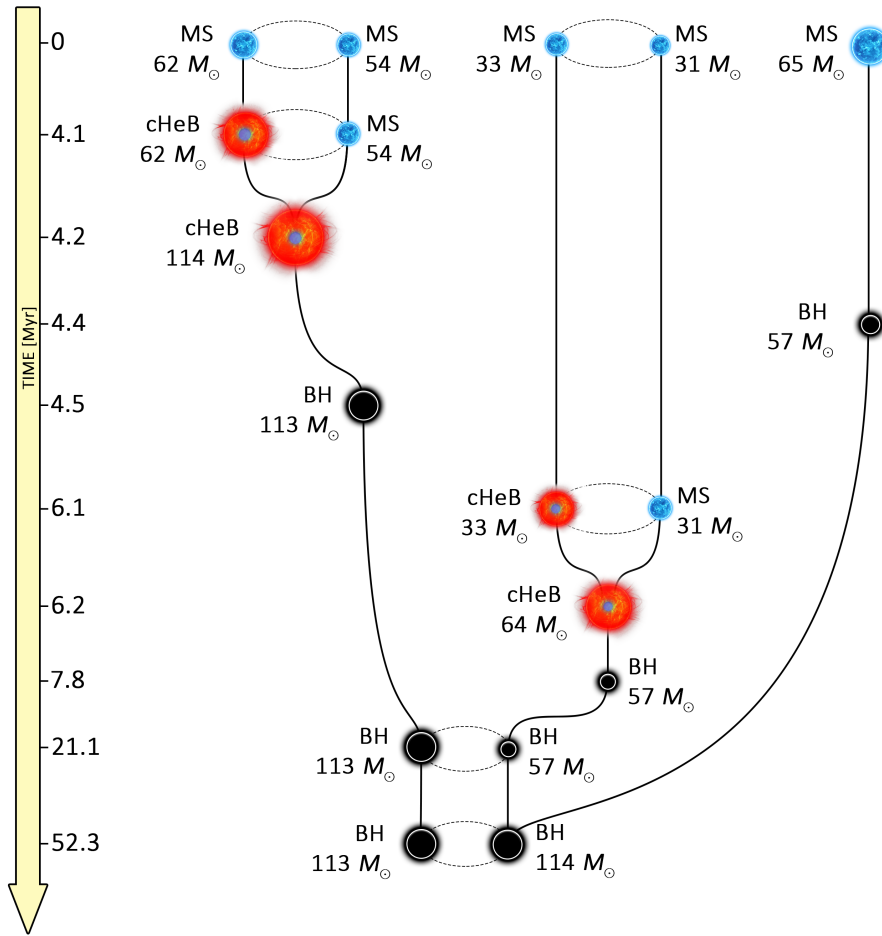


Figure 5.11: Formation history of the binary IMBH found in our simulations. Main sequence stars (with label MS) are represented as blue stars; core helium burning stars (label cHeB) are visualized as red stars with a blue core; black holes (label BH) are shown as black circles. The mass of each object is shown next to them. The time axis and the size of the objects are not to scale.

5.3.5 Properties of the host SCs

The presence of an IMBH may influence the evolution and the characteristics of the host SC (Mastrobuono-Battisti et al., 2014; Bianchini et al., 2015; Arca-Sedda, 2016; Askar et al., 2017b). Finding possible signatures of the presence of an IMBH in SCs may help us to understand whether observed SCs host or not an IMBH.

5.3.5.1 SC mass

Figure 5.12 shows the initial mass of the host SC as a function of the mass of the IMBH. The most massive IMBHs form preferentially in massive SCs. From the marginal histogram which shows the distribution of M_{SC} , it may seem that IMBHs are slightly more numerous in small SCs. However, since we adopted a mass function $dN/dM_{\text{SC}} \propto M_{\text{SC}}^{-2}$, we simulated many more small SCs than massive ones. As confirmed by Table 5.2, IMBHs form more efficiently in massive SCs where stellar collisions are more effective. For example, IMBHs form in $\sim 8\%$ of the SCs with $10^4 M_{\odot} \leq M_{\text{SC}} \leq 3 \times 10^4 M_{\odot}$ and only in $\lesssim 1\%$ of the SCs with $10^3 M_{\odot} \leq M_{\text{SC}} < 5 \times 10^3 M_{\odot}$. In our simulations, IMBHs at solar metallicity form only in SCs with mass $\gtrsim 20500 M_{\odot}$. This feature may also be an effect of the fact that more massive SCs statistically tend to have more massive stars. For example, the median of the maximum initial stellar masses for SCs of mass 10^3 , 2.5×10^3 , 5×10^3 , 10^4 and $3 \times 10^4 M_{\odot}$ is 54, 84, 108, 125 and 140 M_{\odot} respectively.

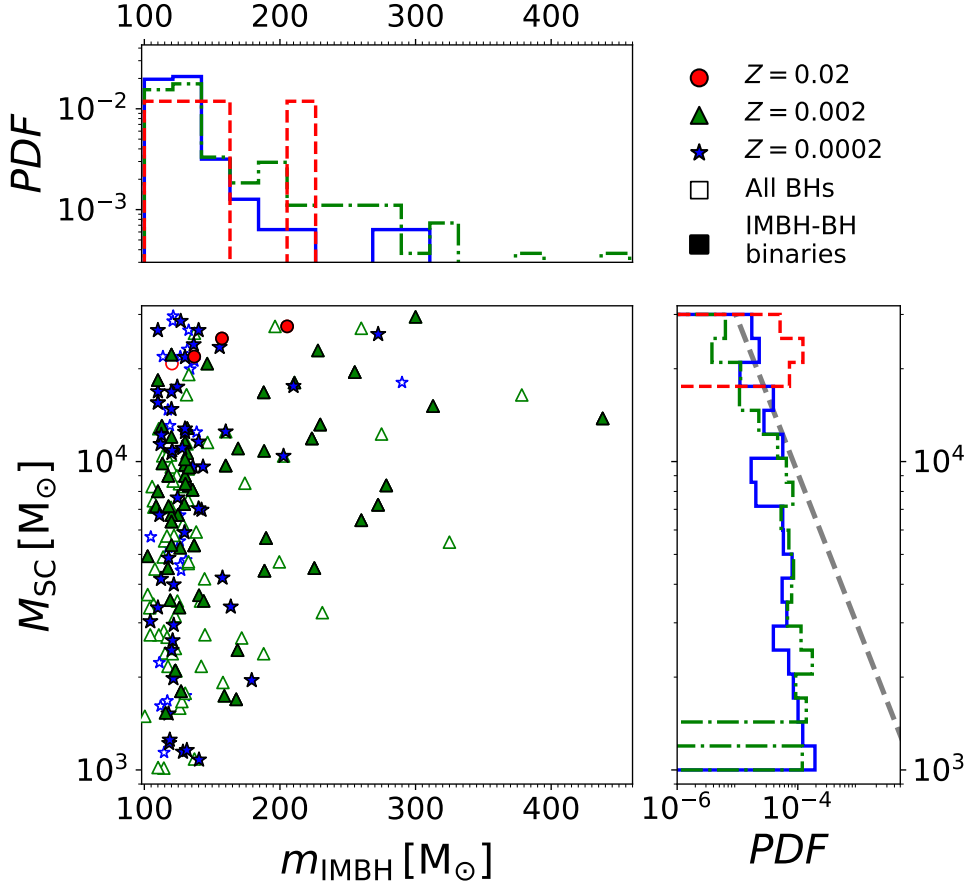


Figure 5.12: Mass of the host SC (M_{SC}) versus the mass of the IMBH (m_{IMBH}). The marginal histograms show the distribution of M_{SC} (y -axis) and m_{IMBH} (x -axis). The filled symbols refer to IMBHs in IMBH–BH binaries, while the open symbols are single BHs. The solid blue, dot-dashed green and dashed red colors refer to $Z = 0.0002$, 0.002 and 0.02 , respectively. The grey dashed line shows the initial mass function of SCs ($dN/dM_{\text{SC}} \propto M_{\text{SC}}^{-2}$).

5.3.5.2 Fractality and initial half mass radius

In Figure 5.13, we compare the IMBH mass distribution of different simulation sets. Simulations with low fractality (D2019LF) produce more massive IMBHs than high fractality ones (D2019HF). From Table 5.2, however, we see that the D2019HF set is more efficient than D2019LF in producing IMBHs. This means that high fractality helps to produce a larger number of IMBHs, but with lower mass. This happens because SCs with high fractality are composed of smaller and denser clumps (with a shorter two-body relaxation timescale), where stellar collisions are more likely to occur. On the one hand, this increases their efficiency in forming IMBHs. On the other hand, a small clump does not host many massive stars (in our high-fractality SCs, a single clump may host up to two massive stars at most). Hence, in order to have a runaway collision of massive stars and to form a more massive IMBH, it is

necessary that more clumps merge together before the death of their massive stars. In the high-fractality case, the various clumps merge together over a timescale similar or longer than the IMBH formation timescale. While it is easier to form a small IMBH in a single clump, stars from more clumps may be needed to form higher mass IMBHs.

In contrast, low fractality SCs are more similar to monolithic SCs and have a longer two-body relaxation timescale. This means that the runaway collisions will begin later, involving all the massive stars of the SC. On the one hand, the mass of the collision product will not be limited by the mass of the clump, allowing the formation of more massive IMBHs. On the other hand, since the collisions start later, massive stars may die before assembling a sufficiently massive star. This makes low fractality SCs less efficient in forming IMBHs.

We now compare sets D2020A and D2020B in Figure 5.13 and in Table 5.2. The SCs in D2020A have a smaller initial half-mass radius than in D2020B, but they both have the same degree of fractality ($D = 1.6$). This means that the clumps will have approximately the same number of stars, but different densities. As shown in Figure 5.1, the SCs in D2020A have a larger core density in the first ~ 8 Myr, when the runaway collisions take place. Because of this higher initial density, set D2020A is more efficient in forming IMBHs, but the IMBH mass distributions are comparable.

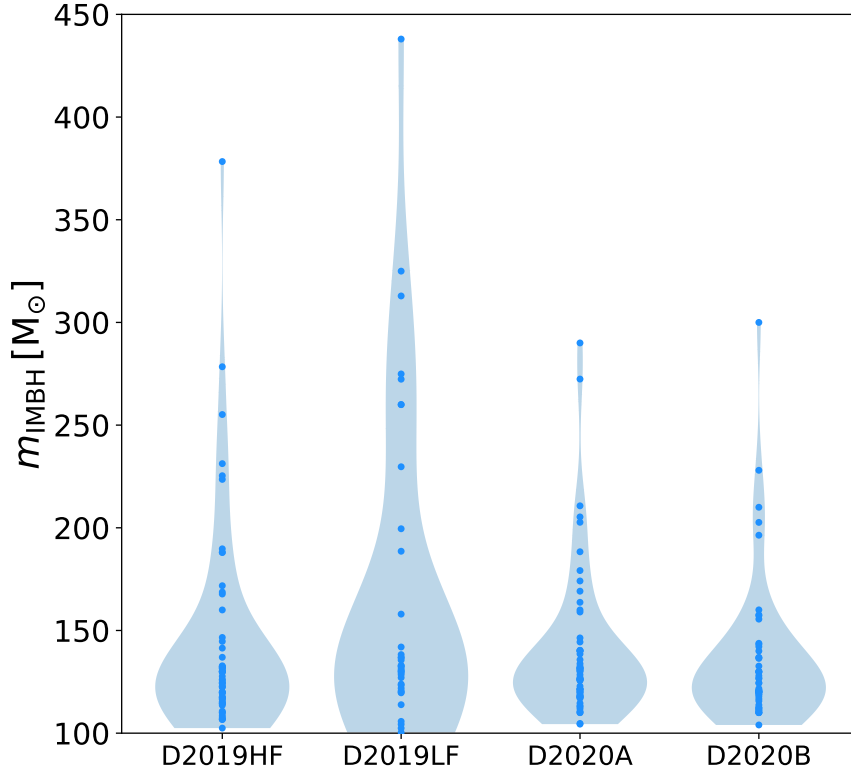


Figure 5.13: Distributions of IMBH masses for the different simulation sets. Blue filled circles mark the values of the masses, while the horizontal extent of each light blue region (violin plot) is proportional to the number of IMBHs at a given mass value. We refer to Table 5.1 for details on the different sets.

5.3.5.3 SC radii

We check if the presence of an IMBH affects the evolution of the Lagrangian radii of the simulated SCs. Figure 5.14 shows the evolution of the 10%, 30%, 50% and 70% Lagrangian radii of SCs with and without IMBHs. The SCs with IMBHs expand more rapidly in the first few Myrs than the SCs without IMBHs. Higher Lagrangian radii expand more, meaning that the expansion is stronger in the outer regions of the SC. This effect is a consequence of IMBH dynamics: the IMBH heats the SC, scattering stars to less bound orbits and making the cluster expand (Baumgardt et al., 2004b). After the initial expansion, the radii of the SCs with IMBHs flatten out. After ~ 65 Myr, the 10% Lagrangian radii (r_{10}) of the SCs with and without IMBH overlap and start behaving in the same way. At the end of the simulations, the values of the 10% and 30% Lagrangian radii of SCs with and without IMBHs are almost the same. The presence of the IMBH has a stronger impact on Lagrangian radii in the first stages of the evolution of the SCs.

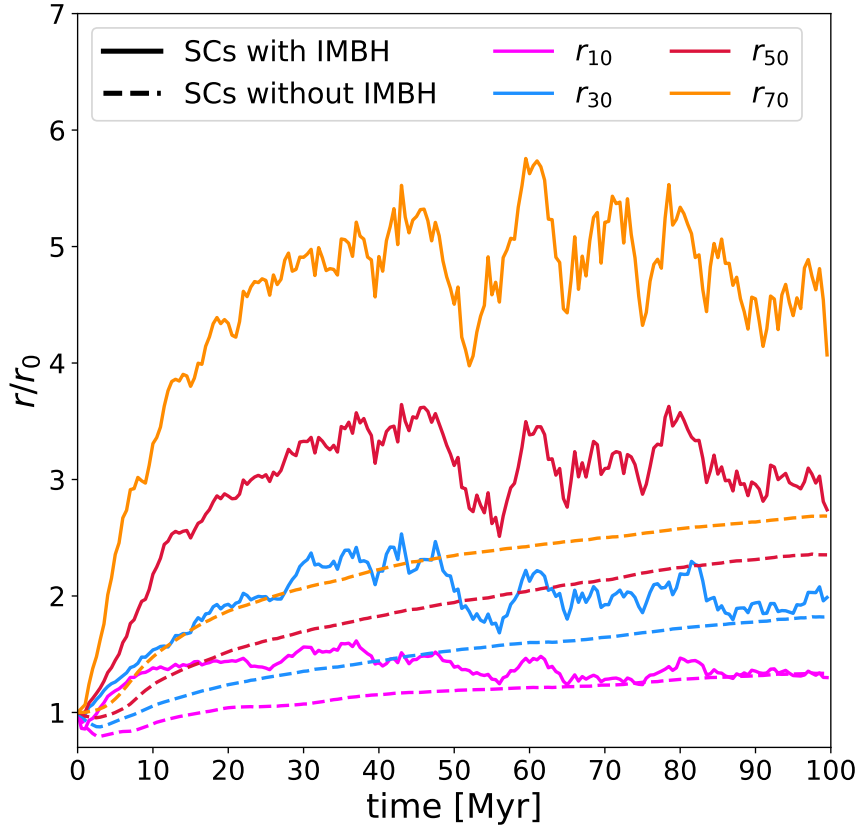


Figure 5.14: Time evolution of the median of the 10%, 30%, 50% and 70% Lagrangian radii (r_{10} , r_{30} , r_{50} and r_{70}). Solid lines refer to SCs which contain at least one IMBH; dashed lines refer to SCs which do not contain IMBHs. Each radius is normalized to its initial value r_0 . A simple moving average over 5 timesteps has been performed to filter out statistical fluctuations.

We also check the behavior of Lagrangian radii calculated excluding neutron stars and BHs. In this way, we exclude the dark component and we obtain radii more similar to what observations can tell us, even if we do not account for any other observational bias (for example, we do not remove the lowest mass stars). Hereafter, we call this version of the Lagrangian radii *visible* Lagrangian radii. Figure 5.15 shows the differences between the 10% and 50% Lagrangian radii and the visible 10% and 50% Lagrangian radii. Visible Lagrangian radii are slightly larger than the Lagrangian radii likely due to mass segregation, but the difference does not affect our main result: SCs with IMBHs tend to expand more than SCs without IMBHs. This result is consistent with previous studies (e.g. Baumgardt et al., 2004b; Baumgardt et al., 2004a; Trenti et al., 2007; Trenti et al., 2010), which find that the presence of an IMBH in the SC leads to an initial stronger expansion.

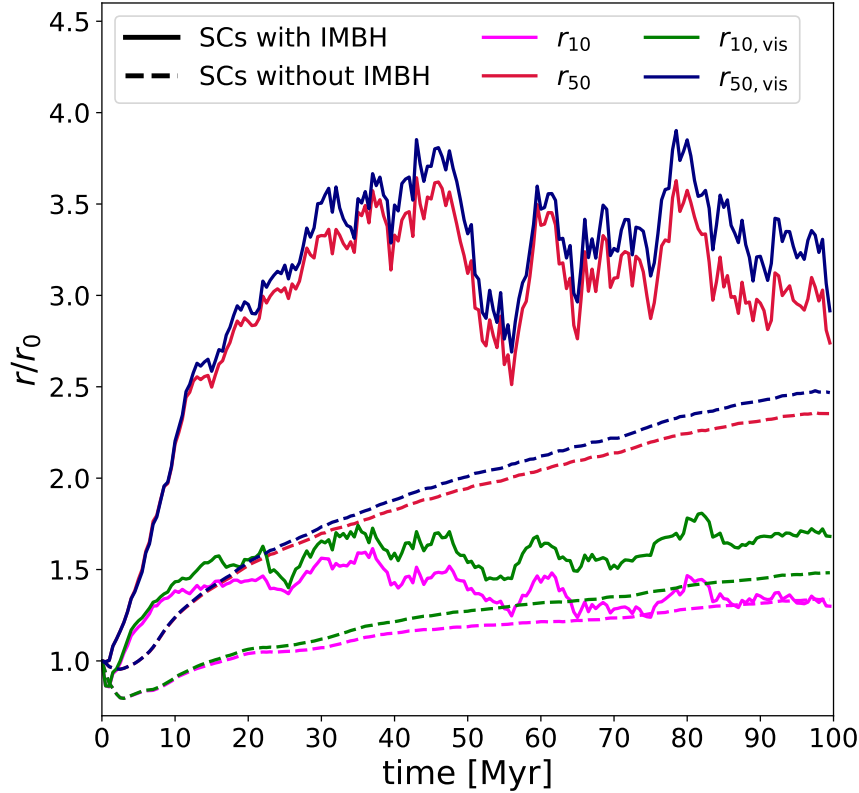


Figure 5.15: Time evolution of the median of the 10% and 50% Lagrangian radii (r_{10} and r_{50}) and of the corresponding *visible* Lagrangian radii $r_{10,vis}$ and $r_{50,vis}$ (i.e. the 10% and 50% Lagrangian radii calculated excluding BHs and neutron stars). Solid lines refer to SCs which contain at least one IMBH; dashed lines refer to SCs without IMBHs. Each radius is normalized to its initial value r_0 . A simple moving average over 5 timesteps has been performed to filter out statistical fluctuations.

5.4 Discussion

5.4.1 Accretion

In our simulations, we assume that if a star merges with a BH or with a neutron star the entire mass of the star is lost. Realistically, a fraction of the star’s mass could have accreted onto the compact object. Studies on tidal disruption events (e.g. Metzger and Stone, 2016) show that this fraction is $\sim 1 - 10\%$. We also stress that most of the star-BH mergers in our simulations tend to involve low-mass stars, because massive stars turn into compact objects in a few Myr. Had we allowed for a higher accretion efficiency in our simulations, some of the formed IMBHs would have grown a slightly larger mass.

5.4.2 Relativistic kicks

We do not include relativistic kicks in our simulations. Were they included, what would have been their influence on our IMBH sample? The only IMBHs which can be affected by relativistic kicks are the 9 IMBHs which form via BBH merger, which make up only 4% of all the formed IMBHs. Eight of these IMBHs form via the merger of only one BBH. This means that all of them would have formed in any case, with the only difference that they could have been ejected from their host SC if the relativistic kick would have exceeded the SC's escape velocity. Hence, we do not expect any significant difference in our results if we account for relativistic kicks.

5.4.3 Ejected IMBHs

We find that $\sim 54\%$ of all the formed IMBHs are ejected from the host SC, but what are the mechanisms behind such ejections? SC evaporation is not a major channel of IMBH ejection, because most IMBHs are ejected in the first tens of Myr of the life of their parent SC. We find that 30 IMBHs escape while in binary systems and 88 IMBHs are ejected as single objects. To better understand the mechanisms behind the ejection of IMBHs in binary systems, we calculated the value of the semi-major axis below which an IMBH binary can be ejected by a single-binary scattering (Miller and Hamilton, 2002; Antonini and Rasio, 2016):

$$a_{\text{ej}} = \frac{\xi m_3^2}{(m_1 + m_2)^3} \frac{G m_1 m_2}{v_{\text{esc}}^2}, \quad (5.1)$$

where $\xi = 3$ (Quinlan, 1996) is a dimensionless parameter, v_{esc} is the escape velocity from the star cluster, m_1 and m_2 are the masses of the members of the binary and m_3 is the mass of the single particle. If we consider encounters with an object of mass 1, 5, 10 M_{\odot} , we find $a < a_{\text{ej}}$ for 0%, 47%, 93% of the binaries. These results suggest that if single-binary encounters are the mechanism behind the ejection of IMBH-BH binaries, the single object is most likely a BH or a massive star. Furthermore, since a_{ej} depends on v_{esc}^{-2} , the semi-major axis threshold is larger in low-mass SCs, where wider binaries can thus escape.

5.5 Conclusions

IMBHs have mass in the range $10^2 - 10^5 M_{\odot}$ and bridge the gap between stellar-sized BHs and super-massive BHs. Currently, we lack unambiguous evidence of IMBH existence from electromagnetic observations, but we know several strong

candidates (e.g., Farrell et al., 2009; Godet et al., 2014; Reines and Volonteri, 2015; Kızıltan et al., 2017; Abbott et al., 2020; Abbott et al., 2020b). Here, we have investigated the formation of IMBHs in young SCs through BBH mergers and the runaway collision mechanism.

In our simulations, 209 IMBHs form via the runaway collision mechanism, while only 9 IMBHs form via BBH mergers. Each SC hosts a maximum of two IMBHs. We find IMBHs with mass up to $\sim 438 M_{\odot}$, but $\sim 78\%$ of all the simulated IMBHs have a mass between $100 M_{\odot}$ and $150 M_{\odot}$: less massive IMBHs are more likely to form than the most massive ones.

As expected, IMBH formation is much less efficient at high metallicity, because stellar winds are more effective: only four IMBHs form at solar metallicity. The percentage of the simulated SCs which form at least one IMBH grows as metallicity decreases, going from 0.15% at $Z = 0.02$ to 3.5% at $Z = 0.0002$.

IMBHs form more efficiently in massive SCs, where dynamics is more important. For example, IMBHs form in $\sim 8\%$ of the SCs with $10^4 M_{\odot} \leq M_{\text{SC}} \leq 3 \times 10^4 M_{\odot}$ and in only $\lesssim 1\%$ of the SCs with $10^3 M_{\odot} \leq M_{\text{SC}} < 5 \times 10^3 M_{\odot}$.

In our simulations, $\sim 54\%$ of all the IMBHs are ejected from their parent SC, preferentially in the first ~ 25 Myr from the beginning of the simulations. The IMBHs that remain inside the cluster rapidly sink towards the centre after their formation and stay there until the end of the simulation. IMBHs are more likely to be ejected if their mass is low ($\lesssim 150 M_{\odot}$) and if the mass of their host SC is large ($> 5 \times 10^3 M_{\odot}$).

Due to their high mass, IMBHs are likely to dynamically interact with other stars and form binary systems. In our simulations, IMBHs spend $\sim 85\%$ of the time, on average, being part of a binary or triple system. IMBHs tend to pair up with other massive BHs in the SC, because dynamical exchanges favour the formation of more massive binaries, which are more energetically stable (Hills and Fullerton, 1980).

Overall, our simulations show that IMBHs form quite efficiently in massive young SCs via runaway stellar collisions, especially if the metallicity is relatively low ($Z = 0.0002, 0.002$). While IMBHs are efficient in pairing up dynamically, the occurrence of IMBH–BH mergers is extremely rare (< 1 every 10^4 young SCs).

5.6 Appendix A: Comparing the high-mass tails of the IMBH mass distributions at different metallicities

Here, we explore if the mass of the heaviest IMBHs formed in our simulations depends on their progenitors' metallicity. In particular, Figure 5.2 seems to suggest that the most massive IMBHs form at intermediate metallicity ($Z = 0.002 \sim 0.1 Z_{\odot}$) rather than at the lowest considered metallicity ($Z = 0.0002 \sim 0.01 Z_{\odot}$). To assess this trend with a more quantitative evaluation, we compare the end tail of the IMBH mass distribution at $Z = 0.0002$ and $Z = 0.002$. The mass distribution of all the BHs in the $Z = 0.002$ and the $Z = 0.0002$ samples are significantly different, with $p = 2.2 \times 10^{-16}$ according to a Kolmogorov-Smirnov (K-S) test. This rises to $p = 0.08$ when only IMBHs (with mass $M > 100 M_{\odot}$) are considered, likely because the K-S test is notoriously insensitive to distribution tails and to small samples (see e.g. Mason and Schuenemeyer, 1983).

Figure 5.16 shows the quantiles of the IMBH masses for $Z = 0.0002$ against those with $Z = 0.002$. This quantile-quantile plot allows us to visualize how the two distributions differ: samples drawn from the same distribution would result in points straddling the identity line (black dashed line in Fig. 5.16), as each and every quantile would be the same for both samples, modulo random fluctuations. This is indeed the case for our two samples in Fig. 5.16 up until about $130 M_{\odot}$, but for higher IMBH masses the $Z = 0.002$ simulations appear to produce IMBHs that are systematically heavier than the $Z = 0.0002$ simulations. For example, the 90-th percentile is $228 M_{\odot}$ for the $Z = 0.002$ and $157 M_{\odot}$ for $Z = 0.0002$.

It is still far from trivial to conclude whether the high-mass tails and in particular the maximum mass produced is different. Comparing maxima is an intrinsically hard problem, because, even for well-behaved distributions, the variance of extremes is much larger than that of, e.g., the mean. A widespread non-parametric approach for testing differences in maxima relies on an exact Fisher test (Fisher, 1992) applied to the contingency table obtained by counting how many BHs lie above selected mass cut-offs in each of the two metallicity samples. This is similar to applying a χ^2 test, but is exact for the case in which cell counts are very low, as we expect them to be for large enough mass cut-offs. We find that the null hypothesis (that both metallicities produce IMBHs above and below each mass cutoff in the same proportion) cannot be rejected for cutoffs at the 90th, 95th, and 99th percentiles of the joined samples, so we conclude that at the moment our data do not constrain the impact of metallicity on maximum IMBH mass, at least if we forego making assumptions on the underlying parent distribution.

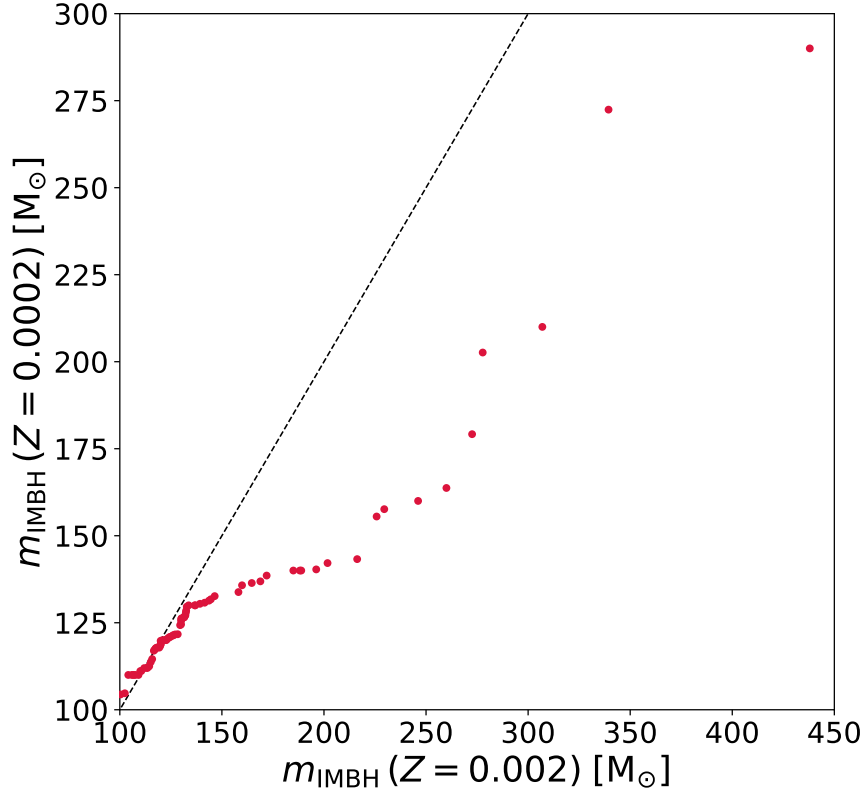


Figure 5.16: Quantile-quantile plot for the IMBH masses in SCs with $Z = 0.002$ and $Z = 0.0002$. The x -axis shows the values corresponding to selected quantiles of the $Z = 0.002$ sample, while the values of the y -axis represent the same quantiles for $Z = 0.0002$. If the IMBH masses were extracted from the same distribution, deviations from the diagonal 1:1 black dashed line would be due to random fluctuations only.

A general concern with this comparison could be that the number of simulations run at the two different metallicities is different, so the samples can be compared fairly only through a bootstrap re-sampling that takes this difference into account. We thus repeated our analysis by randomly re-sampling from the $Z = 0.002$ sample either a number of IMBHs equal to that in the less numerous $Z = 0.0002$ sample or a number of IMBHs corresponding to an equivalent number of simulations. Even with this test the results from the above still hold, i.e. no significant difference in the high-mass tails of the distributions could be ascertained non-parametrically.

CONCLUSIONS

In this Thesis, I have used numerical simulations to investigate the formation pathways and the characteristics of black holes (BHs) and binary black holes (BBHs) in young star clusters (SCs), focusing on gravitational wave (GW) sources.

To perform the study, I used direct N-body simulations and population-synthesis simulations. In particular, I have interfaced the widely used direct N-body code NBODY6++GPU (Wang et al., 2015) with the population-synthesis code MOBSE (Giacobbo et al., 2018), in order to perform state-of-the-art simulations with up-to-date stellar evolution. I produced a vast set of $\sim 10^4$ simulations of SCs with different initial masses ($10^3 M_\odot \leq M_{\text{SC}} \leq 3 \cdot 10^4 M_\odot$), metallicity and radius and analyzed them to extrapolate my results. With respect to previous work, which included no initial binaries or $\leq 20\%$ initial binary fraction, I have integrated my SCs with a 40% initial binary fraction, which rises to 100% if only massive stars are considered (Küpper et al., 2011). This is a fundamental choice, if we consider that observations suggest a $\sim 100\%$ initial binary fraction among massive young stars in SCs (e.g. Sana et al. 2012). Furthermore, we adopted fractal initial conditions to mimic the clumpiness of star-forming regions.

First of all, my simulations show that BBHs are strongly affected by dynamics (Di Carlo et al., 2019). Merging BBHs which evolve in SCs are significantly heavier than the ones evolved in isolation: merging BBHs with total mass up to $\sim 140 M_\odot$ form in young SCs, while the maximum total mass of merging BBHs in isolated binaries is only $\sim 80 M_\odot$. Merging BBHs in SCs tend to have smaller mass ratios than BBHs in isolated binaries. Exchanged BBHs reach higher total masses and lower mass ratios than original BBHs (i.e. BBHs that form from stellar binaries already present in the initial conditions). We find that metallicity strongly affects the mass spectrum: low metallicity favours the formation of more massive BHs, BBHs and merging BBHs because stars lose less mass by stellar winds (Di Carlo et al., 2020b).

Another important difference between isolated and dynamical binaries is the merger efficiency (i.e. the number of mergers divided by the total simulated mass). Even if at lower metallicities the differences are negligible, at solar metallicity the merger efficiency is about two orders of magnitude higher for dynamical BBHs with respect to isolated BBHs. Assuming that all the cosmic star formation rate takes place in YSCs, we find a local merger rate $\sim 55 - 110 \text{ Gpc}^{-3} \text{ yr}^{-1}$. This shows that most BBH mergers might have originated in young SCs.

My simulations show that BHs with mass in the pair instability (PI) mass gap can form via multiple stellar mergers in young SCs (Di Carlo et al., 2020a); the merger between an evolved star (a giant with a well developed helium core) and a main sequence star can give birth to a BH with mass in the gap, provided that the star collapses before its helium core grows above $\sim 32 M_{\odot}$. At the end of my simulations, $\sim 5.6\%$, $\sim 1.5\%$ and $\sim 0.1\%$ of all BHs have mass in the PI gap for metallicity $Z = 0.0002$, 0.002 and 0.02 , respectively. BHs in the gap can form via isolated binary evolution as well (Spera et al., 2019b), but when they form in a SC they can acquire a new companion through dynamical exchanges and eventually merge via GW emission. In my simulations, several BHs with masses in the gap end up forming a BBH through dynamical exchanges. BBHs having at least one component in the mass gap are $\sim 20.6\%$, $\sim 9.8\%$ and $\sim 0.5\%$ of all BBHs in our simulations, for metallicity $Z = 0.0002$, 0.002 and 0.02 , respectively. Thanks to dynamical hardening, such BBHs may also merge via GW emission: $\sim 2.1\%$ ($\sim 2.2\%$) of all BBHs merging within a Hubble time have at least one component in the mass gap for metallicity $Z = 0.002$ ($Z = 0.0002$). We find no merging BBHs in the mass gap at solar metallicity. Merging BBHs in the mass gap form preferentially in the most massive SCs we simulate ($M_{\text{SC}} \geq 6000 M_{\odot}$). We predict that $\sim 5\%$ of all BBH mergers detected by LIGO and Virgo at design sensitivity have at least one component in the PI mass gap, under the assumption that all stars form in young SCs.

My models are in agreement with the detections of the LIGO and Virgo collaboration (LVC). In particular, the most massive events reported by the LVC (GW170729 and GW190521, Abbott et al. 2019a; Abbott et al. 2020), can be explained only with dynamical BBHs, and mostly by exchanged BBHs in metal-poor SCs. Even GW190412, the first unequal-mass BBH merger, can be explained only by BBHs born in SCs: according to our models, isolated binaries can hardly explain such extreme mass ratios. Di Carlo et al., 2019 predicted the existence of merging BBHs in the PI mass gap before GW190521 was detected (Abbott et al., 2020).

Finally, intermediate black holes (IMBHs) with masses up to $\sim 440 M_{\odot}$ form in my simulations via the runaway collision scenario (e.g. Portegies Zwart and McMillan 2002; Mapelli 2016). IMBHs form preferentially in more massive SCs. The fraction of IMBHs with respect to the total number of BHs is $\sim 0.4\%$, $\sim 0.2\%$ and $\sim 0.02\%$ for metallicity $Z = 0.0002$, 0.002 and 0.02 , respectively. IMBHs are extremely efficient in finding a companion BH: $\sim 70\%$ of all IMBHs reside in a BBH at the end of the simulations. We find no merging BBHs which host an IMBH. SCs with IMBHs tend to expand more than SCs without IMBHs. The expansion is faster

in the first ~ 25 Myr. Larger Lagrangian radii expand more, meaning that the expansion is stronger in the outer regions of the SC.

ACRONYMS

BH : black hole

BBH : binary black hole

CE : common envelope

ECSN : electron capture supernova

GC : globular cluster

GW : gravitational wave

IMF : initial mass function

OC : open cluster

PISN : pair-instability supernova

PPI : pulsational pair-instability

SC : star cluster

SN : supernova

WR : Wolf-Rayet

YSC : young star cluster

ZAMS : zero age main sequence

LIST OF TABLES

1.1	List of some of the most impactful events observed by the LVC	5
1.2	Comparison of fundamental parameters for star cluster families	14
2.1	Initial conditions.	39
2.2	Number of SC BBHs.	44
2.3	Results of the U-Test and KS-Test to compare two BBH samples.	48
2.4	Heavy merging BBHs.	50
2.5	Number of mergers per unit stellar mass.	54
3.1	Initial conditions.	65
3.2	Fraction of BHs, BBHs and merging BBHs with mass in the PI gap.	71
4.1	Initial conditions.	80
4.2	Percentage of original and exchanged BBHs.	85
4.3	Results of the KS-Test and U-Test to compare sets of merging BBHs.	86
4.4	List of the BBH mergers with primary mass $m_1 \geq 45 M_\odot$ in our simulations.	92
4.5	Progenitors of exchanged BBH mergers at the time of the first exchange	98
5.1	Initial conditions.	105
5.2	Percentage of SCs that form 0, 1 and 2 IMBHs per different metallicity, initial SC mass and simulation set.	108

LIST OF FIGURES

1.1	Schematic GW deformations	3
1.2	GW Strain	6
1.3	Charateristics of O3a detections	7
1.4	Masses in the stellar graveyard	8
1.5	Common envelope phase	11
1.6	SC observations	15
1.7	Distribution of star clusters in the Milky Way	15
1.8	Two body encounter	19
1.9	Radius-mass diagram of Milky Way SCs	19
1.10	Hardening and exchange	23
2.1	Initial conditions representation	39
2.2	BH masses vs ZAMS mass	41
2.3	BH masses distribution	42
2.4	IMBH masses distribution	43
2.5	Distribution of total masses of merging BBHs	45
2.6	Distribution of chirp masses of merging BBHs	46
2.7	Distribution of mass ratios of merging BBHs	46
2.8	Mass of the primary BH versus mass of the secondary BH of merging BBHs.	49
2.9	Distribution of eccentricities of merging BBHs in SCs and in IBs.	51
2.10	Delay time distribution	52
2.11	Formation times of merging exchanged BBHs	56
3.1	Mass evolution of the progenitors of BHs in the PI gap	66
3.2	Mass ratio versus total mass of BBHs which host at least a BH in the PI gap	69
3.3	Mass of the host star cluster versus the mass of a BH in the PI gap	70
4.1	Initial binary fractoin as a function of stellar mass	81
4.2	BH masses distribution for set A and set B	83
4.3	Distribution of total masses of merging BBHs for set A and set B	87
4.4	Distribution of chirp masses of merging BBHs for set A and set B	88
4.5	Distribution of mass ratios of merging BBHs for set A and set B	89
4.6	Mass of the primary BH versus mass of the secondary BH of merging BBHs at different metallicities	90
4.7	Evolution of the most massive BBH merger in our simulations	91
4.8	Distribution of delay times of merging BBHs for set A and set B	93
4.9	Merger efficiency	94

4.10	Formation times of merging exchanged BBHs for set A and set B	99
5.1	Evolution of the mass density of SCs at the half mass radius and at the core radius.	107
5.2	Distributions of IMBH masses for each metallicity.	109
5.3	Formation history of the most massive IMBH found in our simulations.	110
5.4	Mass evolution of three stars which end up forming an IMBH.	111
5.5	Evolution of the distance of IMBHs from the centre of mass of the host SC.	112
5.6	Probability distribution function of the escape time of IMBHs in different mass ranges.	113
5.7	Probability distribution function of the escape time of IMBHs with different initial SC mass.	114
5.8	Evolution of IMBH binaries.	115
5.9	Distribution of the stellar types of the companions of all the simulated IMBHs.	116
5.10	Mass ratio $q = m_2/m_1$ versus total mass $M_{\text{tot}} = m_1 + m_2$ of IMBH–BH binaries.	118
5.11	Formation history of a binary IMBH found in our simulations	119
5.12	Mass of the host SC (M_{SC}) versus the mass of the IMBH (m_{IMBH}).	121
5.13	Distributions of IMBH masses for the different simulation sets.	123
5.14	Evolution of Lagrangian radii of SCs with/without IMBHs.	124
5.15	Evolution of Lagrangian radii and of visibleLagrangian radii of SCs with/without IMBHs.	125
5.16	Quantile-quantile plot for the IMBH masses in SCs with $Z = 0.002$ and $Z = 0.0002$	129

BIBLIOGRAPHY

- Aarseth, S. J. (2003). *Gravitational N-Body Simulations*, p. 430.
- Aasi et al. et al. (2015). “Advanced LIGO”. In: *Classical and Quantum Gravity* 32.7, 074001, p. 074001.
- Abadie, J. et al. (2010). “TOPICAL REVIEW: Predictions for the rates of compact binary coalescences observable by ground-based gravitational-wave detectors”. In: *Classical and Quantum Gravity* 27.17, 173001, p. 173001.
- Abbott, B. P. et al. (2016a). “Astrophysical Implications of the Binary Black-hole Merger GW150914”. In: *ApJ* 818, L22, p. L22.
- Abbott, B. P. et al. (2016b). “Astrophysical Implications of the Binary Black-hole Merger GW150914”. In: *ApJ* 818, L22, p. L22.
- Abbott, B. P. et al. (2016c). “Binary Black Hole Mergers in the First Advanced LIGO Observing Run”. In: *Physical Review X* 6.4, 041015, p. 041015.
- Abbott, B. P. et al. (2016d). “Binary Black Hole Mergers in the First Advanced LIGO Observing Run”. In: *Physical Review X* 6.4, 041015, p. 041015.
- Abbott, B. P. et al. (2016e). “GW151226: Observation of Gravitational Waves from a 22-Solar-Mass Binary Black Hole Coalescence”. In: *Phys. Rev. Lett.* 116.24, 241103, p. 241103.
- Abbott, B. P. et al. (2016f). “Observation of Gravitational Waves from a Binary Black Hole Merger”. In: *Physical Review Letters* 116.6, 061102, p. 061102.
- Abbott, B. P. et al. (2016). “The Rate of Binary Black Hole Mergers Inferred from Advanced LIGO Observations Surrounding GW150914”. In: *Astrophys. J.* 833.1, p. L1.
- Abbott, B. P. et al. (2017). “Gravitational Waves and Gamma-Rays from a Binary Neutron Star Merger: GW170817 and GRB 170817A”. In: *ApJ* 848, L13, p. L13.
- Abbott, B. P. et al. (2017). “Gravitational Waves and Gamma-Rays from a Binary Neutron Star Merger: GW170817 and GRB 170817A”. In: *The Astrophysical Journal Letters* 848.2, p. L13.
- Abbott, B. P. et al. (2017a). “GW170104: Observation of a 50-Solar-Mass Binary Black Hole Coalescence at Redshift 0.2”. In: *Physical Review Letters* 118.22, 221101, p. 221101.
- Abbott, B. P. et al. (2017b). “GW170608: Observation of a 19 Solar-mass Binary Black Hole Coalescence”. In: *ApJ* 851, L35, p. L35.
- Abbott, B. P. et al. (2017c). “GW170814: A Three-Detector Observation of Gravitational Waves from a Binary Black Hole Coalescence”. In: *Physical Review Letters* 119.14, 141101, p. 141101.

- Abbott, B. P. et al. (2017d). “GW170817: Observation of Gravitational Waves from a Binary Neutron Star Inspiral”. In: *Phys. Rev. Lett.* 119.16, 161101, p. 161101.
- Abbott, B. P. et al. (2017e). “Multi-messenger Observations of a Binary Neutron Star Merger”. In: *ApJ* 848, L12, p. L12.
- Abbott, B. P. et al. (2018). “Prospects for Observing and Localizing Gravitational-Wave Transients with Advanced LIGO, Advanced Virgo and KAGRA”. In: *Living Rev. Rel.* 21.1, p. 3.
- Abbott, B. P. et al. (2019a). “Binary Black Hole Population Properties Inferred from the First and Second Observing Runs of Advanced LIGO and Advanced Virgo”. In: *ApJ* 882.2, L24, p. L24.
- Abbott, B. P. et al. (2019b). “GWTC-1: A Gravitational-Wave Transient Catalog of Compact Binary Mergers Observed by LIGO and Virgo during the First and Second Observing Runs”. In: *Physical Review X* 9.3, 031040, p. 031040.
- Abbott, B. P. et al. (2020a). “GW190412: Observation of a Binary-Black-Hole Coalescence with Asymmetric Masses”. In: *arXiv e-prints*, arXiv:2004.08342, arXiv:2004.08342.
- Abbott, B. P. et al. (2020b). “GW190425: Observation of a Compact Binary Coalescence with Total Mass $\sim 3.4 M_{\odot}$ ”. In: *ApJ* 892.1, L3, p. L3.
- Abbott, R. et al. (2020). “GW190521: A Binary Black Hole Merger with a Total Mass of $150 M_{\odot}$ ”. In: *Phys. Rev. Lett.* 125 (10), p. 101102.
- Abbott, R. et al. (2020a). “GWTC-2: Compact Binary Coalescences Observed by LIGO and Virgo During the First Half of the Third Observing Run”. In: *arXiv e-prints*, arXiv:2010.14527, arXiv:2010.14527.
- Abbott, R. et al. et al. (2020b). “Properties and Astrophysical Implications of the $150 M_{\odot}$ Binary Black Hole Merger GW190521”. In: *ApJ* 900.1, L13, p. L13.
- Acernese, F. et al. (2015). “Advanced Virgo: a second-generation interferometric gravitational wave detector”. In: *Classical and Quantum Gravity* 32.2, 024001, p. 024001.
- Ade, P. A. R. et al. (2016). “Planck 2015 results. XIII. Cosmological parameters”. In: *A&A* 594, A13, A13.
- Ahmad, A. and L. Cohen (1973). “A numerical integration scheme for the N-body gravitational problem.” In: *Journal of Computational Physics* 12, pp. 389–402.
- Alexander, K. D. et al. (2017). “The Electromagnetic Counterpart of the Binary Neutron Star Merger LIGO/Virgo GW170817. VI. Radio Constraints on a Relativistic Jet and Predictions for Late-time Emission from the Kilonova Ejecta”. In: *ApJ* 848.2, p. L21.

- Amaro-Seoane, P. et al. (2017a). “Laser Interferometer Space Antenna”. In: *ArXiv e-prints*.
- Amaro-Seoane, Pau et al. (2017b). “Laser Interferometer Space Antenna”. In: *arXiv e-prints*, arXiv:1702.00786, arXiv:1702.00786.
- Anders, E. and N. Grevesse (1989). “Abundances of the elements: Meteoritic and solar”. In: *Geochim. Cosmochim. Acta* 53.1, pp. 197–214.
- Anderson, J. and R. P. van der Marel (2010). “New Limits on an Intermediate-Mass Black Hole in Omega Centauri. I. Hubble Space Telescope Photometry and Proper Motions”. In: *ApJ* 710, pp. 1032–1062.
- Antonini, F. and F. A. Rasio (2016). “Merging Black Hole Binaries in Galactic Nuclei: Implications for Advanced-LIGO Detections”. In: *ApJ* 831, 187, p. 187.
- Antonini, F. et al. (2016). “Black Hole Mergers and Blue Stragglers from Hierarchical Triples Formed in Globular Clusters”. In: *ApJ* 816, 65, p. 65.
- Antonini, Fabio et al. (2012). “Dissipationless Formation and Evolution of the Milky Way Nuclear Star Cluster”. In: *ApJ* 750.2, 111, p. 111.
- Antonini, Fabio et al. (2019a). “Black hole growth through hierarchical black hole mergers in dense star clusters: implications for gravitational wave detections”. In: *MNRAS* 486.4, pp. 5008–5021.
- Antonini, Fabio et al. (2019b). “Black hole growth through hierarchical black hole mergers in dense star clusters: implications for gravitational wave detections”. In: *MNRAS* 486.4, pp. 5008–5021.
- Arca-Sedda, M. (2016). “On the formation of compact, massive subsystems in stellar clusters and its relation with intermediate-mass black holes”. In: *MNRAS* 455, pp. 35–50.
- Arca Sedda, M. and M. Benacquista (2019). “Using final black hole spins and masses to infer the formation history of the observed population of gravitational wave sources”. In: *MNRAS* 482.3, pp. 2991–3010.
- Arca-Sedda, M. and A. Gualandris (2018). “Gravitational wave sources from inspiralling globular clusters in the Galactic Centre and similar environments”. In: *MNRAS* 477, pp. 4423–4442.
- Arca-Sedda, M. et al. (2018). “Ordering the chaos: stellar black hole mergers from non-hierarchical triples”. In: *arXiv e-prints*.
- Arca Sedda, Manuel et al. (2020). “Fingerprints of Binary Black Hole Formation Channels Encoded in the Mass and Spin of Merger Remnants”. In: *ApJ* 894.2, 133, p. 133.
- Arzoumanian, Z. et al. (2002). “The Velocity Distribution of Isolated Radio Pulsars”. In: *ApJ* 568, pp. 289–301.

- Askar, A. et al. (2018). “MOCCA-SURVEY Database I: Galactic globular clusters harbouring a black hole subsystem”. In: MNRAS 478, pp. 1844–1854.
- Askar, Abbas et al. (2017a). “MOCCA-SURVEY Database - I. Coalescing binary black holes originating from globular clusters”. In: MNRAS 464.1, pp. L36–L40.
- Askar, Abbas et al. (2017b). “MOCCA-SURVEY Database I: Is NGC 6535 a dark star cluster harbouring an IMBH?” In: MNRAS 464.3, pp. 3090–3100.
- Baibhav, Vishal et al. (2019). “Gravitational-wave detection rates for compact binaries formed in isolation: LIGO/Virgo O3 and beyond”. In: Phys. Rev. D 100.6, 064060, p. 064060.
- Baldassare, Vivienne F. et al. (2015). “A $\sim 50,000 M_{\odot}$ Solar Mass Black Hole in the Nucleus of RGG 118”. In: ApJ 809.1, L14, p. L14.
- Ballone, Alessandro et al. (2020). “Evolution of fractality and rotation in embedded star clusters”. In: *arXiv e-prints*, arXiv:2001.10003, arXiv:2001.10003.
- Banerjee, S. (2018a). “Stellar-mass black holes in young massive and open stellar clusters and their role in gravitational-wave generation - II”. In: MNRAS 473, pp. 909–926.
- Banerjee, S. et al. (2010). “Stellar-mass black holes in star clusters: implications for gravitational wave radiation”. In: MNRAS 402, pp. 371–380.
- Banerjee, S. et al. (2019). “BSE versus StarTrack: implementations of new wind, remnant-formation, and natal-kick schemes in NBODY7 and their astrophysical consequences”. In: *arXiv e-prints*.
- Banerjee, Sambaran (2018b). “Stellar-mass black holes in young massive and open stellar clusters and their role in gravitational-wave generation - II”. In: MNRAS 473.1, pp. 909–926.
- Banerjee, Sambaran (2020). “Stellar-mass black holes in young massive and open stellar clusters and their role in gravitational-wave generation IV: updated stellar-evolutionary and black hole spin models and comparisons with the LIGO-Virgo O1/O2 merger-event data”. In: *arXiv e-prints*, arXiv:2004.07382, arXiv:2004.07382.
- Barkat, Z. et al. (1967). “Dynamics of Supernova Explosion Resulting from Pair Formation”. In: *Physical Review Letters* 18, pp. 379–381.
- Barth, Aaron J. et al. (2004). “POX 52: A Dwarf Seyfert 1 Galaxy with an Intermediate-Mass Black Hole”. In: ApJ 607.1, pp. 90–102.
- Bauer, David F (1972). “Constructing confidence sets using rank statistics”. In: *Journal of the American Statistical Association* 67.339, pp. 687–690.

- Baumgardt, H. (2017). “N -body modelling of globular clusters: masses, mass-to-light ratios and intermediate-mass black holes”. In: MNRAS 464.2, pp. 2174–2202.
- Baumgardt, H. et al. (2019). “No evidence for intermediate-mass black holes in the globular clusters ω Cen and NGC 6624”. In: MNRAS 488, pp. 5340–5351.
- Baumgardt, Holger et al. (2004a). “Massive Black Holes in Star Clusters. I. Equal-Mass Clusters”. In: ApJ 613.2, pp. 1133–1142.
- Baumgardt, Holger et al. (2004b). “Massive Black Holes in Star Clusters. II. Realistic Cluster Models”. In: ApJ 613.2, pp. 1143–1156.
- Beccari, G. et al. (2019). “Discovery of a Double Blue Straggler Sequence in M15: New Insight into the Core-collapse Process”. In: ApJ 876.1, 87, p. 87.
- Belczynski, K. et al. (2002). “A Comprehensive Study of Binary Compact Objects as Gravitational Wave Sources: Evolutionary Channels, Rates, and Physical Properties”. In: ApJ 572, pp. 407–431.
- Belczynski, K. et al. (2007). “On the Rarity of Double Black Hole Binaries: Consequences for Gravitational Wave Detection”. In: ApJ 662, pp. 504–511.
- Belczynski, K. et al. (2008). “Compact Object Modeling with the StarTrack Population Synthesis Code”. In: ApJS 174, 223–260, pp. 223–260.
- Belczynski, K. et al. (2010). “On the Maximum Mass of Stellar Black Holes”. In: ApJ 714.2, p. 1217.
- Belczynski, K. et al. (2016a). “The effect of pair-instability mass loss on black-hole mergers”. In: A&A 594, A97, A97.
- Belczynski, K. et al. (2016b). “The first gravitational-wave source from the isolated evolution of two stars in the 40-100 solar mass range”. In: Nature 534, pp. 512–515.
- Belczynski, K. et al. (2017). “The evolutionary roads leading to low effective spins, high black hole masses, and O1/O2 rates of LIGO/Virgo binary black holes”. In: *arXiv e-prints*, arXiv:1706.07053, arXiv:1706.07053.
- Belloni, Diogo et al. (2018). “Dynamical equivalence, the origin of the Galactic field stellar and binary population, and the initial radius-mass relation of embedded clusters”. In: MNRAS 474.3, pp. 3740–3745.
- Bethe, H. A. and G. E. Brown (1998). “Evolution of Binary Compact Objects That Merge”. In: ApJ 506, pp. 780–789.
- Bianchini, Paolo et al. (2015). “Understanding the central kinematics of globular clusters with simulated integrated-light IFU observations”. In: MNRAS 453.1, pp. 365–376.

- Birnbaum, ZW, Fred H Tingey, et al. (1951). “One-sided confidence contours for probability distribution functions”. In: *The Annals of Mathematical Statistics* 22.4, pp. 592–596.
- Bishop, Nigel T. and Luciano Rezzolla (2016). “Extraction of gravitational waves in numerical relativity”. In: *Living Reviews in Relativity* 19.1, 2, p. 2.
- Bisnovatyi-Kogan, G. S. (1993). “Asymmetric neutrino emission and formation of rapidly moving pulsars”. In: *Astronomical and Astrophysical Transactions* 3.4, pp. 287–294.
- Blaauw, A. (1961). “On the origin of the O- and B-type stars with high velocities (the “run-away” stars), and some related problems”. In: *Bull. Astron. Inst. Netherlands* 15, p. 265.
- Blecha, L. et al. (2006). “Close Binary Interactions of Intermediate-Mass Black Holes: Possible Ultraluminous X-Ray Sources?” In: *ApJ* 642.1, pp. 427–437.
- Bond, J. R. et al. (1984). “The evolution and fate of Very Massive Objects”. In: *ApJ* 280, pp. 825–847.
- Bouffanais, Yann et al. (2019). “Constraining the Fraction of Binary Black Holes Formed in Isolation and Young Star Clusters with Gravitational-wave Data”. In: *ApJ* 886.1, 25, p. 25.
- Bouffanais, Yann et al. (2021). “New insights on binary black hole formation channels after GWTC-2: young star clusters versus isolated binaries”. In: *arXiv e-prints*, arXiv:2102.12495, arXiv:2102.12495.
- Bressan, A. et al. (2012). “PARSEC: stellar tracks and isochrones with the Padova and Trieste Stellar Evolution Code”. In: *MNRAS* 427, pp. 127–145.
- Brinkmann, Nina et al. (2017). “The bound fraction of young star clusters”. In: *A&A* 600, A49, A49.
- Burrows, A. et al. (2018). “Crucial Physical Dependencies of the Core-Collapse Supernova Mechanism”. In: *Space Sci. Rev.* 214.1, 33, p. 33.
- Carr, B. J. and S. W. Hawking (1974). “Black Holes in the Early Universe”. In: *Gravitational Radiation and Gravitational Collapse*. Ed. by C. Dewitt-Morette. Vol. 64. IAU Symposium, p. 184.
- Carr, Bernard et al. (2016). “Primordial black holes as dark matter”. In: *Phys. Rev. D* 94.8, 083504, p. 083504.
- Cartwright, A. and A. P. Whitworth (2004). “The statistical analysis of star clusters”. In: *MNRAS* 348, pp. 589–598.
- Chandrasekhar, S. (1943). “Dynamical Friction. I. General Considerations: the Coefficient of Dynamical Friction.” In: *ApJ* 97, p. 255.

- Chatterjee, S. et al. (2017). “Dynamical Formation of Low-mass Merging Black Hole Binaries like GW151226”. In: *ApJ* 836, L26, p. L26.
- Chen, Y. et al. (2015). “PARSEC evolutionary tracks of massive stars up to $350 M_{\odot}$ at metallicities $0.0001 \leq Z \leq 0.04$ ”. In: *MNRAS* 452, pp. 1068–1080.
- Choksi, Nick et al. (2019). “The Star Clusters That Make Black Hole Binaries across Cosmic Time”. In: *ApJ* 873.1, 100, p. 100.
- Chon, Sunmyon and Kazuyuki Omukai (2020). “Supermassive star formation via super competitive accretion in slightly metal-enriched clouds”. In: *MNRAS* 494.2, pp. 2851–2860.
- Chornock, R. et al. (2017). “The Electromagnetic Counterpart of the Binary Neutron Star Merger LIGO/Virgo GW170817. IV. Detection of Near-infrared Signatures of r -process Nucleosynthesis with Gemini-South”. In: *ApJ* 848.2, p. L19.
- Chruslinska, M. et al. (2018). “Double neutron stars: merger rates revisited”. In: *MNRAS* 474, pp. 2937–2958.
- Claeys, J. S. W. et al. (2014). “Theoretical uncertainties of the Type Ia supernova rate”. In: *A&A* 563, A83, A83.
- Clesse, Sebastien and Juan Garcia-Bellido (2020). “GW190425, GW190521 and GW190814: Three candidate mergers of primordial black holes from the QCD epoch”. In: *arXiv e-prints*, arXiv:2007.06481, arXiv:2007.06481.
- Colgate, S. A. (1967). “Stellar Coalescence and the Multiple Supernova Interpretation of Quasi-Stellar Sources”. In: *ApJ* 150, p. 163.
- Colpi, M. et al. (2003). “Probing the Presence of a Single or Binary Black Hole in the Globular Cluster NGC 6752 with Pulsar Dynamics”. In: *ApJ* 599, pp. 1260–1271.
- Coulter, D. A. et al. (2017). “Swope Supernova Survey 2017a (SSS17a), the optical counterpart to a gravitational wave source”. In: *Science* 358, pp. 1556–1558.
- Cowperthwaite, P. S. et al. (2017). “The Electromagnetic Counterpart of the Binary Neutron Star Merger LIGO/Virgo GW170817. II. UV, Optical, and Near-infrared Light Curves and Comparison to Kilonova Models”. In: *ApJ* 848.2, p. L17.
- Dal Canton, Tito et al. (2014). “Implementing a search for aligned-spin neutron star-black hole systems with advanced ground based gravitational wave detectors”. In: *Phys. Rev. D* 90.8, p. 082004.
- Dale, James E. and Melvyn B. Davies (2006). “Collisions and close encounters involving massive main-sequence stars”. In: *MNRAS* 366.4, pp. 1424–1436.
- Das, Arpan et al. (2021). “Formation of supermassive black hole seeds in nuclear star clusters via gas accretion and runaway collisions”. In: *MNRAS* 503.1, pp. 1051–1069.

- De Cia, Annalisa et al. (2018). “The cosmic evolution of dust-corrected metallicity in the neutral gas”. In: *A&A* 611, A76, A76.
- De Luca, V. et al. (2021). “GW190521 Mass Gap Event and the Primordial Black Hole Scenario”. In: *Phys. Rev. Lett.* 126.5, 051101, p. 051101.
- de Mink, S. E. and I. Mandel (2016). “The chemically homogeneous evolutionary channel for binary black hole mergers: rates and properties of gravitational-wave events detectable by advanced LIGO”. In: *MNRAS* 460, pp. 3545–3553.
- Dessart, L. et al. (2006). “Multidimensional Simulations of the Accretion-induced Collapse of White Dwarfs to Neutron Stars”. In: *ApJ* 644, pp. 1063–1084.
- Di Carlo, Ugo N. et al. (2019). “Merging black holes in young star clusters”. In: *MNRAS* 487.2, pp. 2947–2960.
- Di Carlo, Ugo N. et al. (2020a). “Binary black holes in the pair instability mass gap”. In: *MNRAS* 497.1, pp. 1043–1049.
- Di Carlo, Ugo N. et al. (2020b). “Binary black holes in young star clusters: the impact of metallicity”. In: *MNRAS* 498.1, pp. 495–506.
- Di Cintio, Pierfrancesco et al. (2021). “Introducing a new multi-particle collision method for the evolution of dense stellar systems II. Core collapse”. In: *arXiv e-prints*, arXiv:2103.02424, arXiv:2103.02424.
- Dominik, M. et al. (2012). “Double Compact Objects. I. The Significance of the Common Envelope on Merger Rates”. In: *ApJ* 759, 52, p. 52.
- Dominik, M. et al. (2013). “Double Compact Objects. II. Cosmological Merger Rates”. In: *ApJ* 779, 72, p. 72.
- Dominik, M. et al. (2015). “Double Compact Objects III: Gravitational-wave Detection Rates”. In: *ApJ* 806, 263, p. 263.
- Dong, Xiao-Bo et al. (2012). “A Uniformly Selected Sample of Low-mass Black Holes in Seyfert 1 Galaxies”. In: *ApJ* 755.2, 167, p. 167.
- Downing, J. M. B. et al. (2010). “Compact binaries in star clusters - I. Black hole binaries inside globular clusters”. In: *MNRAS* 407, pp. 1946–1962.
- Downing, J. M. B. et al. (2011). “Compact binaries in star clusters - II. Escapers and detection rates”. In: *MNRAS* 416, pp. 133–147.
- Einstein, A. (1916). “Näherungsweise Integration der Feldgleichungen der Gravitation”. In: *Sitzungsberichte der Königlich Preussischen Akademie der Wissenschaften (Berlin)*, Seite 688-696.
- Einstein, A. (1918). “Über Gravitationswellen”. In: *Sitzungsberichte der Königlich Preussischen Akademie der Wissenschaften (Berlin)*, Seite 154-167.
- Eldridge, J. J. et al. (2019). “A consistent estimate for gravitational wave and electromagnetic transient rates”. In: *MNRAS* 482, pp. 870–880.

- Elmegreen, B. G. and Y. N. Efremov (1997). “A Universal Formation Mechanism for Open and Globular Clusters in Turbulent Gas”. In: *ApJ* 480, pp. 235–245.
- Elson, Rebecca et al. (1987). “Dynamical evolution of globular clusters.” In: *ARA&A* 25, pp. 565–601.
- Fan, Xiaohui et al. (2001). “A Survey of $z > 5.8$ Quasars in the Sloan Digital Sky Survey. I. Discovery of Three New Quasars and the Spatial Density of Luminous Quasars at $z \sim 6$ ”. In: *AJ* 122.6, pp. 2833–2849.
- Farmer, R. et al. (2019). “Mind the Gap: The Location of the Lower Edge of the Pair-instability Supernova Black Hole Mass Gap”. In: *ApJ* 887.1, 53, p. 53.
- Farr, W. M. et al. (2011). “The Mass Distribution of Stellar-mass Black Holes”. In: *ApJ* 741, 103, p. 103.
- Farrell, Sean A. et al. (2009). “An intermediate-mass black hole of over 500 solar masses in the galaxy ESO243-49”. In: *Nature* 460.7251, pp. 73–75.
- Favata, Marc et al. (2004). “How Black Holes Get Their Kicks: Gravitational Radiation Recoil Revisited”. In: *ApJ* 607.1, pp. L5–L8.
- Feng, Hua and Roberto Soria (2011). “Ultraluminous X-ray sources in the Chandra and XMM-Newton era”. In: *New A Rev.* 55.5, pp. 166–183.
- Filippenko, Alexei V. and Luis C. Ho (2003). “A Low-Mass Central Black Hole in the Bulgeless Seyfert 1 Galaxy NGC 4395”. In: *ApJ* 588.1, pp. L13–L16.
- Filippenko, Alexei V. and Wallace L. W. Sargent (1989). “Discovery of an Extremely Low Luminosity Seyfert 1 Nucleus in the Dwarf Galaxy NGC 4395”. In: *ApJ* 342, p. L11.
- Finn, Lee Samuel and David F. Chernoff (1993). “Observing binary inspiral in gravitational radiation: One interferometer”. In: *Phys. Rev. D* 47, pp. 2198–2219.
- Fishbach, Maya and Daniel E. Holz (2017). “Where Are LIGO’s Big Black Holes?” In: *ApJ* 851.2, L25, p. L25.
- Fisher, Ronald Aylmer (1992). “Statistical methods for research workers”. In: *Breakthroughs in statistics*. Springer, pp. 66–70.
- Flannery, B. P. and E. P. J. van den Heuvel (1975). “On the origin of the binary pulsar PSR 1913 + 16”. In: *A&A* 39, pp. 61–67.
- Fragione, Giacomo et al. (2020). “On the Origin of GW190521-like Events from Repeated Black Hole Mergers in Star Clusters”. In: *ApJ* 902.1, L26, p. L26.
- Freitag, M. et al. (2006a). “Runaway collisions in young star clusters - I. Methods and tests”. In: *MNRAS* 368, pp. 121–140.
- Freitag, M. et al. (2006b). “Runaway collisions in young star clusters - II. Numerical results”. In: *MNRAS* 368, pp. 141–161.

- Fryer, C. et al. (1998). “Population Syntheses for Neutron Star Systems with Intrinsic Kicks”. In: ApJ 496, pp. 333–351.
- Fryer, C. L. et al. (2012). “Compact Remnant Mass Function: Dependence on the Explosion Mechanism and Metallicity”. In: ApJ 749, 91, p. 91.
- Fujii, M. S. and S. Portegies Zwart (2013a). “The growth of massive stars via stellar collisions in ensemble star clusters”. In: MNRAS 430.2, pp. 1018–1029.
- Fujii, M. S. and S. Portegies Zwart (2013b). “The growth of massive stars via stellar collisions in ensemble star clusters”. In: MNRAS 430.2, pp. 1018–1029.
- Fujii, M. S. and S. Portegies Zwart (2014). “The moment of core collapse in star clusters with a mass function”. In: MNRAS 439, pp. 1003–1014.
- Fujii, M. S. et al. (2017). “The detection rates of merging binary black holes originating from star clusters and their mass function”. In: PASJ 69, 94, p. 94.
- Fuller, Jim and Linhao Ma (2019). “Most Black Holes Are Born Very Slowly Rotating”. In: ApJ 881.1, L1, p. L1.
- Fuller, Jim et al. (2019). “Slowing the spins of stellar cores”. In: MNRAS 485.3, pp. 3661–3680.
- Gaburov, E. et al. (2008). “Mixing in massive stellar mergers”. In: MNRAS 383, pp. L5–L9.
- Gaburov, E. et al. (2010). “On the onset of runaway stellar collisions in dense star clusters - II. Hydrodynamics of three-body interactions”. In: MNRAS 402, pp. 105–126.
- Gebhardt, Karl et al. (2002). “A 20,000 M_{Solar} Black Hole in the Stellar Cluster G1”. In: ApJ 578.1, pp. L41–L45.
- Gebhardt, Karl et al. (2005). “An Intermediate-Mass Black Hole in the Globular Cluster G1: Improved Significance from New Keck and Hubble Space Telescope Observations”. In: ApJ 634.2, pp. 1093–1102.
- Gerosa, D. (2019). *gwdet: Detectability of gravitational-wave signals from compact binary coalescences*.
- Gerosa, D. and E. Berti (2017). “Are merging black holes born from stellar collapse or previous mergers?” In: Phys. Rev. D 95.12, 124046, p. 124046.
- Gerosa, Davide and Emanuele Berti (2019). “Escape speed of stellar clusters from multiple-generation black-hole mergers in the upper mass gap”. In: Phys. Rev. D 100.4, 041301, p. 041301.
- Gerosa, Davide et al. (2018). “Spin orientations of merging black holes formed from the evolution of stellar binaries”. In: Phys. Rev. D 98.8, 084036, p. 084036.

- Gerssen, Joris et al. (2002). “Hubble Space Telescope Evidence for an Intermediate-Mass Black Hole in the Globular Cluster M15. II. Kinematic Analysis and Dynamical Modeling”. In: *AJ* 124.6, pp. 3270–3288.
- Giacobbo, N. and M. Mapelli (2018). “The progenitors of compact-object binaries: impact of metallicity, common envelope and natal kicks”. In: *MNRAS* 480, pp. 2011–2030.
- Giacobbo, N. and M. Mapelli (2019). “The impact of electron-capture supernovae on merging double neutron stars”. In: *MNRAS* 482, pp. 2234–2243.
- Giacobbo, N. et al. (2018). “Merging black hole binaries: the effects of progenitor’s metallicity, mass-loss rate and Eddington factor”. In: *MNRAS* 474, pp. 2959–2974.
- Giacobbo, Nicola and Michela Mapelli (2020). “Revising Natal Kick Prescriptions in Population Synthesis Simulations”. In: *ApJ* 891.2, 141, p. 141.
- Gieles, M. et al. (2006). “Star cluster disruption by giant molecular clouds”. In: *MNRAS* 371, pp. 793–804.
- Gieles, Mark et al. (2018). “Concurrent formation of supermassive stars and globular clusters: implications for early self-enrichment”. In: *MNRAS* 478.2, pp. 2461–2479.
- Giersz, M. et al. (2015). “MOCCA code for star cluster simulations - IV. A new scenario for intermediate mass black hole formation in globular clusters”. In: *MNRAS* 454, pp. 3150–3165.
- Glebbeek, E. et al. (2009). “The evolution of runaway stellar collision products”. In: *A&A* 497, pp. 255–264.
- Godet, O. et al. (2014). “Implications of the Delayed 2013 Outburst of ESO 243-49 HLX-1”. In: *ApJ* 793.2, 105, p. 105.
- Goldstein, A. et al. (2017). “An Ordinary Short Gamma-Ray Burst with Extraordinary Implications: Fermi-GBM Detection of GRB 170817A”. In: *ApJ* 848, L14, p. L14.
- Goodman, J. and P. Hut (1993). “Binary-single-star scattering. V - Steady state binary distribution in a homogeneous static background of single stars”. In: *ApJ* 403, pp. 271–277.
- Goodman, Jeremy and Piet Hut (1989). “Primordial binaries and globular cluster evolution”. In: *Nature* 339.6219, pp. 40–42.
- Goodwin, S. P. and A. P. Whitworth (2004). “The dynamical evolution of fractal star clusters: The survival of substructure”. In: *A&A* 413, pp. 929–937.
- Goswami, S. et al. (2014). “Black Holes in Young Stellar Clusters”. In: *ApJ* 781, 81, p. 81.

- Gräfener, G. and W.-R. Hamann (2008). “Mass loss from late-type WN stars and its Z-dependence. Very massive stars approaching the Eddington limit”. In: *A&A* 482, pp. 945–960.
- Gratton, Raffaele et al. (2019). “What is a globular cluster? An observational perspective”. In: *A&A Rev.* 27.1, 8, p. 8.
- Greene, Jenny E. and Luis C. Ho (2004). “Active Galactic Nuclei with Candidate Intermediate-Mass Black Holes”. In: *ApJ* 610.2, pp. 722–736.
- Greene, Jenny E. and Luis C. Ho (2007). “A New Sample of Low-Mass Black Holes in Active Galaxies”. In: *ApJ* 670.1, pp. 92–104.
- Greene, Jenny E. et al. (2020). “Intermediate-Mass Black Holes”. In: *ARA&A* 58, pp. 257–312.
- Gürkan, M. A. et al. (2004). “Formation of Massive Black Holes in Dense Star Clusters. I. Mass Segregation and Core Collapse”. In: *ApJ* 604, pp. 632–652.
- Gürkan, M. A. et al. (2006). “Massive Black Hole Binaries from Collisional Runaways”. In: *ApJ* 640, pp. L39–L42.
- Gutermuth, R. A. et al. (2005). “The Initial Configuration of Young Stellar Clusters: A K-Band Number Counts Analysis of the Surface Density of Stars”. In: *ApJ* 632, pp. 397–420.
- Heger, A. and S. E. Woosley (2002). “The Nucleosynthetic Signature of Population III”. In: *ApJ* 567, pp. 532–543.
- Heger, A. et al. (2003). “How Massive Single Stars End Their Life”. In: *ApJ* 591, pp. 288–300.
- Heger, A. et al. (2005). “Presupernova Evolution of Differentially Rotating Massive Stars Including Magnetic Fields”. In: *ApJ* 626.1, pp. 350–363.
- Heggie, D. C. (1975). “Binary evolution in stellar dynamics”. In: *MNRAS* 173, pp. 729–787.
- Hills, J. G. and L. W. Fullerton (1980). “Computer simulations of close encounters between single stars and hard binaries”. In: *AJ* 85, pp. 1281–1291.
- Hoang, B.-M. et al. (2018). “Black Hole Mergers in Galactic Nuclei Induced by the Eccentric Kozai-Lidov Effect”. In: *ApJ* 856, 140, p. 140.
- Hobbs, G. et al. (2005). “A statistical study of 233 pulsar proper motions”. In: *MNRAS* 360, pp. 974–992.
- Hollander, Myles and Douglas A. Wolfe (1999). *Nonparametric Statistical Methods, 2nd Edition*. 2nd ed. Wiley-Interscience. ISBN: 0471190454.
- Holley-Bockelmann, Kelly et al. (2008). “Gravitational Wave Recoil and the Retention of Intermediate-Mass Black Holes”. In: *ApJ* 686.2, pp. 829–837.

- Hurley, J. R. et al. (2000). “Comprehensive analytic formulae for stellar evolution as a function of mass and metallicity”. In: *MNRAS* 315, pp. 543–569.
- Hurley, J. R. et al. (2002). “Evolution of binary stars and the effect of tides on binary populations”. In: *MNRAS* 329, pp. 897–928.
- Hurley, J. R. et al. (2016). “A Dynamical Gravitational Wave Source in a Dense Cluster”. In: *PASA* 33, e036, e036.
- Hurley, Jarrod R. and Michael M. Shara (2012). “A direct N-body model of core-collapse and core oscillations”. In: *MNRAS* 425.4, pp. 2872–2879.
- Janka, H. T. and E. Mueller (1996). “Neutrino heating, convection, and the mechanism of Type-II supernova explosions.” In: *A&A* 306, p. 167.
- Jiménez-Forteza, Xisco et al. (2017). “Hierarchical data-driven approach to fitting numerical relativity data for nonprecessing binary black holes with an application to final spin and radiated energy”. In: *Phys. Rev. D* 95.6, 064024, p. 064024.
- Jones, S. et al. (2013). “Advanced Burning Stages and Fate of 8-10 M_{\odot} Stars”. In: *ApJ* 772, 150, p. 150.
- Justham, Stephen et al. (2014). “Luminous Blue Variables and Superluminous Supernovae from Binary Mergers”. In: *ApJ* 796.2, 121, p. 121.
- Kaaret, P. et al. (2001). “Chandra High-Resolution Camera observations of the luminous X-ray source in the starburst galaxy M82”. In: *MNRAS* 321.2, pp. L29–L32.
- Kaaret, Philip et al. (2017). “Ultraluminous X-Ray Sources”. In: *ARA&A* 55.1, pp. 303–341.
- Kalogera, Vicky et al. (2019). “Deeper, Wider, Sharper: Next-Generation Ground-based Gravitational-Wave Observations of Binary Black Holes”. In: *BAAS* 51.3, 242, p. 242.
- Kawaguchi, Toshihiro et al. (2008). “Formation of intermediate-mass black holes as primordial black holes in the inflationary cosmology with running spectral index”. In: *MNRAS* 388.3, pp. 1426–1432.
- Kimpson, T. O. et al. (2016). “Hierarchical black hole triples in young star clusters: impact of Kozai-Lidov resonance on mergers”. In: *MNRAS* 463, pp. 2443–2452.
- King, I. R. (1966). “The structure of star clusters. III. Some simple dynamical models”. In: *AJ* 71, p. 64.
- Kızıltan, Bülent et al. (2017). “An intermediate-mass black hole in the centre of the globular cluster 47 Tucanae”. In: *Nature* 542.7640, pp. 203–205.
- Kormendy, John and Luis C. Ho (2013). “Coevolution (Or Not) of Supermassive Black Holes and Host Galaxies”. In: *ARA&A* 51.1, pp. 511–653.

- Kouwenhoven, M. B. N. et al. (2010). “The formation of very wide binaries during the star cluster dissolution phase”. In: MNRAS 404, pp. 1835–1848.
- Kozai, Y. (1962). “Secular perturbations of asteroids with high inclination and eccentricity”. In: AJ 67, p. 591.
- Krause, Martin G. H. et al. (2016). “Gas expulsion in massive star clusters?. Constraints from observations of young and gas-free objects”. In: A&A 587, A53, A53.
- Kremer, Kyle et al. (2019). “Post-Newtonian dynamics in dense star clusters: Binary black holes in the LISA band”. In: Phys. Rev. D 99.6, 063003, p. 063003.
- Kremer, Kyle et al. (2020). “Populating the Upper Black Hole Mass Gap through Stellar Collisions in Young Star Clusters”. In: ApJ 903.1, 45, p. 45.
- Kroupa, P. (2001). “On the variation of the initial mass function”. In: MNRAS 322, pp. 231–246.
- Kroupa, P. and C. M. Boily (2002). “On the mass function of star clusters”. In: MNRAS 336, pp. 1188–1194.
- Kruckow, Matthias U. et al. (2018). “Progenitors of gravitational wave mergers: binary evolution with the stellar grid-based code COMBINE”. In: MNRAS 481.2, pp. 1908–1949.
- Kruijssen, J. M. Diederik (2012). “On the fraction of star formation occurring in bound stellar clusters”. In: MNRAS 426.4, pp. 3008–3040.
- Kulkarni, S. R. et al. (1993). “Stellar black holes in globular clusters”. In: Nature 364, pp. 421–423.
- Kumamoto, J. et al. (2019a). “Gravitational-wave emission from binary black holes formed in open clusters”. In: MNRAS 486, pp. 3942–3950.
- Kumamoto, Jun et al. (2019b). “Gravitational-wave emission from binary black holes formed in open clusters”. In: MNRAS 486.3, pp. 3942–3950.
- Kumamoto, Jun et al. (2020). “Merger rate density of binary black holes formed in open clusters”. In: *arXiv e-prints*, arXiv:2001.10690, arXiv:2001.10690.
- Küpper, A. H. W. et al. (2011). “Mass segregation and fractal substructure in young massive clusters - I. The McLuster code and method calibration”. In: MNRAS 417, pp. 2300–2317.
- Kustaanheimo, Pavel and E. Stiefel (1965). “Perturbation theory of Kepler motion based on spinor regularization.” In: *J. Reine Angew. Mathematik* 218.2.
- Lada, C. J. and E. A. Lada (2003). “Embedded Clusters in Molecular Clouds”. In: ARA&A 41, pp. 57–115.
- Lanzoni, B. et al. (2013). “The Velocity Dispersion Profile of NGC 6388 from Resolved-star Spectroscopy: No Evidence of a Central Cusp and New Constraints on the Black Hole Mass”. In: ApJ 769, 107, p. 107.

- Lidov, M. L. (1962). “The evolution of orbits of artificial satellites of planets under the action of gravitational perturbations of external bodies”. In: *Planet. Space Sci.* 9, pp. 719–759.
- Limongi, Marco and Alessandro Chieffi (2018). “Presupernova Evolution and Explosive Nucleosynthesis of Rotating Massive Stars in the Metallicity Range $-3 \leq [\text{Fe}/\text{H}] \leq 0$ ”. In: *ApJS* 237.1, 13, p. 13.
- Lin, Dacheng et al. (2018). “A luminous X-ray outburst from an intermediate-mass black hole in an off-centre star cluster”. In: *Nature Astronomy* 2, pp. 656–661.
- Lin, Dacheng et al. (2020). “Multiwavelength Follow-up of the Hyperluminous Intermediate-mass Black Hole Candidate 3XMM J215022.4-055108”. In: *ApJ* 892.2, L25, p. L25.
- Lousto, Carlos O. and Yosef Zlochower (2011). “Hangup Kicks: Still Larger Recoils by Partial Spin-Orbit Alignment of Black-Hole Binaries”. In: *Phys. Rev. Lett.* 107.23, 231102, p. 231102.
- Lovegrove, Elizabeth and S. E. Woosley (2013). “Very Low Energy Supernovae from Neutrino Mass Loss”. In: *ApJ* 769.2, 109, p. 109.
- Lützgendorf, N. et al. (2011). “Kinematic signature of an intermediate-mass black hole in the globular cluster NGC 6388”. In: *A&A* 533, A36, A36.
- Lützgendorf, N. et al. (2013). “Limits on intermediate-mass black holes in six Galactic globular clusters with integral-field spectroscopy”. In: *A&A* 552, A49, A49.
- MacLeod, Morgan et al. (2016). “The Close Stellar Companions to Intermediate-mass Black Holes”. In: *ApJ* 819.1, 70, p. 70.
- Madau, P. and M. J. Rees (2001). “Massive Black Holes as Population III Remnants”. In: *ApJ* 551, pp. L27–L30.
- Madau, Piero and Tassos Fragos (2017). “Radiation Backgrounds at Cosmic Dawn: X-Rays from Compact Binaries”. In: *ApJ* 840.1, 39, p. 39.
- Madau, Piero and Eliot Quataert (2004). “The Effect of Gravitational-Wave Recoil on the Demography of Massive Black Holes”. In: *ApJ* 606.1, pp. L17–L20.
- Maggiore, M. (2018). *Gravitational Waves: Volume 2: Astrophysics and Cosmology*. Gravitational Waves. Oxford University Press. ISBN: 9780198570899.
- Maggiore, Michele et al. (2020). “Science case for the Einstein telescope”. In: *J. Cosmology Astropart. Phys.* 2020.3, 050, p. 050.
- Makino, J. and S. J. Aarseth (1992). “On a Hermite integrator with Ahmad-Cohen scheme for gravitational many-body problems”. In: *PASJ* 44, pp. 141–151.
- Mandel, I. and S. E. de Mink (2016). “Merging binary black holes formed through chemically homogeneous evolution in short-period stellar binaries”. In: *MNRAS* 458, pp. 2634–2647.

- Mann, C. R. et al. (2019). “A Multimass Velocity Dispersion Model of 47 Tucanae Indicates No Evidence for an Intermediate-mass Black Hole”. In: *ApJ* 875, 1, p. 1.
- Mapelli, M. (2016). “Massive black hole binaries from runaway collisions: the impact of metallicity”. In: *MNRAS* 459, pp. 3432–3446.
- Mapelli, M. (2018). “Astrophysics of stellar black holes”. In: *arXiv e-prints*.
- Mapelli, M. and A. Bressan (2013). “Impact of metallicity on the evolution of young star clusters”. In: *MNRAS* 430, pp. 3120–3127.
- Mapelli, M. and N. Giacobbo (2018). “The cosmic merger rate of neutron stars and black holes”. In: *MNRAS* 479, pp. 4391–4398.
- Mapelli, M. and L. Zampieri (2014). “Roche-lobe Overflow Systems Powered by Black Holes in Young Star Clusters: The Importance of Dynamical Exchanges”. In: *ApJ* 794, 7, p. 7.
- Mapelli, M. et al. (2009). “Low metallicity and ultra-luminous X-ray sources in the Cartwheel galaxy”. In: *MNRAS* 395, pp. L71–L75.
- Mapelli, M. et al. (2010). “Ultra-luminous X-ray sources and remnants of massive metal-poor stars”. In: *MNRAS* 408, pp. 234–253.
- Mapelli, M. et al. (2013). “Dynamics of stellar black holes in young star clusters with different metallicities - I. Implications for X-ray binaries”. In: *MNRAS* 429, pp. 2298–2314.
- Mapelli, M. et al. (2017). “The cosmic merger rate of stellar black hole binaries from the Illustris simulation”. In: *MNRAS* 472, pp. 2422–2435.
- Mapelli, M. et al. (2019a). “The properties of merging black holes and neutron stars across cosmic time”. In: *MNRAS*.
- Mapelli, Michela et al. (2018). “The host galaxies of double compact objects merging in the local Universe”. In: *MNRAS* 481.4, pp. 5324–5330.
- Mapelli, Michela et al. (2019b). “Impact of progenitor’s rotation and compactness on the mass of black holes”. In: *arXiv e-prints*, arXiv:1909.01371, arXiv:1909.01371.
- Mapelli, Michela et al. (2020a). “Impact of the Rotation and Compactness of Progenitors on the Mass of Black Holes”. In: *ApJ* 888.2, 76, p. 76.
- Mapelli, Michela et al. (2020b). “Impact of the Rotation and Compactness of Progenitors on the Mass of Black Holes”. In: *ApJ* 888.2, 76, p. 76.
- Mapelli, Michela et al. (2021). “Hierarchical black hole mergers in young, globular and nuclear star clusters: the effect of metallicity, spin and cluster properties”. In: *MNRAS* 505.1, pp. 339–358.
- Marchant, P. et al. (2016). “A new route towards merging massive black holes”. In: *A&A* 588, A50, A50.

- Marchant, Pablo et al. (2019). “Pulsational Pair-instability Supernovae in Very Close Binaries”. In: *ApJ* 882.1, 36, p. 36.
- Margutti, R. et al. (2017). “The Electromagnetic Counterpart of the Binary Neutron Star Merger LIGO/Virgo GW170817. V. Rising X-Ray Emission from an Off-axis Jet”. In: *ApJ* 848.2, p. L20.
- Marks, M. and P. Kroupa (2012). “Inverse dynamical population synthesis. Constraining the initial conditions of young stellar clusters by studying their binary populations”. In: *A&A* 543, A8, A8.
- Marks, M. et al. (2012). “Evidence for top-heavy stellar initial mass functions with increasing density and decreasing metallicity”. In: *MNRAS* 422, pp. 2246–2254.
- Mason, David M. and John H. Schuenemeyer (1983). “A Modified Kolmogorov-Smirnov Test Sensitive to Tail Alternatives”. In: *The Annals of Statistics* 11.3, pp. 933–946. ISSN: 00905364.
- Mastrobuono-Battisti, Alessandra et al. (2014). “Effects of Intermediate Mass Black Holes on Nuclear Star Clusters”. In: *ApJ* 796.1, 40, p. 40.
- Matsumoto, H. et al. (2001). “Discovery of a Luminous, Variable, Off-Center Source in the Nucleus of M82 with the Chandra High-Resolution Camera”. In: *ApJ* 547.1, pp. L25–L28.
- McKernan, B. et al. (2012). “Intermediate mass black holes in AGN discs - I. Production and growth”. In: *MNRAS* 425.1, pp. 460–469.
- McKernan, Barry et al. (2018). “Constraining Stellar-mass Black Hole Mergers in AGN Disks Detectable with LIGO”. In: *ApJ* 866.1, 66, p. 66.
- Mennekens, N. and D. Vanbeveren (2014). “Massive double compact object mergers: gravitational wave sources and r-process element production sites”. In: *A&A* 564, A134, A134.
- Merritt, David et al. (2004). “Consequences of Gravitational Radiation Recoil”. In: *ApJ* 607.1, pp. L9–L12.
- Metzger, Brian D. and Nicholas C. Stone (2016). “A bright year for tidal disruptions”. In: *MNRAS* 461.1, pp. 948–966.
- Mezcua, M. et al. (2015). “The powerful jet of an off-nuclear intermediate-mass black hole in the spiral galaxy NGC 2276”. In: *MNRAS* 448.2, pp. 1893–1899.
- Mezcua, M. et al. (2016). “A Population of Intermediate-mass Black Holes in Dwarf Starburst Galaxies Up to Redshift=1.5”. In: *ApJ* 817.1, 20, p. 20.
- Mezcua, M. et al. (2018). “Intermediate-mass black holes in dwarf galaxies out to redshift ~ 2.4 in the Chandra COSMOS-Legacy Survey”. In: *MNRAS* 478.2, pp. 2576–2591.

- Mezcua, Mar (2017). “Observational evidence for intermediate-mass black holes”. In: *International Journal of Modern Physics D* 26.11, 1730021, p. 1730021.
- Mikkola, Seppo and Sverre J. Aarseth (1993a). “An Implementation of N-Body Chain Regularization”. In: *Celestial Mechanics and Dynamical Astronomy* 57.3, pp. 439–459.
- Mikkola, Seppo and Sverre J. Aarseth (1993b). “An Implementation of N-Body Chain Regularization”. In: *Celestial Mechanics and Dynamical Astronomy* 57.3, pp. 439–459.
- Miller, M. C. and D. P. Hamilton (2002). “Production of intermediate-mass black holes in globular clusters”. In: *MNRAS* 330, pp. 232–240.
- Miller, M. C. and V. M. Lauburg (2009). “Mergers of Stellar-Mass Black Holes in Nuclear Star Clusters”. In: *ApJ* 692, pp. 917–923.
- Miller, M. Coleman and E. J. M. Colbert (2004). “Intermediate-Mass Black Holes”. In: *International Journal of Modern Physics D* 13.1, pp. 1–64.
- Miller-Jones, J. C. A. et al. (2012). “The Absence of Radio Emission from the Globular Cluster G1”. In: *ApJ* 755, L1, p. L1.
- Moe, Maxwell and Rosanne Di Stefano (2017). “Mind Your Ps and Qs: The Interrelation between Period (P) and Mass-ratio (Q) Distributions of Binary Stars”. In: *ApJS* 230.2, 15, p. 15.
- Moody, K. and S. Sigurdsson (2009). “Modeling the Retention Probability of Black Holes in Globular Clusters: Kicks and Rates”. In: *ApJ* 690, pp. 1370–1377.
- Morscher, M. et al. (2015). “The Dynamical Evolution of Stellar Black Holes in Globular Clusters”. In: *ApJ* 800, 9, p. 9.
- Neijssel, Coenraad J. et al. (2019). “The effect of the metallicity-specific star formation history on double compact object mergers”. In: *MNRAS* 490.3, pp. 3740–3759.
- Nicholl, M. et al. (2017). “The Electromagnetic Counterpart of the Binary Neutron Star Merger LIGO/Virgo GW170817. III. Optical and UV Spectra of a Blue Kilonova from Fast Polar Ejecta”. In: *ApJ* 848.2, p. L18.
- Nishizawa, A. et al. (2016). “eLISA eccentricity measurements as tracers of binary black hole formation”. In: *Phys. Rev. D* 94.6, 064020, p. 064020.
- Nishizawa, A. et al. (2017). “Constraining stellar binary black hole formation scenarios with eLISA eccentricity measurements”. In: *MNRAS* 465, pp. 4375–4380.
- Nitadori, K. and S. J. Aarseth (2012). “Accelerating NBODY6 with graphics processing units”. In: *MNRAS* 424, pp. 545–552.
- Nitadori, Keigo and Junichiro Makino (2008). “Sixth- and eighth-order Hermite integrator for N-body simulations”. In: *New A* 13.7, pp. 498–507.

- Nyland, K. et al. (2012). “The Intermediate-mass Black Hole Candidate in the Center of NGC 404: New Evidence from Radio Continuum Observations”. In: *ApJ* 753, 103, p. 103.
- O’Leary, R. M. et al. (2006). “Binary Mergers and Growth of Black Holes in Dense Star Clusters”. In: *ApJ* 637, pp. 937–951.
- O’Leary, R. M. et al. (2009). “Gravitational waves from scattering of stellar-mass black holes in galactic nuclei”. In: *MNRAS* 395, pp. 2127–2146.
- O’Leary, R. M. et al. (2016). “Dynamical Formation Signatures of Black Hole Binaries in the First Detected Mergers by LIGO”. In: *ApJ* 824, L12, p. L12.
- Orosz, J. A. (2003). “Inventory of black hole binaries”. In: *A Massive Star Odyssey: From Main Sequence to Supernova*. Ed. by K. van der Hucht et al. Vol. 212. IAU Symposium, p. 365.
- Özel, F. et al. (2010). “The Black Hole Mass Distribution in the Galaxy”. In: *ApJ* 725, pp. 1918–1927.
- Paczynski, B. (1976). “Common Envelope Binaries”. In: *Structure and Evolution of Close Binary Systems*. Ed. by Peter Eggleton et al. Vol. 73. IAU Symposium, p. 75.
- Perera, B. B. P. et al. (2017). “Evidence for an intermediate-mass black hole in the globular cluster NGC 6624”. In: *MNRAS* 468, pp. 2114–2127.
- Peters, P. C. (1964). “Gravitational Radiation and the Motion of Two Point Masses”. In: *Phys. Rev.* 136 (4B), B1224–B1232.
- Pian, E. et al. (2017). “Spectroscopic identification of r-process nucleosynthesis in a double neutron-star merger”. In: *Nature* 551, pp. 67–70.
- Planck Collaboration et al. (2016). “Planck 2015 results. XIII. Cosmological parameters”. In: *A&A* 594, A13, A13.
- Podsiadlowski, P. et al. (2004). “The Effects of Binary Evolution on the Dynamics of Core Collapse and Neutron Star Kicks”. In: *ApJ* 612, pp. 1044–1051.
- Podsiadlowski, P. et al. (2005). “The double pulsar J0737-3039: testing the neutron star equation of state”. In: *MNRAS* 361, pp. 1243–1249.
- Portegies Zwart, S. F. (2016). “Stellar disc destruction by dynamical interactions in the Orion Trapezium star cluster”. In: *MNRAS* 457, pp. 313–319.
- Portegies Zwart, S. F. and S. L. W. McMillan (2000a). “Black Hole Mergers in the Universe”. In: *ApJ* 528, pp. L17–L20.
- Portegies Zwart, S. F. and S. L. W. McMillan (2000b). “Black Hole Mergers in the Universe”. In: *ApJ* 528, pp. L17–L20.
- Portegies Zwart, S. F. and S. L. W. McMillan (2002). “The Runaway Growth of Intermediate-Mass Black Holes in Dense Star Clusters”. In: *ApJ* 576, pp. 899–907.

- Portegies Zwart, S. F. and L. R. Yungelson (1998). “Formation and evolution of binary neutron stars”. In: *A&A* 332, pp. 173–188.
- Portegies Zwart, S. F. et al. (2004). “Formation of massive black holes through runaway collisions in dense young star clusters”. In: *Nature* 428, pp. 724–726.
- Portegies Zwart, S. F. et al. (2010). “Young Massive Star Clusters”. In: *ARA&A* 48, pp. 431–493.
- Prialnik, D. (2000). *An Introduction to the Theory of Stellar Structure and Evolution*.
- Punturo, M. et al. (2010). “The Einstein Telescope: a third-generation gravitational wave observatory”. In: *Classical and Quantum Gravity* 27.19, 194002, p. 194002.
- Qin, Y. et al. (2018). “The spin of the second-born black hole in coalescing binary black holes”. In: *A&A* 616, A28, A28.
- Qin, Ying et al. (2019). “On the Origin of Black Hole Spin in High-mass X-Ray Binaries”. In: *ApJ* 870.2, L18, p. L18.
- Quinlan, Gerald D. (1996). “The dynamical evolution of massive black hole binaries I. Hardening in a fixed stellar background”. In: *New A* 1.1, pp. 35–56.
- Raccanelli, A. et al. (2016). “Determining the progenitors of merging black-hole binaries”. In: *Phys. Rev. D* 94.2, 023516, p. 023516.
- Rastello, S. et al. (2019). “Stellar black hole binary mergers in open clusters”. In: *MNRAS* 483.1, pp. 1233–1246.
- Reines, Amy E. and Marta Volonteri (2015). “Relations between Central Black Hole Mass and Total Galaxy Stellar Mass in the Local Universe”. In: *ApJ* 813.2, 82, p. 82.
- Reines, Amy E. et al. (2020). “A New Sample of (Wandering) Massive Black Holes in Dwarf Galaxies from High-resolution Radio Observations”. In: *ApJ* 888.1, 36, p. 36.
- Reitze, David et al. (2019). “Cosmic Explorer: The U.S. Contribution to Gravitational-Wave Astronomy beyond LIGO”. In: *Bulletin of the American Astronomical Society*. Vol. 51, p. 35.
- Renzo, M. et al. (2020). “Sensitivity of the lower-edge of the pair instability black hole mass gap to the treatment of time dependent convection”. In: *MNRAS*.
- Repetto, S. et al. (2012). “Investigating stellar-mass black hole kicks”. In: *MNRAS* 425, pp. 2799–2809.
- Repetto, S. et al. (2017). “The Galactic distribution of X-ray binaries and its implications for compact object formation and natal kicks”. In: *MNRAS* 467, pp. 298–310.
- Rizzuto, Francesco Paolo et al. (2021). “Intermediate mass black hole formation in compact young massive star clusters”. In: *MNRAS* 501.4, pp. 5257–5273.

- Rodriguez, C. L. et al. (2015). “Binary Black Hole Mergers from Globular Clusters: Implications for Advanced LIGO”. In: *Physical Review Letters* 115.5, 051101, p. 051101.
- Rodriguez, C. L. et al. (2016). “Illuminating Black Hole Binary Formation Channels with Spins in Advanced LIGO”. In: *ApJ* 832, L2, p. L2.
- Rodriguez, C. L. et al. (2018). “Post-Newtonian dynamics in dense star clusters: Formation, masses, and merger rates of highly-eccentric black hole binaries”. In: *Phys. Rev. D* 98.12, 123005, p. 123005.
- Rodriguez, Carl L. and Abraham Loeb (2018). “Redshift Evolution of the Black Hole Merger Rate from Globular Clusters”. In: *ApJ* 866.1, L5, p. L5.
- Rodriguez, Carl L. et al. (2019). “Black holes: The next generation—repeated mergers in dense star clusters and their gravitational-wave properties”. In: *Phys. Rev. D* 100.4, 043027, p. 043027.
- Sadowski, A. et al. (2008). “The Total Merger Rate of Compact Object Binaries in the Local Universe”. In: *ApJ* 676, pp. 1162–1169.
- Samsing, J. (2018). “Eccentric black hole mergers forming in globular clusters”. In: *Phys. Rev. D* 97.10, 103014, p. 103014.
- Samsing, J. and D. J. D’Orazio (2018). “Black Hole Mergers From Globular Clusters Observable by LISA I: Eccentric Sources Originating From Relativistic N-body Dynamics”. In: *MNRAS* 481, pp. 5445–5450.
- Samsing, J. et al. (2017). “Formation of Tidal Captures and Gravitational Wave Inspirals in Binary-single Interactions”. In: *ApJ* 846, 36, p. 36.
- Samsing, J. et al. (2018). “MOCCA-SURVEY Database. I. Eccentric Black Hole Mergers during Binary-Single Interactions in Globular Clusters”. In: *ApJ* 855, 124, p. 124.
- Sana, H. et al. (2012). “Binary Interaction Dominates the Evolution of Massive Stars”. In: *Science* 337, p. 444.
- Sanders, R. H. (1970). “The Effects of Stellar Collisions in Dense Stellar Systems”. In: *ApJ* 162, p. 791.
- Santoliquido, Filippo et al. (2020). “The cosmic merger rate density evolution of compact binaries formed in young star clusters and in isolated binaries”. In: *arXiv e-prints*, arXiv:2004.09533, arXiv:2004.09533.
- Sasaki, M. et al. (2016). “Primordial Black Hole Scenario for the Gravitational-Wave Event GW150914”. In: *Physical Review Letters* 117.6, 061101, p. 061101.
- Savchenko, V. et al. (2017). “INTEGRAL Detection of the First Prompt Gamma-Ray Signal Coincident with the Gravitational-wave Event GW170817”. In: *ApJ* 848.2, p. L15.

- Scelfo, G. et al. (2018). “GW LSS: chasing the progenitors of merging binary black holes”. In: *J. Cosmology Astropart. Phys.* 9, 039, p. 039.
- Schneider, R. et al. (2002). “First Stars, Very Massive Black Holes, and Metals”. In: *ApJ* 571, pp. 30–39.
- Schödel, R. et al. (2014). “Surface brightness profile of the Milky Way’s nuclear star cluster”. In: *A&A* 566, A47, A47.
- Schwab, J. et al. (2015). “Thermal runaway during the evolution of ONeMg cores towards accretion-induced collapse”. In: *MNRAS* 453, pp. 1910–1927.
- Seth, Anil C. et al. (2010). “The NGC 404 Nucleus: Star Cluster and Possible Intermediate-mass Black Hole”. In: *ApJ* 714.1, pp. 713–731.
- Shao, Yong and Xiang-Dong Li (2018). “Black hole/pulsar binaries in the Galaxy”. In: *MNRAS* 477.1, pp. L128–L132.
- Shukirgaliyev, B. et al. (2017). “Impact of a star formation efficiency profile on the evolution of open clusters”. In: *A&A* 605, A119, A119.
- Sigurdsson, S. and L. Hernquist (1993). “Primordial black holes in globular clusters”. In: *Nature* 364, pp. 423–425.
- Sigurdsson, S. and E. S. Phinney (1995). “Dynamics and Interactions of Binaries and Neutron Stars in Globular Clusters”. In: *ApJS* 99, p. 609.
- Soares-Santos, M. et al. (2017). “The Electromagnetic Counterpart of the Binary Neutron Star Merger LIGO/Virgo GW170817. I. Discovery of the Optical Counterpart Using the Dark Energy Camera”. In: *ApJ* 848.2, p. L16.
- Spera, M. and M. Mapelli (2017). “Very massive stars, pair-instability supernovae and intermediate-mass black holes with the sevn code”. In: *MNRAS* 470, pp. 4739–4749.
- Spera, M. et al. (2015). “The mass spectrum of compact remnants from the PARSEC stellar evolution tracks”. In: *MNRAS* 451, pp. 4086–4103.
- Spera, M. et al. (2019a). “Merging black hole binaries with the SEVN code”. In: *MNRAS* 485, pp. 889–907.
- Spera, Mario et al. (2019b). “Merging black hole binaries with the SEVN code”. In: *MNRAS* 485.1, pp. 889–907.
- Spitzer Jr., L. (1969). “Equipartition and the Formation of Compact Nuclei in Spherical Stellar Systems”. In: *ApJ* 158, p. L139.
- Spitzer, Lyman (1987). *Dynamical evolution of globular clusters*.
- Stevenson, Simon et al. (2017). “Formation of the first three gravitational-wave observations through isolated binary evolution”. In: *Nature Communications* 8, 14906, p. 14906.

- Stevenson, Simon et al. (2019). “The Impact of Pair-instability Mass Loss on the Binary Black Hole Mass Distribution”. In: *ApJ* 882.2, 121, p. 121.
- Stiefel, E. (1965). “Perturbation theory of Kepler motion based on spinor regularization.” In: *Journal für die reine und angewandte Mathematik* 218, pp. 204–219.
- Stone, Nicholas C. et al. (2017). “Assisted inspirals of stellar mass black holes embedded in AGN discs: solving the ‘final au problem’”. In: *MNRAS* 464.1, pp. 946–954.
- Strader, Jay et al. (2012). “No Evidence for Intermediate-mass Black Holes in Globular Clusters: Strong Constraints from the JVLA”. In: *ApJ* 750.2, L27, p. L27.
- Strohmayer, Tod E. and Richard F. Mushotzky (2003). “Discovery of X-Ray Quasi-periodic Oscillations from an Ultraluminous X-Ray Source in M82: Evidence against Beaming”. In: *ApJ* 586.1, pp. L61–L64.
- Sugimoto, D. and E. Bettwieser (1983). “Post-collapse evolution of globular clusters”. In: *MNRAS* 204, 19P–22P.
- Sukhbold, T. et al. (2016). “Core-collapse Supernovae from 9 to 120 Solar Masses Based on Neutrino-powered Explosions”. In: *ApJ* 821, 38, p. 38.
- Sutton, Andrew D. et al. (2012). “The most extreme ultraluminous X-ray sources: evidence for intermediate-mass black holes?” In: *MNRAS* 423.2, pp. 1154–1177.
- Swartz, Douglas A. et al. (2004). “The Ultraluminous X-Ray Source Population from the Chandra Archive of Galaxies”. In: *ApJS* 154.2, pp. 519–539.
- Tagawa, Hiromichi et al. (2021a). “Mass-gap Mergers in Active Galactic Nuclei”. In: *ApJ* 908.2, 194, p. 194.
- Tagawa, Hiromichi et al. (2021b). “Signatures of Hierarchical Mergers in Black Hole Spin and Mass distribution”. In: *arXiv e-prints*, arXiv:2104.09510, arXiv:2104.09510.
- Takekawa, Shunya et al. (2019). “Indication of Another Intermediate-mass Black Hole in the Galactic Center”. In: *ApJ* 871.1, L1, p. L1.
- Takekawa, Shunya et al. (2020). “The Fifth Candidate for an Intermediate-mass Black Hole in the Galactic Center”. In: *ApJ* 890.2, 167, p. 167.
- Tanaka, Kunihiro (2018). “ALMA Images of the Host Cloud of the Intermediate-mass Black Hole Candidate CO-0.40-0.22*: No Evidence for Cloud-Black Hole Interaction, but Evidence for a Cloud-Cloud Collision”. In: *ApJ* 859.2, 86, p. 86.
- Tang, Petra N. et al. (2020). “Dependence of gravitational wave transient rates on cosmic star formation and metallicity evolution history”. In: *MNRAS* 493.1, pp. L6–L10.

- Tanikawa, A. (2013). “Dynamical evolution of stellar mass black holes in dense stellar clusters: estimate for merger rate of binary black holes originating from globular clusters”. In: MNRAS 435.2, pp. 1358–1375.
- Tanikawa, Ataru et al. (2021). “Merger Rate Density of Population III Binary Black Holes Below, Above, and in the Pair-instability Mass Gap”. In: ApJ 910.1, 30, p. 30.
- Tauris, T. M. et al. (2015). “Ultra-stripped supernovae: progenitors and fate”. In: MNRAS 451, pp. 2123–2144.
- Tauris, T. M. et al. (2017). “Formation of Double Neutron Star Systems”. In: ApJ 846, 170, p. 170.
- Trani, A. A. et al. (2014). “The impact of metallicity-dependent mass-loss versus dynamical heating on the early evolution of star clusters”. In: MNRAS 445, pp. 1967–1976.
- Tremou, E. et al. (2018). “The MAVERIC Survey: Still No Evidence for Accreting Intermediate-mass Black Holes in Globular Clusters”. In: ApJ 862, 16, p. 16.
- Trenti, Michele et al. (2007). “Star clusters with primordial binaries - III. Dynamical interaction between binaries and an intermediate-mass black hole”. In: MNRAS 374.3, pp. 857–866.
- Trenti, Michele et al. (2010). “Tidal Disruption, Global Mass Function, and Structural Parameter Evolution in Star Clusters”. In: ApJ 708.2, pp. 1598–1610.
- Tutukov, A. et al. (1973). “Evolution of primaries of massive close binary systems”. In: *Nauchnye Informatsii* 27, p. 3.
- Usman, Samantha A. et al. (2016). “The PyCBC search for gravitational waves from compact binary coalescence”. In: *Class. Quant. Grav.* 33.21, p. 215004.
- van der Marel, R. P. and J. Anderson (2010). “New Limits on an Intermediate-Mass Black Hole in Omega Centauri. II. Dynamical Models”. In: ApJ 710, pp. 1063–1088.
- van der Marel, Roeland P. (2004). “Intermediate-mass Black Holes in the Universe: A Review of Formation Theories and Observational Constraints”. In: *Coevolution of Black Holes and Galaxies*. Ed. by Luis C. Ho, p. 37.
- VanLandingham, J. H. et al. (2016). “The Role of the Kozai–Lidov Mechanism in Black Hole Binary Mergers in Galactic Centers”. In: ApJ 828, 77, p. 77.
- Verbunt, F. et al. (2017). “The observed velocity distribution of young pulsars”. In: A&A 608, A57, A57.
- Vigna-Gómez, Alejandro et al. (2019). “Massive Stellar Mergers as Precursors of Hydrogen-rich Pulsational Pair Instability Supernovae”. In: ApJ 876.2, L29, p. L29.
- Vink, J. S. (2016). “Mass loss and stellar superwinds”. In: *ArXiv e-prints*.

- Vink, J. S. et al. (2001). “Mass-loss predictions for O and B stars as a function of metallicity”. In: *A&A* 369, pp. 574–588.
- Vink, J. S. et al. (2011). “Wind modelling of very massive stars up to 300 solar masses”. In: *A&A* 531, A132, A132.
- Volonteri, Marta (2010). “Formation of supermassive black holes”. In: *A&A Rev.* 18.3, pp. 279–315.
- Voss, R. and T. M. Tauris (2003). “Galactic distribution of merging neutron stars and black holes - prospects for short gamma-ray burst progenitors and LIGO/VIRGO”. In: *MNRAS* 342, pp. 1169–1184.
- Wang, Chen et al. (2016). “The binding energy parameter for common envelope evolution”. In: *Research in Astronomy and Astrophysics* 16.8, 126, p. 126.
- Wang, Jingbo et al. (2003). “Evaluating Kolmogorov’s distribution”. In: *Journal of Statistical Software* 8.18.
- Wang, L. et al. (2015). “NBODY6++GPU: ready for the gravitational million-body problem”. In: *MNRAS* 450, pp. 4070–4080.
- Ward, Jacob L. et al. (2020). “Not all stars form in clusters - Gaia-DR2 uncovers the origin of OB associations”. In: *MNRAS* 495.1, pp. 663–685.
- Woosley, S. E. (1987). “Theoretical Models for SN1987a”. In: *Bulletin of the American Astronomical Society*. Vol. 19, p. 740.
- Woosley, S. E. (2017). “Pulsational Pair-instability Supernovae”. In: *ApJ* 836.2, 244, p. 244.
- Woosley, S. E. (2019). “The Evolution of Massive Helium Stars, Including Mass Loss”. In: *ApJ* 878.1, 49, p. 49.
- Woosley, S. E. et al. (2007). “Pulsational pair instability as an explanation for the most luminous supernovae”. In: *Nature* 450, pp. 390–392.
- Wu, Samantha et al. (2020). “The Art of Modeling Stellar Mergers and the Case of the B[e] Supergiant R4 in the Small Magellanic Cloud”. In: *arXiv e-prints*, arXiv:2006.01940, arXiv:2006.01940.
- Yang, Y. et al. (2019). “AGN Disks Harden the Mass Distribution of Stellar-mass Binary Black Hole Mergers”. In: *ApJ* 876.2, 122, p. 122.
- Zampieri, L. and T. P. Roberts (2009). “Low-metallicity natal environments and black hole masses in ultraluminous X-ray sources”. In: *MNRAS* 400.2, pp. 677–686.
- Zevin, M. et al. (2017). “Constraining Formation Models of Binary Black Holes with Gravitational-wave Observations”. In: *ApJ* 846, 82, p. 82.
- Zevin, M. et al. (2019a). “Eccentric Black Hole Mergers in Dense Star Clusters: The Role of Binary-Binary Encounters”. In: *ApJ* 871, 91, p. 91.

- Zevin, Michael et al. (2019b). “Eccentric Black Hole Mergers in Dense Star Clusters: The Role of Binary-Binary Encounters”. In: *ApJ* 871.1, 91, p. 91.
- Ziosi, B. M. et al. (2014). “Dynamics of stellar black holes in young star clusters with different metallicities - II. Black hole-black hole binaries”. In: *MNRAS* 441, pp. 3703–3717.
- Zocchi, A. et al. (2019). “The effect of stellar-mass black holes on the central kinematics of ω Cen: a cautionary tale for IMBH interpretations”. In: *MNRAS* 482, pp. 4713–4725.